



## City Research Online

### City, University of London Institutional Repository

---

**Citation:** Henington, P. (1982). An improved boundary condition for perforated wall windtunnel flows. (Unpublished Doctoral thesis, The City University, London)

This is the accepted version of the paper.

This version of the publication may differ from the final published version.

---

**Permanent repository link:** <https://openaccess.city.ac.uk/id/eprint/35662/>

**Link to published version:**

**Copyright:** City Research Online aims to make research outputs of City, University of London available to a wider audience. Copyright and Moral Rights remain with the author(s) and/or copyright holders. URLs from City Research Online may be freely distributed and linked to.

**Reuse:** Copies of full items can be used for personal research or study, educational, or not-for-profit purposes without prior permission or charge. Provided that the authors, title and full bibliographic details are credited, a hyperlink and/or URL is given for the original metadata page and the content is not changed in any way.

AN IMPROVED BOUNDARY CONDITION FOR PERFORATED WALL WINDTUNNEL FLOWS

by Paul Henington

Thesis submitted for the degree of Doctor of Philosophy.

The City University, London.

Department of Aeronautics.

June 1982



## CONTENTS.

	<u>PAGE.</u>
List of Figures.	4
List of Tables and List of Plates.	7
Abstract.	10
List of Abbreviations.	11
 <u>Report Sections:</u>	
1 INTRODUCTION.	14
 2 BACKGROUND TO THE PERFORATED WALL BOUNDARY CONDITION.	21
2.1 History.	21
2.2 Summary of reasons for improving the perforated wall boundary condition.	32
 3 PROPOSAL FOR A NEW BOUNDARY CONDITION.	33
3.1 Position of application of Boundary Condition.	33
3.2 The Calculation Scheme to be Employed.	37
3.3 Objectives of the Computer Program; 'PILOT'.	41
3.4 Formulation of the Computer Program; 'PILOT'.	42
3.5 Boundary Layer Prediction Method.	62
3.6 Scheme for the Cross-flow Characteristic.	69
3.7 The New Boundary Condition Equation.	74
3.7.1 Mode of application of the new boundary condition.	79
3.8 Results from the Computer Program PILOT.	80
3.8.1 Demonstration that the computer program PILOT converges and that in some cases, results from the method are realistic.	80
3.8.2 Investigation of some new aspects of wind-tunnel flow simulation.	85
 4 EXPERIMENTS AND ANALYSIS.	100
4.1 Experimental Objectives.	100
4.2 Experimental Equipment.	102
4.2.1 Practical Approach.	102
4.2.2 The Windtunnel.	103
4.2.3 The Contoured Top Wall.	105
4.2.4 The Lower Plenum Chamber and Perforated Wall.	108
4.2.5 Choosing an Instrument to Measure Flow Angle.	115
4.2.6 The Combined Boundary Layer and Yawmeter Rake.	119
4.2.7 Ancillary Equipment.	130
4.2.8 A note on Windtunnel Flow Uniformity.	133

	<u>PAGE.</u>
4.3 Experiments and Initial Analysis.	139
4.3.1 Experimental Conditions.	139
4.3.2 Experimental Method.	140
4.3.3 Initial Analysis of Experimental Data.	142
4.3.4 Accuracy of Experimental Data.	151
4.3.5 Discussion of Experimental Results.	156
4.4 The Empirical Wall Characteristic.	167
4.4.1 Evaluation of the Wall Characteristic.	167
4.4.2 Discussion of the Characteristic.	171
5 PREDICTION OF FLOW NEAR THE PERFORATED WALL.	177
5.1 Objectives of the Computer Program 'PREDICT'.	177
5.2 Details of the Computer Program 'PREDICT'.	178
5.2.1 The overall Scheme.	178
5.2.2 Details of the Scheme.	180
5.3 Results from the Computer Program PREDICT.	184
5.4 Discussion of the Accuracy of PREDICT.	191
6 COMPARISON BETWEEN EXPERIMENTAL RESULTS AND THOSE FROM 'PILOT'.	195
7 SUMMARY OF CONCLUSIONS WITH RECOMMENDATIONS.	205
<u>Appendices:</u>	
1. Prediction of the pressure distribution in an empty perforated working section.	210
2. Development of equations of continuity to be applied at a porous wall.	213
3. Practical running of the FORTRAN computer program PILOT.	216
4. Example adaption of a practical transonic flow calculation to use the proposed wall boundary condition.	236
5. Proof that a yawmeter may dip into a boundary layer without this significantly affecting predicted crossflows.	239
6. Proof that the results obtained with the flow angle instruments are not significantly influenced by small angles of yaw.	244
7. Calibration of yawmeters.	247
8. Estimation of errors in yawmeter calibration.	262
9. The computer program PROF for analysing boundary layer profiles.	266
10. Calculation of the parameter $\frac{\rho U_0}{\rho U_{\infty}}$ in terms of known variables.	270
11. Listing of the Computer Program PREDICT.	272
<u>References.</u>	279



## LIST OF FIGURES

Figure:	Title:	Page:
1	Typical pressure distributuion on upper and lower walls of a two-dimensional windtunnel with lifting aerofoil mounted. $-M=0.72$ .	17
2	Wall characteristic due to Goethert, for various boundary layer thicknesses, at $M=0.9$	23
3	Wall characteristic due to Goethert, for various Mach numbers, with a boundary layer thickness of approximately 1.5mm.	24
4	Comparison of calculated aerofoil pressure distributions with that from experiment -Catherall(1975).	27
5	Diagram of streamlines near and through a perforated wall	34
6	Diagram of control volumes near wall.	36
7	Flow diagram of proposed computing scheme.	39
8	Diagram of overall flow situation modelled by PILOT.	43
9	Schematic diagram of typical windtunnel representation in PILOT.	44
10	Diagram of general distributed source element.	47
11	Flow diagram of computer program PILOT.	50
12	Diagram to elucidate method of obtaining a local linear wall characteristic.	58
13	Results from boundary layer method compared with experiments using smooth wall.	66
14	Results from boundary layer method compared with experiments using rough wall.	68
15	Results from boundary layer method compared with experiments using rough wall -Sterland.	70
16	Wall characteristic due to Goethert, for various Mach numbers, with a boundary layer thickness of approximately 1.5mm.	73
17	Comparison of results from PILOT, with two boundary condition types with those from experiments.	77
18	Diagram of windtunnel configuration modelled, in comparison of PILOT with exact potential theory.	81
19	Comparison of PILOT results with exact theory.	83
20	Comparison of results from PILOT, with those obtained using the method of Goethert, for an empty working section	84
21	Results from PILOT to demonstrate the effect of varying plenum chamber pressure, on a windtunnel flow.	86
22	Results from PILOT to indicate the effect of varying wall porosity, on the windtunnel flow.	88
23	Results from PILOT to demonstrate the influence of finite perforated sections of wall.	90



Figure:	Title:	Page:
24	Results from PILOT to demonstrate the effects of the new boundary condition on flows with a lifting aerofoil-wall pressures.	93
25	Results from PILOT to demonstrate the effect of the new boundary condition on flows with a lifting aerofoil-wall crossflows.	95
26	Results from PILOT to demonstrate the influence of wall boundary layer on the windtunnel flow- configuration and boundary layer development.	97
27	Results from PILOT to demonstrate the influence of wall boundary layer on the windtunnel flow -wall pressure and crossflow distribution.	98
28	Diagram of Transonic windtunnel.	104
29	Typical pressure distribution on upper and lower walls of a two-dimensional windtunnel with lifting aerofoil mounted -M=0.82.	109
30	Drawing of lower perforated wall and plenum chamber.	112
31	Diagram of wall perforation pattern.	116
32	Diagram of forward part of combined boundary layer rake and yawmeter assembly.	121
33	Schematic diagram showing ancillary equipment used in experiments.	131
34	Positions of boundary layer rake foot during non-uniformity investigation.	136
35	Boundary layer results obtained during non-uniformity investigation.	137
36	Graph of $\delta^*$ with $M_{\infty}$ for experimental data obtained at X=309mm.	147
37	Graph of boundary layer displacement thickness with longitudinal position -experimental results.	150
38	Graph of $\frac{\rho U_e}{\rho_{\infty} U_{\infty}}$ with longitudinal position -experimental results.	152
39	Pressure distributions along perforated wall -opposite wall contoured, no rake mounted.	157
40	Pressure distributions along perforated wall -opposite wall contoured, rake installed.	159
41	Boundary layer velocity profiles obtained at various longitudinal positions with a range of freestream Mach numbers.	161
42	Graph of flow angle outside boundary layer with longitudinal position -experimental results.	163
43	Graph of wall pressure coefficient with longitudinal position -experimental results.	164

Figure:	Title:	Page:
44	Graph of average crossflow at the perforated wall, with longitudinal position -experimental results.	166
45	Graph of $\theta_w$ with $\Delta p/q$ -experimental wall characteristic.	172
46	Proposed wall characteristic in graphical form.	174
47	Flow diagram of computer program PREDICT.	179
48	Graph of plenum chamber pressure coefficient with longitudinal position -limited experimental results.	186
49	Results from PREDICT compared with experiment - crossflows at wall.	188
50	Results from PREDICT compared with experiment - boundary layer displacement thickness.	190
51	Diagram showing transfer of information within program PREDICT.	192
52	Results from PILOT compared with experiment -wall pressures	199
53	Results from PILOT compared with experiment -wall crossflow angles.	201
54	Results from PILOT compared with experiment - boundary layer displacement thickness.	204
55	Diagram of velocity components in flow striking nose of yawmeter.	245
56	Diagram of yawmeter calibration device.	249
57	Graph of $p_{04}(1-\delta^*)$ with longitudinal position - yawmeter calibration tests.	253
58	Graph of yawmeter pressure difference with yawmeter angle -calibration tests.	255
59	Final yawmeter calibration curves.	257
60	Yawmeter calibration curve, intercept data.	259
61	Boundary layer displacement thickness distributions - yawmeter calibration tests.	260



LIST OF TABLES AND LIST OF PLATES.

Table:	Title:	Page:
1	Ordinates of contoured wall.	110
2	Positions of perforated wall, and plenum chamber static tapings.	114
3	Heights of boundary layer rake tubes from wall.	124
4	Yawmeter calibration equation data.	128
5	Data reduced from main experiments.	143
6	Uncertainties in basic experimental data.	154
7	Data for operation of PILOT.	197

Plate:	Title:	Page:
1	General view of windtunnel working section.	16
2	Transonic windtunnel and auxiliary ejector.	106
3	Contoured top wall and plenum box.	111
4	Bottom plenum chamber and perforated wall.	115
5	Combined boundary layer rake and yawmeter assembly in windtunnel.	122
6	Device for determining the gradient of the yawmeter calibration; mounted in windtunnel.	248

## ACKNOWLEDGEMENTS

In the pursuit of this research and the production of this report, I have received help from many friends and members of my family. I am especially grateful to my mother for her faithful support and encouragement. Among my friends, I wish to make special mention of the staff and technicians of the Aeronautics Department, without whose help this work would have been impossible.

The leadership and support given to me by Dr. Mike Freestone has been the best possible. His direct contributions to the work reported include; a significant part of the development of the overall calculation scheme; the production of the boundary layer method; and the design of the contoured wall.

I gratefully acknowledge the considerable moral, material and financial support given by the Aircraft Research Association and its staff. In addition, the members of the Aerodynamics Department of the Royal Aircraft Establishment have lent their enthusiastic support to this work.

The early stages of this research were carried out with the financial support of the Science and Engineering Research Council.

[REDACTED]



CONSULTATION AND COPYING.

I grant powers of discretion to the University Librarian to allow this thesis to be copied in whole or in part without further reference to me. This permission covers only single copies made for study purposes, subject to normal conditions of acknowledgement.

### ABSTRACT.

The linear homogeneous boundary condition, currently applied to flow calculations, to represent perforated windtunnel walls, is known to be inadequate. An improved boundary condition, which takes account of viscous effects in the flow near such walls, is proposed here. This boundary condition requires data relating to the flow through the particular type of wall of interest, and experiments have been carried out to generate data for this cross-flow, for a wall with an open area ratio of 6 percent and 60 degree inclined perforations. The results from these experiments yield the wall crossflow characteristic. When used in conjunction with a boundary layer prediction method, also developed during this research, it is possible to generate the required boundary condition, for application to inviscid flow calculations.

It is demonstrated that the new boundary condition is capable of modelling the viscous flows, near and through the perforated wall with some success, for a range of high subsonic Mach number flows through the windtunnel, wall crossflow angles being simulated with a standard deviation of discrepancy of 0.11 degree about the experimental values.

A potential flow method has been developed, for calculating the subsonic flow of air through a windtunnel with solid and porous regions of wall, with a lifting aerofoil mounted in the working section. This method operates successfully, and when incorporating the proposed boundary condition, gives results which agree favourably with experiment.

Although calculations carried out using the proposed boundary condition are certainly more accurate than those using conventional linear boundary conditions, it is considered that still further improvement is required. This improvement is likely to be achieved using the present method, if experiments are performed more accurately and some changes are made to present computer programs.



# SYMBOLS AND ABBREVIATIONS.

A	matrix or scalar constant in perforated wall boundary condition, also cross-sectional area of aerofoil, $m^2$
a	speed of sound, $ms^{-1}$
B	matrix or scalar constant in perforated wall boundary condition
C	constant in yawmeter calibration equation - flow angle as independent variable
$C_f$	skin friction coefficient ( $\tau_w / \frac{1}{2} \rho_e u_e^2$ )
$C_L$	lift coefficient
$C_p$	pressure coefficient
c	aerofoil chord, m, also constant in yawmeter calibration equation - flow angle as dependent variable, degree
d	perforation diameter, mm
E	porosity parameter, in transformed plane
EK	offset in proposed boundary condition, in transformed plane
e	base of Napierian logarithms (2.7183)
F	slot parameter
H	boundary layer shape parameter ( $\delta^*/\theta$ ), also working section height (half height in Catherall's notation), m
K	constant in proposed boundary condition, also porosity parameter in Goethert's notation
L	height of yawmeter or distance of 'e' station, from wall, mm
l	reference length, m
M	Mach number, also constant in yawmeter calibration equation - flow angle as independent variable
m	constant in yawmeter calibration equation - flow angle as dependent variable, degree
O	order of magnitude
P	porosity parameter
p	pressure, Pascal
q	local dynamic head ( $\frac{1}{2} \rho U^2$ )
Re	Reynolds number ( $\rho u l / \mu$ )
T	absolute temperature, Kelvin
U, u	longitudinal speed, $ms^{-1}$
u	velocity perturbation in longitudinal direction, $ms^{-1}$
v	velocity (or velocity perturbation) normal to longitudinal direction, $ms^{-1}$
$V_w$	local average of normal component of velocity at perforated wall in viscous flow, $ms^{-1}$
$\bar{V}_w$	normal component of velocity in effective inviscid stream at wall position, $ms^{-1}$
X, x	longitudinal ordinate in windtunnel flow, mm

y lateral ordinate across windtunnel wall in experiment, mm,  
also vertical ordinate in computer program PILOT, m

z,3 ordinate normal to freestream direction, mm

$\beta$  Prandtl-Glauert factor  $\sqrt{1-M_\infty^2}$

$\Gamma$  aerofoil vortex strength,  $m^2 s^{-1}$

$\gamma$  ratio of specific heats (1.401)

$\Delta$  change in a quantity

$\Delta p/q$  non-dimensional pressure difference, measured across perforated wall, also between measured pressures at both orifices of yawmeter head

$\Delta x, z$  change in value of x or z between successive points in finite-difference grid

$\delta$  boundary layer thickness ( $U(\delta) = 0.99 U_e$ )

$\delta^*$  boundary layer displacement thickness, mm  $\left( \int_0^\infty \left( 1 - \frac{\rho u}{\rho_e u_e} \right) dz \right)$

$\theta$  boundary layer momentum thickness, mm  $\left( \int_0^\infty \frac{\rho u}{\rho_e u_e} \left( 1 - \frac{\rho u}{\rho_e u_e} \right) dz \right)$   
also angle of flow striking yawmeter head (degree), also flow angle, radian

$\theta_w$  local average of crossflow parameter at wall in viscous flow  $\left( \frac{\rho_w v_w}{\rho_e u_e} \right)$

$\bar{\theta}_w$  crossflow parameter at wall position in effective inviscid flow  $\left( \frac{\rho_w v_w}{\rho_e u_e} \right)$

$\mu$  aerofoli doublet strength ( $m^3 s^{-1}$ ), also dynamic viscosity,  $kg m^{-1} s^{-1}$

$\pi$  3.14159

$\rho$  density,  $kg m^{-3}$

$\bar{\rho}_w u_w$  longitudinal mass flux at wall position in effective inviscid flow

$\bar{\rho}_w v_w$  mass flux normal to freestream, at wall position, in effective inviscid flow

$\rho_w v_w$  local average mass flux normal to freestream, at wall, in viscous flow

$\sigma$  standard deviation of discrepancy

$\tau_w$  wall shearing stress

$\phi$  velocity potential

$\chi$  statistical variance

$\infty$  infinity

### Subscripts

e just outside boundary layer

h normal to wall

L lower wall

p, pl plenum chamber

R reference



r rake tube  
 s static  
 U upper wall  
 w at wall position  
 x signifying a derivative with respect to 'x', also signifying  
 a parameter evaluated at a particular value of 'x'  
 z signifying a derivative with respect to 'z'  
 $\theta$  evaluated with momentum thickness as reference length  
 0 stagnation or pitot  
 1 at lower orifice of yawmeter  
 2 at upper orifice of yawmeter  
 $\infty$  freestream condition

#### Abbreviations

exp exponentiate  
 kg kilogramme  
 ln natural logarithm  
 m metre  
 mm millimetre  
 NASA National Aeronautics and Space Administration  
 ONERA Office National d'Études et de Recherches Aérospatiales  
 Pa Pascal ( $\text{Nm}^{-2}$ )  
 s second

## 1. INTRODUCTION

The testing of aircraft models in transonic windtunnels, to simulate free air conditions, presents special problems. Notably, at freestream Mach numbers approaching unity, the flow is susceptible to choking with even small changes in the effective cross-sectional area of the windtunnel. Also, flow disturbances produced by a model diminish relatively slowly in lateral directions at transonic speeds and consequently interference between the windtunnel walls and the model flowfield is then generally more important than at low speeds. To reduce the interference, transonic windtunnels are fitted with ventilated liners. Whilst the problems are alleviated by ventilated walls, the precise nature of and conditions relating to the flow at such perforated or slotted walls are not yet clearly understood, as they involve highly complicated shear flows. If the effects of perforated wall windtunnel interference are to be predicted accurately, then improvements in the boundary condition currently applied at the walls are needed. Failure to use accurate conditions may result in significant errors in deducing aerodynamic forces on the test model, applicable to the free air situation (Vidal, Erickson and Catlin, 1975).

Ventilated wall windtunnels of the perforated type<sup>†</sup> are used in two and three-dimensional tests in many countries. A linear homogeneous boundary condition appropriate to a porous wall and commonly used to represent a perforated wall in two-dimensional, inviscid, calculation methods is of the form

$$\phi_x \pm \frac{1}{p} \phi_z = 0 \quad . \quad (1.1)$$

Here  $\phi_x$  is the longitudinal derivative of the velocity potential (and thus is related to local pressure coefficient),  $\phi_z$  is the derivative of the velocity potential with respect to the normal ordinate (and thus is related to the angle of the flow relative to the freestream direction)

<sup>†</sup> The present work is restricted to a study of perforated walls. The nature of the flow near slotted walls is considerably different to that near perforated ones. Advances are being made in understanding of such slotted wall flows, for example Berndt and Sorensen (1975).



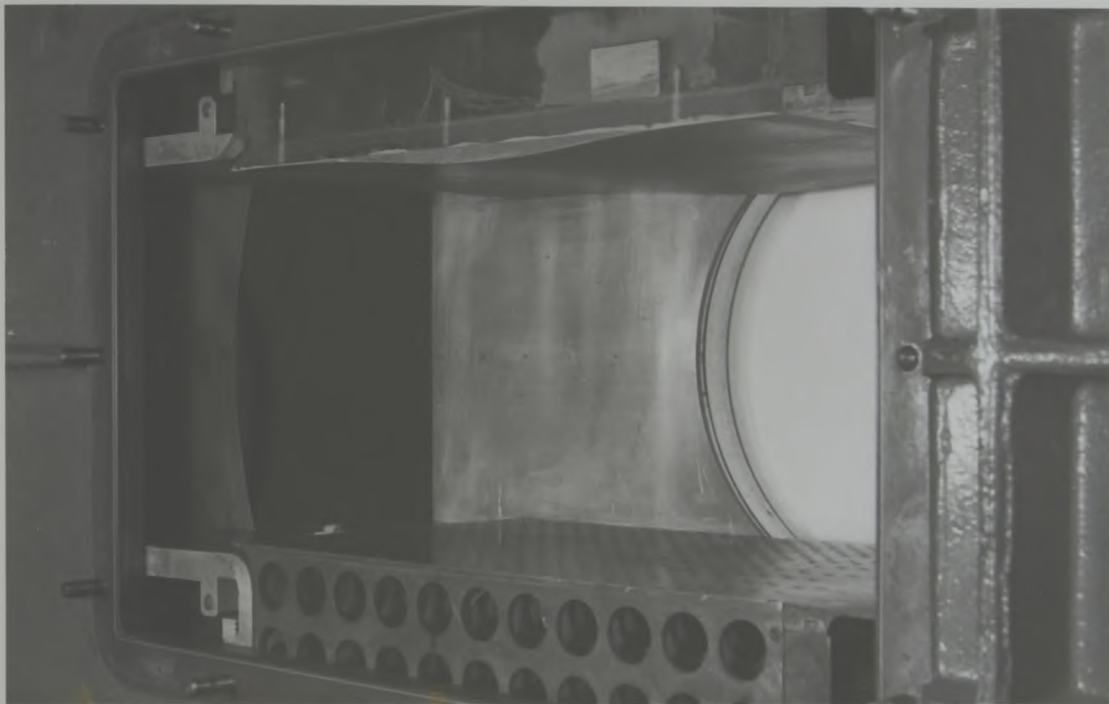
and  $P$  is a constant, the 'porosity parameter' generally obtained from experiment. This condition is known to be inadequate for perforated walls (Catherall, 1975 and Chan, 1980a), as indeed are the various other conditions which are dealt with in the brief history which follows this introduction. Improvement of the perforated wall boundary condition is sought in the research reported here.

The experimental and analytical work reported here is confined to a perforated wall in a two-dimensional windtunnel. The range of freestream test Mach numbers considered is approximately 0.6-0.8. At the upper end of this range of Mach number, regions of supersonic flow would exist in the flow field around a typical aerofoil. However, there is evidence (Mokry, Peake and Bowker, 1974) that such regions would not extend to the windtunnel walls, so only subsonic conditions are considered to exist there.

Experiments have been carried out on the perforated wall in the transonic windtunnel in the Department of Aeronautics, The City University. Normally, the top and bottom liners of this windtunnel are of the 60° inclined hole type, in the parallel working section, and have an open area ratio of 6% based on hole diameter, which is 2.95mm. The side walls are solid. However, for the tests to be described, the top liner was replaced by a solid contoured one (see Plate (1)) designed to produce pressure coefficient ( $C_p$ ) variations on the bottom perforated wall similar to those in Figure (1)<sup>†</sup>, with a peak suction of  $C_p = -0.08$  at a freestream Mach number of 0.72. The tests provided values of the boundary layer displacement thickness,  $\delta^*$ , the normal component of velocity outside the boundary layer,  $V_e$ , and the static pressure, on both the plenum chamber and working section sides of the wall ( $P_{pl}$  and  $P_e$  respectively). These data were obtained at discrete points on the bottom wall, the longitudinal positions of these points varying over a distance of 0.17m. From these data, values of  $\theta_w$  (the local average throughflow parameter at the wall) were calculated.

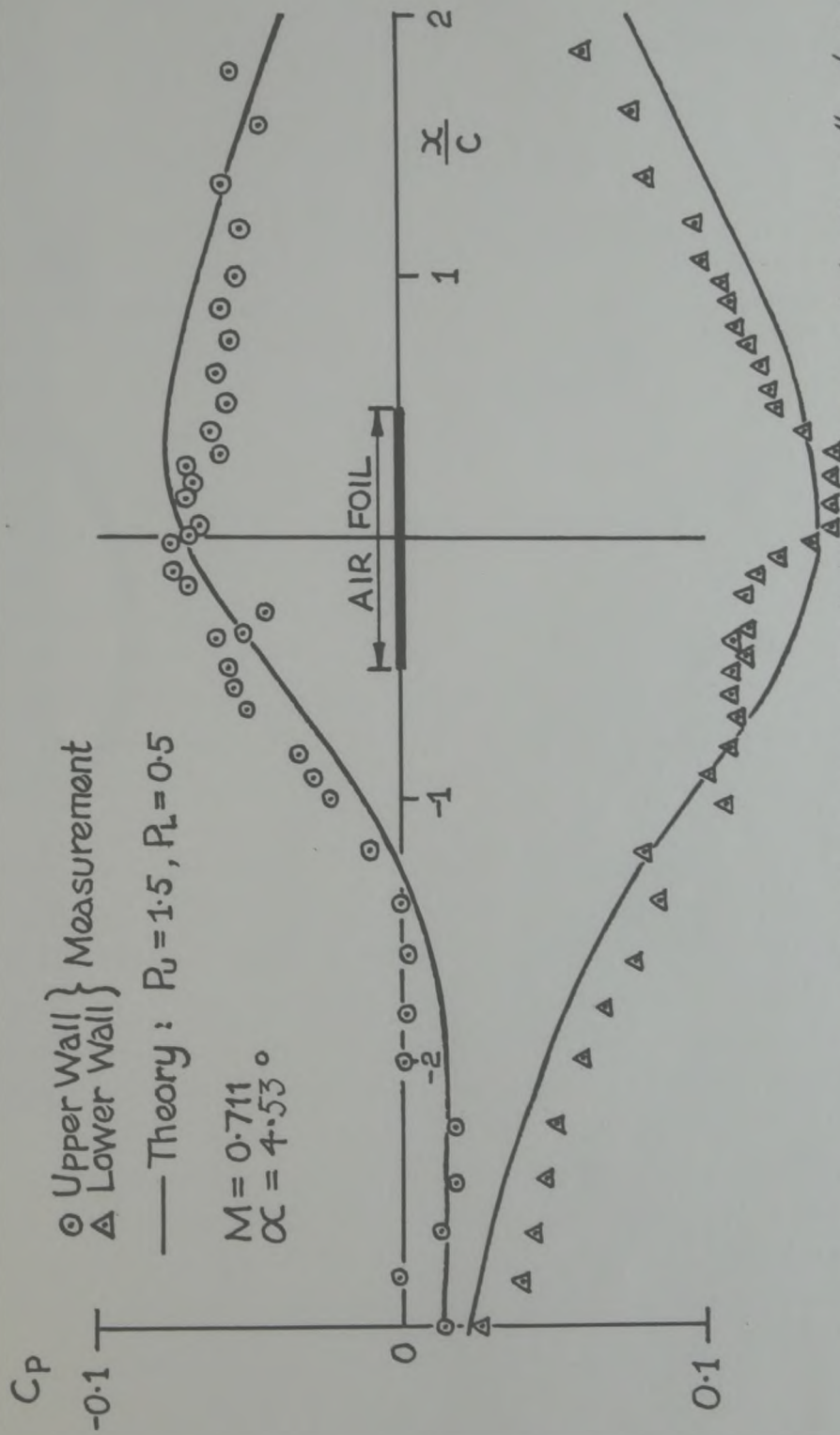
<sup>†</sup> Figure (1), which is drawn from Mokry et al, 1974, shows the distribution of pressure coefficient along both upper and lower walls of a two-dimensional windtunnel, during a typical aerofoil test. Thus, these distributions represent a suitable condition for imitation in the tests reported here.





PLATE(I) General view of windtunnel working section.

Reproduced from lower graph in Figure (15) of Mokry, Peake and Bowker (1974).



Typical pressure distribution on upper and lower walls of a two-dimensional wind tunnel with lifting aerofoil mounted —  $M=0.72$ .

FIGURE (1)



These values remained within the approximate limits;

$$-0.02 \leq \theta_w \leq 0.02 \quad \text{rad.}$$

The above data were then adapted into a functional form for use as a boundary condition in windtunnel flow calculations. The general form of the function, which contains dimensional quantities, is;

$$f(\theta_w, \frac{\Delta P_q}{q}, \delta^*, M) = 0 \quad (1.2)$$

Here,  $\frac{\Delta P_q}{q}$  is the pressure difference between the working section and plenum chamber sides of the wall, non-dimensionalized with respect to the local dynamic head and  $M$  is the local Mach number. To link the above function with an inviscid flow calculation procedure, a boundary condition;

$$\phi_x \pm \frac{1}{P(x)} \cdot \phi_z = K(x) \quad (1.3)$$

is formulated. In this equation,  $P$  and  $K$  are derived from the empirical function (Equation (1.2)) above and are functions of the longitudinal ordinate 'x'. In relating Equations (1.2) and (1.3) it is also necessary to include the effect of the variation in the boundary layer displacement thickness.

To examine the ability of this boundary condition, Equation (1.3), to simulate the flow of air close to the perforated windtunnel wall, a computer program, named 'PREDICT' has been written to implement it. The values of  $P$  and  $K$  in Equation (1.3) are calculated from the empirical function  $f$  above (Equation (1.2)) and an entrainment integral boundary layer prediction method, which takes account of compressibility and transpiration through the wall. When supplied with a distribution of pressure, measured along the perforated wall, the program gave converged solutions of the longitudinal variation of  $\delta^*$  and  $\theta_w$ , which have been compared with measured distributions. The comparisons are considered good in some respects and encourage further development

of the method. The example flows used in this comparison were less extreme in terms of the range of  $\theta_w$  than the experiments which had been undertaken;  $\theta_w$  of the computed flows being confined between -0.01 and +0.005 radian.

To ensure that the new form of the inviscid boundary condition (Equation (1.3)) would converge successfully when used with existing inviscid flow calculation methods, a computer program (named 'PILOT') has been written. This program uses an incompressible potential field to represent the flow of air in a two-dimensional, perforated wall windtunnel. The flow produced by a lifting aerofoil situated at the windtunnel centre-line is simulated by vortex and doublet singularities. The boundary layer developments along the walls is modelled using an incompressible form of the entrainment integral method utilized in the computer program 'PREDICT'. The application of the wall boundary condition is flexible in the sense that it permits simulation of solid walls, or perforated walls of various types, or a mixture of both solid and perforated segments, which is important in simulating a finite length, perforated working section. The application of the proposed boundary condition proved successful.

For those transonic windtunnel runs, where the flow near the walls had been simulated by PREDICT, the overall estimate of the windtunnel flow has been attempted using PILOT. The agreement between the computed results and the measured values is encouraging.

As indicated earlier, the purpose of the research described in this report is to improve the boundary condition to be applied at the walls in two-dimensional, transonic, perforated wall windtunnel flow calculations. Specifically, one wishes to improve on the linear homogeneous boundary condition normally applied to transonic flow calculation methods. In order to achieve this aim, one needs first to prove that the boundary condition proposed as a result of the research accurately simulates the flow of air in the vicinity of the perforated walls, and second, to show that the proposed boundary



condition operates successfully in conjunction with flow calculation methods typical of the type used to predict two-dimensional transonic flows.

The sequence of report sections following this introduction contains first a brief history of the perforated wall boundary condition, followed by a proposal for the new boundary condition. To demonstrate that the new boundary condition functions in a satisfactory way overall, the program PILOT is then described and some sample operations of the program presented. This is followed by a description of the experiments, from which the quantitative nature of the boundary condition is determined. Then to show that the boundary condition is capable of predicting the flow of air near the perforated wall, the program PREDICT is presented, and results from it are compared with experiment.

Subsequent to these chief report sections, a brief description is given of a comparison made between results from the program PILOT and those from experiment. Finally, a summary of conclusions is presented, with recommendations.

## 2. BACKGROUND TO THE PERFORATED WALL BOUNDARY CONDITION

### 2.1 History

Goethert's extensive work (Goethert, 1961) presents a detailed account of the practical and theoretical development of testing in transonic windtunnels up to 1961. At present we are concerned only with his work on perforated wall windtunnels and specifically on the nature of the flow near the walls. For as Goethert makes clear, the interference produced by a perforated wall of such a windtunnel will depend upon (and may be determined by) the relation between the local pressure disturbance (non-dimensionalized with respect to the undisturbed flow dynamic pressure,  $q_\infty$ ) and the effective inclination of the local stream,  $\theta$ . This angle, assumed small, is given as the ratio of the velocity component normal to the wall,  $v$ , to the undisturbed longitudinal speed,  $u_\infty$ , again assuming the disturbances from  $u_\infty$  near the wall are small. Thus

$$\theta = v / u_\infty \quad (2.1)$$

and the relation of interest Goethert considers is

$$(p_w - p_{pl}) / q_\infty = f(\theta) \quad (2.2)$$

(Here  $p_w$  and  $p_{pl}$  are the static pressures on the working section and plenum chamber sides of the wall respectively and the term  $(p_w - p_{pl})$  is hereafter named  $\Delta p$ ). Bearing in mind the small disturbance relation

$$(p_w - p_\infty) / q_\infty = -2u / u_\infty \quad (2.3)$$

(Where  $u$  is the longitudinal perturbation from the freestream speed  $u_\infty$ ) we see that Equation (2.2) which Goethert calls the "crossflow characteristic", together with Equations (2.1) and (2.3) yield a relation between  $u / u_\infty$  and  $v / u_\infty$  (and a term involving the constant plenum chamber pressure). In particular, a linear relation in Equation (2.2) will give a linear relation between  $u$  and  $v$ .

In Goethert's work it was implicitly assumed that the angle  $\theta$  may be equated to the actual mean mass flow intensity normal to the wall plane (at the wall), which he termed  $(\rho v)_h$ , divided by the mass flux intensity of the undisturbed stream,  $\rho_\infty u_\infty$ , or in his notation,  $(\rho v)_\infty$ . This assumption, together with relatively simple experiments in which wall pressures, plenum pressures and mass flow through various perforated walls



were measured, provided the required cross-flow characteristics. Sample results of Goethert's are presented in Figures (2) and (3). Referring to these figures, which relate to perforated walls virtually the same as those in the City University transonic windtunnel, it is seen that the cross-flow characteristics depend significantly on the thickness of the boundary layer in the flow over the perforated wall and on the undisturbed flow Mach number. It is also to be noted that the characteristics are not straight lines, particularly in the case of thick boundary layers, and that none of the characteristics passes through the origin.

Goethert also gives the results of various simplified theories which might be deemed relevant to cross-flow through a perforated wall. In the limiting case of very small holes, the wall will behave as a porous medium. Dynamic effects will then be small relative to frictional pressure losses and for a given porous wall it has been shown that

$$\Delta p \propto (\rho v)_h . \quad (2.4)$$

Thus

$$\frac{\Delta p}{q_\infty} \propto \frac{\theta}{U_\infty} . \quad (2.5)$$

However, this result bears little relation to the observed behaviour for perforated walls, as the influence of  $U_\infty$  shown in Equation (2.5) is certainly not found. Various other theoretical approaches are outlined by Goethert, for example, a flow through a single transverse slot is considered, as is the flow through a lattice of thin wall elements. Goethert concludes that for small disturbance flows, a linear cross-flow relation (passing through the origin) results from both these approaches. Goethert uses such a cross-flow relation in an analysis of one-dimensional flow in a finite perforated test section. His analysis is closely followed here, in Appendix (1), for subsequent comparison with a method developed in this report.

Despite Goethert's realization of the importance of the boundary layer on the cross-flow characteristic of a perforated wall, he failed to mention that the variation of boundary layer thickness along the wall will give rise to a difference between the effective inviscid cross-flow at the wall and the actual mean cross-flow there,  $(\rho v)_h / (\rho v)_\infty$ .



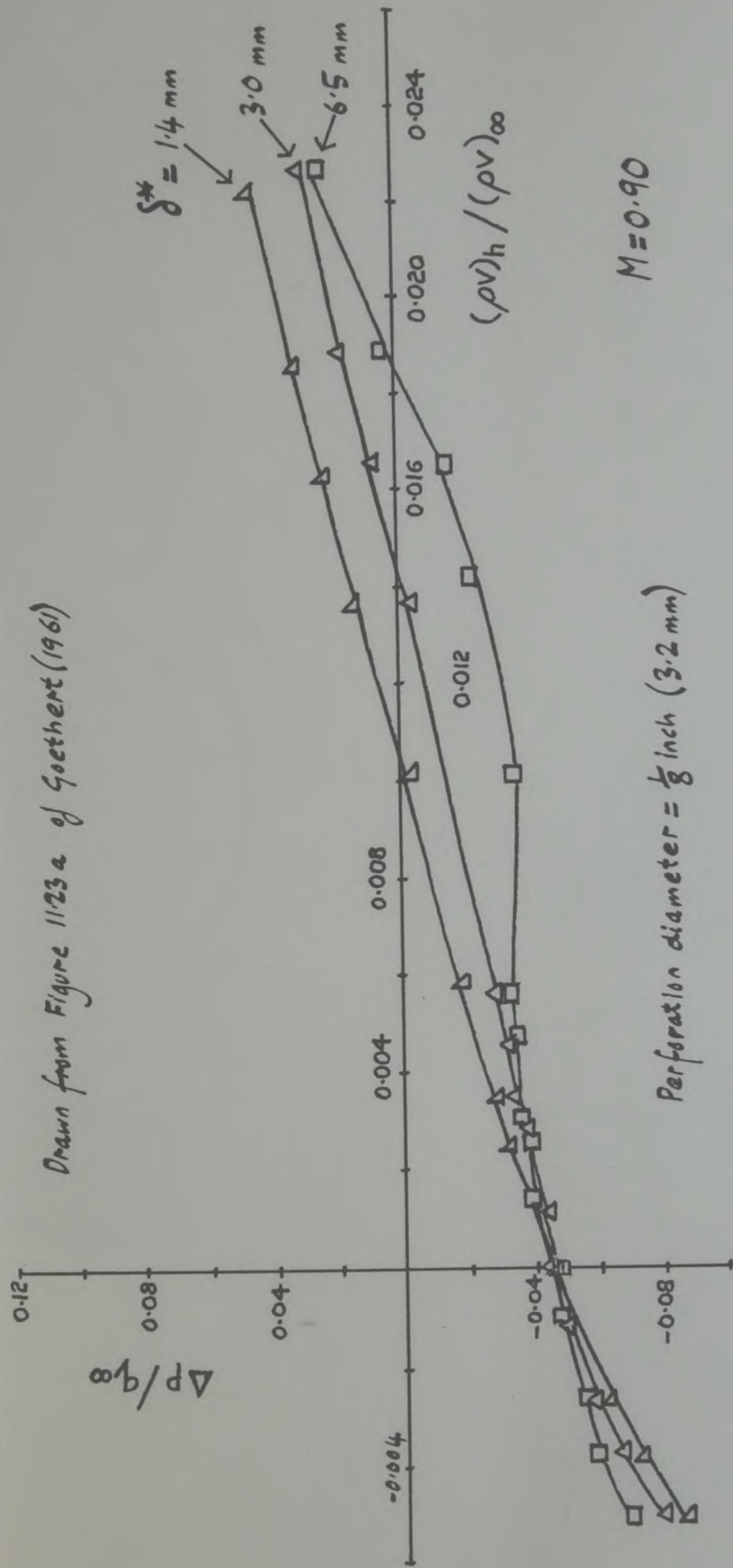


FIGURE (2) Wall characteristic due to Goethert, for various boundary layer thicknesses, at  $M=0.9$

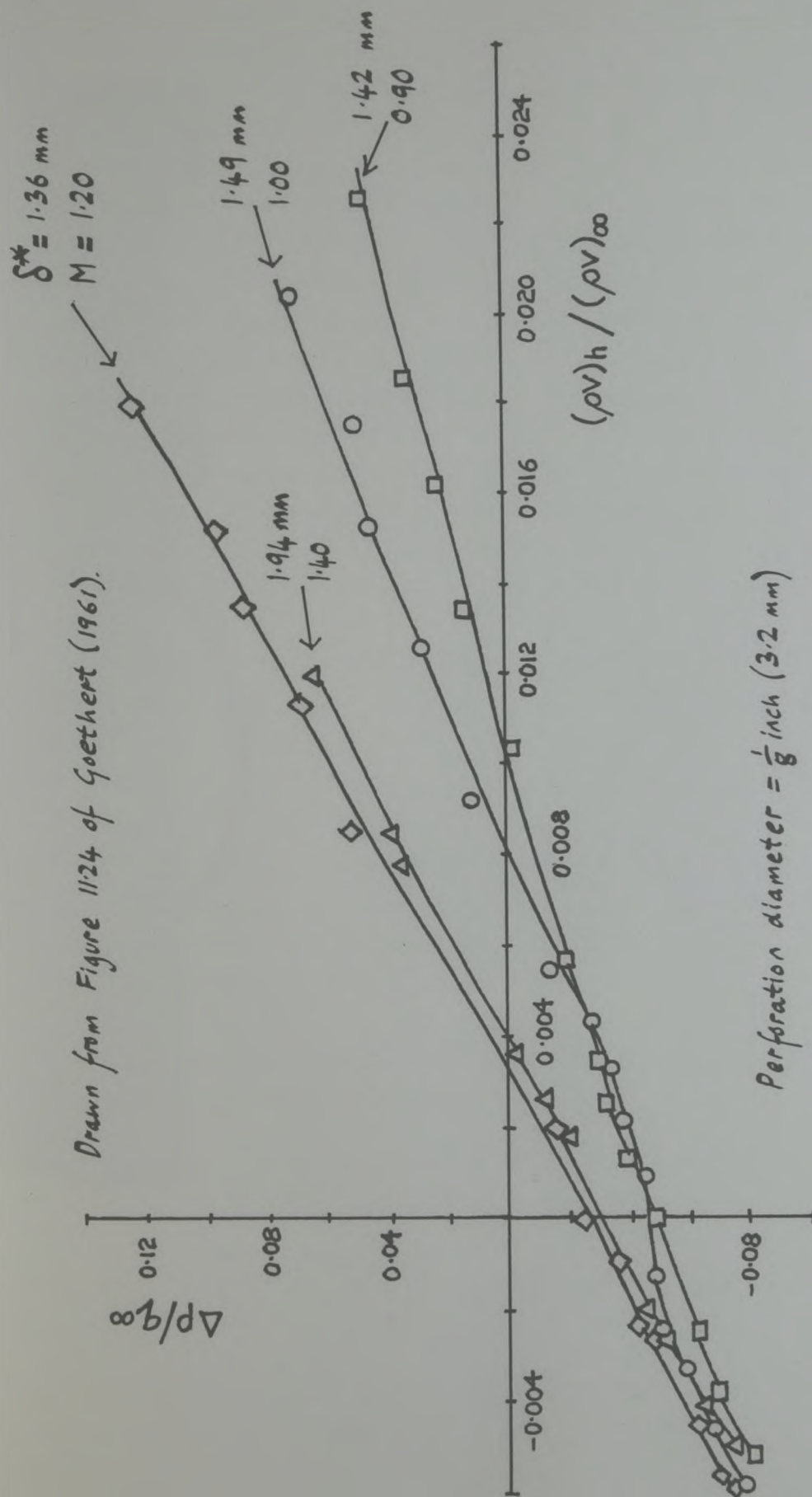


FIGURE (3) Wall characteristic due to Goethert, for various Mach numbers, with a boundary layer thickness of approximately 1.5 mm.



The fact that boundary layer growth could be very important indeed in modifying the effective inviscid wall boundary condition was pointed out by Vidal et al (1975). They referred to the inviscid flow normal component,  $V_e$  (determined outside the boundary layer) and the average viscous, flow speed,  $V_w$  (determined at the wall), and stated that for cases of outflow (boundary layer suction) the amplification factor  $(V_e/V_w)$  could be up to 6 and probably larger when fluid is injected into the windtunnel, for this is the case when the wall boundary layer would grow rapidly. Their results were mainly concerned with the design of a self-correcting windtunnel, and so they were not concerned to follow up the implications of their experimental findings for perforated wall cross-flow characteristics. However they do comment that a linear boundary condition is not applicable because in relating  $V_e$  to  $\Delta P/q_w$ , the amplification factor (mentioned above) which varies is involved, as is the relationship between  $V_w$  and  $\Delta P/q_{\infty}$  which again, they say, is not linear.

Without a more precise boundary condition available, a number of workers have chosen to use a linear version, of the form of Equation (1.1), namely

$$\phi_x \pm \frac{1}{P} \phi_z = 0 \quad (2.6)$$

Here,  $P$  (the porosity parameter) is assumed to be a constant, the value of which is obtained from experiment for each wall geometry and freestream Mach number considered. In using such a boundary condition one assumes; (Freestone and Henington, 1981)

(a) that the windtunnel liner boundary layers are either negligible in thickness, or uniform in thickness,

(b) that the static pressure drop across a perforated liner is proportional to the local mass flow rate through it.

and (c) that the pressure in the plenum chamber is constant and equal to the pressure of the undisturbed stream.

Additionally, one usually assumes that the walls continue, straight and perforated to infinity, both upstream and downstream from the aerofoil position.



Catherall (1975) presents a method for solving the transonic small perturbation equation for the flow in a two-dimensional windtunnel. To represent walls of slotted, porous, perforated or solid type, Catherall uses the following boundary condition;

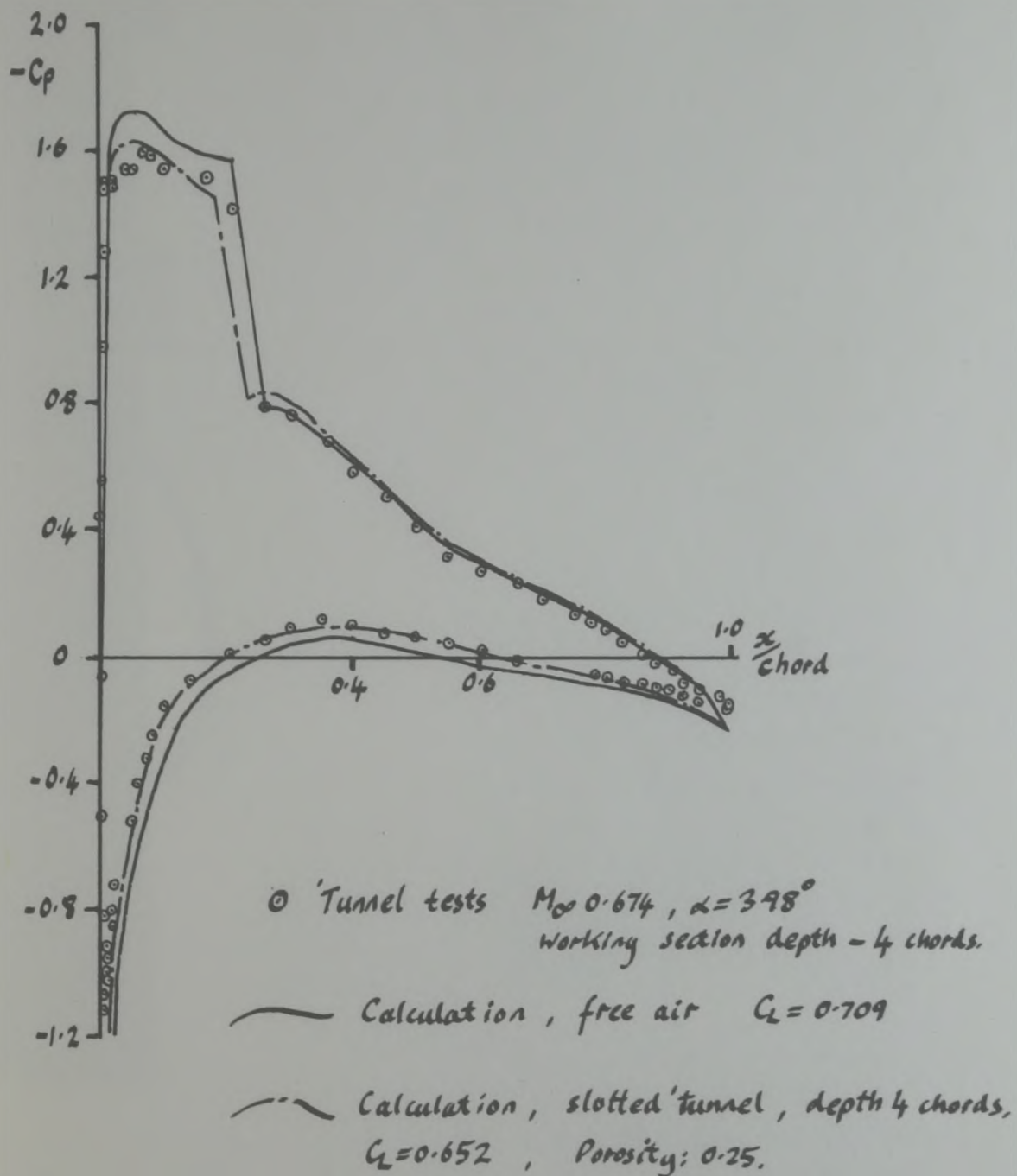
$$\phi_x \pm FH \phi_{xz} \pm \frac{1}{P} \phi_z = 0 \quad (2.7)$$

(on the windtunnel walls at  $z = \pm H$ ).

Here  $F$  is a 'slot parameter' derived from a simple inviscid flow model. Clearly, Equation (2.7) is only a slightly more general form of Equation (2.4). When used in a free-air configuration, results from the method are in satisfactory agreement with an exact potential method, for a wide range of practical aerofoil shapes and at Mach numbers as low as 0.6 (Albone et al, 1974). With ventilated walls modelled, comparisons of calculated aerofoil pressure distributions with those obtained from wind-tunnel tests are also encouraging. In Figure (4) (taken from Fig. 4 of Catherall, 1975), such a comparison is made. Here, the windtunnel walls simulated are slotted, but the level of agreement obtained is not expected to be very different from that which would be observed if the walls were perforated (In fact it was necessary in the calculation to choose a value of  $P$  to represent the slotted wall, as well as calculating the value of  $F$  to use). Clearly, accounting for the presence of the windtunnel walls improves the agreement between calculated and measured pressure distributions. Despite this agreement, for a number of reasons Catherall is not confident that the calculation method is able to predict accurately the interference produced at the aerofoil position by the walls. Notably, he mentions the inaccuracy of the homogeneous boundary condition (Equation (2.7)) and in particular, the assumption that  $P$  is a constant.

Ebihara (1972) had earlier carried out a careful study of two-dimensional wall interference methods. He focussed his attention mainly on the use of the linear homogeneous boundary condition (Equation (2.6)). He stated that the value of  $P$  in the equation must be determined experimentally, as it would depend upon wall geometry and boundary layer thickness. Difficulties encountered in attempting to determine  $P$  indirectly caused him to reconsider the form of the boundary condition.

Drawn from Fig.(4) of Catherall (1975)  
for aerofoil RAE 101.



FIGURE(4) Comparison of calculated aerofoil pressure distributions  
with that from experiment - Catherall (1975).



He had earlier stated that the boundary condition should be non-linear or at least be a straight line which does not pass through the origin, and in the event, proposed for future use the following form of boundary condition;

$$\phi_x \pm \frac{1}{\rho} \phi_z = K . \quad (2.8)$$

Again,  $P$  and  $K$  are constants to be determined from experiment, where  $K$  he believes, will be dependent on wall geometry and freestream Mach number only. He does state however that some account of a plenum chamber pressure differing from the freestream pressure could be taken by suitable choice of the value of  $K$ .

Kacprzynski (1976) was concerned to improve the boundary condition applicable to a perforated wall. He commented on the inadequacy of boundary conditions of the form of Equation (2.6) and proposed to use an improved version;

$$|\bar{V}_w| = A|C_p| + B C_p^2 . \quad (2.9)$$

Here,  $\bar{V}_w$  is the normal velocity component in the effective inviscid flow at the wall position (non-dimensionalized) and  $C_p$  is a conventional pressure coefficient determined at the wall  $(p_w - p_\infty / q_\infty)$ . Using a suitable method \* for calculating the flow in a two-dimensional windtunnel (with aerofoil) and incorporating the above boundary condition, he manipulates the value of  $A$  and  $B$  until the calculation yields wall pressures which closely match those measured in the experiment being modelled. For the examples given, good agreement in wall pressures is obtained, and it leads Kacprzynski to conclude that indeed, the perforated wall characteristics are non-linear and are a function of "a variety of parameters". The constants  $A$  and  $B$  above are permitted to hold different values for positive and negative  $C_p$ 's, that is, there are effectively four constants in Equation (2.9). However, it should be noted that the values of  $A$  and  $B$  determined are relevant only to one particular test, where wall pressures have been measured. Kacprzynski's reference to a "variety of parameters" indicates perhaps the influence of different plenum chamber pressures and

\* Kacprzynski uses two methods. In the first, he solves the transonic small-perturbation equation and in the second he solves the full non-linear potential equation.



wall boundary layer developments, from test to test. Indeed he gives evidence which suggests that these effects may be present.

Mokry Peake and Bowker (1974) also recognize the need for a non-linear wall cross-flow characteristic to be supplied as a boundary condition, but due to the complexity of incorporating such a boundary condition into an inviscid flow calculation, they use a linear version with different gradients for inflow and outflow. They assume that above an aerofoil, on the top liner of the windtunnel, the cross-flow will be predominantly into the working section and below it, on the bottom, there will be predominantly outflow. Thus they apply one porosity parameter to one wall and a different one to the other. With a view to determining wall induced interference, the flow of air in the windtunnel is modelled using subsonic linearized potential theory and the far field flow effects of the aerofoil are simulated by a point doublet, vortex and source. They discover that careful selection of both  $P_u$  and of  $P_L$  (the upper and lower liner porosity parameters respectively) allows them to predict measured wall pressures very well and certainly with greater accuracy than would be obtained using identical values of  $P_u$  and  $P_L$ . Typically for their normal holed walls, they find that  $P_u$  should be three times greater than  $P_L$ , or the resistance to flow out of the working section, greater than that for inflow. Similar simple guidelines were found to give good comparisons, between calculated and measured wall pressures for test cases other than that from which the guidelines were themselves produced. Despite these encouragements, Mokry et al state that unless one measures wall static pressures during the relevant tests (to use as direct boundary conditions in interference calculations), one should ideally have an accurate knowledge of the cross-flow characteristics of the wall for the conditions to be considered. They also discovered a region of outflow existing upstream of the aerofoil on the upper liner which became severe as the freestream Mach number rose to 0.92. This region of outflow contravenes their initial assumption of inflow and for this among other reasons, they do not believe their approach should be applied at such high Mach numbers.

Jacocks (1976) carried out an investigation into the cross-flow characteristics of a number of different ventilated wall types, including a perforated wall which is almost identical with those fitted in the



City University transonic windtunnel. He commented that some experimental characteristics determined earlier and presented in Goethert (1961), Figures (2) and (3) of this report for example, constitute only average data obtained on a quite large section of perforated wall. Notably, the values of  $\delta^*$  are not obtained locally. Jacocks mentions that the development of  $\delta^*$  along the wall would affect the value of  $\theta$ , the effective inviscid cross-flow angle. He highlighted that Goethert had not mentioned this, but had assumed that  $\theta$  would be equal to the actual viscous cross-flow at the wall. Jacocks was concerned to determine the value of  $\theta$  and to determine it locally. His experimental set-up consisted of a two-dimensional working section with one ventilated wall, one solid contoured wall and two solid sidewalls. To avoid very complex measurements, he used a transonic, small perturbation calculation method with measured boundary conditions applied (notably static pressures on the ventilated wall). He was then able to calculate the distribution of  $\theta$  near the perforated wall, and in cases where flow angle measurements were available for comparison, his predictions were proved very encouraging. Jacocks then presents his wall characteristics as graphs of  $C_p$  against  $\theta$ . These graphs are, in parts, distinctly non-linear. It is clear from his work that the relationship between  $C_p$  and  $\theta$  is dependent on the geometry of the perforated wall and the thickness of the boundary layer on it. Jacocks went some way toward quantifying these dependencies, but not far enough for his work to be considered as presenting an improved perforated wall boundary condition.

Chan (1980) carried out experiments to determine the development of the boundary layer on the walls of perforated wall windtunnels, with a view to defining more accurately the boundary conditions applying there. He recognized the inadequacy of the linear boundary condition (Equation (2.6)) to simulate the non-linear condition which exist at the wall. He commented that Jacocks' use of an average boundary layer thickness in developing his wall characteristic may be inadequate, and thus Chan carried out experiments where values of  $\delta^*$  were measured at three longitudinal stations. Chan did not measure cross-flow angles, but using wall pressures and the values of  $\delta^*$  obtained, he was able to determine a cross-flow characteristic for the wall. This was achieved



by using a boundary layer prediction method and a series of trial characteristics. The characteristic was manipulated until the cross-flow predicted (when supplied to the boundary layer method) produced values of  $\delta^*$  which closely matched those which were measured during the experiments. The level of agreement obtained was not perfect, but was certainly encouraging. Chan presents a graph of  $C_p$  against the flow angle outside the boundary layer, which though non-linear, does pass through the origin (which he attributes to the growth rate of  $\delta^*$  counteracting the offset that would exist in the cross-flow characteristic involving the flow angle at the wall). He states that the cross-flow velocity at the wall is a non-linear function of  $C_p$  and also dependent on the growth rate of  $\delta^*$  along the wall. In relating this cross-flow to that outside the boundary layer, he discovered that two distinct relationships exist; one for wall suction where both cross-flows are almost the same, and another for blowing where (due to boundary layer growth) the edge cross-flow is 3.25 times that at the wall. This lends support to the discovery by Mokry et al (1974) that the porosity of the top liner of the windtunnel (wall blowing) should be three times that of the lower liner (wall suction). Chan recommended that, for more accurate calculations, there should be direct experimental determination of both cross-flow at the wall and boundary layer displacement thickness. The cross-flow characteristic resulting from these measurements should then be used, with a boundary layer prediction method and an inviscid flow calculation, in a three component iteration process to solve the complete windtunnel flow.

Alternative approaches to the problem of determining the levels of interference caused by windtunnels on model test results, have recently been suggested. Possibly the earliest of these was due to Kemp (1978). The crucial element of such methods is that additional information about the wall condition is acquired during each test to be corrected and used in the subsequent correction calculations (where in Kemp's case the extra information are the wall pressure distributions). There is then sufficient information about the effective inviscid flowfield near the walls available to render it possible to predict the disturbance produced by the walls at the model position. In Kemp's case, using the additional



wall pressures makes it unnecessary to employ a wall boundary condition in the conventional way. His method, along with other 'post-test interference calculation' methods are having some success. This success is perhaps emphasised when one considers that, for the present at least, research on the nature of the slotted and perforated wall boundary conditions has been stopped at NAE (National Aeronautical Establishment) Canada and at AEDC (Arnold Engineering Development Centre). These two centres have previously made considerable contributions to this research.

Finally, mention needs to be made of the self-adapting windtunnel. In this type of windtunnel, the shape of the walls or the flow through the walls where these are perforated, is adjusted during the tests in an attempt to produce the minimum wall induced interference at the model position. Although not widely used yet, examples of this type of windtunnel exist in England (at Southampton University), France (at ONERA-Chatillon) and in the United States (at the Calspan Corporation - Buffalo). During a given test in a self adapting windtunnel, when the wall shapes have been finalized, it is unlikely that one would require to calculate the flow in the windtunnel using predetermined boundary conditions. Any residual wall induced interference would probably be calculated using measured wall pressures and a procedure similar to that of Kemp (1978).

## 2.2 Summary of reasons for improving the perforated wall boundary condition

Despite the current trends in transonic windtunnel flow calculations towards post-test interference estimates and the development of the self-adapting windtunnel, there remain significant advantages in gaining a better understanding of the perforated wall boundary condition.

First, there is always a need to examine the accuracy of methods for calculating the transonic flow of air around two-dimensional aerofoils. Transonic aerofoil design methods are usually derived from such calculation methods. This gives such an examination an even wider relevance. To achieve this examination one needs to compare the predicted flow with an experimentally



measured flow. The experimental flow must normally be the flow in a windtunnel working section where the aerofoil is mounted. Consequently, this comparison can only be achieved if a wind-tunnel wall boundary condition is included in the flow calculation, where the boundary condition has already been shown to simulate the flow of air near the walls with sufficient accuracy.

Second, when aerofoils are tested in perforated wall windtunnels, the discrepancies in such features as shock position, or surface pressure distribution, between the windtunnel flow and that in free air for the same free stream condition are not accurately known. In some instances they are actually ignored because there is so little information available about them. This situation would be alleviated if an accurate perforated wall boundary condition were available, since the changes due to the walls could then be accurately predicted.

Finally, methods such as Kemp's (1978), explained earlier, operate by applying measured windtunnel wall static pressures directly as a boundary condition to a flow calculation scheme. In the case of perforated walls, no assumption is made concerning the normal component of velocity at the wall except perhaps that it is small compared to the longitudinal component. In some cases an iteration is undertaken to determine a suitable distribution for the normal component. If a wall "package" were available, which for a given distribution of wall pressures could predict accurately the distribution of normal velocity in the effective inviscid stream, then this could be used to make the applied boundary conditions more comprehensive. It would seem sensible that the implementation of methods such as Kemp's would then be more efficient.

It would seem justified then to carry out an experimental investigation into the nature of the perforated wall boundary condition, and subsequently to present the results of those experiments as a boundary condition suitable for use with a wide variety of inviscid, aerofoil flow calculation schemes. It is also necessary to demonstrate that this boundary condition does simulate accurately the flow of air near a perforated wall in transonic flow.

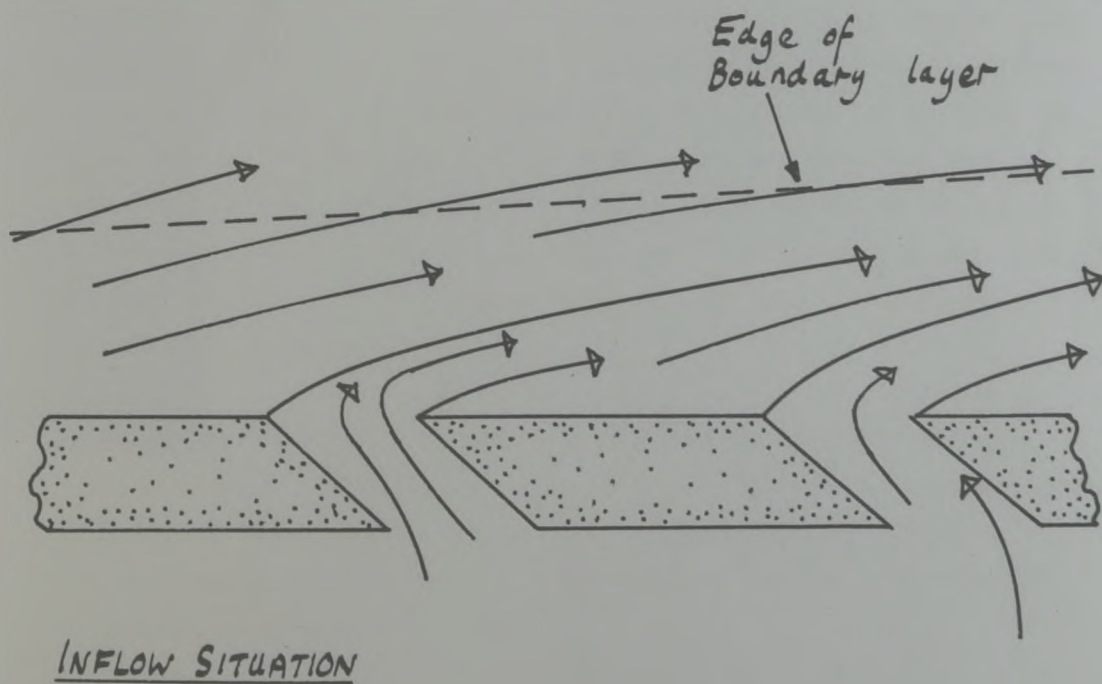
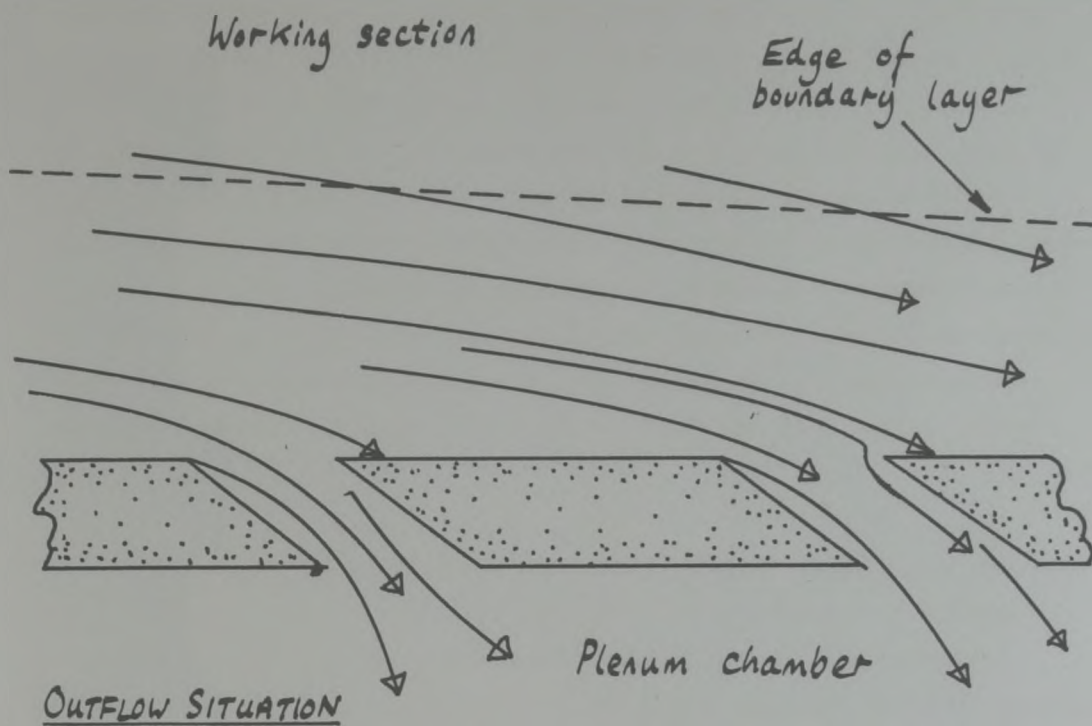


### 3. PROPOSAL FOR A NEW BOUNDARY CONDITION.

#### 3.1 Position of Application of Boundary Condition.

The flow of air near a perforated windtunnel wall liner is almost certain to be extremely complex. Figure (5) shows how the streamlines near such a wall with inclined perforations might appear. In the present work, it is considered that the local variations in the flow due to individual perforations become negligibly small within the boundary layer thickness. Consequently, it is considered that the effects of individual perforations are averaged locally outside the boundary layer.

Initially, it would seem sensible to apply a boundary condition to the inviscid flow at some station outside the boundary layer. Admittedly this would divide the flow in a convenient manner, keeping all regions of viscous flow "behind" the boundary condition line. The boundary condition could then present the nett effect of these viscous regions to the inviscid flow calculations without apparent complication. However, some drawbacks in the above approach were discovered when an attempt was made to model the flow of air around a lifting circular cylinder in the presence of a solid wall. An incompressible, potential field was used to model the flow. The growth of the boundary layer on the solid wall was also taken into account. It was impossible to decide precisely where to position the boundary condition line in advance of a calculation because the development of the boundary layer thickness was not known. Using a position which responded continually to the local calculated thickness of the viscous regions, caused increased complexity in the computing. Such an approach also appears unrealistic if one considers application to the large, complex, finite difference grid of a transonic flow calculation method. In the method of Catherall (1975), the boundary condition is applied, for convenience, at the wall position itself. It is logical for Catherall to use such a position if one considers that he neglects any viscous layers that may exist on the wall anyway.



FIGURE(5)

Diagram of Streamlines near and through a perforated wall.



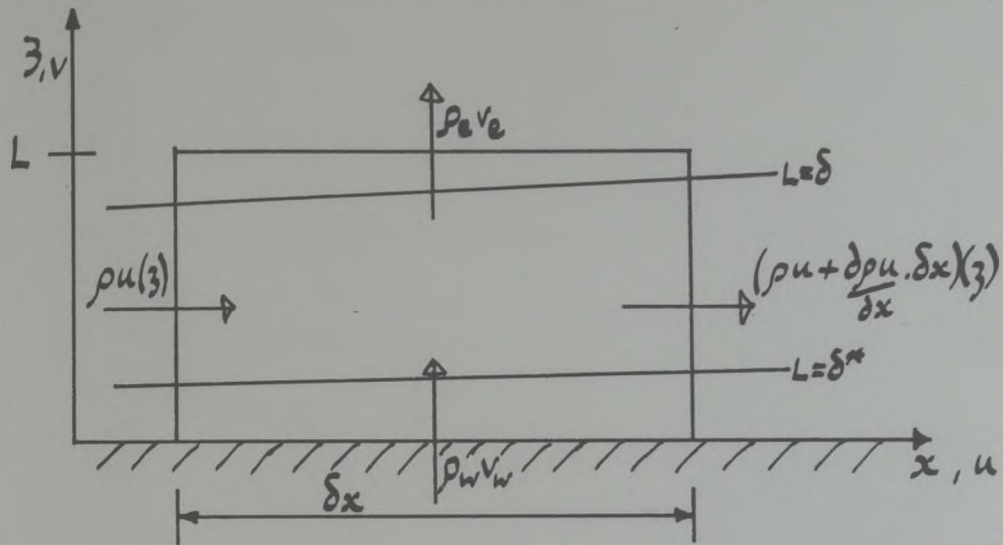
Lock (1975b) describes an approach by which any viscous layers that may exist on an aerofoil surface may be accounted for in an inviscid flow calculation method. Here also, the inviscid flow is extended to the solid surface position, and a boundary condition is applied there. As a consequence, the finite difference grid is generated so as to coincide with the aerofoil surface and left unaltered throughout the calculation. This approach is considerably simpler than the alternative approach of updating the grid boundary to coincide with the edge of the displacement surface on the aerofoil. With the exception of alterations to account for transpiration through a porous surface, the same approach is used in the present work.

In Figure (6)a, a two-dimensional control volume on a porous wall is shown. In the Figure, the flow is considered to be the real flow near a porous wall where viscous layers are present. Application of the principle of conservation of mass to this control volume yields the following equation; (Equation (4) of Appendix 2.)

$$(L - \delta^*) \frac{d(\rho_e u_e)}{dx} - \rho_e u_e \frac{d\delta^*}{dx} + \rho_e v_e - \rho_w v_w = 0 \quad (3.1)$$

The development of this equation is described fully in Appendix (2). The control surface which is a distance  $L$  above the wall is outside the boundary layer (at least locally). If one were to measure the flow angle at the edge position ( $L$ ) and knew the longitudinal development of  $\delta^*$  and  $\rho_e u_e$  then clearly using Equation (3.1), it is possible to determine the average local crossflow ( $\rho_w v_w$ ) at the wall itself. This equation is essential for the analysis of the experiments to be described later.

In Figure (6)b a similar control volume is shown to that described above. Now however, the inviscid flow field is considered to extend to the porous wall. Clearly the situation represented here is fictitious. Application of the principle of conservation of mass now yields



(a). Viscous Flow near wall

DIAGRAM OF CONTROL VOLUMES NEAR WALL.

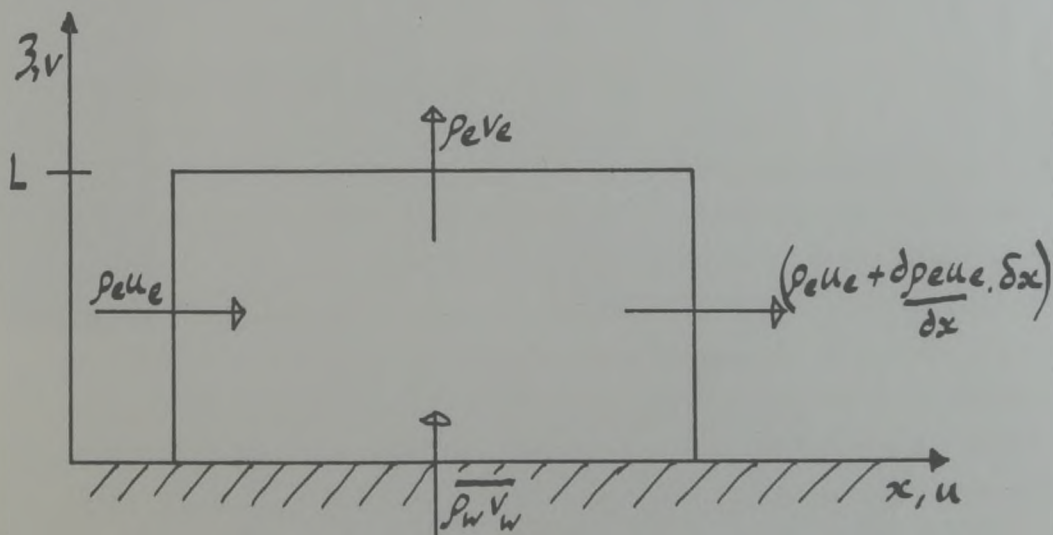


FIGURE (6) (b). Inviscid Flow near wall.



$$-L \frac{d(\rho_e u_e)}{dx} + \overline{\rho_w v_w} - \rho_e v_e = 0. \quad (3.2)$$

The derivation of this equation also is presented in Appendix (2), (Equation (6) of that Appendix).

Combining Equations (3.1) and (3.2) we find that

$$\delta^* \frac{d(\rho_e u_e)}{dx} + \rho_e u_e \frac{d\delta^*}{dx} + \rho_w v_w - \overline{\rho_w v_w} = 0 \quad (3.3)$$

Now it is possible to relate the actual crossflow at the wall,  $\rho_w v_w$  to the fictitious inviscid crossflow at the wall,  $\overline{\rho_w v_w}$  in terms of the longitudinal development of  $\delta^*$  and the parameter  $\rho_e u_e$ . The wall position line then represents a convenient place to define the boundary condition. The inviscid flow can be extended (in a fictitious manner) to this line and interacted with the actual mean viscous flows that exist there, through use of Equation (3.3).

### 3.2 The Calculation Scheme to be Employed.

The vast majority of methods of calculating the transonic flow of air around two-dimensional aerofoils involve some iteration procedure. Any wall boundary condition which is to be used in such methods, must be formulated in a manner suitable to an iteration procedure. For instance, at any stage in the calculation, the inviscid flow which has been previously predicted to be present around the aerofoil could be used to improve the boundary condition to be applied at the wall. This improved boundary condition could then be used in the subsequent calculation of the inviscid flow in

the working section. An approach of this sort has been suggested by a number of workers, notably Chan (1980a). An iterative approach of this type is used in the present work also.

As much as possible, the calculation scheme to be described is split into modules. It is most helpfully described by referring to Figure (7), which shows in very broad detail how the proposed scheme may be incorporated into a flow calculation method. The diagram is only intended to represent that part of the overall calculation method relevant to the scheme. As such, sections of the flow diagram such as the part dealing with the calculation of viscous layers on the aerofoil are not shown.

At a particular point in the calculation, the inviscid flow of air around the aerofoil in the wind tunnel has been calculated. (box (1)). The distributions of the longitudinal and lateral components of velocity at the wall positions are then available. To start the following calculation, some initial assumption is then made concerning the distribution of boundary layer displacement thickness on the upper and lower wind tunnel walls (box (2)). Using Equation (3.3), namely

$$\delta^* \frac{d(\rho_e u_e)}{dx} + \rho_e u_e \cdot \frac{d\delta^*}{dx} + \rho_w v_w - \overline{\rho_w v_w} = 0$$

and isentropic relationships for determining the values of  $\rho_e$  and  $\rho_w$  the distribution of viscous crossflow ( $\rho_w v_w$ ) at the wall position is then calculated (box (3)). For the reasons described in Appendix (2), it is possible to use values for density and longitudinal component of velocity determined at the wall position, in place of the parameters,  $\rho_e$  and  $u_e$  in the above equation. A boundary layer calculation method is then used with the distributions of the viscous crossflow parameter and longitudinal component of velocity at the wall, to predict a better distribution of boundary layer displacement thickness (box (4)). A convergence check is then carried out, to examine whether there remains a

FIGURE (7) Flow Diagram of Proposed Working Scheme



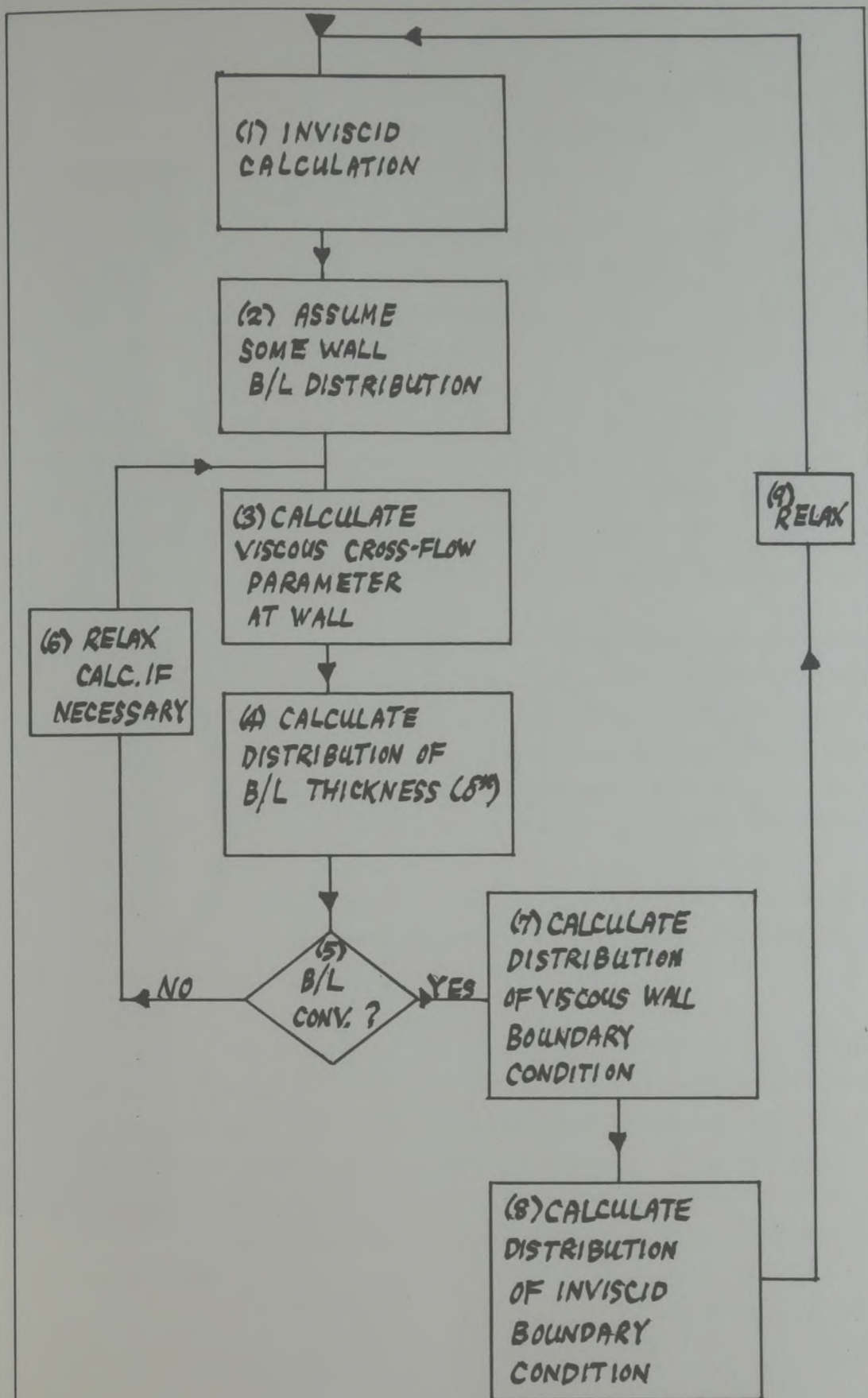


FIGURE (7) Flow Diagram of proposed computing scheme.

significant difference between the boundary layer development just calculated and the distribution initially assumed (box (2)). This convergence check is signified by box (5).

If the level of convergence obtained is unsatisfactory, control is returned to box (3), where now, the new distribution of  $\delta^*$  is used. Clearly, an iteration loop is formed here which may require the application of relaxation (box (6)) to achieve the desired convergence.

Once however, the convergence level in box (5) is found to be satisfactory, the following situation exists. The distributions of boundary layer thickness and viscous crossflow at the wall are compatible with the distributions of both components of the velocity in the effective inviscid stream at the wall position.

The crossflow characteristic of the perforated wall is expressed in box (7) as an empirical function. This empirical function would have to be determined by experiment for each type of perforated wall considered. The variables in the function will certainly include  $C_{p_w}$  (the non-dimensional pressure difference across the wall), the viscous crossflow parameter and the boundary layer displacement thickness. Distributions of these variables, supplied by the iteration procedure described earlier, are then used with the empirical function to predict the relationship between  $C_{p_w}$  and  $\rho_w v_w$  at discrete points along both walls (box (7)).

Before the calculated crossflow characteristic can be applied to the inviscid flow calculation as a boundary condition, it must be altered into a form containing only parameters relating to the effective inviscid flow at the wall (box (8)). This is done principally by use of Equation (3.3). Previously calculated values of  $\delta^*$ , and  $\rho_e u_e$  are used to express the equation in a suitable form; namely that

$$\rho_w v_w = \overline{\rho_w v_w} + C \quad (3.4)$$



where the constant  $C$  is calculated at discrete points along each wall.

The new boundary condition (as a relationship between the longitudinal and normal components of velocity at the wall position) is then applied to the inviscid flow calculation method (box (1)). The larger iteration loop shown on Figure (7) may also require the use of relaxation to achieve satisfactory convergence (box (9)). This completes the outline description of the overall calculation scheme proposed.

### 3.3 Objectives of the Computer Program; 'PILOT'

The calculation scheme described in Section 3.2 would, if successful, eventually be incorporated into a transonic aerofoil flow calculation method. However, to carry out such a piece of work would take considerable time and effort. For this reason, a simple inviscid flow calculation method is to be used to examine the overall operating efficiency of the proposed scheme.

The simple calculation method adopted, models the inviscid, incompressible flow of air through a two-dimensional wind tunnel working section, with an idealized aerofoil mounted at the centre of the section. The calculation method (in the form of a FORTRAN computer program named 'PILOT') is to be used to examine the efficiency of various wall boundary conditions. Efficiency here means that use of a particular boundary condition permits convergence of the calculation scheme, within the limits of reasonable computing resources. Considering the idealizations described above, it would also be encouraging if there were even a broad agreement between the overall wind tunnel flow predicted by the computer program and that measured during experiment.

### 3.4 Formulation of the Computer Program; 'PILOT'.

In the computer program named 'PILOT', the flow of air in a perforated, two-dimensional windtunnel is represented by an inviscid incompressible potential field. The overall situation modelled is shown in Figure (8). The wind tunnel has straight top and bottom liners which are perforated over some length. These perforated regions mark the extent of the working section. The air flows from left to right, and at the centre of this section, a lifting aerofoil is mounted. Behind the perforated walls are large plenum chambers from which air may be removed by some pumping device. The air is free to pass into or out of the working section through the perforated walls. On both liners of the windtunnel, there is a boundary layer flow which extends over the full length of the liners including both solid and perforated sections of wall.

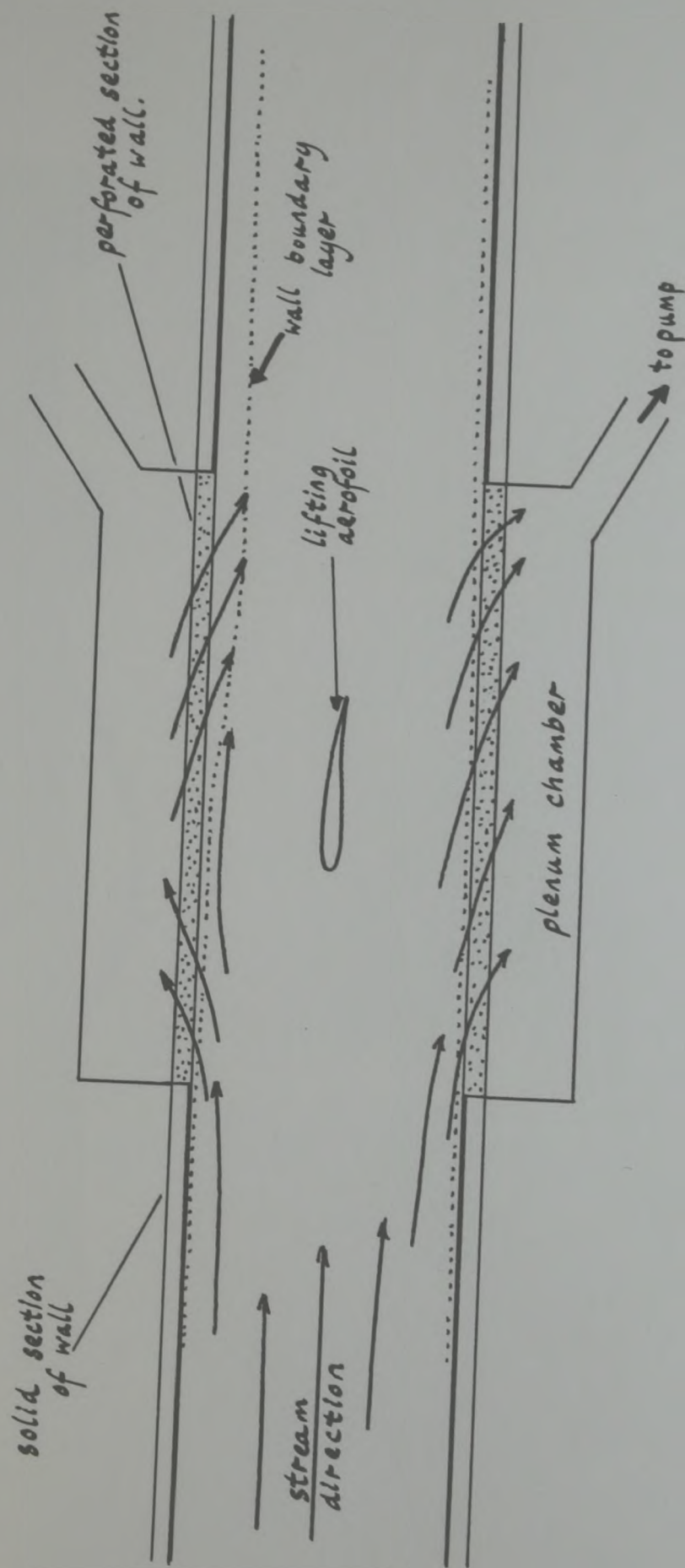
A representation of the wind tunnel flow, as it is treated analytically, is shown in Figure (9). The ordinate normal to the freestream direction is given the variable name 'y' in this case, and the origin of co-ordinates is at the centre of the bottom liner of the wind tunnel. The variable  $H$  denotes the height of the working section.

The influence of the aerofoil on the flow in the wind tunnel is represented by a point vortex and doublet at the centre of the working section. The doublet strength,  $\mu$  is related to the required cross-sectional area of the aerofoil,  $A$ , by the following equation;

$$\mu = \frac{u_{\infty} A}{\pi} \quad (3.5)$$

Reducing the complex velocity due to a doublet to its components,  $u$  and  $v$ , we find that the perturbations experienced at a point  $(x, y)$  in the wind tunnel are;





FIGURE(8) Diagram of overall flow situation modelled by PILOT.

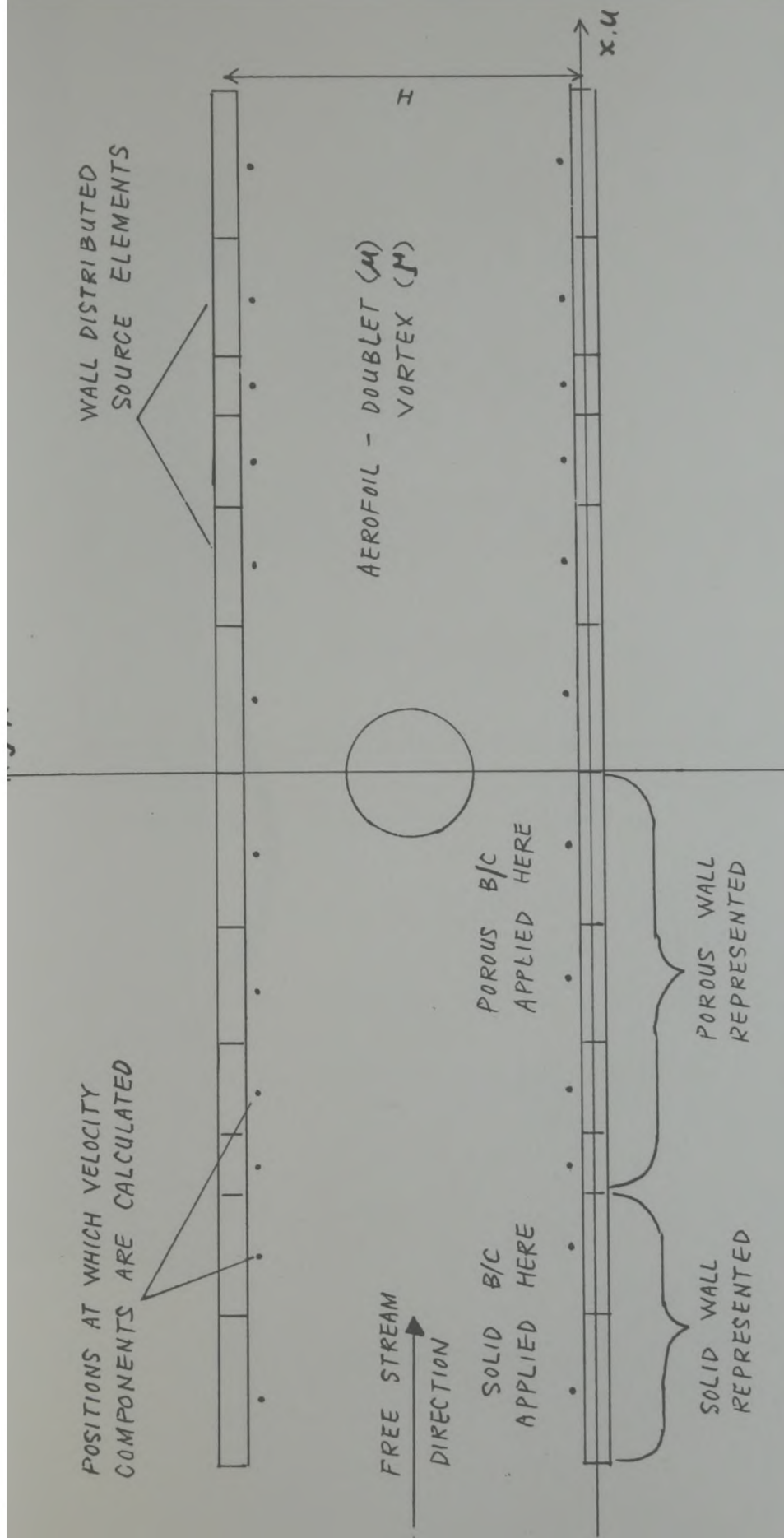


FIG.(9) SCHEMATIC DIAGRAM OF TYPICAL WINDTUNNEL REPRESENTATION IN 'PILOT'.



$$u = \mu \left\{ \frac{(y - \frac{H}{2})^2 - x^2}{(x^2 + (y - \frac{H}{2})^2)^2} \right\} \quad (3.6)$$

and

$$v = \mu \left\{ \frac{-2x(y - \frac{H}{2})}{(x^2 + (y - \frac{H}{2})^2)^2} \right\} . \quad (3.7)$$

For an aerofoil with a required chord 'C', the vortex strength,  $\Gamma$  is related to the chosen lift coefficient in the following way;

$$\Gamma = - \frac{U_{\infty} C_L C}{2} . \quad (3.8)$$

Equation (3.8) is derived from the normal definition of the lift coefficient ( $C_L$ ) of an aerofoil and the expression for the lift of a bound vortex in potential flow, namely

$$L = -\rho U_{\infty} \Gamma .$$

The negative sign here is the convention resulting from the definition of  $\Gamma$ , the vortex strength.

The perturbations produced by this singularity are;

$$u = \frac{-\Gamma (y - \frac{H}{2})}{2\pi (x^2 + (y - \frac{H}{2})^2)} \quad (3.9)$$

and

$$v = \frac{\Gamma x}{2\pi (x^2 + (y - \frac{H}{2})^2)} . \quad (3.10)$$

In an attempt to simulate a similar wind tunnel flow, Mokry, Peake and Bowker (1974) use (effectively) an infinite series of images of the aerofoil, reflected about the wall position line. For the present work, this approach appears inadequate, in that it seems unlikely to be capable of simulating step changes in the effective wall boundary conditions. Such changes would certainly take place at the transition from solid to perforated wall, or the reverse situation. Kemp (1976) uses distributed vortex elements along the wall position line when attempting to generate a wind tunnel flow field using measured boundary conditions. Due to the nature of a vortex, it is futile to use only vortices along the wall position line when attempting to predict a flow field where some nett outflow from the working section is expected. In the present work, distributed source elements are used. They are positioned continuously, but not overlapping, along the wall position lines. Each source element is of uniform strength along its length (but not necessarily of the same strength as its neighbours). This approach is considerably simpler than that of Kemp (1976), who uses overlapping vortex elements, where each element has a strength distribution consisting of three different (but continuous) quadratic arcs.

A straight, horizontal, distributed source element of strength ' $m$ ' per unit length is shown in Figure (10). The velocity perturbations due to this element at the position  $(x, y)$  may be expressed as follows. The longitudinal component,

$$u = \frac{-m}{4\pi} \ln \left\{ \frac{(x'_2 - x)^2 + (y' - y)^2}{(x'_1 - x)^2 + (y' - y)^2} \right\} \quad (3.11)$$

and the normal component

$$v = \frac{m}{2\pi} \left\{ \tan^{-1} \left( \frac{y - y'}{x - x'_2} \right) - \tan^{-1} \left( \frac{y - y'}{x - x'_1} \right) \right\}. \quad (3.12)$$

The points along the wall at which the velocity perturbations



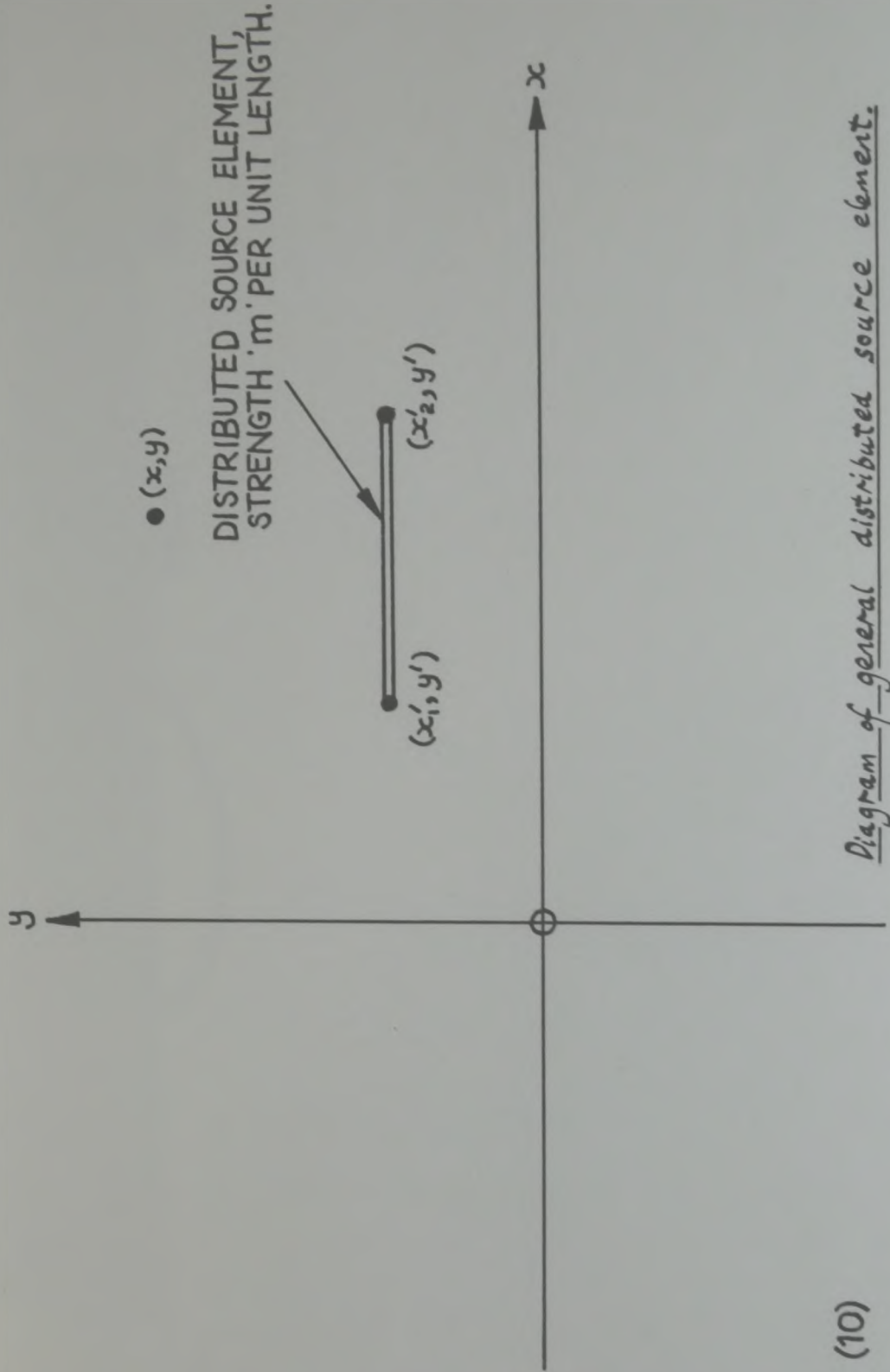


FIGURE (10)

Diagram of general distributed source element.

are calculated are positioned half-way along each source element. In Figure (10), if the value of  $x$  were bounded by  $x_1'$  and  $x_2'$ , then as  $y'$  tends to  $y$ , the value of the perturbation  $V$  in Equation (3.12) above tends to  $\frac{\pi}{2}$ . This property of the distributed source element is convenient and in contrast to the point source, for which the magnitude of the perturbation velocity tends to infinity as one approaches the singularity position. In the computer program, the position at which the velocity components are calculated, is chosen to be a distance 0.0001 of the wind tunnel height from the source element line. This slight displacement from the source element line causes the arctangent terms in Equation (3.12) to be simpler to compute, while only negligibly affecting the predicted flow in the wind tunnel. A typical distribution of wall elements is shown in Figure (9).

Using Equations (3.11) and (3.12) above, influence matrices are generated which relate the perturbation components at each control point to the distributed source strength ( $m$ ) of each wall element. In addition, column vectors containing the direct influence of the aerofoil representation at each control point are generated. This is done using Equations (3.6), (3.7), (3.9) and (3.10). The total perturbation components experienced at the control points may then be expressed (in matrix algebra) as;

$$[U] = [UINF][M] + [UA] \quad (3.13)$$

$$\text{and} \quad [V] = [VINF][M] + [VA] \quad (3.14)$$

Here,  $UINF$  and  $VINF$  are the respective influence coefficients relating the wall source strengths to the perturbations,  $UA$  and  $VA$  are the direct influence of the aerofoil representation at the control points and  $M$  is the column vector of distributed wall source element strengths.



At this point, it is helpful to present a flow diagram of the computer program 'PILOT'. This is shown in Figure (11). With the exception of the boundary layer calculation, the whole of the proposed calculation scheme is shown on this diagram. Some points relating to the diagram remain, as yet, undiscussed.

The matrices UINF and VINP are calculated once only for each wind tunnel geometry considered (position (A) on Figure (11)). The matrices representing the influence of the aerofoil, UA and VA are generated for each aerofoil geometry considered (position (B)).

Once the above matrices have been generated, and the relationship between u and v, the perturbation components at the wall, has been calculated, it is possible to solve directly for the distributed wall source element strengths. If for example, the relationship between u and v is

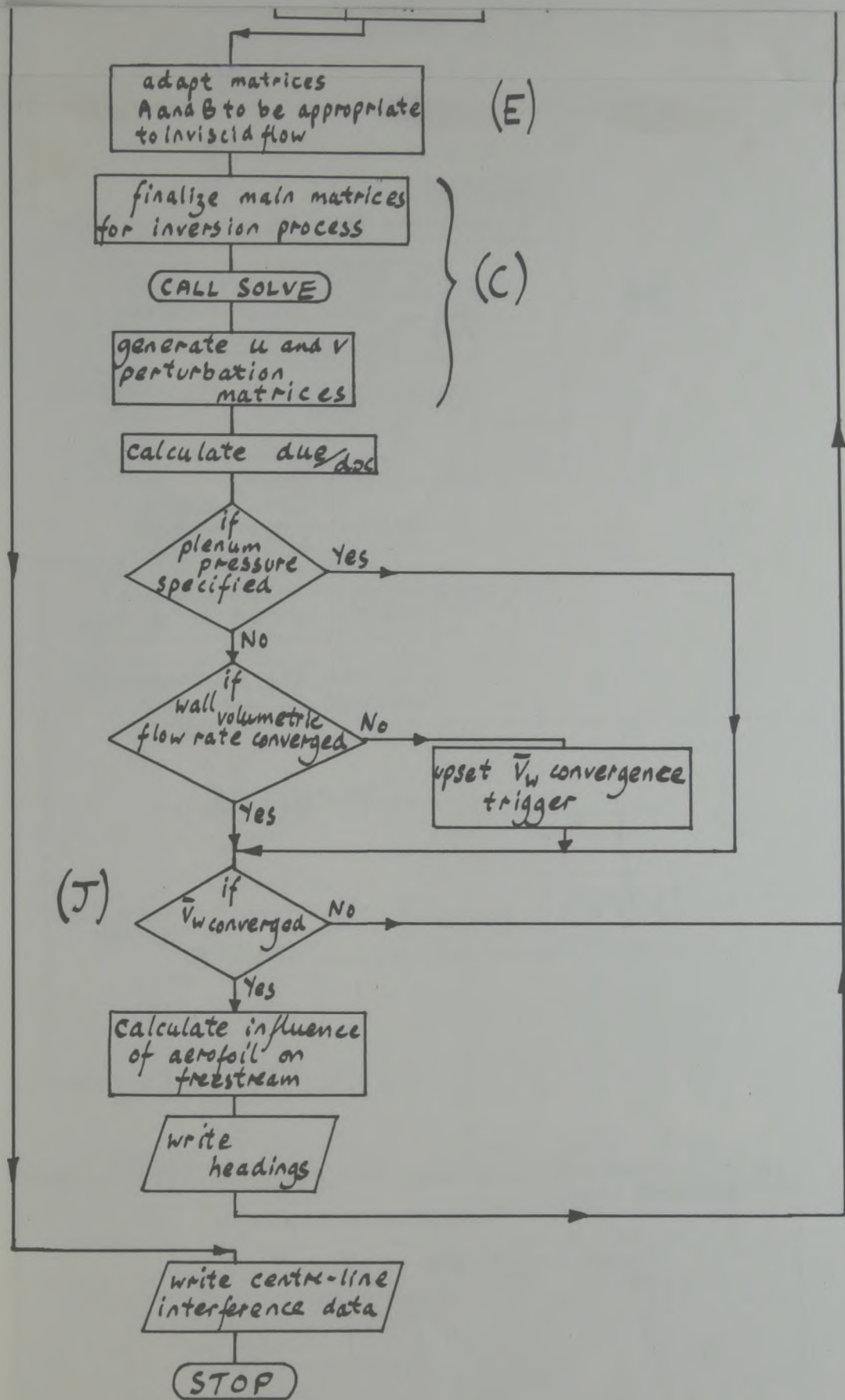
$$[u] = [A'] + [B'] [v] \quad (3.15)$$

(a relationship which will be frequently used later), then a simple matrix inversion is possible. Combining Equations (3.13), (3.14) and (3.15), we find that;

$$[UINF][M] + [UA] = [A'] + [B'] [VINP][M] + [VA],$$

$$\text{or } ([UINF] - [B'] [VINP])[M] = [A'] + [B'] [VA] - [UA].$$

Multiplying both sides of this equation by the inverse of the major bracketed term on the left hand side, we find that,



FIGURE(11). Flow diagram of computer program PILOT.



$$[M] = [U_{INF}] - [B'] [V_{INF}]^{-1} \cdot ([A'] + [B'] [VA] - [UA]) . \quad (3.16)$$

A direct solution for the distributed source strengths,  $M$ , is then carried out and using Equations (3.13) and (3.14), the values of the perturbation components are then calculated. This process of matrix algebra, inversion and the subsequent use of the matrix  $M$  is marked on Figure (11) at position (C).

The boundary condition to be applied at the position of the perforated wall normally takes the form of a simple relationship between the longitudinal and normal components of the perturbation velocity there. To match conveniently with this approach, a relationship between  $u$  and  $v$  is also used as a solid wall boundary condition, rather than the more familiar expression;

$$V = 0 .$$

In the viscous flow, the following solid wall boundary condition is used;

$$C_{pw} = 1000 \theta . \quad (3.17)$$

Here,  $\theta$  is the actual viscous outflow angle at the wall  $(v/u_e)$ . In the computer program,  $C_{pw}$  is calculated from velocity perturbations using the expression;

$$C_p = -2 u / u_{\infty} \quad (3.18)$$

(which is correct to first order and almost without error in flows with only small perturbations from the free stream conditions).

However, Equation (3.18) gives only the pressure coefficient relative to the freestream conditions. The plenum chamber pressure coefficient, defined as

$$C_{ppl} = \frac{P_{\infty} - P_{pl}}{\frac{1}{2} \rho U_{\infty}^2} \quad (3.19)$$

must be taken into account. The non-dimensional pressure difference between the working section and plenum chamber sides of the windtunnel liner ( $C_{pw}$ ) is then defined

$$C_{pw} = C_p + C_{ppl} \quad (3.20)$$

In most practical windtunnels, the transition from a solid to a fully perforated wall takes place gradually along the liners (although the transition back to a solid wall is usually abrupt). In the present method (see Figure (9)), the transitions to and from a porous wall are effected abruptly, at the boundary between pairs of wall source elements. On one side of the transition, the boundary condition effective at the centre of the element is that appropriate to a porous wall, while at the centre of the element on the other side of the transition, the solid wall boundary condition is operative,

By using a perturbation field to represent the flow in the wind-tunnel, a situation is produced where there may be no undisturbed flow at any point in the windtunnel working section or, upstream or downstream of it. However, for comparison with experiment, it is helpful to be able to define a reference or undisturbed stream position. In the computer program, this is done in the following manner. The position along the centre-line of the working section (relative to the origin of the co-ordinates) where the flow is to be defined as freestream, is included in the input data for the computer program (and denoted 'XUS'). When the calculation has converged, the nett perturbation (in the longitudinal direction) at the reference position and the resulting effective freestream speed there are calculated. All data required to be output (such as



values of  $C_{pw}$ , etc) are then re-calculated using the new reference speed, before being output.

In this description of the program formulation, no mention has been made of the calculation of viscous flows. A description of these calculations now follows, covering the part of the computer flow diagram in Figure (11) from point (D) to point (E).

The perturbation velocity normal to the freestream direction in the effective inviscid flow at the walls (  $\bar{v}_w$  ) is initially altered so that it is defined as positive for inflow at both walls. This step is helpful in that it permits the flow near both walls to be expressed in a manner compatible with that in Figure (6). Equation (3.3), in a form suitable to incompressible flow, namely,

$$\delta^* \frac{du_e}{dx} + u_e \frac{d\delta^*}{dx} + v_w - \bar{v}_w = 0 \quad (3.21)$$

is then used to convert  $\bar{v}_w$  to the average normal velocity in the viscous flow near the wall (  $v_w$  ). The two terms involving  $u_e$  and  $\delta^*$  are derived either (as in the first iteration of the program), from the assumption that they are constant or (during subsequent iterations) from their values calculated during the previous iteration. The equation is applied at discrete points on each wall of the windtunnel. These points are at the centre of each distributed source element, where values of  $u_e$ ,  $\delta^*$ , and  $\bar{v}_w$ , are available. The derivatives of  $u_e$  and  $\delta^*$  in the equation are calculated using finite difference analogues. These analogues are the average of forward and backward differenced derivatives wherever possible, but at the beginning and end of the wind-tunnel wall are reduced to forward and backward differenced derivatives respectively,

The largest subroutine ( **BL** ) is then called, to calculate the development of the boundary layer displacement thickness on both walls of the windtunnel. It is provided with the distributions of the longitudinal and normal component of velocity at the wall position

(  $u_e$  and  $v_w$  ) and the longitudinal derivative of  $u_e$ .

Other data required by the subroutine for operation are starting conditions for the boundary layer, the freestream unit Reynolds number and the positions of the points at which values of  $u_e$ ,  $v_w$  and  $du_e/dx$  are specified. On returning control to the major program segment, the subroutine provides values of  $\delta^*$  and the longitudinal derivative of  $\delta^*$ ;  $(d\delta^*/dx)$  at each of the control points along the windtunnel walls. The calling of this subroutine is marked at position (F) on Figure (11). A more detailed description of the contents of subroutine BL will be given later.

The development of the boundary layer along each wall predicted by subroutine BL will not, in the early iterations, be very close to that assumed at position (D) on Figure (11). A convergence check is carried out at (G) in the Figure, to establish whether the values of  $\delta^*$  predicted at the downstream end of the windtunnel walls are in agreement with their assumed values (within a specified margin). If convergence has been achieved, control is passed beyond position (G); if not, the new boundary layer development is provided as new data for Equation (3.21) at position (D). An iteration loop is thus formed between positions (D) and (F). To achieve rapid convergence, it has been found desirable to employ relaxation in Equation (3.21) in the following way;

$$V_{w_{NEW}} = 0.4 \left( \bar{V}_w - \delta^* \frac{du_e}{dx} - \frac{d\delta^*}{dx} \right) + 0.6 \cdot V_{w_{OLD}} .$$

Here,  $V_{w_{OLD}}$  is the value of the average viscous crossflow speed at the wall position, calculated in the previous iteration.

Having calculated the details of the flow near the windtunnel walls compatible with the velocity perturbations in the effective inviscid flow, a new boundary condition to be applied at the walls is generated. Although in some specific calculations (to be described later), a somewhat different approach to calculating the



boundary condition is taken, the following description is relevant to the majority of cases undertaken. The generation of the new boundary condition is marked at position (H) in Figure (11).

During the development of this computer program, two separate characteristics relating to the perforated wall were used. The first is derived from Jacocks (1976), which was discussed in section (2) of this report. Figures (16)a. -(17) of Jacocks report contain information relating to the characteristics of a number of different perforated wall types, but all having holes inclined at  $60^\circ$  to the perpendicular. A simple analysis of these Figures revealed that for walls with an open area ratio of 6% and wall thicknesses and hole diameters of about 3mm, the applicable wall characteristic is approximately

$$C_{pw} = (10\delta^* - 0.05) + \theta_w \exp(1.5 - 200\delta^*) \quad (3.22)$$

(Here  $\theta_w$  is defined positive for out-flow).

Clearly, for any value of  $\delta^*$ , a straight line relationship exists between  $C_{pw}$  and  $\theta_w$ . In the computer program, a relationship of the form

$$C_{pw} = A'' + B''\theta_w$$

is generally used to represent the new boundary condition to be eventually applied to the inviscid flow calculation. Then using Jacocks' wall characteristic,

$$A'' = 10\delta^* - 0.05 \quad (3.23)$$

and

$$B'' = \exp(1.5 - 200\delta^*) \quad (3.24)$$

Jacocks wall characteristic was later discovered to represent the

inviscid flow angle at the wall position ( $\bar{\theta}_w$ ) rather than  $\theta_w$ , but as the present computer program was in the development stage, this error was neglected. At each control point on the windtunnel walls, the predicted value of  $\delta^*$  is used with Equations (3.23) and (3.24) to generate values of A" and B" that apply at that point. Finally, to express the boundary condition in the following way;

$$C_p = A + B \theta_w, \quad (3.25)$$

Equation (3.20) is used. Thus

$$A = A'' - C_{ppl} \quad (3.26)$$

and 
$$B = B'' \quad (3.27)$$

The second wall characteristic used in the computer program 'PILOT' is that derived from experiments described in the present report. This characteristic, which is a fourth order polynomial, relating  $\frac{\Delta p}{q}$ ,  $\theta_w$  (again positive for outflow) and  $\delta^*$ , is rather more complex in its application than the first type due to Jacocks (1976). This is because  $\frac{\Delta p}{q}$ , the non-dimensional pressure difference between the working section and plenum chamber sides of the wall is based on 'q' the local dynamic head unlike  $C_{pw}$ , which is based on the freestream dynamic head. The wall characteristic function is

$$\begin{aligned} \theta_w = & 0.00562 - 0.538 \delta^* + 0.093175 \left( \frac{\Delta p}{q} \right) - 11.704 \left( \frac{\Delta p}{q} \right) \delta^* \\ & - 145.437 \left( \frac{\Delta p}{q} \right)^2 \delta^* + 0.90049 \left( \frac{\Delta p}{q} \right)^3 - 824.644 \left( \frac{\Delta p}{q} \right)^3 \delta^*. \end{aligned} \quad (3.28)$$

This function is obtained from the wall characteristic function derived in Section (4) of this report, whilst certain changes have been made. First, the signs have been reversed to specify  $\theta_w$  positive for outflow. Second, terms involving  $\delta^*$  have been multiplied by 339., as  $\delta^*$  was originally non-dimensionalized with respect to a perforation diameter of 2.95 mm, and in the present computer program,  $\delta^*$  is specified in metres. Finally, an average test Mach number of 0.78 has



been assumed. To match later calculations,  $\theta_w$  has been expressed as a function of  $\Delta p_q$ , rather than the reverse (which would be simpler for present purposes).

At each control point along the windtunnel walls, calculated values of  $\delta^*$  and  $\Delta p_q$  are available. These are used to calculate the gradient  $(\frac{d\theta_w}{d\Delta p_q})$  of the wall characteristic at that point on the wall and at those particular values of  $\delta^*$  and  $\Delta p_q$  (see Figure (12)). The required gradient for the boundary condition  $(\frac{d\Delta p_q}{d\theta_w})$  is then found by inverting the first gradient. The intercept of the local characteristic on the  $\Delta p_q$  axis is then calculated. Thus the boundary condition ( $\Delta p_q$  as a linear function of  $\theta_w$ ) required at each control point is calculated. This boundary condition represents only the local linear fit to the wall characteristic at values of  $\delta^*$  and  $\Delta p_q$  which have been predicted to exist at a particular point in the windtunnel during the previous iteration of the calculation procedure (see the hard line, ringed on Figure (12)). Using the notation in the computer program, the boundary condition equation is

$$\Delta p_q = 'TINT' + 'QR' \cdot \theta_w \quad (3.29)$$

Using Equations (3.19), (3.20) and the exact equation for the wall pressure coefficient;

$$C_p = \frac{p_w - p_\infty}{\frac{1}{2} \rho u_\infty^2}, \quad (3.30)$$

it can be shown that when  $C_p$  is much less than unity (and therefore  $C_p^2$  is negligible),

$$\frac{\Delta p}{q} = \frac{1}{(1 - C_p)} \cdot (C_p + C_{ppl}). \quad (3.31)$$

Combining this equation with Equation (3.29) we find

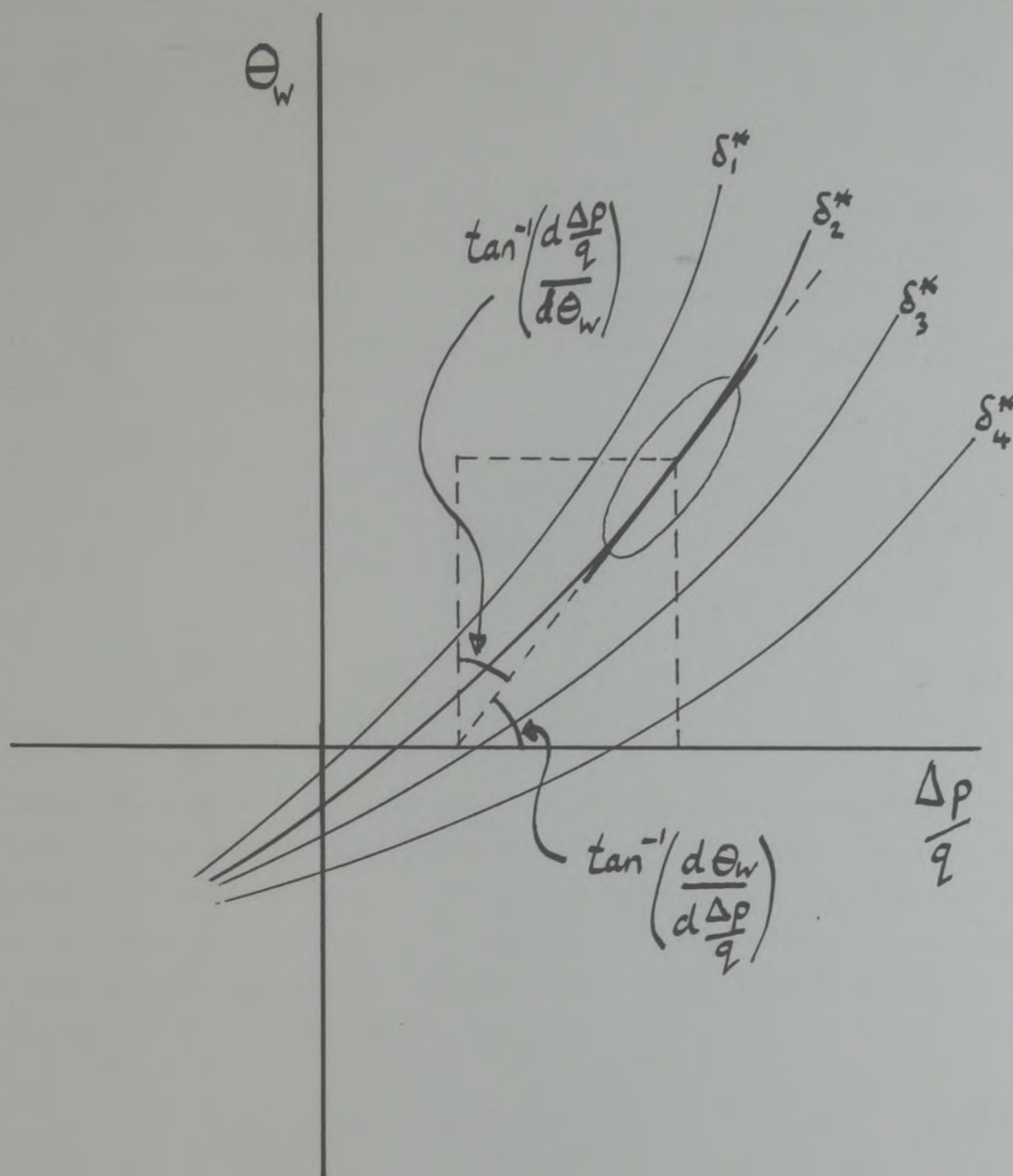


FIGURE (12)

Diagram to elucidate method of obtaining a local linear wall characteristic.



$$C_p = \frac{('TINT' - C_{ppl}) + ('QR') \Theta_w}{1 + 'TINT' + 'QR' \Theta_w} \quad (3.32)$$

The desired simple relationship between  $C_p$  and  $\Theta_w$  is now available, except that in Equation (3.32), the denominator includes the term  $\Theta_w$ . In the computer program, this  $\Theta_w$  is calculated from values of  $V_w$  and  $u_e$  from the previous iteration. Thus an equation of the form of Equation (3.25) is formed, where

$$A = \frac{('TINT' - C_{ppl})}{\left(1 + 'TINT' + 'QR' \left(\frac{-V_w}{u_e}\right)\right)} \quad (3.33)$$

and

$$B = \frac{'QR'}{\left(1 + 'TINT' + 'QR' \left(\frac{-V_w}{u_e}\right)\right)} \quad (3.34)$$

Having generated a new wall boundary condition using either the empirical equation derived from Jacocks (1976) work, or that from the experiments in the present report, it is necessary to correct this to account for solid sections of wall. Equation (3.17) is used, but because the concept of a plenum chamber does not apply where the wall is solid, the equation is used in the form

$$C_p = 1000 \Theta_w \quad (3.35)$$

Using the notation of Equation (3.25), A is zero and B is 1000. For all control points on areas of wall specified to be solid, the above values of A and B replace these values calculated from the wall characteristics earlier. This procedure is carried out at position (I) in Figure (11).

The boundary condition, Equation (3.25), must be altered to relate only effective inviscid flow velocity perturbations, before it can be applied to the inviscid flow calculation. This is done in the following

manner (and marked at position (E) on Figure (11)). Equation (3.4), adapted for use in cases of incompressible flow has the form

$$V_w = \bar{V}_w + C \quad (3.36)$$

Here (referring to Equation (3.3)),

$$C = -\delta^* \frac{du_e}{dx} - u_e \frac{d\delta^*}{dx}. \quad (3.37)$$

Now in Equation (3.25),

$$C_p = -\frac{2u}{u_\infty}$$

and

$$\theta_w = -\frac{V_w}{u_e} \quad (3.38)$$

In Equation (3.36) the term  $\bar{V}_w$  is in fact the perturbation normal to the freestream in the inviscid flow (defined for the moment; inflow positive on both walls). Combining Equation (3.25) with the above four equations we find

$$u = \left( -\frac{u_\infty}{2} \left\{ A + B \left( \frac{\delta^*}{u_e} \frac{du_e}{dx} + \frac{d\delta^*}{dx} \right) \right\} \right) + \left( \frac{u_\infty}{2} \frac{B}{u_e} \right) \bar{V}_w. \quad (3.39)$$

All values of  $u_e$  and  $\delta^*$  within the pairs of parentheses are taken from previous iterations of the overall computing scheme. The right hand term in parentheses is then reversed in sign for control points on the top wall to make the equation completely consistent with the inviscid flow calculation scheme. Equation (3.39) is then in the required form (that of Equation (3.15)) for application as a wall boundary condition, where in Equation (3.15)



$$A' = \left( -\frac{u_\infty}{2} \left\{ A + B \left( \frac{\delta^*}{u_e} \cdot \frac{du_e}{dx} + \frac{d\delta^*}{dx} \right) \right\} \right) \quad (3.40)$$

and

$$B' = \mp \left( \frac{u_\infty}{2} \cdot \frac{B}{u_e} \right) \quad (3.41)$$

Virtually all the components of the iteration procedure in the computer program 'PILOT' have now been described. At position (J) in Figure (11), a convergence check is carried out on all control point values of  $\bar{V}_w$ . If the check is successful, the program proceeds to calculate the effective freestream speed (described earlier) and output the required results before finally stopping. If the convergence check is unsuccessful, control is returned to position (K) and the calculation proceeds. No relaxation is used in the iteration loop bounded by (J) and (K), in contrast to the other iteration loop between (D) and (G).

In most commercial windtunnels (and windtunnel flow calculation methods) it is unnecessary to measure or specify the nett flow rate of air through the perforated walls. However, the capability to specify this flow rate has been included in the computer program 'PILOT' as an option. This alternative is useful in a number of instances; to model the flow in the windtunnel with closed box plena (where the nett flow rate of air from the working section is zero), for example. During each iteration of the computer program, the nett flow rate of air through the perforated section of each wall is calculated. This is carried out by integrating discrete values of the mean viscous crossflow component ( $V_w$ ) at the wall using the trapezium rule. If the nett flow rate of air through the walls has been specified at the outset of the calculation, then a comparison is made between the required and calculated flow rates, and if a discrepancy exists between them, the plenum chamber pressures are altered by a small amount. Clearly then, the actual flow calculation is affected

directly by the plenum chamber pressures specified during each iteration (rather than by the specified flow rate through the walls) and in some calculations these are specified at the outset and fixed during all subsequent iterations. The above process of specifying the wall flow rates or plenum chamber pressures can be put into effect simulating either connected or unconnected plena at will.

This completes the description of the formulation for the FORTRAN computer program 'PILOT'. A listing of this program and instructions for running it are contained in Appendix(3).

### 3.5 Boundary Layer Prediction Method.

A boundary layer prediction method is required, to serve the purposes of the present research. Ideally, this prediction method would be capable of predicting accurately the development of a turbulent boundary layer on a rough surface in two-dimensional flow. Account should be taken in the method of compressibility effects and the presence of longitudinal pressure gradients. Finally, the effect of transpiration through the wall should be included. In Freestone and Henington (1979), Section(5.1), a list is presented of points which need considering when choosing such a boundary layer prediction method. The list includes, obviously, considering the method's accuracy (mentioned above) and other points relating to the availability, and suitability of the method for application to the inviscid flow calculation schemes to be used.

It would not be unfair to state that, at present, there are no boundary layer calculation methods available which can adequately meet all the requirements stated above. Methods have been developed to meet one or perhaps two of the above requirements, but not all four together. This inadequacy is particularly clear for the prediction of boundary layer development where wall transpiration is present. It is expected in the present research that wall transpiration rates  $(\rho_w v_w / \rho_e u_e)$ ,



$$-0.02 < \frac{\rho_w v_w}{\rho_e u_e} < 0.02$$

will be encountered. Such transpiration rates are at least in excess of those which can be accurately accounted for by all calculation methods considered (for example that of Bradshaw and Unsworth (1974)).

The advantages, at least in simplicity, of the simple integral methods over those involving eddy-viscosity assumptions (usually leading to the use of a finite difference approach) are clear. Also with careful use of empiricism, there is no reason why an integral method should not give quite accurate results. For these reasons the integral method approach was chosen, to be based on the entrainment method of Head and Patel (1968). The method as presented by Head and Patel does not account for compressibility, wall transpiration, or wall roughness.

Two initial alterations were made to the method of Head and Patel (1968). The first was to replace their rather complicated expression for  $C_f$  with that of Ludwig and Tillman (1950), namely;

$$C_f = 0.246 e^{-1.56/H} \cdot R_{\theta}^{-0.268} \quad (3.42)$$

Second was to use the relationship between  $H_1$  (that is;  $\delta - \delta^*/\theta$ ) and  $H$  proposed by Patel (1965) in place of the interpolation table of Head\*. This relationship is

$$H_1 = \frac{2H}{(H-1)} \quad (3.43)$$

To account for transpiration, the wall is treated as homogeneous, that is, porous rather than perforated. The momentum integral equation used by Head is altered by the addition of a further term, namely the crossflow angle at the porous wall;  $v_w/u_e$ . The equation then becomes

\* Reference to 'Head' indicates a reference to Head and Patel (1968)

$$\frac{d\theta}{dx} = \frac{C_f}{2} - \left(\frac{\theta}{l}\right) \cdot \frac{d\frac{u_e}{u_R}}{d\frac{x}{l}} \cdot \frac{(H+2)}{\frac{u_e}{u_R}} + \frac{v_w}{u_e} \quad (3.44)$$

Here, the equation has been non-dimensionalized using a reference length ( $l$ ) and speed ( $u_R$ ), normally taken as  $1m$  and  $1ms^{-1}$  respectively. The increase in skin friction caused by surface suction is accounted for very simply. Based on the experimental data of Kruse (1978), for suction cases only, an alteration is made to the value of  $C_f$  calculated by Head's method. The alteration is as follows;

For blowing

$$C_f = C_{f\text{HEAD}} \quad (3.45)$$

For suction

$$C_f = C_{f\text{HEAD}} - 1.5 \left(\frac{v_w}{u_e}\right) \quad (3.46)$$

Head's entrainment equation, expressed in non-dimensional form, using Equation (3.43) to replace terms in  $H_1$  then becomes

$$\frac{dH}{d\frac{x}{l}} = -H \frac{(H^2-1)}{\frac{u_e}{u_R}} \cdot \frac{d\frac{u_e}{u_R}}{d\frac{x}{l}} - \frac{(H-1)}{2\left(\frac{\theta}{l}\right)} \left\{ (H-1) \left( F + \left(\frac{v_w}{u_e}\right) \right) - H \left( C_f + 2 \left(\frac{v_w}{u_e}\right) \right) \right\} \quad (3.47)$$

For suction cases, here  $C_f$  is calculated using Equation (3.46), the terms in the entrainment equation involving  $(v_w/u_e)$  become quite finely balanced. To ensure that  $dH/d\frac{x}{l}$  is of the right sign (negative for suction), an amendment is made to Equation (3.47). This then becomes

$$\frac{dH}{d\frac{x}{l}} = -H \frac{(H^2-1)}{\frac{u_e}{u_R}} \cdot \frac{d\frac{u_e}{u_R}}{d\frac{x}{l}} - \frac{(H-1)}{2\left(\frac{\theta}{l}\right)} \left\{ (H-1) \left( F + \left(\frac{v_w}{u_e}\right) \right) - H \left( C_f + 2 \left(\frac{v_w}{u_e}\right) \right) - 1.2 H \left(\frac{v_w}{u_e}\right) \right\} \quad (3.48)$$

Throughout the calculation procedure the value of  $H$  is confined within the range 1.1 to 3.0. This step, taken to maintain values of  $H$  within observed experimental limits, proved unnecessary as during



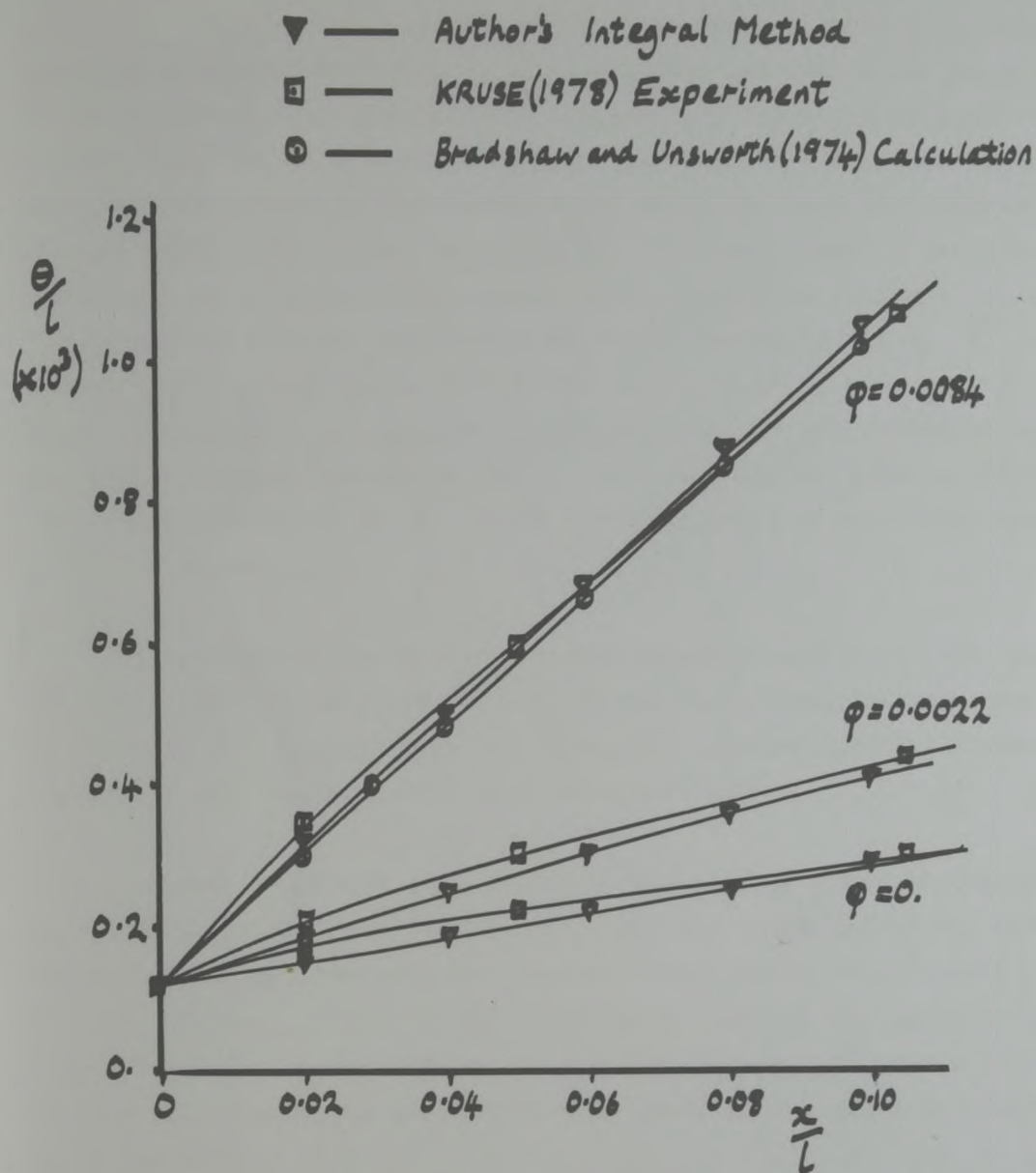
calculations to date,  $H$  has never approached either limit. To prevent values of  $\theta$  becoming negative, a minimum limit is set on  $Re_\theta$  of 500. Clearly many of the alterations made to Head's method are quite crude, but accuracy alone is not the objective of the present study and, as will be seen later, the method does give quite promising results.

It has been demonstrated (Green, 1968) that the effects of compressibility can be incorporated into Head's boundary layer method. For most of the present work, these effects are not included. Only in the latter stages (during development of the computer program 'PREDICT') is any account taken of compressibility; the local variation in freestream fluid density being used to calculate local momentum thickness Reynolds number.

Head's equations, once altered, are solved using a fourth order Runge-Kutta forward integration procedure. The complete algorithm is coded as a FORTRAN subroutine. This subroutine is incorporated into the programs 'PILOT' (as 'BL'), and 'PREDICT' (as 'WALLBL'). In both programs, it is more convenient to pass values of the displacement thickness,  $\delta^*$ , to and from the boundary layer calculation, rather than momentum thickness ( $\theta$ ) values. This is carried out, and conversions are made between  $\delta^*$  and  $\theta$  at the beginning and end of the boundary layer calculation subroutine.

For situations where the wall perforation size is small compared to the thickness of the boundary layer on it and there is blowing through the wall (positive  $V_w$ ), the method described above gives encouraging results. In Figure (13), results from the experiments of Kruse (1978) are shown. The prediction due to the present calculation method and that of the method of Bradshaw and Unsworth (1974) are also shown. Clearly for this comparison, the simple empirical method appears to be adequate.

Results from the present calculation method are also compared with experimental data obtained under rather more demanding conditions. These experiments were carried out during the course of this research. The



Blowing Parameter:  $\phi = \frac{\rho v_w}{\rho u_\infty}$

$L = 1\text{ m}$   
 $Re_L = 4 \times 10^6$

Results from Boundary Layer Method compared with  
 FIGURE (13) Experiments using Smooth wall.



windtunnel wall used was the 60° inclined hole, perforated liner, mounted in the transonic windtunnel at the City University. For the cases predicted, the local Mach number on the wall remained between 0.7 and 0.85. The local longitudinal pressure gradients were not severe and their effect on the boundary layer displacement thickness is likely to be small compared to the effect of the crossflow through the wall. A comparison between the measured development of displacement thickness and that predicted by the present calculation method is presented in Figure (14). Clearly the comparison is less encouraging than that presented in Figure (13). Although the deviations between theoretical and experimental values of  $\delta^*$  would continue to increase downstream of the region in which measurements were made, it is helpful to express the discrepancy, for the region shown, in terms of a standard deviation ( $\sigma$ ). This discrepancy between measured and calculated values of  $\delta^*$ , for the four cases of crossflow shown has a  $\sigma$  of 0.44 mm.

It seems unlikely that at the Mach numbers considered, the effects of compressibility would cause such significant errors in predicted results. In fact, in the calculations, the effect of compressibility is taken into account in the limited manner described earlier.

A brief investigation into the sensitivity of computed results to errors in input data was carried out. All data supplied to the calculation are reduced from experiment and contain experimental and analysis error. However, the sensitivity study revealed that errors in experimental data input could not account for the discrepancy observed in Figure (14). In fact the discrepancy possibly due to these errors has a standard deviation of only 0.15 mm.

The comparison made earlier with the experimental data of Kruse (1978) revealed that for walls with very fine perforations (which could be considered smooth), the present calculation method gives acceptable results. In figure (14), the first two curves, representing predicted values of  $\delta^*$  in blowing or approximately neutral conditions, reproduce approximately the data generated during the comparison with the results of Kruse. Clearly now the experimental rate of growth of displacement thickness is larger than in Kruse's experiments. This is almost certainly due to the

Results from boundary layer method compared with experiments  
using rough wall.

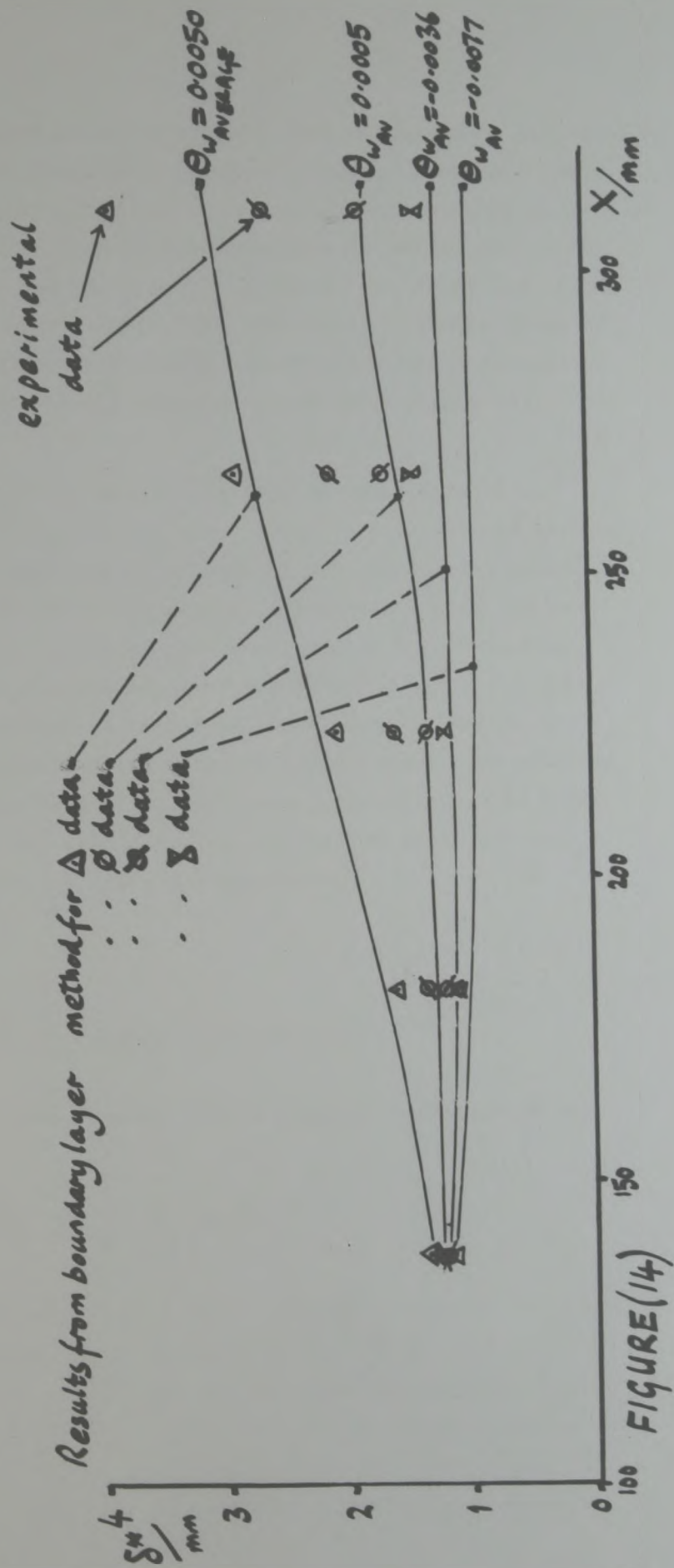


FIGURE (14)



large size of the perforations relative to the thickness of the boundary layer. This perforated wall is effectively rough. Sterland (1981) discovers the same difficulty, in using the present calculation method to predict the boundary layer development along a perforated plate with normal holes in low speed flow. In Figure (5.15) of his report (reproduced here as Figure (15)), Sterland presents a comparison of the development of momentum thickness on the wall, where calculated values are again consistently less than those from experiment.

It is clear that the effect of roughness will need to be incorporated in Head's method as used. This is likely to be carried out by altering the empirical constants in the controlling equations. In carrying out these alterations using experimental data, it may become apparent that a physical parameter such as  $\frac{\delta^*}{a}$  adequately represents the effective roughness of a perforated wall. If this were so, it would reduce the number of experiments necessary to complete the alterations to the boundary layer method. In addition, the method could then be applied with some confidence to the flow near other similar, but not identical, perforated walls without further alteration of the empirical constants.

### 3.6 Scheme for the Cross-flow Characteristic.

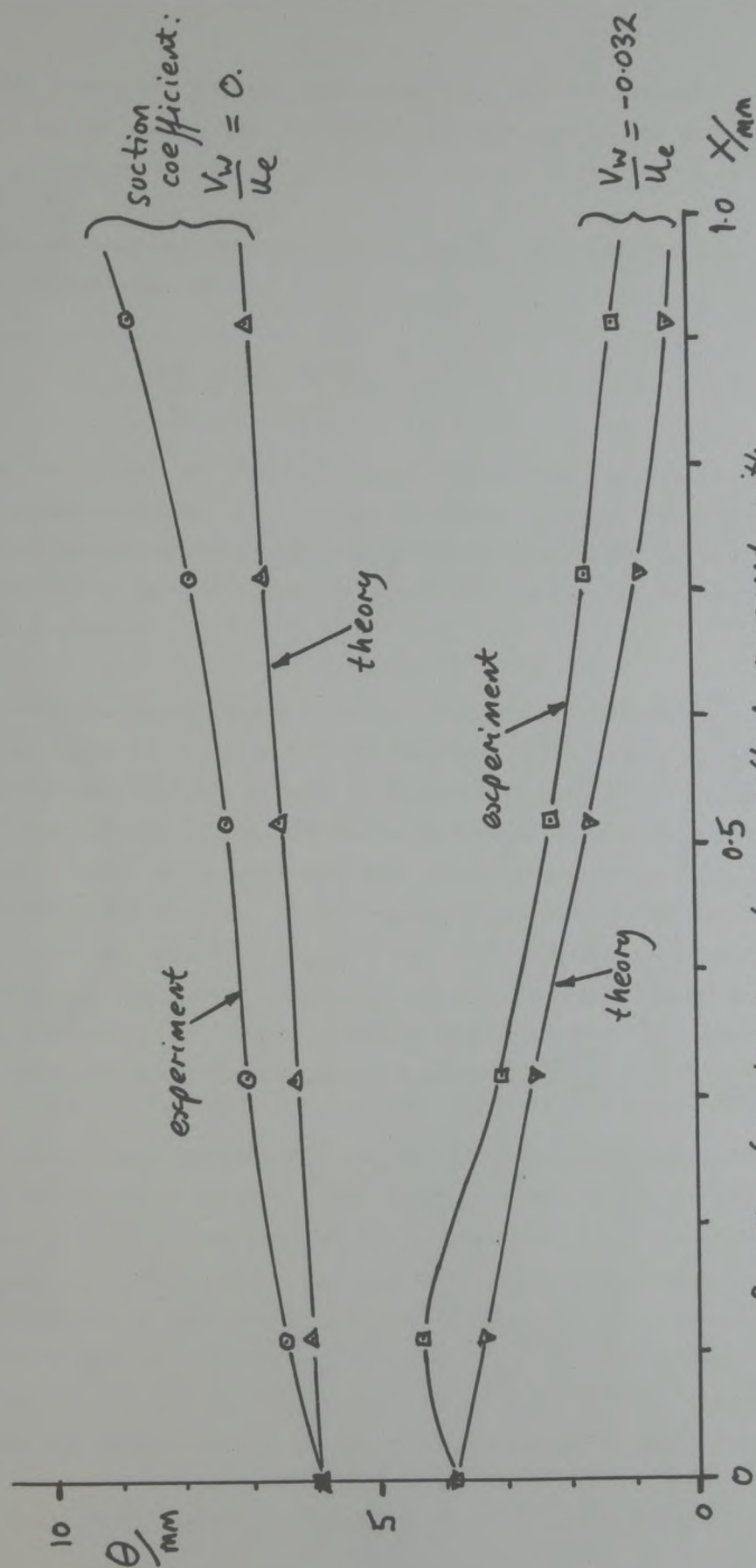
The disadvantages of using a wall boundary condition of the type

$$\phi_x \pm \frac{1}{\rho} \phi_z = 0$$

were mentioned in Section (2.1). These consist chiefly of erroneous assumptions concerning

- a) the boundary layer on the wall,
- b) the relationship between the pressure difference across the wall and the rate of flow through it
- and c) the pressure in the plenum chamber.

Reproduced from Figure 15.5 of Sterland (1981)



Results from boundary layer method compared with experiments using rough wall - Sterland.

FIGURE (15)



The new crossflow characteristic (and thus the new boundary condition to be applied to the inviscid flow) improves on the old one, in all three areas mentioned.

The non-dimensional pressure difference across the perforated wall ( $\frac{\Delta p}{q}$ ) is now used, where

$$\frac{\Delta p}{q} = \frac{p_w - p_{pl}}{q}$$

In this way, the value of  $p_{pl}$  is not now assumed to be equal to the freestream pressure and as all terms in the above equation are evaluated locally, the plenum chamber pressure need not be considered to be constant, but rather may be taken, if necessary, as varying in the longitudinal direction.

Any crossflow characteristic for the wall which relates  $\frac{\Delta p}{q}$ , either to the inviscid crossflow at the boundary layer edge ( $\rho_e v_e$ ), or to the effective inviscid crossflow at the wall ( $\overline{\rho_w v_w}$ ), would in general need to take account of the longitudinal derivatives of  $\delta^*$  and  $\rho_e u_e$ . This is because both the crossflows mentioned are influenced by these derivatives. It is expected that the actual average viscous crossflow at the wall ( $\rho_w v_w$ ) will not be influenced locally by the derivatives mentioned, but purely by local boundary layer and external flow properties. Hence, a relationship between  $\frac{\Delta p}{q}$  and  $\rho_w v_w$  is employed which also takes no account of  $\frac{d\delta^*}{dx}$  and  $\frac{d\rho_e u_e}{dx}$ .

This relationship between  $\frac{\Delta p}{q}$  and  $\rho_w v_w$  is however considered to depend on two other factors. The first of these is the nature of the boundary layer on the wall at the position at which values of  $\frac{\Delta p}{q}$  and  $\rho_w v_w$  are determined. The boundary layer displacement thickness is chosen as the single variable representing the nature of the boundary layer, as its close relationship to the displacement of streamlines in the inviscid flow seems more relevant to a "crossflow" function than any properties of the momentum thickness or shape factor. The second factor is the local Mach number in the inviscid flow. In Goethert (1961), Mach number is clearly shown to be an important

parameter in any simulation of a perforated wall characteristic. Figure (11.24) of his work is reproduced here as Figure (16). The characteristic for a wall very similar to that considered here is shown in this Figure. The variables on both axes have been non-dimensionalized with respect to freestream conditions and for all data shown, the boundary layer thickness is approximately constant. The gradient of the characteristic increases by 36% from a Mach number of 0.9 to 1.0. Although there are no data to indicate how Mach number might influence the characteristic below a value of 0.9, it is considered an important parameter, and thus is included as an independent variable in modelling the wall characteristic.

In the present work, no other variables are incorporated in the crossflow characteristic. However, some new variables might need future consideration (the local Reynolds numbers based on unit length for example). It should be noted that the crossflow characteristic is treated as a relationship between non-dimensional parameters. To achieve this, values of  $\delta^*$  are divided by the perforated diameter (2.95 mm), and values of  $\rho_w v_w$  by the term  $\rho_e u_e$ . Effectively then, two further variables are incorporated into the characteristic.

The relationship between the four chosen non-dimensional quantities,  $\frac{\Delta p}{q}$ ,  $\frac{\rho_w v_w}{\rho_e u_e}$ ,  $\frac{\delta^*}{d}$  and  $M$  is determined by experiment. At each of forty different flow conditions, values of the four variables are determined from windtunnel data. One major complication in this process is the difficulty in measuring  $\rho_w v_w$  directly. Values of  $v_e/u_e$  are determined outside the boundary layer and Equation (3.1), namely,

$$(L - \delta^*) \cdot \frac{d}{dx} (\rho_e u_e) - \rho_e u_e \cdot \frac{d\delta^*}{dx} + \rho_e v_e - \rho_w v_w = 0$$

is used (with other experimental data reduced to values of  $\delta^*$  and  $\rho_e u_e$ ) to calculate from these data, values of  $\frac{\rho_w v_w}{\rho_e u_e}$ . The forty sets of data mentioned, are fitted by a fourth order function. This function, when fitted, is



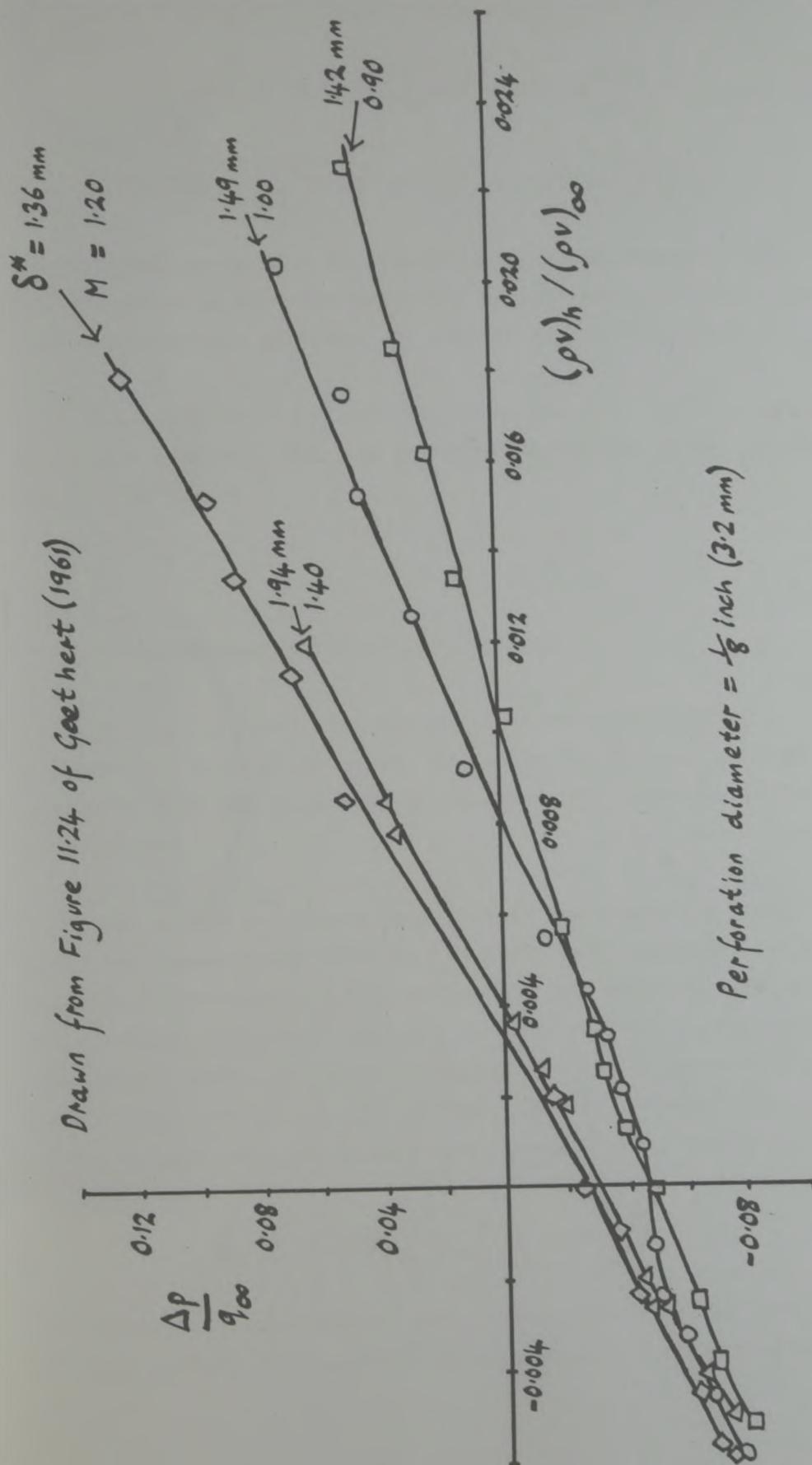


FIGURE (16) Wall characteristic due to Goethert, for various Mach numbers, with a boundary layer thickness of approximately 1.5 mm.

$$\begin{aligned}
\frac{p_{wV}}{p_{eV}} = & 0.37859 - 0.88046 M - 0.39602 \left( \frac{\delta^*}{a} \right) + 0.49733 M^2 \\
& + 1.0349 \left( \frac{\delta^*}{a} \right) M - 0.67327 \left( \frac{\delta^*}{a} \right) M^2 - 0.093175 \left( \frac{\Delta p}{q} \right) + 0.034528 \left( \frac{\delta^*}{a} \right) \left( \frac{\Delta p}{q} \right) \\
& + 0.42904 \left( \frac{\delta^*}{a} \right) \left( \frac{\Delta p}{q} \right)^2 - 0.90049 \left( \frac{\Delta p}{q} \right)^3 + 2.4327 \left( \frac{\delta^*}{a} \right) \left( \frac{\Delta p}{q} \right)^3 \quad (3.49)
\end{aligned}$$

The function, being of a greater order than one, allows a wall characteristic to be simulated which is non-linear and (notably) has a different average gradient for blowing and suction cases.

The experiments and analysis described briefly above are in fact quite complex. They are described in greater detail in Section (4) of this report.

### 3.7 The New Boundary Condition Equation.

In Section (3.6), the viscous flow wall characteristic is presented. It is now necessary to decide the form of the boundary condition equation to be used in applying the method to inviscid flow calculations.

One of the major long term aims of the present research is to apply the new boundary condition to practical transonic flow calculation methods. It is clear therefore that the new boundary condition should be as simple as possible to apply to such methods. One representative calculation method is that of Catherall (1975) (discussed in Section 2.1 of this report). In this method, the wall boundary condition (which is generally applicable to a number of wall types) is

$$\phi_x \pm FH\phi_{xz} \pm \frac{1}{\rho} \phi_z = 0$$

For the present, the central term in the above equation (which is only normally brought into operation for slotted wall windtunnel calculations)



is ignored. The type of wall characteristic selected in Section (3.6) does not permit us to consider using it. The remaining boundary condition, appropriate to perforated walls is

$$\phi_x \pm \frac{1}{P} \phi_z = 0 \quad (3.50)$$

(Here we note that  $P$  is a constant).

The simplest alteration possible to this boundary condition, would be to allow the value of  $P$  to be different for the top and bottom walls and, of equal importance, to vary in the longitudinal direction. Catherall's method, which uses a finite-difference approach to solve the governing equations of the flow, generates and assumes discrete values for  $\phi_x$  and  $\phi_z$  along both walls. Hence, it would be a simple step to specify  $P$  also, as having different values at discrete points along each wall. However, this simplest of alterations wastes to some extent the detail contained in the proposed wall characteristic. Notably, it is not possible with this boundary condition to account for a plenum chamber pressure which is not equal to the pressure in the freestream, although the new wall characteristic does account for this,

The next logical step in increasing the complexity, and the usefulness, of the boundary condition in Equation (3.50), is to replace the zero on the right hand side with a constant ( $K$  say). In referring to  $P$  and  $K$  as constants, it is intended that they are so, only for the boundary condition as it is applied at any particular control or grid point on the windtunnel walls. In general, the values of  $P$  and  $K$  will both vary with the longitudinal ordinate 'x' and from iteration to iteration in any inviscid flow calculation scheme employed. Using a non-zero value of  $K$  allows a difference between plenum and freestream pressures to be directly simulated (as for example, some crossflow, or  $\phi_z$ , will be induced with even zero  $\phi_x$ ). Also, if the crossflow characteristic does not pass through the origin of co-ordinates (as in Figure (16)), this can also be easily simulated using the constant  $K$ .

Higher order relationships could also be used as boundary conditions in flow calculations. However the complexity of incorporating them into existing practical flow calculation methods is likely to be high and they are not considered in the present work.

The computer program 'PILOT' was used in a simple evaluation of some of the various types of boundary condition. Using a boundary condition of the form of Equation (3.50), namely

$$\phi_x \pm \frac{1}{\rho} \phi_z = 0 ,$$

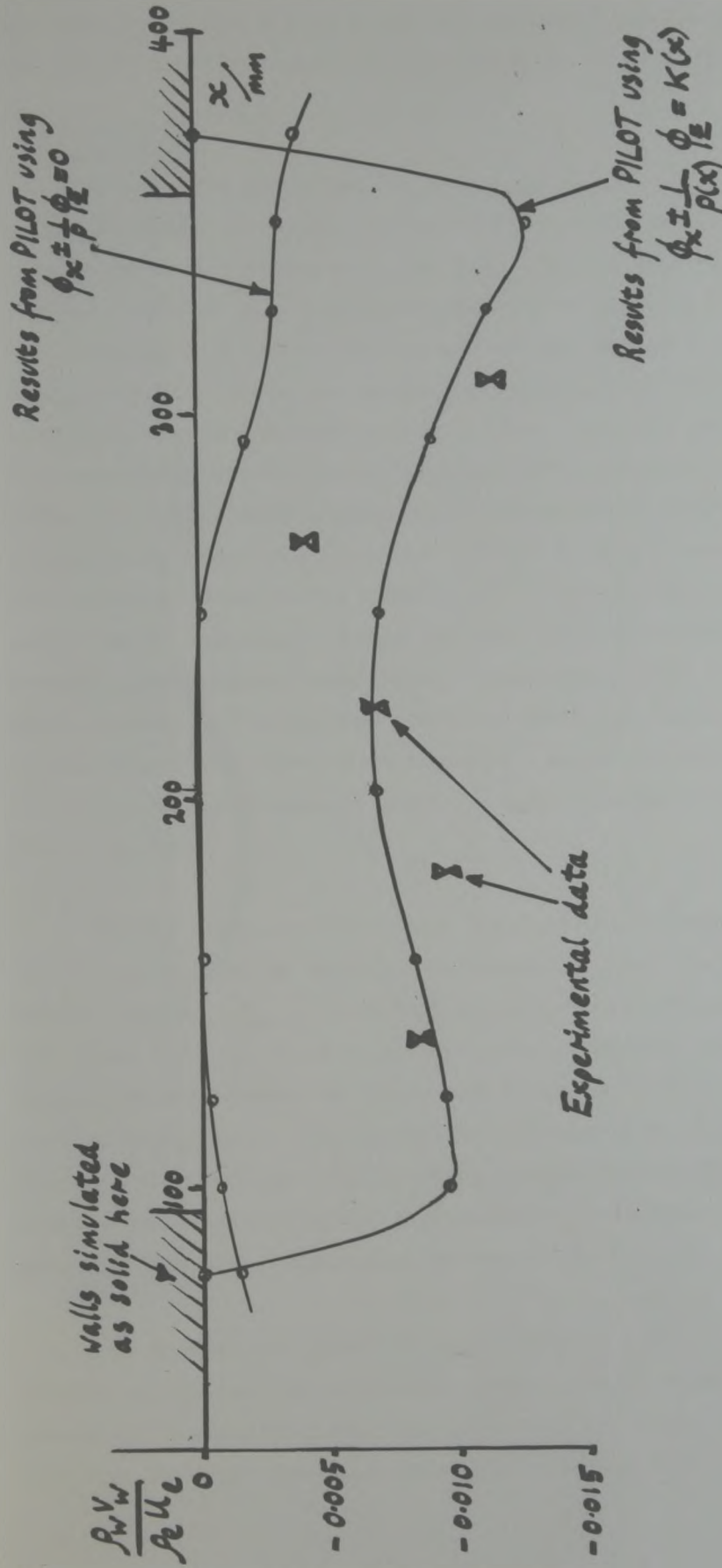
a comparison was made between computed results and those from experiment. The value of P to be used, was derived from a consistent set of experiments with those used in the comparison. This comparison (between values of the viscous crossflow at the wall,  $\frac{\rho_w v_w}{\rho_e u_e}$ ) is shown in Figure (17). Clearly, the program is unable to predict the crossflow with any useful degree of accuracy. This is primarily because the boundary condition can take no account of the actual plenum chamber pressure. It is also notable that because P is constant along the whole length of the region where flow is calculated and it is chosen to represent a porous wall, significant crossflow is predicted well into the regions of the windtunnel where the walls are in fact solid.

Using a boundary condition of the form

$$\phi_x \pm \frac{1}{\rho} \phi_z = K \quad (3.51)$$

give significantly better results. Here, P and K, which are also derived from the experiments used for the comparison in Figure (17), are permitted to vary in the longitudinal direction and from iteration to iteration in the calculation procedure. Some results using this boundary condition are also shown in Figure (17). The general distribution of crossflow is closer to experimental values, and the solid regions of windtunnel wall are now correctly simulated, negligible crossflow being predicted there. The computing times using this





Comparison of Results from PILOT, with two boundary condition types, with those from Experiment.

FIGURE (17)

boundary condition are an order of magnitude greater than those using the simple condition, but the increased level of accuracy is considered to offset this.

In the list given earlier of possible improvements in the form of the boundary condition, no mention was made of any simpler methods than those used at present. One such approach has however been investigated. Rather than a boundary condition equation being specified, the calculated values of the crossflow are directly applied to the inviscid flow. These are determined from previously calculated wall pressures, using a simple boundary layer analysis and the wall characteristic derived from Jacocks (1976) (Equation (3.22) of this report). During each iteration of the program, a distribution of crossflow is used as a directly imposed boundary condition and from the predicted flow in the windtunnel, a new distribution of wall pressures is obtained. Using the same viscous modules in the computer program, the boundary condition; Equation (3.51) was also used. When converged, the methods produced identical results. However, the latter method was considered superior, as it consistently gave converged solutions in approximately half the computing time required by the former method.

Of the boundary conditions considered, the type shown in Equation (3.51) was chosen as the most suitable for use. This equation contains the derivative,  $\phi_x$ , which represents the wall pressure coefficient, evaluated only to first order accuracy. However, for the small perturbations assumed to exist, it is expected that the error introduced will be negligible. The evaluation of the effective inviscid crossflow at the wall position ( $\bar{v}_w$ ), using the derivative  $\phi_z$  is, in contrast exact. The application of this boundary condition to the computer program, PILOT, was described in detail in Section (3.4).

To demonstrate that this new boundary condition is suitable for future application to practical transonic flow calculation methods, the method of Catherall (1975) has been used as a test case. In appendix (4), the relevant parts of Catherall's method are adapted, resulting



in equations, which are not greatly different in character from the original ones. Naturally it is hoped that, with perseverance, such a calculation method could be brought to satisfactory convergence. During the course of this research, only one attempt has been made at bringing this calculation scheme to convergence. This attempt was unsuccessful.

### 3.7.1 Mode of application of the new boundary condition.

It is helpful under the heading of Section (3.7) to discuss the timing and method of application of the new boundary condition to a flow calculation method.

In the computer program, PILOT, the boundary condition is recalculated at each iteration. This is because the method involves a direct solution for all the wall source element strengths simultaneously and without an alteration in the wall boundary condition, no improvement in the flow prediction would occur, over that calculated previously. It would be possible to incorporate a gradual change in the boundary condition by using under-relaxation, but this was found unnecessary.

In a practical calculation method, such as that of Catherall (1975), where a sweeping solution through the computing grid is used, it may be helpful to reduce the number of times the wall boundary condition is calculated. Each change in the wall condition could be delayed (for example) until the corresponding viscous layers on the aerofoil are calculated (Catherall's method has subsequently been altered to account for viscous effects on the aerofoil surface and wake (Lock (1975a))). In this way, the complete new boundary condition is then applied over a number of grid sweeps to the flow field calculation, allowing the solution to settle between alterations. If even this procedure proves to be too severe for the calculation (the solution becoming unstable), then some under-relaxation of the wall boundary condition may also be necessary.

### 3.8 Results from the Computer Program PILOT.

It is the objective of this Section to demonstrate initially that the overall computing scheme proposed converges, that for a chosen simple case, the results are exact and that for another more involved case, the results are in some agreement with the calculation method of Goethert (1961) mentioned in Section (2.1) of this report.

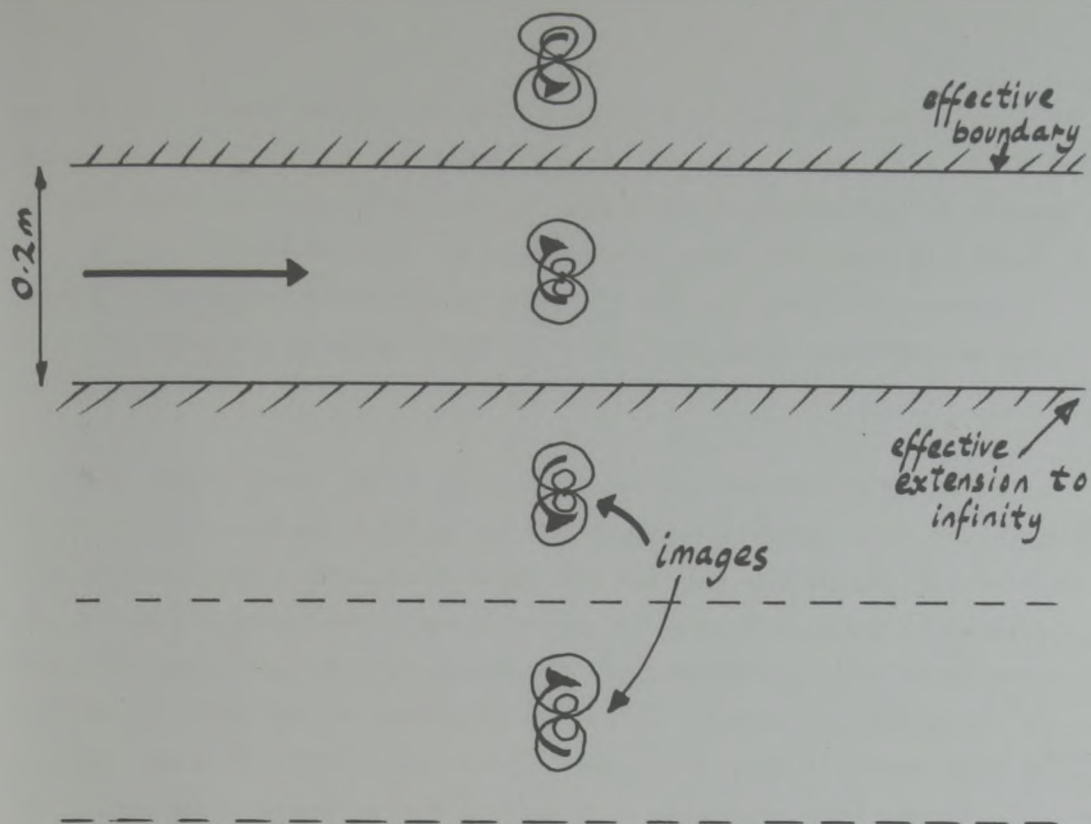
Subsequently, some aspects of windtunnel flow simulation, made possible by use of the new boundary condition are investigated.

#### 3.8.1 Demonstration that the computer Program PILOT

converges and that in some cases, results from the method are realistic.

There was initially some doubt as to whether the inviscid part of the computer program PILOT, using a finite number of distributed wall source elements and a boundary condition applied at discrete points, would give results which were first unique, and second, ever in agreement with exact potential theory. To examine this problem, the flow around a vortex doublet combination between two solid boundaries was simulated using potential flow singularities (see Figure (18,a)). The flow around the vortex doublet combination and the effectively infinite series of images in both walls was calculated using a fairly simple computer program designed for this sole purpose. The series of images is only effectively infinite in that the calculation is halted when the nett crossflow at the boundary lines is very small rather than zero. The resulting flow distribution is approximately the exact flow around a vortex doublet combination between two infinite, straight walls (no viscous effects are present). The computer program PILOT was also used to simulate the same flow (see Figure (18,b)). The windtunnel walls, although straight, are now finite, limited to either 0.8m or 0.38m in length (the total number of wall elements used being 40 and 20 respectively). All the wall elements are specified as representing a solid wall, and no boundary layer is simulated.



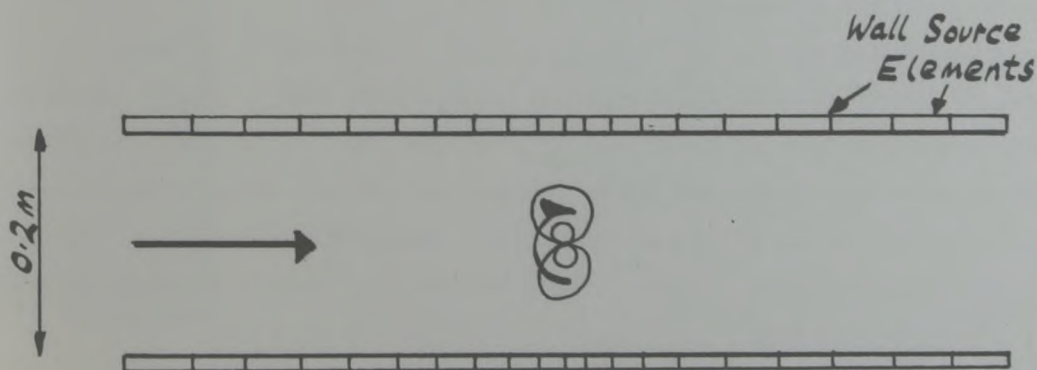


(a) Exact Scheme

Vortex Strength  $\Gamma = -1.0$

Doublet Strength  $\mu = 0.00557$

$U_{\infty} = 100 \text{ ms}^{-1}$



(b) 'PILOT' Scheme

FIGURE (18)

Diagram of windtunnel configuration  
modelled, in comparison of PILOT with  
exact potential theory.

Figure (19) shows the distributions of wall pressure coefficient predicted by PILOT and by the image method. It would seem that PILOT does indeed produce a sensible, unique solution, which for the 40 element case gives results in very close agreement with the exact potential theory. There is no reason to suppose that in other more complex calculations, the program PILOT will not also give sensible, unique solutions.

One factor which could cause the results from PILOT to be in error is the accuracy with which the viscous components of the program can simulate the actual flow near, and through the walls. In Section (5) of this report, the computer program PREDICT is used to examine this ability. The results presented there indicate that these viscous regions of flow can be predicted uniquely. Concerning accuracy, the results are not particularly good. The prediction of cross flow  $(\frac{\rho_w V_w}{\rho_{\infty} V_{\infty}})$  has a standard deviation ( $\sigma$ ) of 0.0019 about the experimental figures and the prediction of  $\delta^*$  has a  $\sigma$  of 0.5 mm about the experimental values. However, the viscous components of the flow calculation used in PREDICT are still considered accurate enough to be employed in PILOT.

In section (2.1) of this report, a one-dimensional analysis of flow in a finite perforated working section was mentioned (Goethert, 1961).

This one-dimensional analysis is now used in a comparison with results from the present computer program, PILOT. The windtunnel configuration used in PILOT is shown in Figure (20, a). No aerofoil is simulated in the working section, nor boundary layer on the windtunnel walls and the freestream speed is  $100 \text{ ms}^{-1}$ . With no boundary layer simulated, the wall characteristic due to Jacocks (1976), which is used in PILOT, reduces approximately to

$$C_{p_w} = -0.05 - 2.0 \theta_w \quad . \quad (3.52)$$



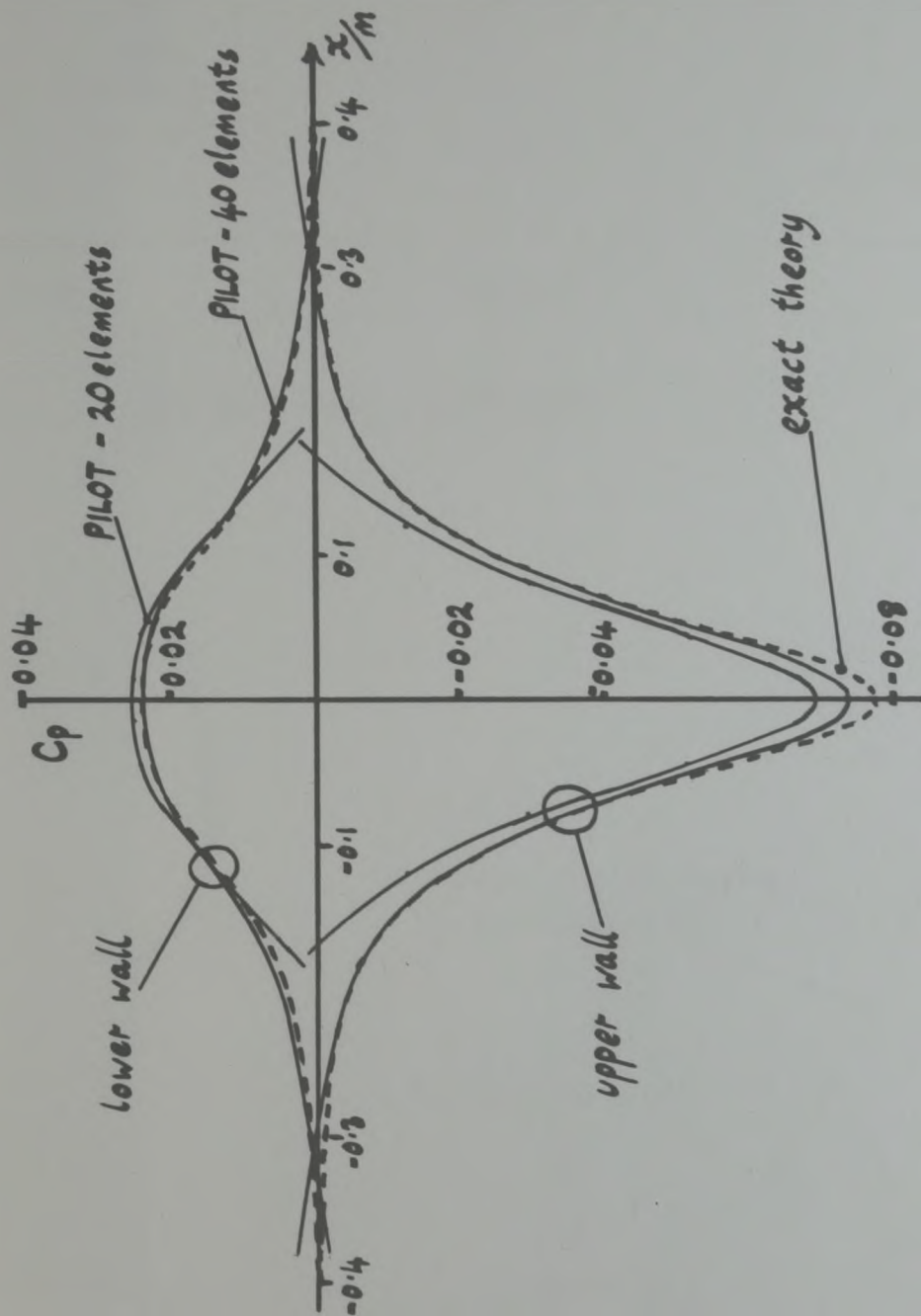
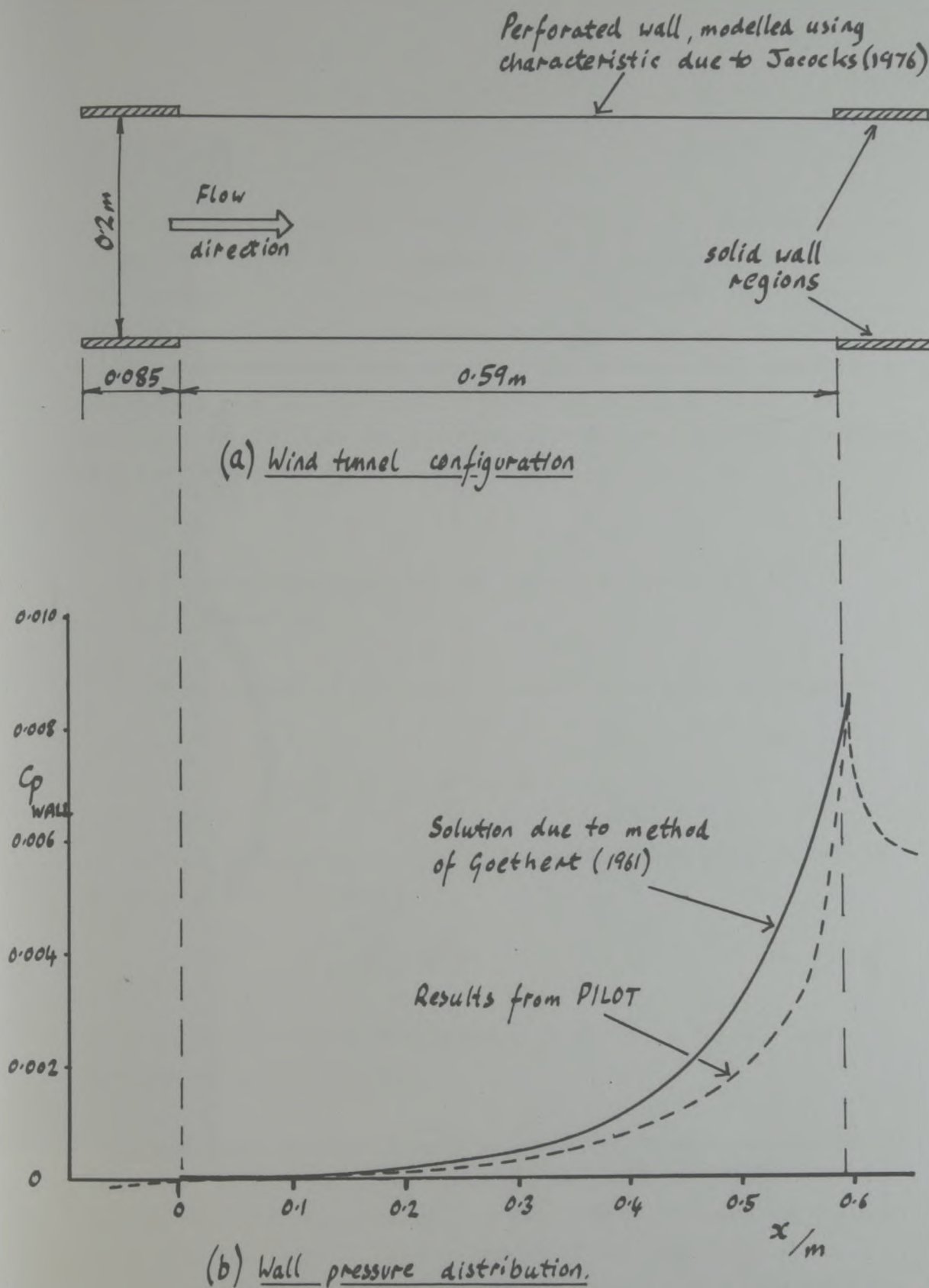


FIGURE (19) Comparison of PILOT results with exact theory.



FIGURE(20) Comparison of results from PILOT, with those obtained using the method of Goethert, for an empty working section



The plenum chamber pressure coefficient (  $C_{ppl}$  ) is specified as -0.048. The factor, 2.0, in Equation (3.52) represents the value of K in Goethert's method (see Equation (11) of Appendix (1)). The solution using Goethert's equations is scaled to fit the results of PILOT for the flow described and the distribution of wall pressure coefficient from both methods are presented on Figure (20,b). The comparison is good when one considers that Goethert's method represents only one-dimensional flow.

### 3.8.2 Investigation of some new aspects of windtunnel flow simulation.

It is helpful at this stage to revert from using the equation

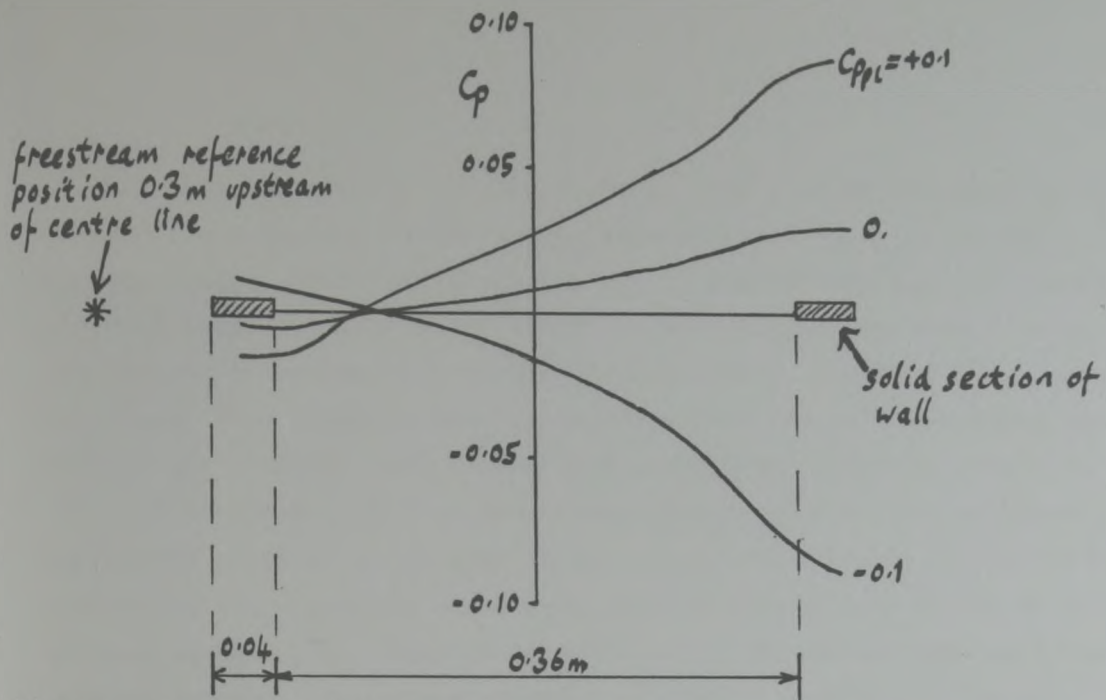
$$\phi_x \pm \frac{1}{\rho} \phi_z = K$$

as the wall boundary condition, to the form of this equation used in the program PILOT, namely,

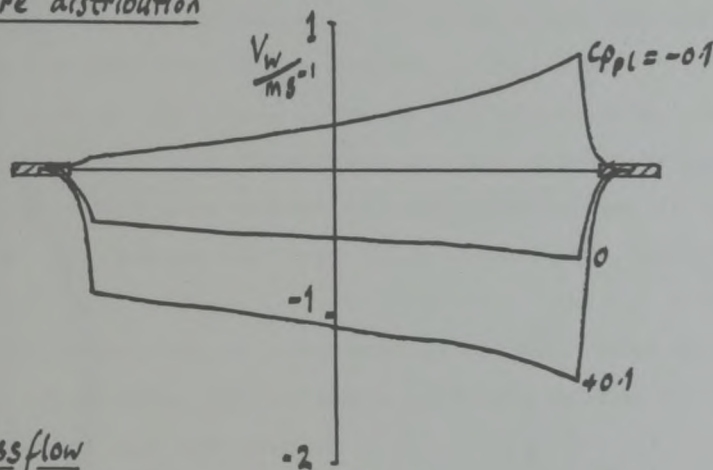
$$u = A' + B'v \quad (3.53)$$

(This equation is taken from Equation (3.15) which was in a form suitable for matrix algebra),

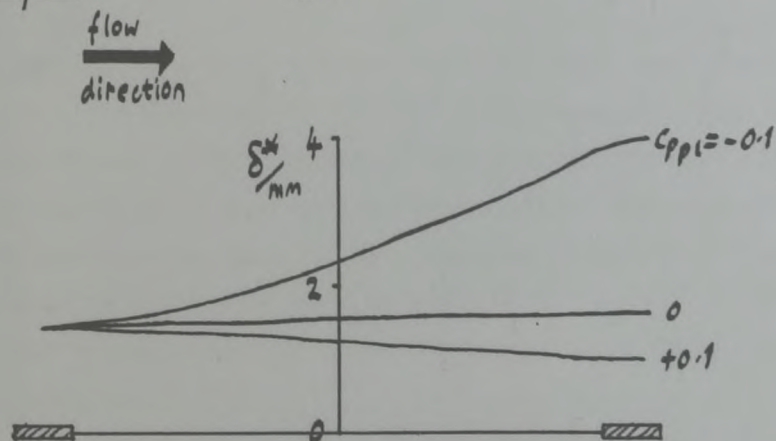
The first piece of work to be described is an investigation into the effect of varying plenum chamber pressure on the windtunnel flow. Varying the controlling parameter, namely  $C_{ppl}$ , alters the value of  $A'$  in Equation (3.53). Results from PILOT for cases with three different values of  $C_{ppl}$  are presented in Figure (21). No aerofoil is simulated in the windtunnel. The wall characteristic developed in



(a) Wall pressure distribution



(b) wall crossflow



(c) Wall boundary layer displacement thickness.

Working section height 0.2m

FIGURE(21) Results from PILOT to demonstrate the effect of varying-plenum chamber pressure, on the windtunnel flow.



in this report (Equation (3.28)) is used. The flow in the windtunnel responds in a logical manner to the alteration of  $C_{ppl}$ . Strong suction ( $C_{ppl}$  positive) draws air out of the working section, causing the wall boundary layer to thin and the pressure on the wall to rise. The reverse situation is true for large negative values of  $C_{ppl}$ , but for those close to zero, the flow still passes out of the working section, against the pressure rise. This is caused by an effective offset in the wall characteristic, a phenomenon which is evident for all types of perforated walls with inclined holes. It is interesting to note that generally, the flow does not merely pass uniformly into or out of the working section, but tends to be stronger at the downstream end of the working section. One clear reason for this is as follows. As air passes, say, into the windtunnel, the flow speed increases along the working section and thus the pressure falls. The increasing pressure difference between the plenum chamber and the working section causes an increasing transpiration rate which in turn serves to speed up the flow still further. The nett effect of this interaction is a flow distribution similar to that of Goethert (1961) which has exponential features. Even when an aerofoil simulation is made in the working section, this divergence of the flow at the downstream end is still present, though it may be masked by the influence of the aerofoil,

The results of a second investigation, into the effect of varying the value of  $B'$  in Equation (3.53) are now presented. The windtunnel geometry and values of the crossflow component of velocity at the wall for 3 values of  $B'$  are shown in Figure (22). The geometry is only slightly different from that in the previous discussion. The wall characteristic used here is that derived from the work of Jacocks (1976). This characteristic, labelled Equation (3.22) in Section (3.4) of this report, is

$$C_{pw} = (10\delta^* - 0.05) + \theta_w \exp(1.5 - 200\delta^*) .$$

For convenience, the boundary layer is not simulated on the walls of the windtunnel. Hence the above equation is effectively reduced to

FIGURE (22) Results from Part II showing the effect of varying wall porosity on the velocity profile

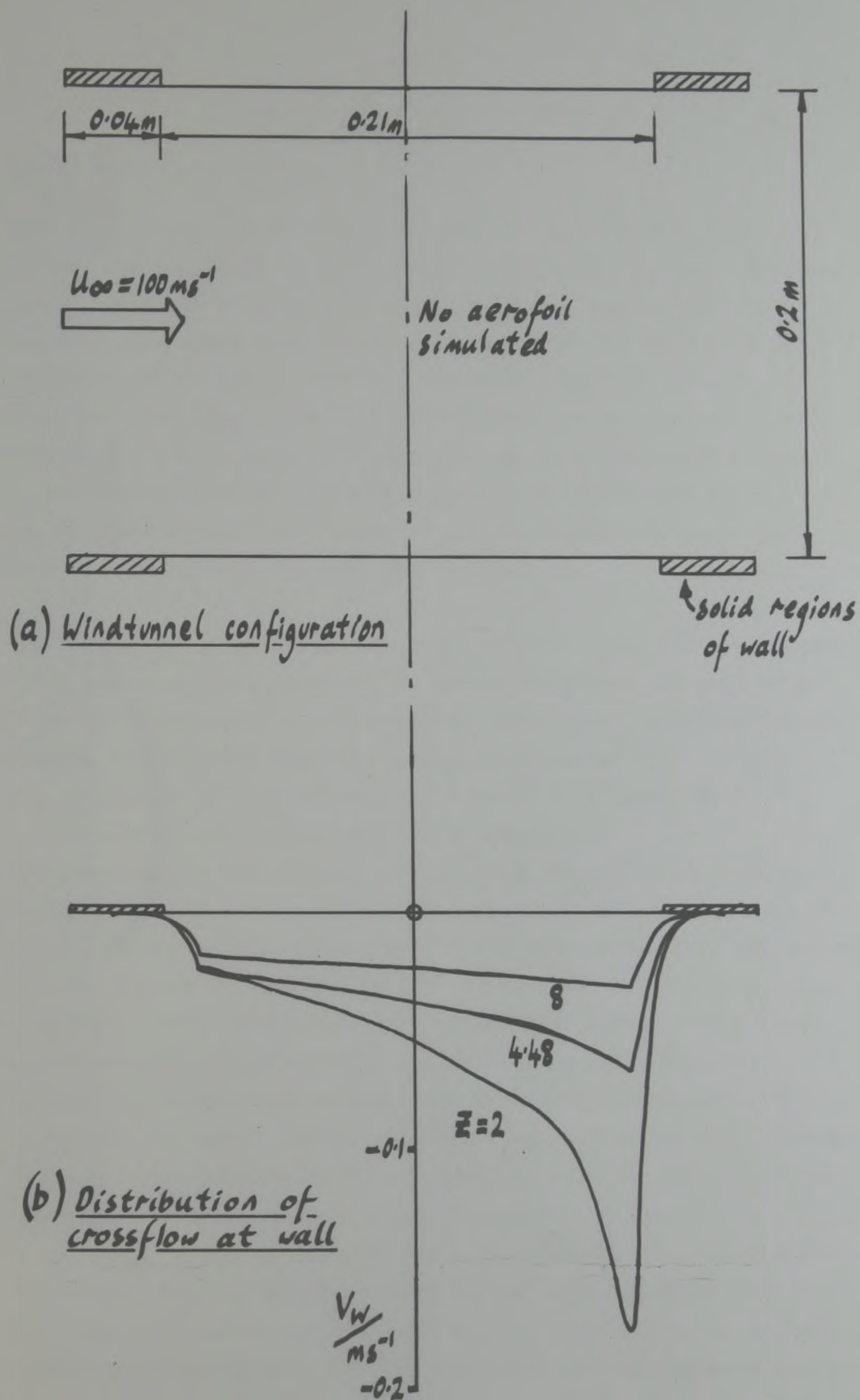


FIGURE (22) Results from PILOT to indicate the effect of varying wall porosity, on the windtunnel flow.



$$C_{pw} = -0.05 + \theta_w e^{1/5} .$$

The term  $e^{1/5}$  is of course invariant with 'x' and is the part of the equation which becomes B' in Equation (3.53) later in the calculation procedure. We refer to this as Z temporarily. In Figure (22), the results shown are taken from calculations using values of Z of 2, 4.48 (the original value) and 8. For all these calculations, a value of -0.048 is used for  $C_{ppl}$ . As one might expect, with increasing porosity (decreasing Z), the crossflow distribution becomes increasingly severe. Again, the rushing flow at the downstream end of the porous working section is experienced. Wall pressure distributions have a similar trend of increasing severity with decreasing Z.

A further brief investigation made possible using the new boundary condition concerns the effects of the finite length of the perforated liners in the windtunnel working section. This topic, which for porous windtunnels at least has received little attention to date, is now being investigated by AEDC (Arnold Engineering Development Centre, U.S.A.) using a porous walled adaptive windtunnel.

The approach used in the present work to model the solid sections of windtunnel liner has already been mentioned. A further improvement in the overall method is now introduced. The interference along the centre-line of the working section due to the presence of the windtunnel walls is calculated. This interference is expressed as values of  $C_p$  and normal perturbation of velocity,  $V$ . The distributions of pressure coefficient on the wall and centre-line of the working section are calculated for two cases. First with no solid sections of wall simulated, and secondly, with comparatively long sections of solid wall simulated both upstream and downstream. These calculations are carried out for two values of  $C_{ppl}$ , namely 0.1 and -0.1. No aerofoil is simulated in the windtunnel, but the boundary layer on the walls is taken into account. The wall characteristic developed in this report is used and the windtunnel geometry is presented, together with the computed results, in Figure (23).

Key:

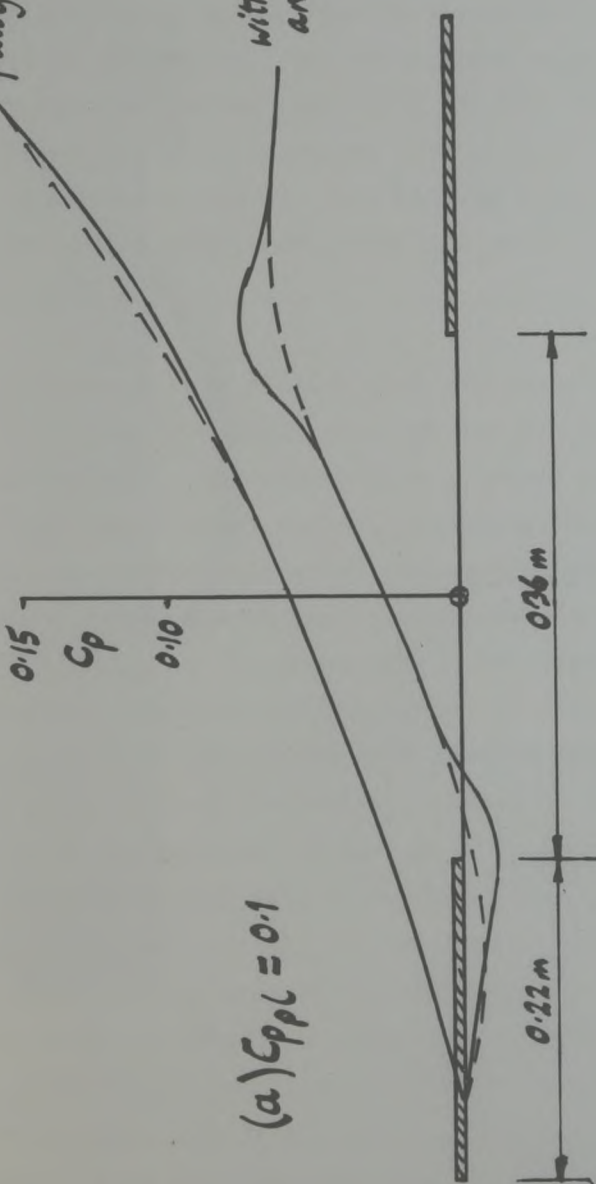
wall data

centre-line data

working section height = 0.2 m

working section:- fully porous

with solid entry and exit.

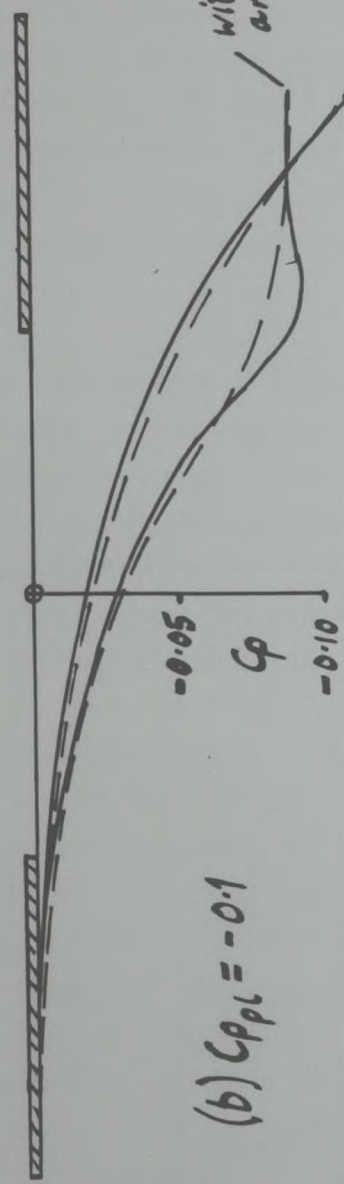


(a)  $C_{pl} = 0.1$

Results from PILOT to demonstrate the influence of finite perforated sections of wall.

with solid entry and exit

fully porous



(b)  $C_{pl} = -0.1$

FIGURE (23)



In both Figure (23) 'a' and 'b', the working section pressures on wall and centre-line are higher for the case where the liner is fully porous, than for the case when the liner includes solid zones. As such one cannot conclude that the fully porous working section produces more severe disturbances, but that some more complicated phenomenon is taking place. In Figure (23,a) in the centre of the working section (where both types of wall modelled are porous) the pressure gradient appears to be very similar for the two cases calculated, while in general, over the solid section of the wall, the pressure remains almost constant. This is sensible, since the only major influence on the flow in the solid duct is the boundary layer growth on the walls. For this case (  $C_{ppl} = 0.1$  ) then, it seems clear why the 'solid zone' case and the 'fully porous' case are different. The fully porous flow is free to expand along the whole working section length, thus gaining a pressure differential relative to the 'solid zone' case along the extent of the upstream section of solid wall.

Looking more carefully at the solid zone case in Figure (23,a), we see a distinct difference between the wall, and centre-line pressure distributions. The centre-line pressure responds in a very simple (and not surprising) manner, remaining level initially, then rising along the porous section of the working section due to the low plenum chamber pressure and finally remaining level again during the final solid section of the windtunnel. The flow near the wall however, overspeeds (relative to centre-line conditions) on entering the porous section and underspeeds on exit from it. This feature of the flow near the wall is probably caused by the abrupt change in the terms in the boundary conditions. In the solid section, the flow direction near the wall is certain to be very close to that of the x axis. However in the porous section, the porous boundary condition combined with the pressure difference across the liner causes a larger flow angle to exist. Although in potential flow, the direction of the streamlines near the wall cannot change abruptly, a convex corner flow is simulated at the upstream junctions of the solid and perforated segments with the corresponding low pressure region around it. The



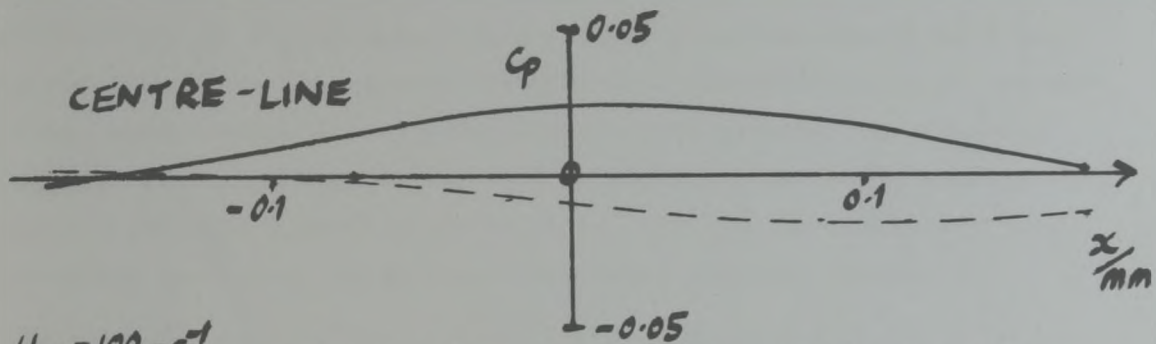
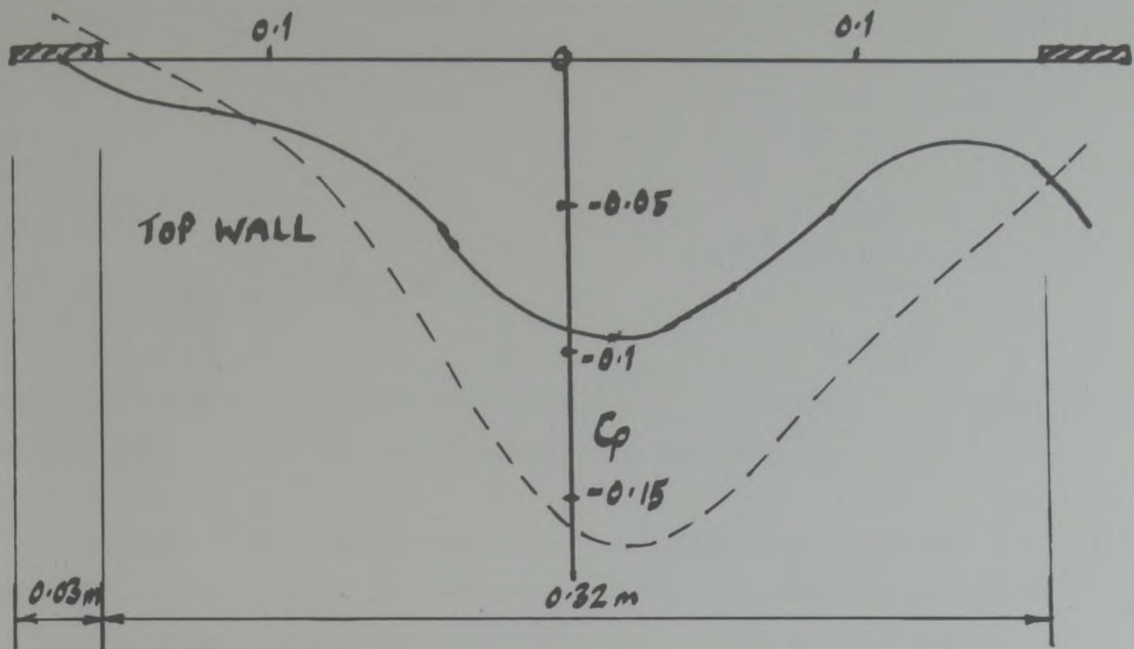
converse of the situation described above takes place at the downstream ends of the porous segments, concave corners being approximately modelled there. The preceding argument applies to flows where air is passing out of the working section. Surprisingly, in Figure (23,b) where there is a flow into the working section, there is no corner flow evident at the entry to the porous section of the windtunnel perhaps because the increased resistance of the porous wall to inflow reduces the rate of change of flow angle. It does seem clear then that although in the cases presented, where no aerofoil is present, there is not a great difference between wall and centre-line pressures, it would be sensible to concentrate wall source elements near any transition between solid and porous sections of wall. This would allow the calculated flow to predict more accurately the effects of truncating the porous working section.

With the capability of calculating the centre-line interference effects it is possible to investigate the overall improvement in the flow predicted around an aerofoil resulting from the use of the new boundary condition. This investigation is carried out with an aerofoil simulated in the working section. In Figure (24) the geometry of the working section is indicated. The point vortex and doublet in the centre of the working section represent an aerofoil with a chord of approximately 0.07m (equivalent to about one third of the windtunnel height) and a lift coefficient of approximately 0.9. In the calculations, the characteristic due to Jacocks (1976) is used again (Equation (3.22)). Once developed into the form of Equation (3.25), this characteristic becomes

$$C_p = (10\delta^* - 0.05) - C_{pL} + \Theta_w \exp(1.5 - 200\delta^*)$$

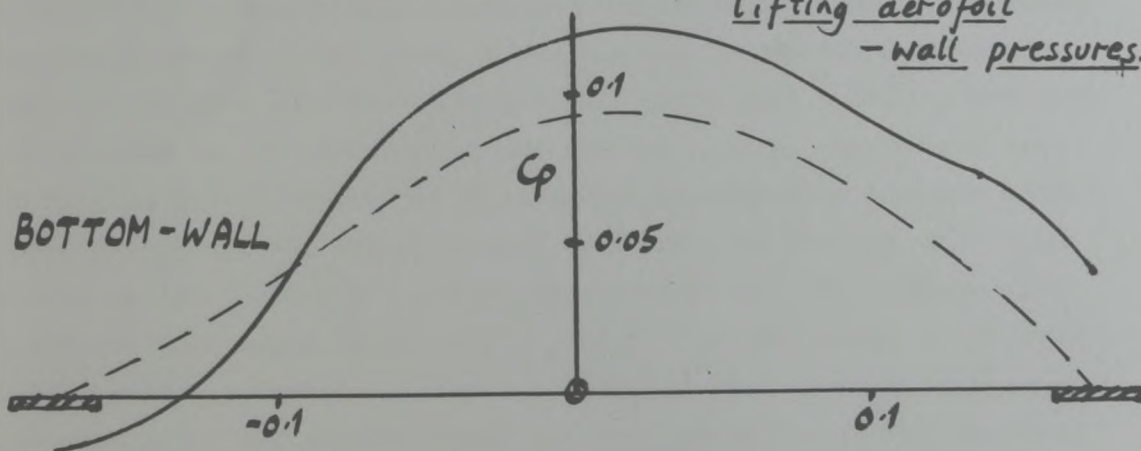
The computer program, PILOT is initially run using the above equation with a value of  $C_{pL}$  of 0.. Then the flow is calculated with no boundary layer simulated and  $C_{pL}$  equal to -0.05. In the latter case, the characteristic is effectively reduced to




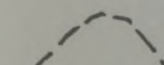


$U_\infty = 100\text{ m s}^{-1}$

Results from PILOT to demonstrate the effects  
of the new boundary condition on flows with a  
lifting aerofoil  
- wall pressures.



Key:-

-  calculation with new boundary condition
-  calculation with old effective boundary condition

FIGURE(24)

Working section  
height =  $0.2\text{ m}$   
Aerofoil doublet strength  
 $\mu = 0.01$   
Aerofoil vortex strength  
 $\Gamma = -3.0$

$$C_p = \theta_w \cdot e^{1.5}$$

Being merely a linear relationship between  $C_p$  and  $\theta_w$ , this equation has the same form as the conventional wall boundary condition.

In figure (24) we see the clear influence of the lifting aerofoil on the flow in the working section. The top wall pressure coefficients are negative and the bottom wall pressure coefficients are positive. On the walls, the influence of the new boundary condition used in PILOT is significant. On the working section centre-line near the position where the aerofoil is simulated, the difference in the wall induced interference is approximately 0.035 in pressure coefficient. Thus calculations using the new wall boundary condition may predict flow speeds at the model position up to 2% (of the free stream speed) more accurately than those using the conventional boundary condition.

In Figure (25), the effective inviscid crossflow ( $\bar{V}_w$ ) at both upper and lower walls, and the normal component of the interference velocity on the centre-line are shown. As one might expect, the strong negative pressure coefficients on the top wall of the working section cause air to flow into the windtunnel and conversely, positive pressure coefficients on the lower wall cause outflow. It is interesting that the surging effect discovered in earlier investigations does not appear to be very strong and indeed is only noticeable on the top wall in the results obtained using the new boundary conditions. The centre-line interference is again significantly affected by the change in the wall characteristic (that is; by the change in the effective wall boundary condition). At the aerofoil position, the difference in wall induced interference between the two calculations constitutes a flow angle increment of over half a degree. Clearly, the flow predicted near the aerofoil position is sensitive to changes in the effective wall boundary condition. Thus, in windtunnel flow calculation methods which account for the presence of perforated walls, it is necessary to know accurately the nature of the wall boundary condition if the flow near the aerofoil



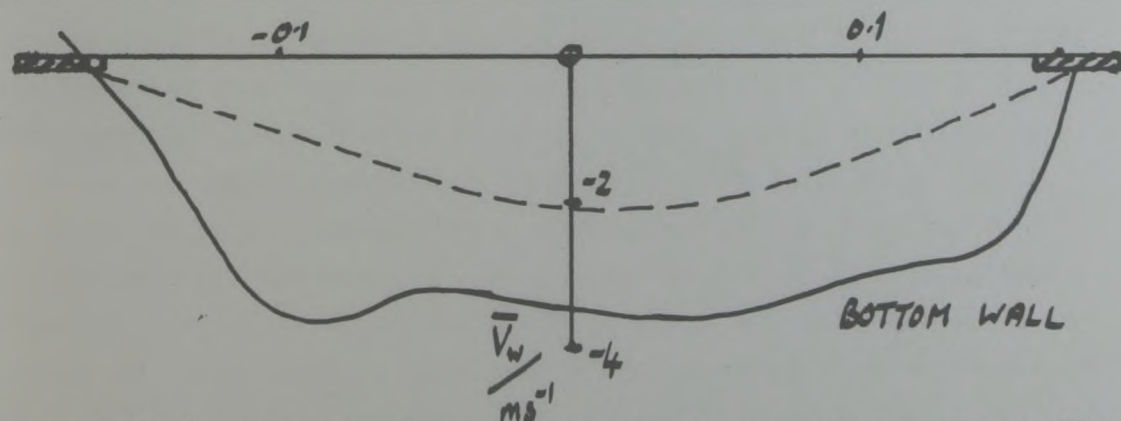
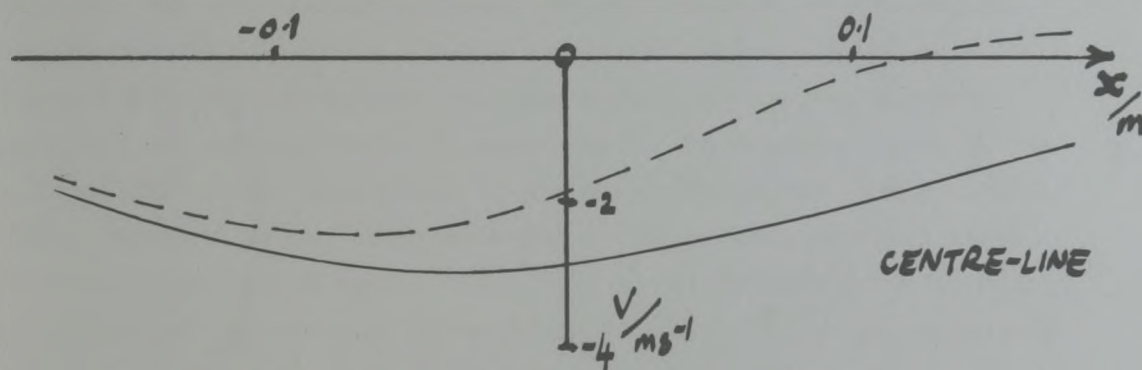
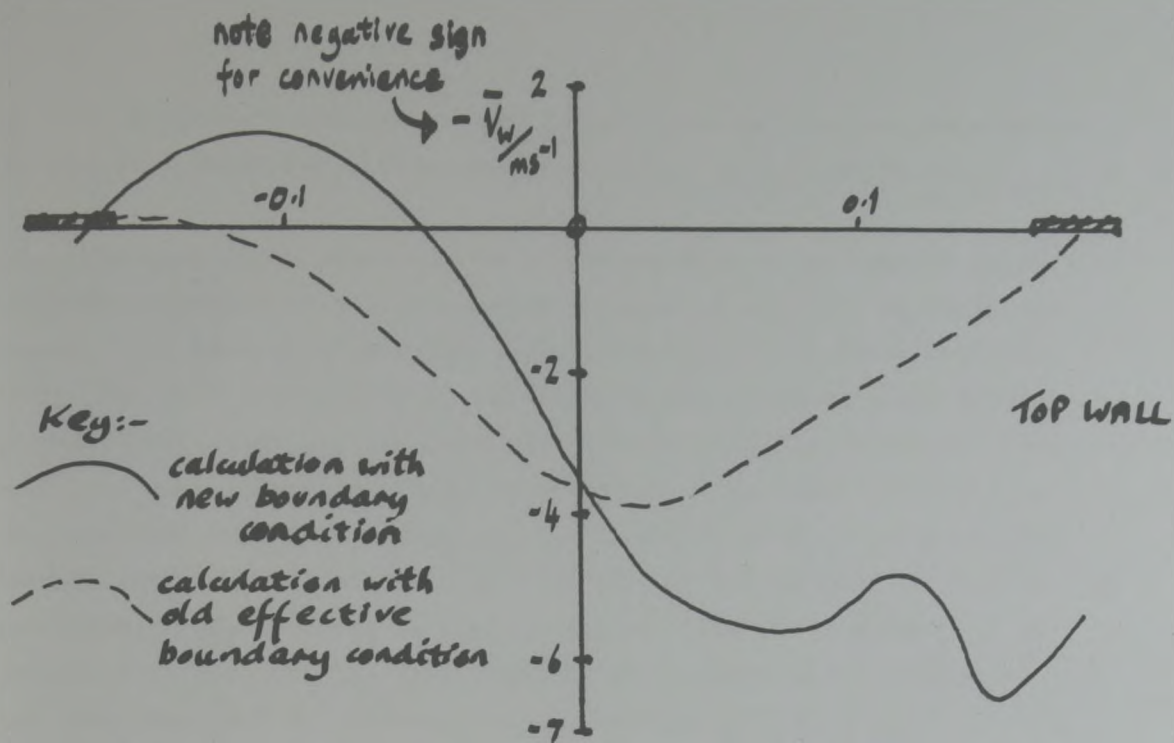


FIGURE (25) Results from PILOT to demonstrate the effect of the new boundary condition on flows with a lifting aerofoil - wall crossflows

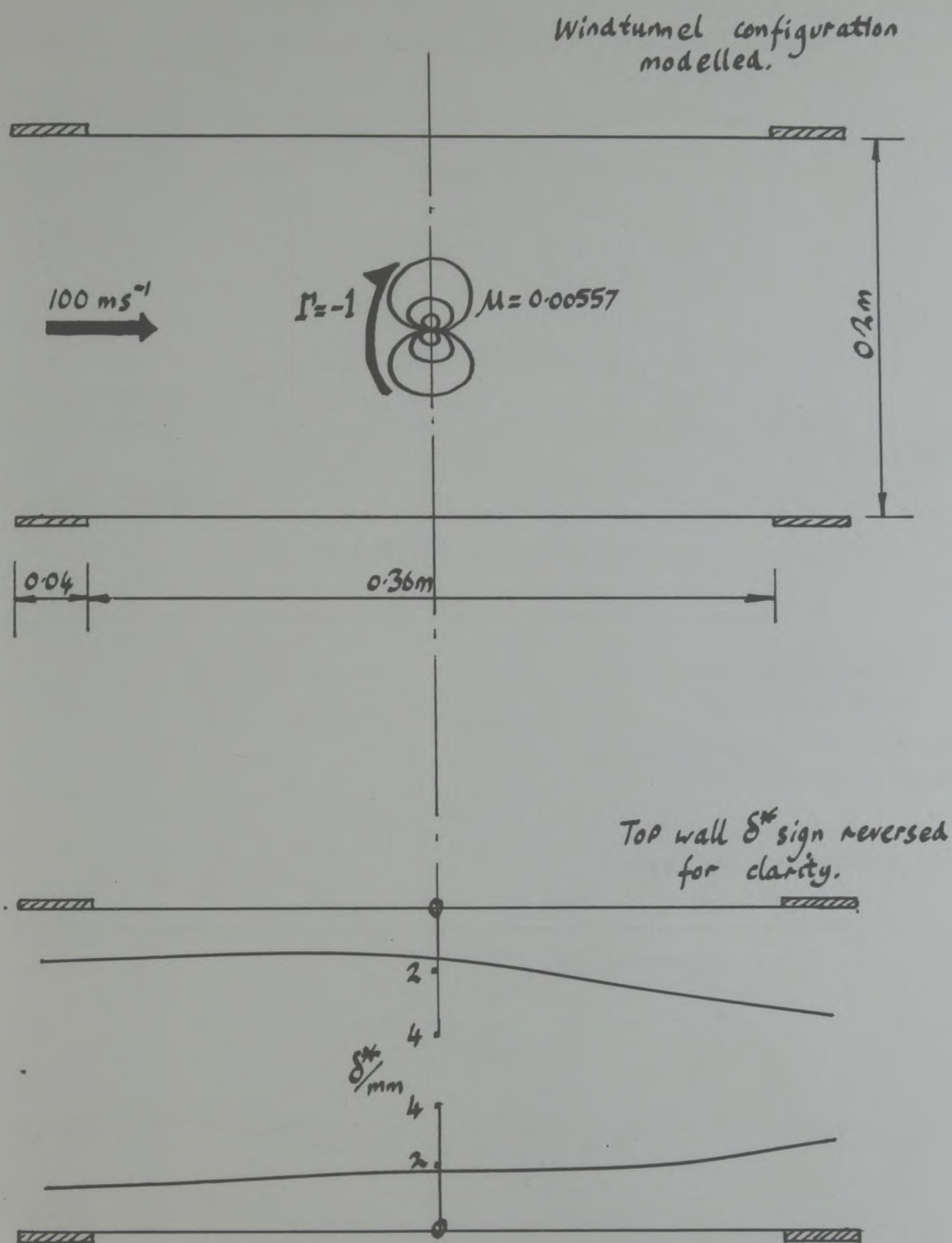
is to be accurately simulated. The actual level of accuracy required in the boundary condition will be discussed later in Section (4.2.6).

The last piece of work to be described here is an investigation into the influence of the wall boundary layer on the flow in the wind-tunnel. The windtunnel geometry selected for study is shown in Figure (26). The wall characteristic developed in the present report is used in the calculations and the facility of specifying the volumetric flow rate into each plenum is brought into action. For these calculations, the flow rate into each plenum chamber is set to zero. In Figure (26) the boundary layer development on each wall of the working section is presented. Before giving an explanation of these developments, it is necessary to consider the distributions of pressure and crossflow at the windtunnel walls. These are shown in Figure (27), a and b.

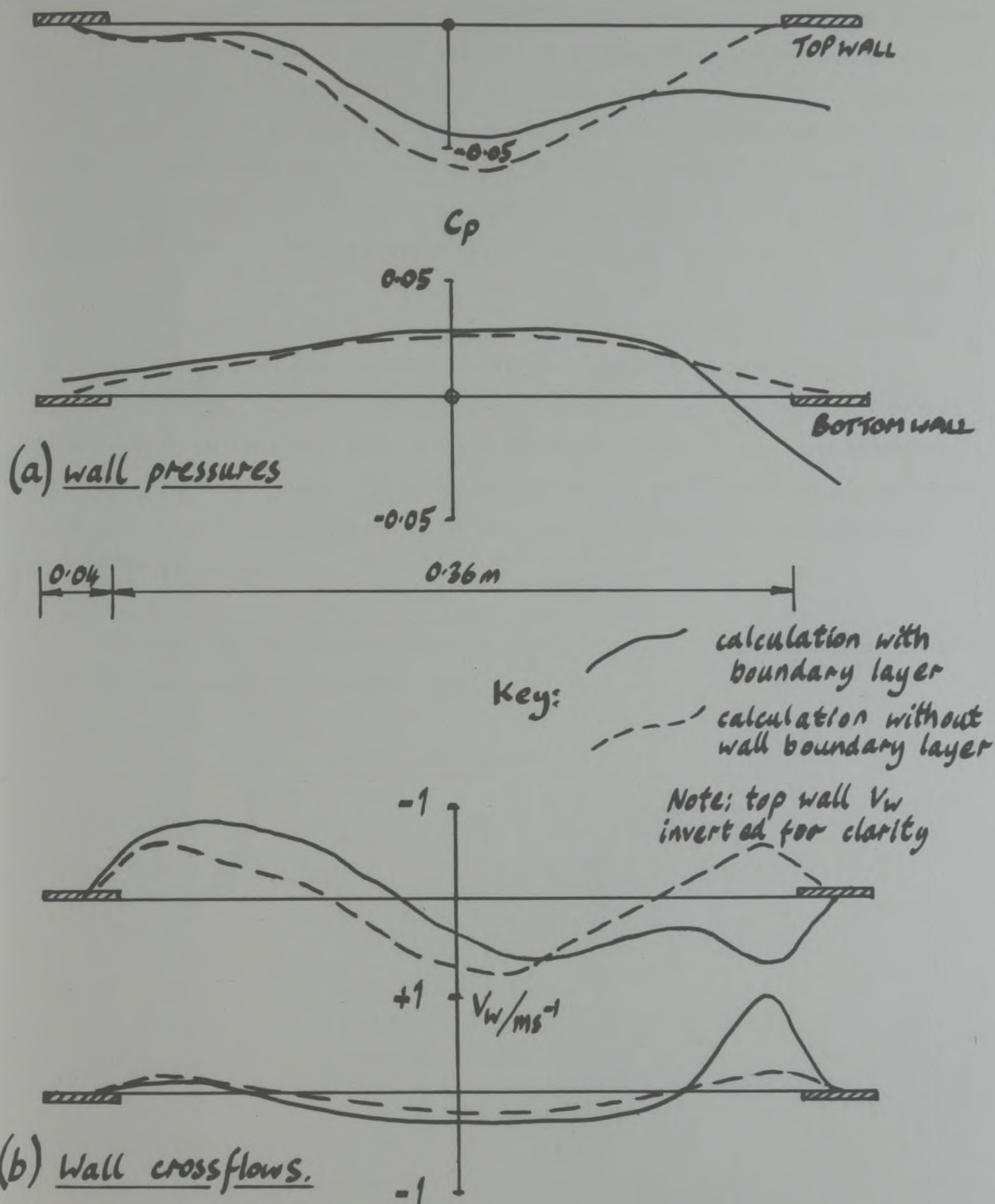
In Figure (27,a), it is clear that the presence of the boundary layer does not significantly affect the wall pressure distributions near the aerofoil position. Indeed, compared to the alteration in wall induced blockage interference when one changes to the new boundary condition, the alteration in blockage due to the boundary layer on the walls is small; less than 0.01, in pressure coefficient, compared to 0.035. However, at the downstream end of the working section, where the walls become solid again, there is a clear blockage effect. Both the top and the bottom wall pressure coefficients end at approximately -0.04 and as there is no nett flow into either plenum chamber, this must be caused by the presence of the thickened boundary layer.

In Figure (27,b) the viscous crossflow at the walls ( $V_w$ ) is shown. The pattern of crossflow is generally familiar, but an appreciable region of outflow is present at the upstream end of the top liner. This region of flow, was also observed by Mokry et al. (1974). It led these authors believe that their method of assuming continuous inflow along the top liner, described in Section (2.1) of this report, would not always be valid. Further downstream along the top liner for the calculation where the boundary layer is included there is a clear region of inflow. It is almost certainly this which is the major influence in causing the large boundary layer growth rate observed there in Figure (26).





Results from PILOT to demonstrate the influence of wall boundary layer on the windtunnel flow—  
 FIGURE(26) configuration and boundary layer development.



FIGURE(27)

Results from PILOT to demonstrate the influence of wall boundary layer on the windtunnel flow - wall pressure and crossflow distribution.



The bottom liner however has a comparatively weak region of outflow along most of its length, causing the boundary layer thickness to remain approximately constant, with a sudden region of inflow at the downstream end of the perforated section, which again causes a swift growth of the boundary layer. The nature of the crossflow distributions is affected noticeably by the incorporation of the boundary layer, although at the aerofoil position it causes little numerical difference and the change in incidence interference due to the wall boundary layer is as low as  $0.06^{\circ}$ .

As a conclusion to this, Section (3.8) of the report, we can state that in Section(3.8.1) it is shown that the computer program PILOT is likely to produce unique, realistic solutions for a variety of different flows. Also it is clear from Section(3.8.2) that using the new boundary condition significantly alters the modelling of perforated wall windtunnel flows and permits investigation of a number of previously undisturbed areas of work.

Information concerning the practical running of the computer program PILOT is contained in Appendix (3).

## 4 EXPERIMENTS AND ANALYSIS.

### 4.1 Experimental Objectives.

To utilize the scheme proposed in Section(3) of this report, it is necessary to provide a crossflow characteristic for each perforated wall type considered. The characteristic drawn from the work of Jacocks (1976) and the one which could be deduced from the experiments presented by Goethert (1961) are not considered to be adequate for this purpose. The characteristic drawn from Jacocks' work (Equation (3.22)) is at best, a poor approximation and the data presented by Goethert (Figure (2) of this report for example) do not adequately cover the range of subsonic (wall) Mach numbers required.

Thus it is necessary to perform experiments to provide data leading to a new crossflow characteristic. For convenience, the type of perforated wall chosen is that mounted in the transonic windtunnel in the Department of Aeronautics at the City University. This wall is of the  $60^\circ$  inclined hole type with an open area ratio of 6%. To remind us, the wall characteristic is to relate the following parameters:-

$$\frac{\Delta p}{q}, \theta_w, \delta^* \text{ and } M.$$

For the characteristic to be useful, it must consist of a large number of distinct sets of the variables listed, obtained under varying conditions of each controlling parameter. Or to reiterate, the data obtained must be spread well in each of the variables listed. Particularly, the Mach number should be spread within the transonic region, for example between 0.65 and 0.85. Cases of blowing and suction should both be included.

Once the wall characteristic has been evaluated, it would be included as one of the viscous components in the computer scheme described earlier. However, before it can be used with confidence, the ability of the viscous components to predict accurately the flow near and through the perforated liner must be examined. The computer program 'PREDICT' is developed for this purpose and will be described in Section (5) of this report. A longitudinal set of measured wall and plenum chamber



pressure coefficients are supplied to PREDICT, which then calculates the distributions of  $\theta_w$  and  $\delta^*$  which are compatible with these pressure coefficients. Clearly these predicted distributions must be compared with ones measured during the tests which supplied the pressure distributions. Hence, a set of experiments is required which provides distributions of the following variables;

$$C_p, C_{p_{\theta}}, \theta_w \text{ and } \delta^*.$$

In addition, for reference purposes and for use as starting values for the calculation, freestream conditions must be measured. Clearly, the range of each variable in the experiments must generally fall within the ranges during the 'characteristic' tests, such that the empirical characteristic may be capable of giving accurate results.

Finally, it will eventually be necessary to examine the accuracy of the overall windtunnel calculation scheme proposed. Initially, for this purpose, the computer program PILOT may be used, although it deals only with incompressible flow. To carry out this examination of the scheme's accuracy, it is necessary to have available data relating to the complete flow distribution in a windtunnel working section. This data would include distributions of the now familiar variables:-

$$\frac{\Delta p}{q}, \theta_w, \delta^* \text{ and } M.$$

Also freestream conditions are required, as are details of the working section geometry and particulars of any aerofoil that may be present there.

To meet the three major experimental objectives described above, it appears initially that three sets of experiments may be necessary. It is however clear that in analysing the experiments required for the third objective of modelling the complete working section flow, the data required by the second objective are also produced. Also, because the empirical wall characteristic to be generated from the

experiments under the first objective is only a statistical fit to the actual experimental data, it cannot be considered to represent exactly the same information as the original data. Hence, if it were supplied with the experimental values of  $\Delta p/q$  upon which it was based, it would not, in general, predict the correct (experimental) relationship between the remaining variables. In this way it is possible to use the same experimental data for both the generation of the characteristic and the operation of the program PREDICT. The resulting comparison between the result from PREDICT and the measured data will give a useful indication of the accuracy of the method.

All three experimental objectives then, are to be satisfied by performing and analyzing one set of experiments. Using the windtunnel mentioned, distributions of the variables

$$C_p, C_{pL}, \theta_w \text{ and } S^*$$

are to be determined under a variety of conditions of wall inflow and outflow with wall Mach numbers generally in the range; 0.65 to 0.85. For each flow configuration, freestream conditions must also be measured. The variables  $C_p$  and  $C_{pL}$  can then be used, with the freestream conditions to determine values of  $M$  and  $\Delta p/q$ .

To produce flow distributions of interest, a contoured top liner is fitted in the windtunnel (a method used by Jacocks (1976) in his work). This liner can be considered to produce the same flow as an aerofoil at zero incidence. To carry out the calculations mentioned, a knowledge of the shape of this liner is required. In addition, the longitudinal position of the upstream and downstream ends of the perforated working section must be available.

## 4.2 Experimental Equipment.

### 4.2.1 Practical Approach.



Using the intermittent transonic windtunnel in the Department of Aeronautics at the City University, the following general approach is taken to achieve the objectives set out in Section (4.1). The working section of the windtunnel is fitted with one solid, contoured wall and one perforated wall. The two sidewalls are solid and flat. A group of eight test configurations is defined. For each configuration, values of the required variables, namely  $\Delta p_q$ ,  $\theta_w$ ,  $\delta^*$  and  $M$ , are obtained at five stations along the perforated wall. A combined instrument is used to measure the boundary layer displacement thickness and the crossflow angle. However, this device is only designed to measure these data at one position in any one run. As such it is necessary to operate the windtunnel five times for each configuration with the measuring device at a different station each time. Pressure data from the perforated wall, plenum chamber and the boundary layer/crossflow instrument are logged after each run for subsequent analysis.

#### 4.2.2 The Windtunnel.

The transonic windtunnel in the Department of Aeronautics is of the intermittent type, with an eight inch deep, nine inch wide working section. The basic design is the same as that of the pilot transonic windtunnel in use at the Aircraft Research Association Ltd. (ARA), Bedford. It is driven by an ejector downstream of the working section and has a closed return circuit, the excess air mass introduced by the ejector drive being released to atmosphere through a balance duct. A diagram of the windtunnel is shown in Figure (28). Using a flexible convergent-divergent nozzle and variable ejector pressure, a Mach number range from 0 to 1.35 is available in the working section. The stagnation pressure and temperature are approximately those of the external atmosphere. Thus in the range of Mach numbers of interest, namely 0.65 to 0.85, the Reynolds number based on one metre length is typically  $1.2 \times 10^7$ . Concerning the uniformity of the flow entering the working section, this will be mentioned in some detail in Section (4.2.8) of this report. Briefly, it is not yet entirely clear whether the flow at entry to the working section has a satisfactory level of uniformity.

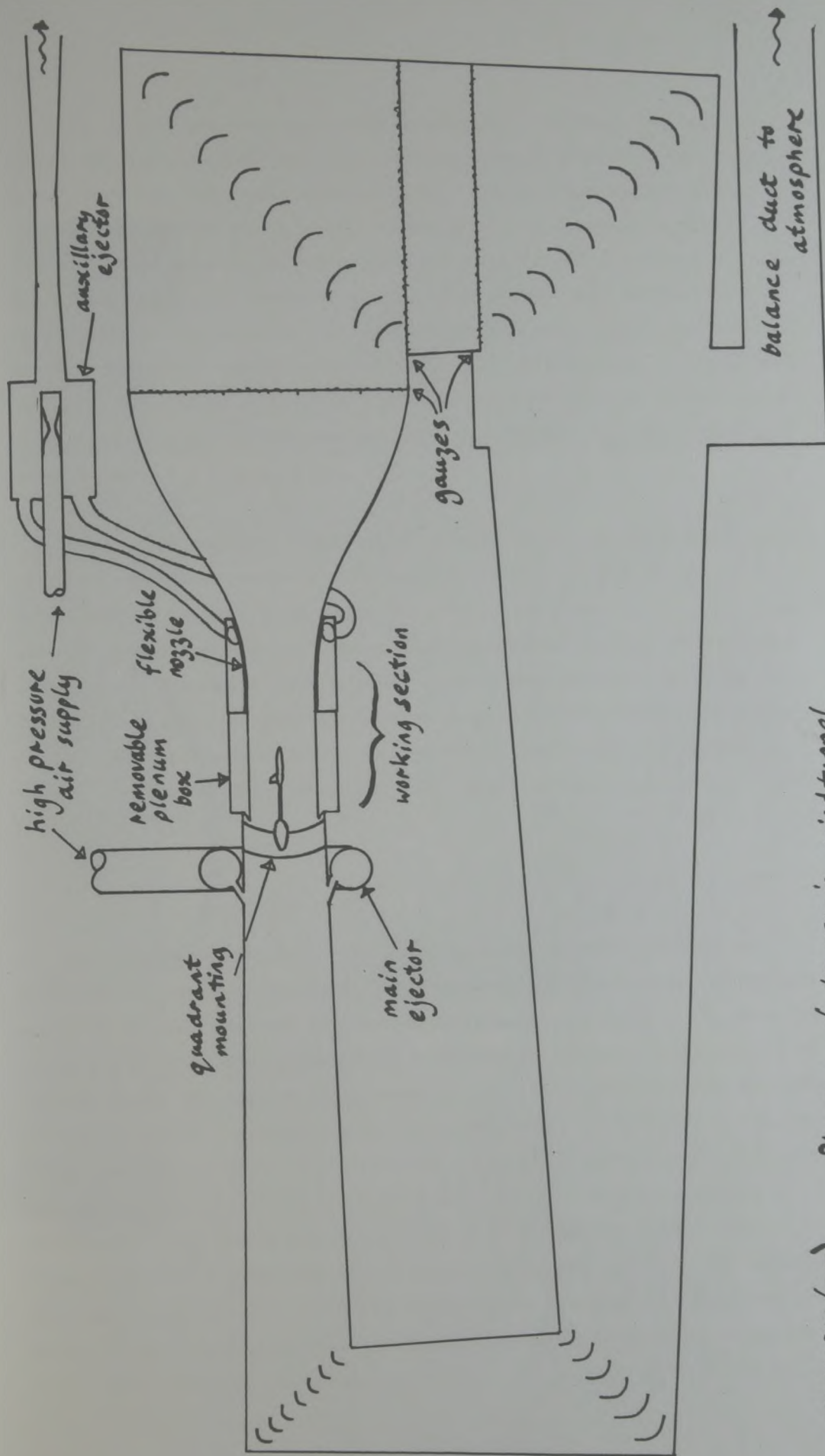


FIGURE (28) Diagram of transonic wind tunnel.



The working section has solid sidewalls, and these may either have Schlieren windows or a set of longitudinal pressure tapings level with the windtunnel centre-line. The top and bottom walls are mounted on removable boxes, which form the respective plena. For the tests considered, the top wall consists of a contoured resin block mounted on one removable box. The bottom wall is perforated, with holes inclined at  $60^{\circ}$  to the vertical, and an open area ratio of 6%. Models or instruments to be used in the working section are normally mounted on a movable quadrant just downstream of the removable plenum boxes. A general view of the working section, looking downstream, is shown in Plate (1).

The plenum chamber pressure is controlled by an auxiliary ejector, which is operated from the same compressed air supply as the main windtunnel ejector. Both plena are connected directly to this ejector, but the contoured top wall makes the top plenum chamber effectively redundant. The auxiliary ejector is however designed to serve two plena and to produce average outflow angles at the perforated walls of up to  $1.25^{\circ}$  at working section Mach numbers in the region of unity. A view of the windtunnel and auxiliary ejector is shown in Plate (2).

#### 4.2.3. The Contoured Top Wall.

The contoured top wall of the windtunnel working section is required to produce pressure distributions, on the bottom perforated wall, which are similar to those which would be experienced there if an aerofoil were being tested in a realistic manner. In Mokry et al (1974) there are presented a number of such wall pressure distributions. The lower graph of their Figure (15) is chosen for present purposes. It is reproduced here as Figure (1). The flow represented is that around an aerofoil at an incidence of  $4.5^{\circ}$  in a windtunnel with perforated wall where the freestream Mach number is 0.72. The theoretical wall pressure distribution above the aerofoil is chosen for the design of our contoured wall. To determine the required shape of the contoured wall, a computer program similar to PILOT is used. This program, developed by Freestone (1979), is similar to

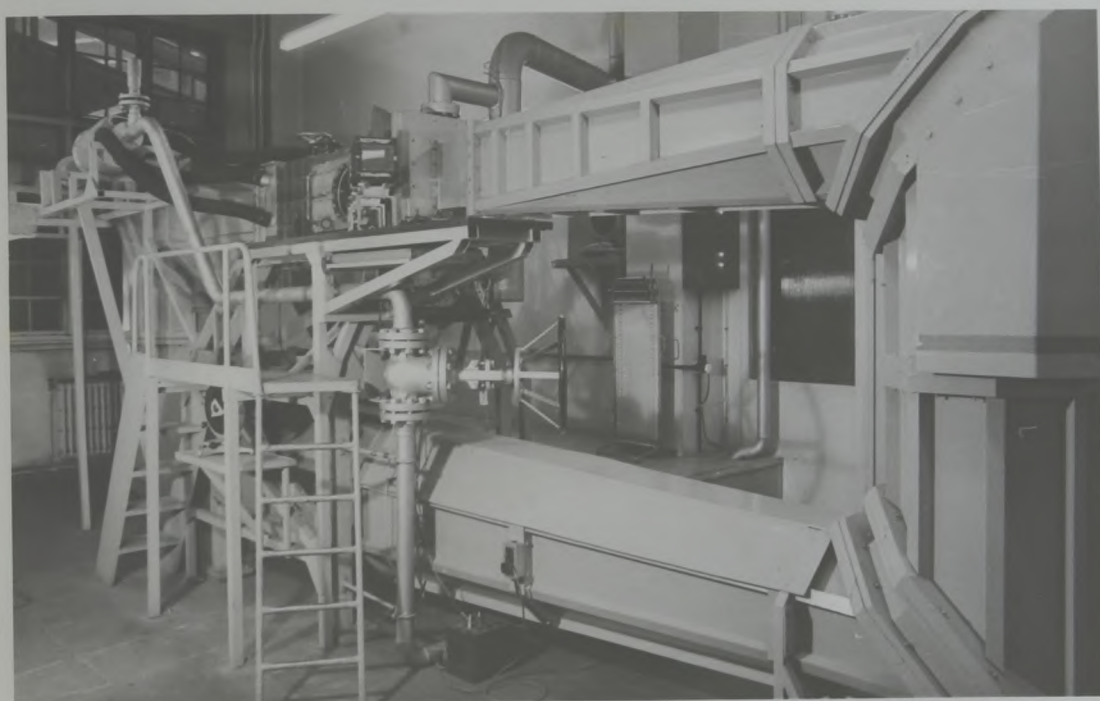


PLATE (2) Transonic windtunnel and auxiliary ejector.



PILOT in that it uses a potential field with windtunnel walls simulated by distributed source elements. However, in contrast, no viscous effects are accounted for, but compressibility is taken into account by scaling the dimensions normal to the freestream using the Prandtl-Glauert factor ( $\beta$ ).

The horizontal scale on Figure (1) is adjusted so that the wall pressure distribution experienced over a distance equivalent to four aerofoil chords will be simulated on the length of our perforated bottom wall. Although the full length of the wall in question is approximately 380 mm, the initial gradual variation in open area ratio from 0% to 6% over a length of approximately 80 mm makes the effective perforated length questionable. Doubt about this was later removed by taping over this transition. For present purposes, it is assumed to be 350 mm in length. Mokry et al (1974) found that at a Mach number of 0.82, a flow calculation in which a porosity parameter ( $P$ ) of 1.5 was used gave quite good results for wall pressures. Although the distribution of wall pressures we are trying to imitate was obtained at a freestream Mach number of 0.72, the above combination of Mach number and porosity parameter is used in the calculations using Freestone's program.

The working section height (correctly, 8 inches) is scaled using the value of  $\beta$  calculated from the Mach number 0.82, namely 0.572. Initially, on the bottom boundary in the flow calculation, the values of  $C_p$  are specified from Figure (1). It is not clear what boundary condition should be applied on the top wall (where the contoured liner will be situated). As an initial guess, the boundary condition

$$0.01 = u - \frac{1}{1.5} v \quad (4.1)$$

is used. This is the form of the boundary condition prior to scaling for compressibility. The factor  $\frac{1}{1.5}$  clearly represents the chosen porosity, but the term '0.01' is arbitrary. From the flow distribution predicted in the working section, the 'v' perturbations along the top boundary are taken as an initial estimate of the influence that would result from a contoured solid wall there.

The flow in the working section is then re-calculated with the distribution of normal perturbation ( $v$ ) that was calculated on the top boundary in the previous calculation applied as a boundary condition there. Equation (4.1) is now applied along the lower boundary. The predicted values of the longitudinal perturbation ( $u$ ) along the bottom boundary appear to match approximately the upper wall curve in the bottom graph of Figure (16) of Mokry et al (1974), rather than the same, in Figure (15) of that report. The graph from their Figure (16) is reproduced here as Figure (29). Therefore the distribution of normal perturbations used as the upper boundary condition is used to generate the required shape of the contoured wall. These perturbations, when divided by the freestream speed, yield the required local gradients of the contour. These gradients are then integrated along the wall to provide the shape of the solid contour they represent. The ordinates of the wall are presented in Table (1). The peak of the contour is situated over the centre of the effective perforated region of the bottom wall (the region 350 mm in length).

The contoured wall was manufactured from a rigid two-part resin. The dimensions of the finished wall are certainly accurate to within 0.25 mm and the surface finish is very even. A view of the contoured wall, removed from the windtunnel on its plenum box is shown in Plate (3). Pressure tapings are made along the centre-line of the wall, but they are not required for present tests.

#### 4.2.4 The Lower Plenum Chamber and Perforated Wall.

In Section (4.2.1), it was concluded that values of  $C_p$  and  $C_{pL}$  should be measured along the perforated wall. This wall which is naturally the focus of the experiments is mounted on the lower plenum chamber box of the windtunnel. A diagram of these two components is shown in Figure (30). During the experiments in question, the open rear end of the plenum box was sealed. The air drawn out of the working section passes out of the front end of the box through the ten 1 inch diameter holes clearly shown in Figure (30). As the perforations in the wall itself are inclined in a direction favourable



Reproduced from the lower graph in Figure (16) of Mokry, Peake and Bowker (1974)

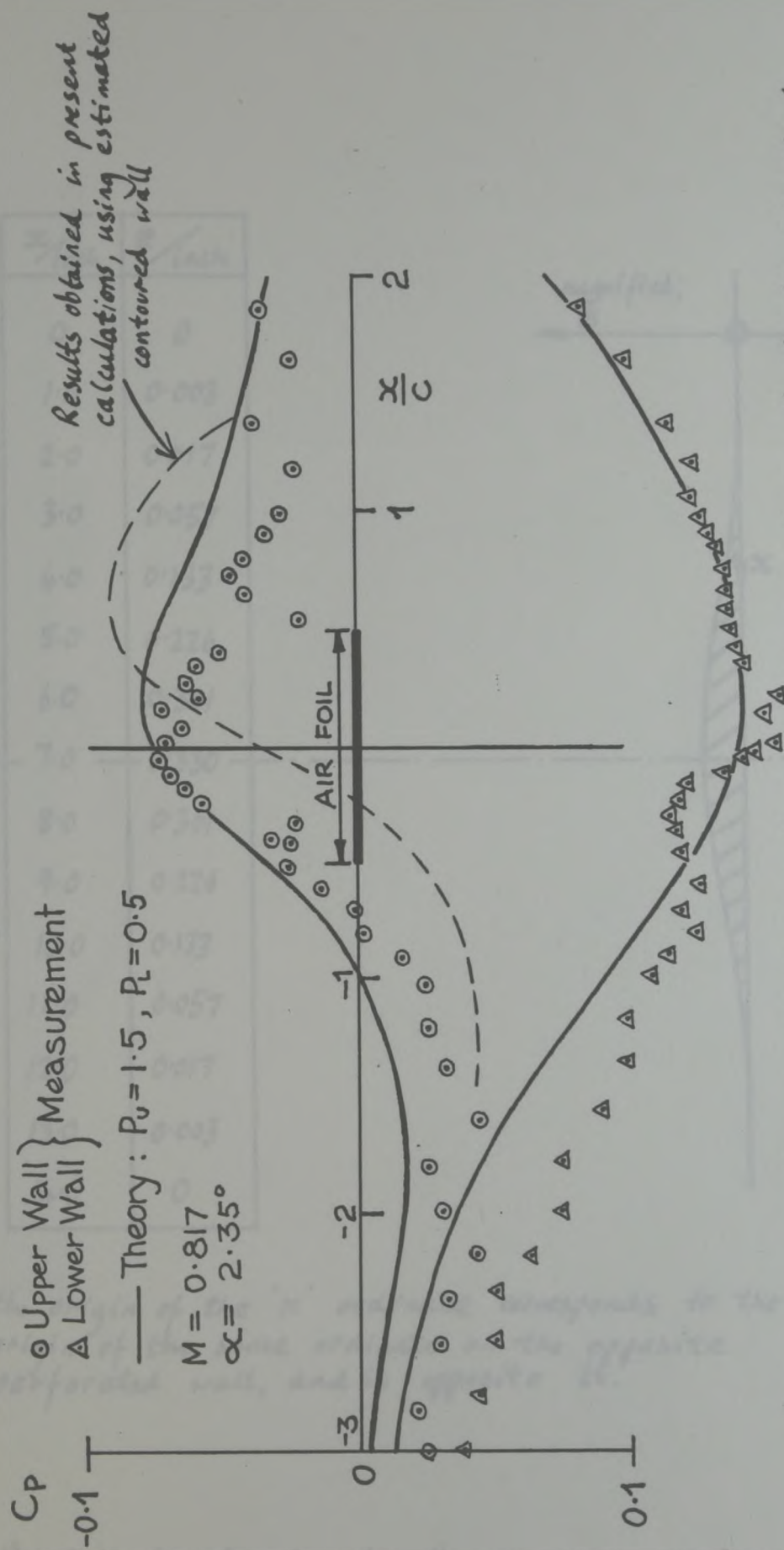
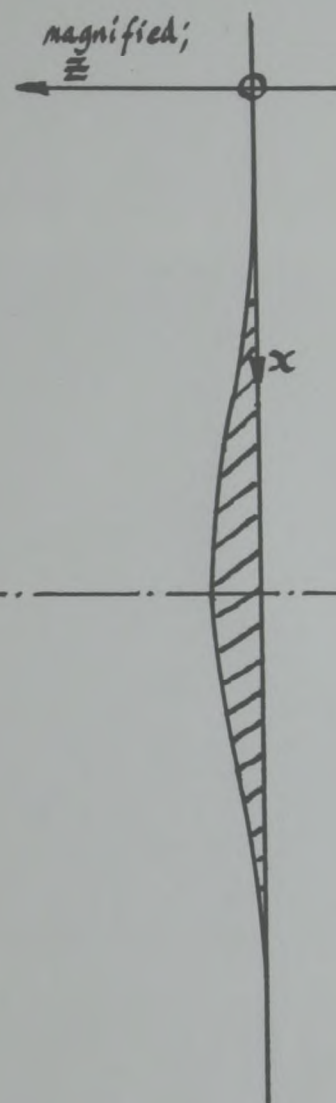


FIGURE (29) Typical pressure distribution on upper and lower walls of a two-dimensional windtunnel with lifting aerofoil mounted -  $M=0.82$

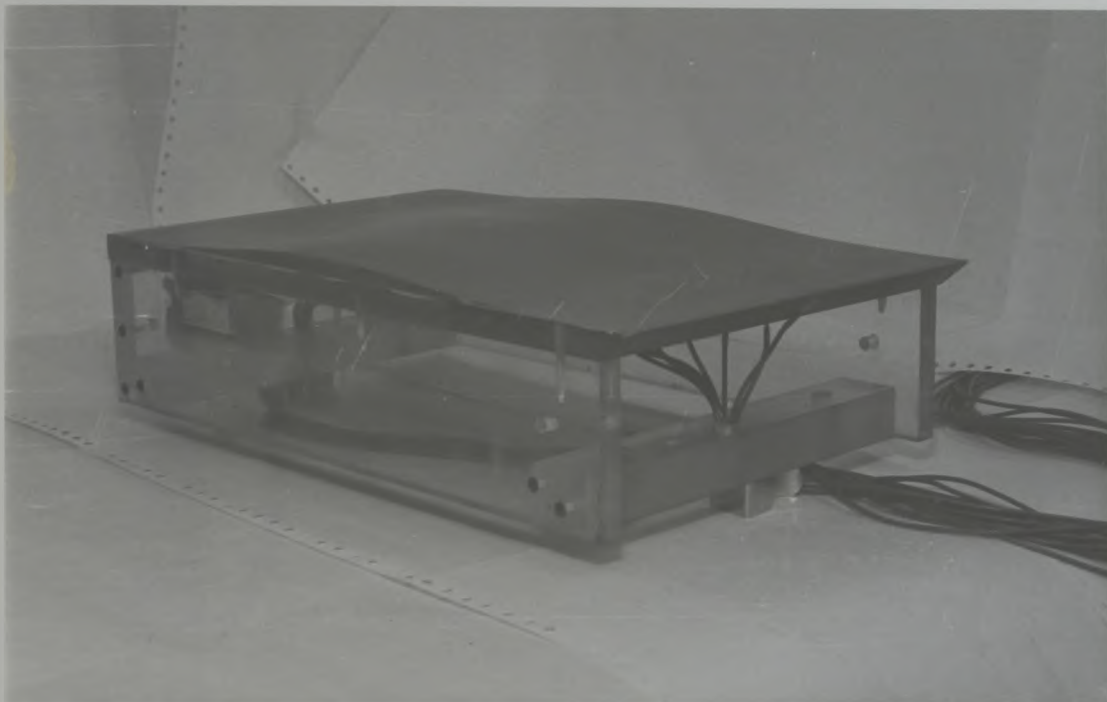
$x$ / inch	$z$ / inch
0	0
1.0	0.003
2.0	0.017
3.0	0.057
4.0	0.133
5.0	0.226
6.0	0.301
7.0	0.330
8.0	0.301
9.0	0.226
10.0	0.133
11.0	0.057
12.0	0.017
13.0	0.003
14.0	0



Note:- the origin of the 'x' ordinate corresponds to the origin of the same ordinate on the opposite perforated wall, and is opposite it.

TABLE (1) Ordinates of contoured wall





PLATE(3) Contoured top wall and plenum box.

Drawing of lower perforated wall and plenum chamber.

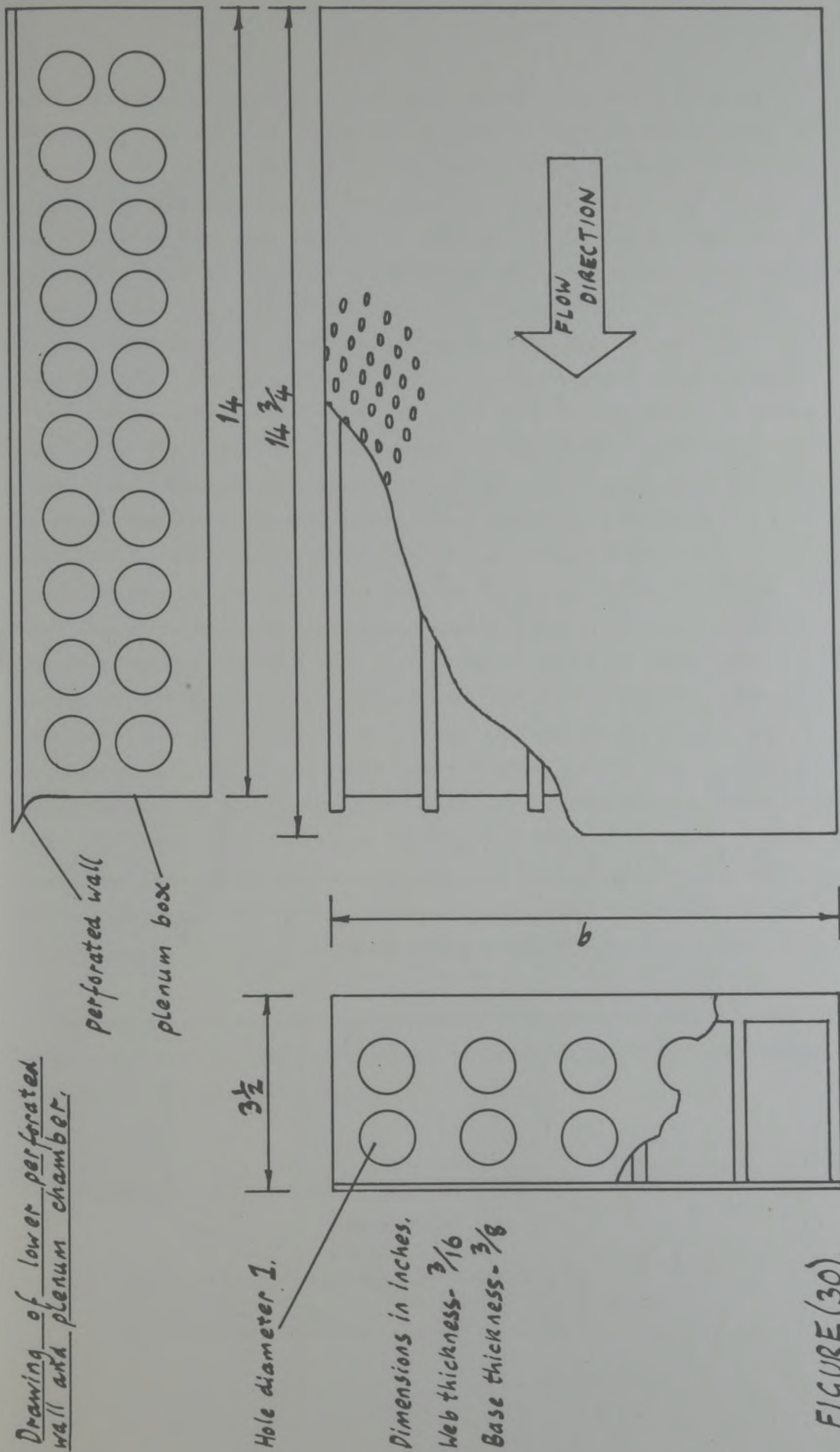
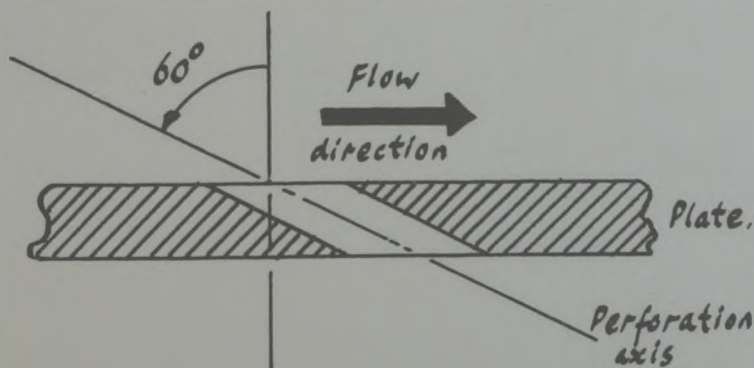


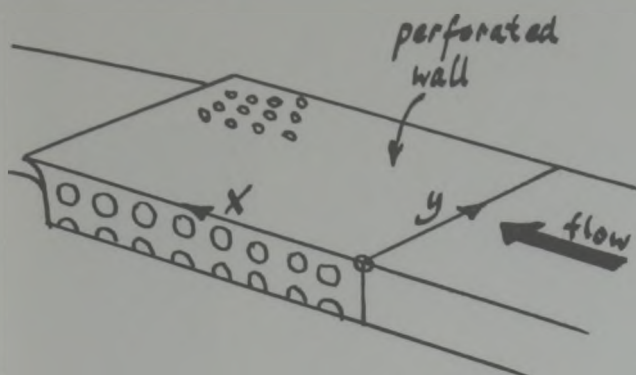
FIGURE (30).



to conservation of momentum in the air flowing out of the working section through the wall, there may well be a tendency for a downstream flowing jet to develop on the underside of the wall. For this air to then pass out of the front (upstream) end of the plenum box, it has to turn back sharply at the sealed downstream end. The high values of flow curvature there could cause the static pressure to vary rapidly in a direction normal to the underside of the wall. For this reason, the plenum chamber static tapings are mounted close (within 1 mm) to the wall on one of the vertical webs adjacent to the plenum centre-line. Some of these webs are visible in Figure (30). Over the majority of the plenum chamber length further upstream, the tapings are mounted on the same web but further from the perforated wall (approximately 6 mm distant). There are a total of ten static tapings in the plenum chamber and their longitudinal positions are indicated in Table (2). The webs mentioned above, support the perforated wall rigidly. They are drilled with an extensive pattern of 1 inch diameter holes to allow free passage of air in a lateral sense inside the plenum chamber. These webs and holes can be seen in a general view of the plenum box and perforated wall, Plate (4). The holes drilled in the outermost webs are redundant, as the solid sidewall of the working section seals them. In Plate (4), the groups of pressure tubes are clearly visible. These come from the plenum static tapings and the perforated wall static tapings. Within the plenum chamber, these tubes are routed so as to minimise the obstruction experienced by the flow there.

The perforated wall was manufactured from brass plate, 3.33 mm thick. The axis of the perforations is inclined at  $60^\circ$  to the normal, as shown in the diagram below.





position of plenum chamber static tapings
X/mm
38
102
162
197
229
264
279
305
330
349

position of perforated wall static tapings	
X/mm	Y/mm
12½	114
43	114
71	117½
92½	112
114½	117½
137½	111½
157	118
181	111½
199½	118
223½	111½
242½	117½
266	112½
285½	118
309	112
320½	109
329	118
340½	114½
352	112
363½	109½

TABLE(2) Positions of perforated wall, and plenum chamber  
static tapings





PLATE(4) Bottom plenum chamber and perforated wall.

Each perforation is 2.95 mm in diameter and they are arranged in a pattern such that the ratio of the open area of the perforations (based on their diameter) to the total wall area is 0.06. Thus, this type of wall is normally referred to as having an 'open area ratio' of 6%. The actual pattern of the perforations is shown in Figure (31). This pattern, or at least a very similar one is used in a number of prominent windtunnels facilities world wide including that at AEDC Tennessee.

The perforated wall has nineteen static pressure tapings longitudinally and eight laterally. Each tapping is positioned centrally between a set of four adjacent perforations as indicated in Figure (31). The longitudinal set are mounted near to the centre-line of the wall at a convenient point in the perforation pattern. The positions of the tapings are given in Table (2) relative to one front corner of the wall.

On many perforated walls, the perforations do not begin abruptly near or at the leading edge of the wall, but are gradually introduced. The same is true of the present wall. However for simplicity, the initial transition is masked on the working section side of the wall using thin adhesive tape. This tape finishes 89 mm from the leading edge of the wall and it is at this point that the 285 mm long perforated wall begins. In the design of the contoured top wall, it was assumed that the perforated wall was 350 mm long, starting 30 mm from the leading edge of the complete wall.

The complete bottom wall and plenum box is mounted in the wind-tunnel working section and the groups of pressure tubes are channeled out to the surrounding room through ducts in the base of the working section which are virtually airtight.

#### 4.2.5 Choosing an Instrument to Measure Flow Angle.

To evaluate the normal component of velocity in the viscous flow at the perforated wall position ( $V_w$ ), the approach outlined in Section (3.1) is adopted. In this approach, the normal component



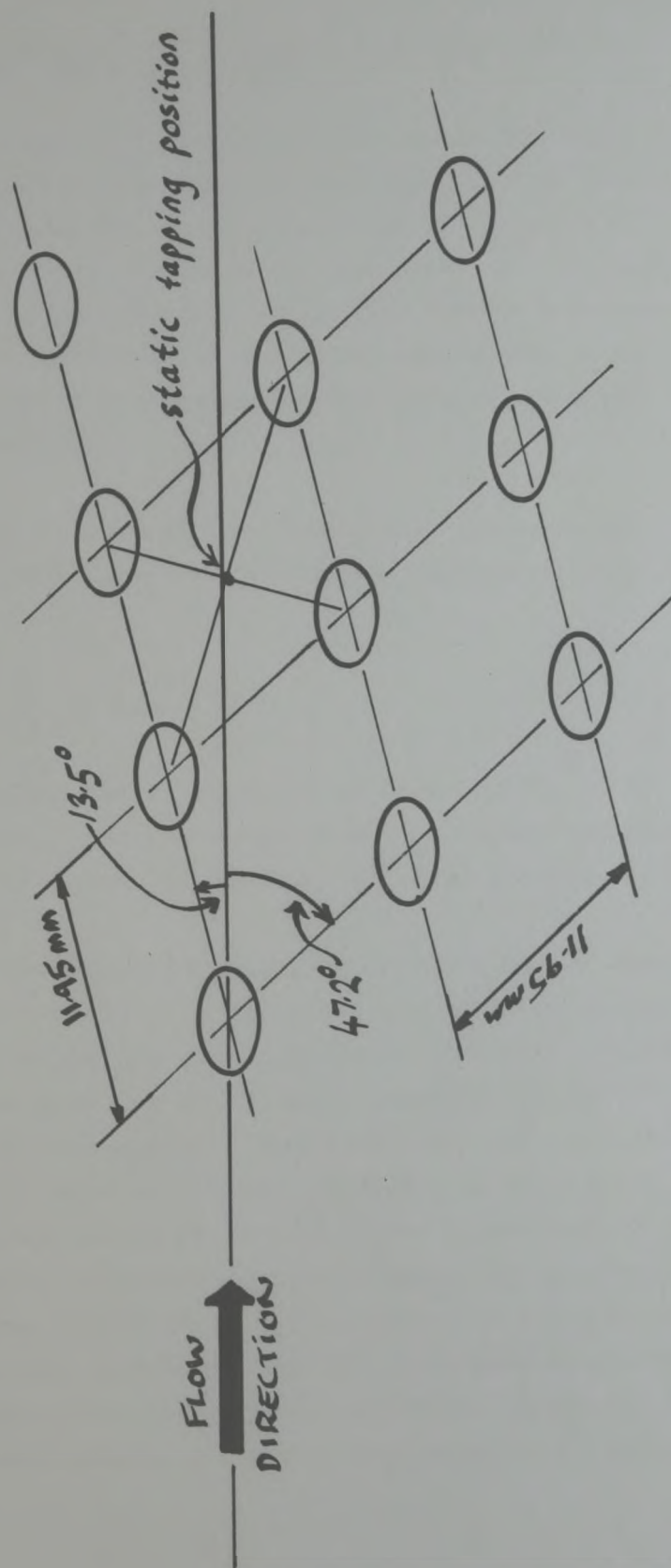


FIGURE (31) Diagram of wall perforation pattern.

of velocity is measured outside the boundary layer (where it is denoted  $V_e$ ) and is altered using Equation (3.1), namely

$$(L - \delta^*) \frac{d(\rho_e u_e)}{dx} - \rho_e u_e \cdot \frac{d\delta^*}{dx} + \rho_e V_e - \rho_w V_w = 0$$

to give the required value of  $V_w$  (strictly, in compressible flow, it is only possible to evaluate the combined term  $\rho_w V_w$ ). The alternative approach, involving the direct measurement of  $V_w$  was not possible using the equipment available for this research. It would involve either detailed investigation of the flow through individual perforations, or some subdivision of the bottom wall plenum chamber to permit careful metering of the transpiration rate at any given point on the perforated wall.

It is helpful when considering the flow outside the boundary layer, to refer to a flow angle relative to the longitudinal axis,  $\theta_e$ , where

$$\theta_e = \tan^{-1} \left( \frac{V_e}{u_e} \right), \quad (42)$$

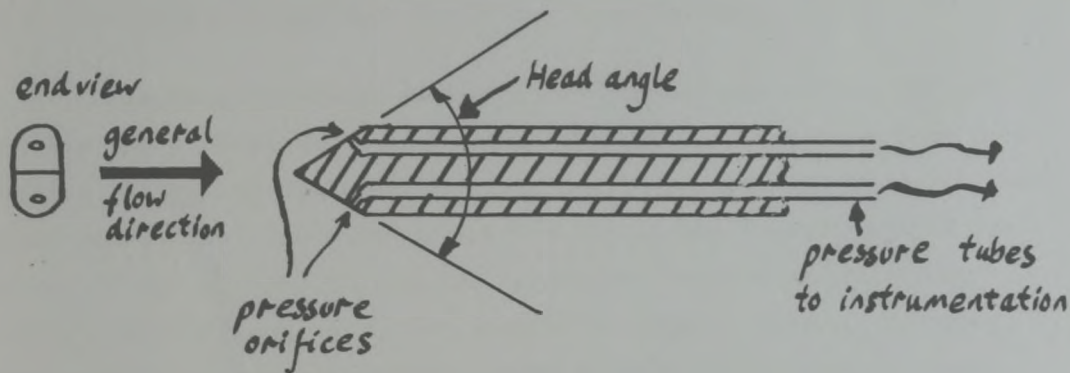
rather than to the actual normal component of velocity,  $V_e$ . It was considered initially that the device chosen to measure the flow angle would need to be capable of resolving  $\theta_e$  to an accuracy of  $0.1^\circ$ .

To measure the flow angle, the technique of Laser Doppler Anemometry was carefully considered. It is a most desirable technique in that it is non-intrusive and for any given application involves a fixed calibration, which depends only upon readily available physical constants, such as the wavelength of the Laser light and the separation angle of two fixed incident Laser beams. However, in using most practical Laser Doppler Anemometer systems, there is necessarily a large amount of complex mathematical analysis which must be carried out after the experiment in order to obtain values for velocity components. An attempt was made to measure the flow angles in question using a Laser Doppler system incorporating a Malvern Instruments, K2023 correlator. This attempt met with almost no success. However,



it did reveal that with the equipment commercially available at the time, it would not be possible to measure the flow angle of interest (being  $3^\circ$  or less in flows with speed around  $250 \text{ ms}^{-1}$ ) with the required accuracy of  $0.1^\circ$ . Indeed, there were strong indications that the available accuracy would be an order of magnitude worse than this.

One other experimental approach to measuring the flow angle was considered. This involves the use of a more conventional yawmeter instrument, where a measured pressure difference is used with a calibration equation to provide the value of the flow angle. A simple diagram of the instrument is shown below.



This type of instrument is described as a Conrad yawmeter and is found to have an approximate calibration equation (Ower and Pankhurst, 1969) of the form

$$\frac{\Delta p}{q} = M \sin \theta \quad (4.3)$$

Here,  $\frac{\Delta p}{q}$  is the difference between the pressures measured at the two orifices non-dimensionalized with respect to the local dynamic head ( $q$ ).  $M$  is a constant which depends upon the head angle (which in the case of our instruments is approximately  $60^\circ$ ) and  $\theta$  is the angle of the oncoming flow relative to the longitudinal axis of the yawmeter. With the instrumentation system available, this method of measuring flow angle was estimated to have an accuracy of  $0.2^\circ$  (being the maximum error in the calculated flow angle).

The above method, using Conrad yawmeters was chosen in preference to the more complex, and less accurate, Laser Doppler Anemometer approach. For simplicity, the term 'yawmeter' is used for the Conrad devices, although strictly they are used to measure the pitch angle of the flow. For yawmeters which are not constructed to be perfectly symmetrical, some initial experiments carried out during this research indicate that Equation (4.3) is altered by the addition of a constant term C. Thus for use in flows at small angles (less than  $5^{\circ}$ ) to the yawmeter axis, the assumed calibration equation is

$$\frac{\Delta p}{\rho} = M\theta + C. \quad (4.4)$$

#### 4.2.6 The Combined Boundary Layer and Yawmeter Rake.

In attempting to design an instrument to measure accurately the boundary layer displacement thickness and the flow angle outside the boundary layer, careful consideration had to be given to the positioning of the various pressure tubes, chiefly at the forward end of the device. It was decided to use two yawmeters, mounted at different heights and displaced on either side of a central vertical boundary layer rake. Two yawmeters were chosen so that for any experienced boundary layer thickness ( $\delta$ ), there could be a yawmeter as close as possible to that height (i.e. neither far above nor beneath it as might be the case if only one instrument were used). To decide the actual height of each yawmeter, a short series of experiments was carried out in the transonic windtunnel using an existing boundary layer rake. When air was drawn out of the working section, through the perforated wall, the boundary layer thickness on the wall remained below 20 mm. When air was blown into the working section through the wall (influenced by a value of  $C_{pw}$  even less than - 0.2) the thickness of the boundary layer increased, but remained below 35 mm. These boundary layers were produced by more severe conditions than those which would be experienced in subsequent tests. The heights chosen for the yawmeters were 20.5 mm and 35 mm.

Under some circumstances, the top of a yawmeter may be just below



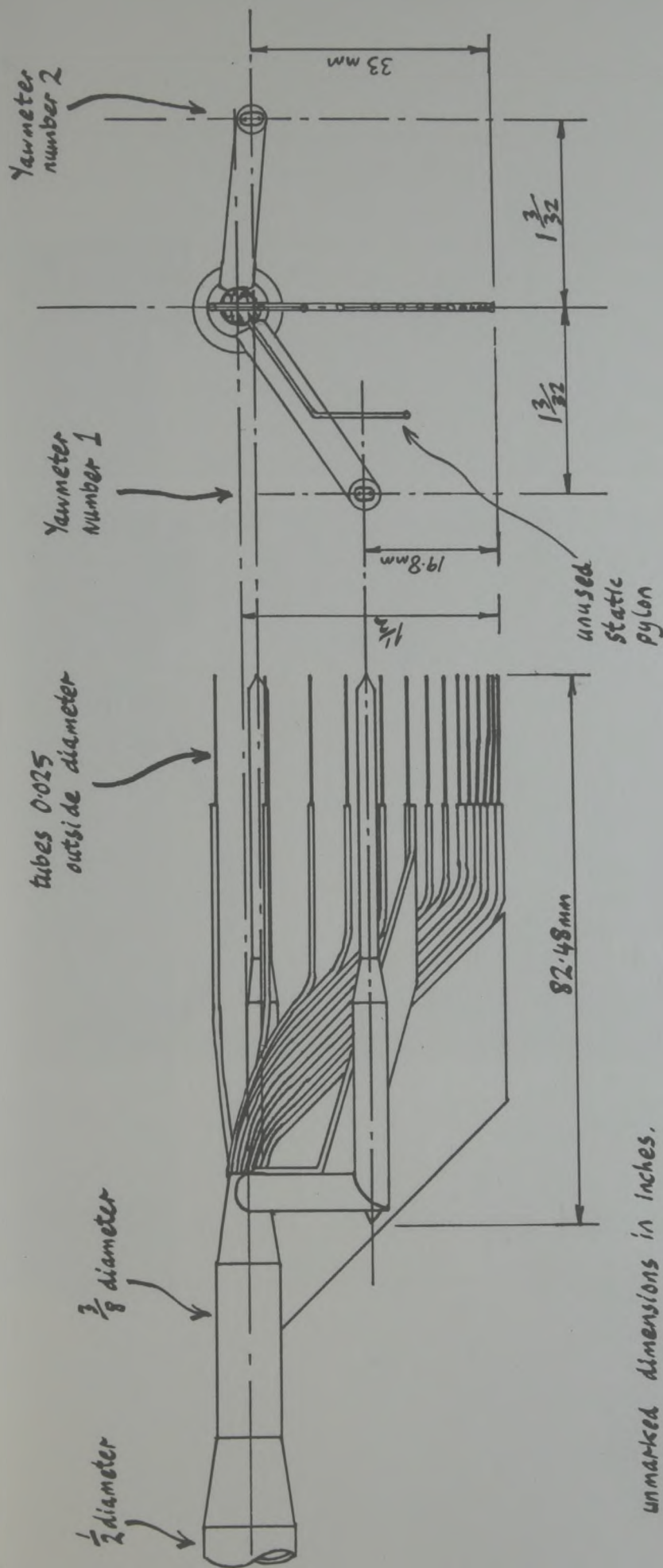
the edge of the boundary layer. In these situations it would probably be more convenient to use results from this yawmeter, rather than reverting to those from the other yawmeter which may be as much as 14 mm (or two thirds of the boundary layer thickness) outside the boundary layer edge. However, the whole approach taken to the evaluation of flow angle requires that it be measured outside the boundary layer (see Section (3.1)). If the experimental data are analysed as though the yawmeter were outside the boundary layer then an error is involved in the final values of crossflow. This error is caused by using Equation (3.1), namely

$$(L-\delta^*) \cdot \frac{d(\rho_e u_e)}{dx} - \rho_e u_e \cdot \frac{d\delta^*}{dx} + \rho_e v_e - \rho_w v_w = 0 \quad (4.5)$$

without alteration. In Appendix (5), the error is shown to be effectively one in the first term of Equation (4.5). It is also shown to be negligible when compared to that term provided that the yawmeter remains in the top 30% of the boundary layer depth. The first term in the above equation is normally of the same order of magnitude as the last two terms, which represent the crossflow. Thus the error caused in the calculation of the term  $\rho_w v_w$  will be of the same order of magnitude as the error in the first term, and in that way, negligible.

With the preceding decisions made, concerning the approximate positions of the yawmeters relative to the wall and boundary layer rake, the complete instrument was designed. Careful consideration was given to the shape of the instrument, particularly at the upstream end, to ensure that the smallest possible interference would be experienced in the flow at the yawmeters and along the boundary layer rake.

A diagram of the forward part of the combined boundary layer rake and yawmeter assembly is shown in Figure (32). Only leading dimensions are shown. A photograph of this part of the apparatus in the transonic windtunnel is shown in Plate (5). The static pressure tube visible in Plate (5) was not present during any of the tests described in this report.



unmarked dimensions in inches.

FIGURE (32) Diagram of forward part of combined boundary layer rake and yawmeter assembly.





PLATE(5) Combined boundary layer rake and yawmeter  
assembly in windtunnel.

In the designing the apparatus, the following approximate approach was taken in deciding the dimensions of some components. A component with a diameter  $D$  say, would be placed no nearer, than a distance of ten times  $D$ , to the upstream plane where the boundary layer rake and yawmeters are positioned. This guideline is intended to keep interference from such components at an acceptable level.

The pitot tubes in the boundary layer rake are manufactured from hard stainless steel tubing, with external and internal diameters of 0.025 and 0.012 inch respectively. The open ends of the tubes are ground normal to the longitudinal axis of the instrument to an accuracy of about one degree. The heights of the tubes are given in Table (3) and the lowest three tubes are in contact, the lowest also being in contact with the wall of the windtunnel. The yawmeters, once mounted are at the heights shown, rather than the chosen heights of 20.5 mm and 35 mm. All stainless steel pressure tubing, when jointed is sealed with soft solder.

The complete boundary layer rake and yawmeter device is supported firmly in the windtunnel working section by a straight tube of half inch external diameter which is clamped in a purpose built mounting block. This block attaches to the circular arc quadrant which already exists in the windtunnel. Supporting the rake assembly from the quadrant has a number of advantages over mounting it directly on the perforated wall. First, it has been possible to design the mounting block to allow continuous longitudinal movement of the rake and support tube. Second, because the rake is not dependant on any particular perforations or fixings on the wall, it may be used on any type of wall which may be fitted in the windtunnel. Thirdly, no bulky rake foot is necessary, as the rake is supported firmly from downstream. In fact, a mechanism in the mounting block is used to tip the support tube downwards, so fixing the rake foot firmly against the perforated wall. However, because the foot of the rake covers only a small area, it does not significantly obstruct the perforations. In an attempt to eliminate the effect of individual perforations from some reduced results (namely those involving longitudinal derivatives), the front of the bottom pitot tube in the boundary layer rake is always sited in the same way relative to the local perforations. To achieve this, a limited freedom in yaw has been

TABLE (3) Heights of boundary layer rake tubes from wall



TUBE	$z/mm$
14	42.1
13	34.1
12	27.5
11	22.0
10	17.5
9	13.7
8	10.6
7	8.1
6	6.0
5	4.4
4	3.1
3	1.59
2	0.95
1	0.32

The heights of tubes 4-14 will vary slightly each time the rake is re-located

Three base tubes, being crammed against wall normally, will have fixed height.

TABLE (3) Heights of boundary layer rake tubes from wall

incorporated into the quadrant mounting block. The maximum yaw angle required, to locate the rake foot in the required position during a longitudinal traverse is about  $1.5^{\circ}$ . In Appendix (6), it is demonstrated that such an angle will not significantly affect the effective flow angle experienced by the yawmeter. It is also assumed here that there will be no change in the overall structure of the flow near the rake due to the yaw angle mentioned above.

The yawmeters are referred to by numbers, Number 1 being the lower, and Number 2 the upper (see Figure (32)). When the yawmeters were mounted in their calibration rig (See Appendix (7)), they were misaligned in the sense of roll angle. To ensure that the calibration remained fully applicable, this misalignment was also built into the yawmeters when fitted onto the combined rake. The rake and support tube are restrained in roll during use by a series of locating pins along the top to the supporting tube which engage in a longitudinal slot in the mounting block. In any case, it may be shown (in a similar manner to that in Appendix (6)) that roll angles below  $5^{\circ}$  do not significantly affect results from the yawmeters.

In designing the rake and support tube, careful consideration was given to maintaining mechanical deflections at a low level. However, as the foot of the rake is sited at different positions along the bottom wall of the windtunnel, the rake will normally take up different orientations. In order to use a yawmeter calibration equation accurately in such a situation, it is necessary to define a longitudinal reference line on the rake. A small pin was inserted into the rear elbow of yawmeter Number 1 (see Figure (32)). The line joining this pin to the tip of yawmeter Number 1 is used as the reference line. Each time the rake is positioned on the bottom wall, the angle of this reference line relative to the horizon is measured, and then using the yawmeter calibration curves, the flow angle can be calculated first relative to the line, and subsequently relative to the horizon.

The complexity of building and mounting a small static pressure tube on the rake was avoided by using the existing perforated wall static tapings. Each time the rake was positioned on the wall, it was sited close to a wall static tapping. In fact



the rake foot was positioned in the same manner relative to respective tappings. Corrections for the effect of the presence of the rake were then made to the measured static pressure to determine the relevant static pressure at the boundary layer rake foot and at each yawmeter. However, such corrections could not account for pressure gradients normal to the wall of the windtunnel. If such pressure gradients were large, it would not be correct to use static pressures measured on the wall to represent the pressure in the vicinity of the yawmeters. Cebeci and Smith (1974, pp 73-75) show that for flows with small curvatures (which the flow in question is likely to be) the change in static pressure across the depth of the boundary layer is negligible, when compared to the magnitude of the pressure itself. On this basis, the wall static pressure is used to represent all the required pressures around the rake (with the corrections mentioned above). Experiments performed in a low speed windtunnel at the City University indicate that a noticeable pressure disturbance is generated on the wall around an isolated perforation when there is flow through it. There was initially concern that such fields of disturbance would render the static pressure measured between perforations useless. However, based on the experiments mentioned, an estimate was made of the influence of a pattern of perforations surrounding a wall static tapping, on the pressure experienced there. For the average flow angles which are experienced in the transonic windtunnel (namely less than  $2^\circ$ ), the error in the recorded static pressure (as a pressure coefficient) is 0.0075. This represents less than half a percent of a typical static pressure (0.7 atmosphere for example). As this error is so small and because no accurate correction could be calculated to eliminate it, it is neglected.

The yawmeters were calibrated prior to the experiments of main interest. The process of calibration is described in detail in Appendix (7). The resulting calibration is a straight line relationship between  $\theta$ , the flow angle relative to the reference line on the rake, and  $\frac{\Delta p_q}{\rho q}$  the difference in pressure between the faces of the yawmeter head non-dimensionalized with respect to the local dynamic head. The value of the gradient and intercept of this calibration equation for each yawmeter and at three values of local non-dimensional static pressure  $\left(\frac{p_s}{p_0}\right)$



are shown in Table (4).

Any error in the yawmeter calibration mentioned above will be carried through the analysis of subsequent experiments and finally in to the calculation procedures developed here. It is helpful then to determine the error in the calibration which would not cause unacceptable errors in the results from the eventual calculation methods. This is carried out using the computer program PILOT. Small errors in the yawmeter calibration are simulated by alterations in the constants of the wall characteristic in the program. The effect of these alterations on the predicted flow distribution in the working section is then observed. It was assumed initially in Section (4.2.5) that the Conrad type yawmeters would give results accurate to within  $0.2^{\circ}$ .

If this error were to exist in the worst possible manner, then the gradients of the calibration curves (obtained in Appendix (7)) would be in error by 4%. Applying this 4% error to the gradient of the wall characteristic in the program PILOT (when it is being used to predict windtunnel flows similar to these described in Section (3.8.2)) produced extremely small alterations in the flow predicted. Changes in the flow angles throughout the working section were typically less than  $0.01^{\circ}$  and changes in the longitudinal component of velocity were below 0.01% of the freestream speed. From this point of view, it appeared that the accuracy of the yawmeter calibrations would certainly be adequate.

However, if the possible error in the calibration were to be introduced in the data used to evaluate the intercept of the calibration curves, then the results are considerably different. To simulate this condition, a fixed error equivalent to  $0.2^{\circ}$  is introduced into the wall characteristic used in the program PILOT. The program is then used to simulate the flows mentioned above. In this case however, the effect of the error is more significant, particularly towards the downstream end of the top liner, where severe inflow exists. Changes in flow angle of up to  $0.4^{\circ}$  due to the introduced error are present there. This figure reduces to  $0.1^{\circ}$  on the windtunnel centre-line. At present,  $0.1^{\circ}$  represents the order of accuracy required in the definition of



$$\theta = m \frac{\Delta P}{q} + c$$

Yaw. meter	local $P_s/p_o$	$m$ / degree	$c$ / degree
1	0.6325	20.978	-0.49
	0.6931	21.510	-0.50
	0.7325	22.878	-0.61
2	0.6318	22.262	-0.54
	0.6925	22.361	-0.79
	0.7320	22.051	-0.78

TABLE (4) Yawmeter calibration equation data.

aerofoil incidence for commercial uses. Although introducing the  $0.2^\circ$  error in the wall characteristic produces only a change of  $0.1^\circ$  in the flow angle on the windtunnel centre-line, it was considered desirable to press for slightly improved accuracy, in fact of  $0.1^\circ$  in the yawmeter calibration. With regard to changes in the longitudinal speed produced by the error in the wall characteristic, a similar argument applies. Changes on the top liner rise to 0.3% of the freestream speed and on the centre-line, to 0.1% of the freestream speed. The latter figure would represent an approximate change in Mach number of 0.001 in a typical high subsonic flow. It also represents the approximate accuracy required in defining the flow approaching an aerofoil. The decision to define the yawmeter calibration to an accuracy of  $0.1^\circ$  is endorsed from the point of view of the longitudinal component of velocity also.

To examine whether or not this level of accuracy is available in the calibration of the yawmeters, a brief examination of cumulative errors from various parts of the calibration was carried out. This is presented in Appendix (8). It is the conclusion of that Appendix that the worst error possible (considering a limited number of sources of error) in the calculation of the yawmeter calibration is  $0.26^\circ$ . Although this is more than double the required error of  $0.1^\circ$ , it is almost certainly a pessimistic estimate and thus it might be that a maximum likely error of  $0.1^\circ$  is achieved. However, as it was commented in Appendix (7), the data used to determine the intercept of the calibration line are significantly scattered (see Figure (60)), beyond even the worst estimate of  $0.26^\circ$ . The data for yawmeter Number 2 are worse than those for Number 1 and therefore only the latter yawmeter is used for determining subsequent experimental data. It is considered that a large amount of the scatter in Figure (60) is a result of the swiftly changing gradients of the curves in Figure (61). Here,  $\delta^*$  is shown as a function of the longitudinal ordinate 'x'. It is suggested in Appendix (7) that the large values of  $\frac{\delta^*}{\Delta x}$  are a result of additional roughness on the bottom wall, caused by the sealing tape being drawn into the perforations. In future, either measurements should be made at more longitudinal positions, or an alternative approach should be taken in calculating the intercept of the yawmeter calibration



curve. In order to include some estimate of the calibration accuracy in later calculations, the distribution of the intercept points with regard to angle for yawmeter Number 1 in Figure (60) was examined. It was assumed to have a normal distribution, and the standard deviation ( $\sigma$ ) of this was calculated to be  $0.19^{\circ}$ .

This concludes the discussion concerning the combined boundary layer and yawmeter rake.

#### 4.2.7 Ancillary Equipment

The ancillary equipment described here, is that used to secure a permanent record of data which will supply values of pressure for subsequent calculation. A schematic diagram of this equipment is shown in Figure (33). It is described in a logical order, beginning at the 'measurement' end of the system.

From each pressure tapping in the windtunnel working section, whether it be a static, stagnation or yawmeter tube, a continuous plastic tube leads to a clamping mechanism which is used to seal off all tubes simultaneously. The connecting tubes mentioned are carefully designed to minimise the response time of the complete duct system. This design process involves consideration of both the diameter (which influences viscous effects in the response process) and length (which, combined with tube diameter influences both the viscous effects and nett volume of the duct system; and hence response time) of the connection tubes.

Each tube then passes to a small reservoir. This reservoir is intended to mask the effect of clamping the tube, which would otherwise increase the pressure in the sealed part of the duct. In addition, it provides the largest possible 'source' of air to sample after the windtunnel operation has ceased. This sampling process, carried out using a pressure transducer, involves releasing some of the air in the sealed duct into the transducer cavity. Clearly this alters the pressure in the sealed duct. With the reservoir, the al-

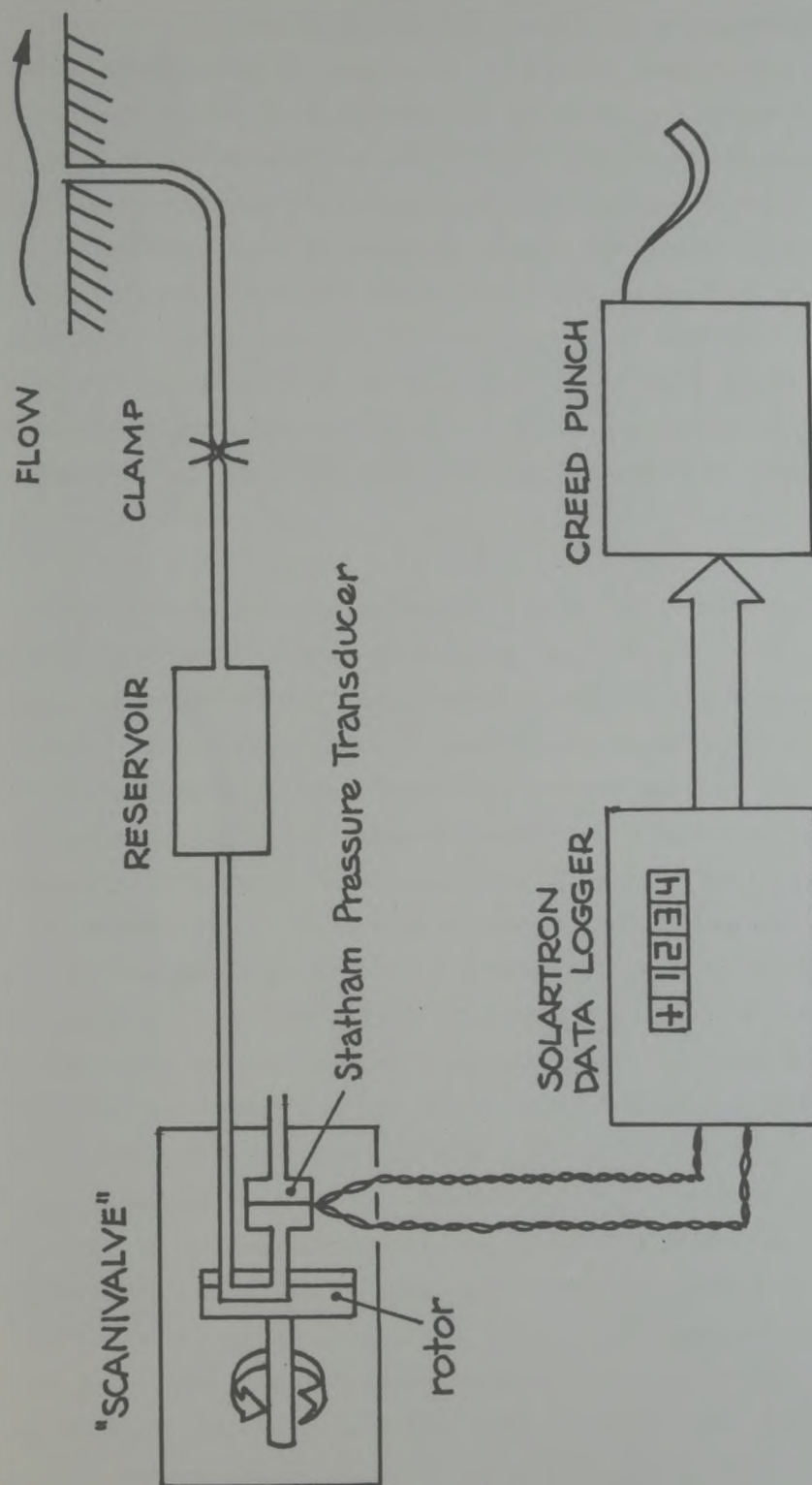


FIGURE (33)

Schematic diagram showing ancillary equipment used in experiments.



teration in pressure on sampling is small.

Discrete sampling is necessary because only one transducer (a Statham PM131TC with a range of  $\pm 12.5$  psi) is employed to measure the pressure in up to 48 tubes. It is connected sequentially to the tubes by a 'Scanivalve', or rotary multi-port connector. The transducer cavity is very small compared to the volume of the reservoir. Thus, after each tube is sampled, the respective reservoir pressures are only slightly altered. The Scanivalve is stepped through two complete rotations after each operation of windtunnel. Thus, for each reservoir, two pressures are recorded, neither of which is equal to the original undisturbed pressure. By simple extrapolation of the two recorded values, this pressure can generally be recovered to a high level of accuracy.

The four-arm resistance bridge in the Statham transducer is excited by a small voltage (normally less than 5 volt). The signal output, measured across the alternate arms of the bridge is led to a Solartron data-logger unit. A very close approximation to a straight line relationship exists between the output voltage and the pressure difference across the transducer diaphragm. The back cavity of the transducer is open to the atmosphere, so during any single operation of the windtunnel, the backing pressure remains constant. With a constant backing pressure, it is possible to use a calibration relating the output voltage directly to the tube pressures of interest. This straight line calibration is determined for each operation of the windtunnel by connecting two known pressures to the Scanivalve tubes. One of these pressures is above all the pressures to be measured (it is the atmospheric pressure, measured using a mercury barometer) and the other is a lower pressure, nearly always below the pressures to be measured. This second pressure is measured using a mercury column, which indicates gauge pressure. Using two accurately known pressures which cover the interval where pressures will be measured ensures the most accurate use of the approximate straight line calibration. Some further details concerning the transducer calibration are included in Appendix (8).



The Solartron data-logger contains both a digital voltmeter (type 1420.2) for quick observation of data and a punch encoder unit (type LU1467). The complete data-logger is manually controlled such that transducer output signals can be selectively displayed and simultaneously digitized. The digitized signal is transmitted to a Creed punch unit which records the signal on paper tape for subsequent processing. After each pressure is logged, the Scanivalve is manually advanced to sample the next tube and that pressure is then logged. This process is repeated until the Scanivalve has been fully rotated twice (as mentioned earlier), i.e. 96 pressures have been logged. As used, the reading accuracy of the Solartron unit is  $10^{-5}$  volt. This represents approximately 30Pa when indicating an output voltage from the Statham transducer operated with a 5 volt excitation potential.

#### 4.2.8 A note on Windtunnel Flow Uniformity.

The scheme proposed in this report is applied, during the course of the present research, only to flows which are (or are assumed to be) essentially two-dimensional in nature. If the flows which are investigated experimentally involve any variations in the third (lateral) dimension, then clearly some additional inaccuracy will be included in the calculation procedures which rely upon these experimental data. Indeed it would seem a rather severe test, to expect a calculation procedure which involves the assumption of two-dimensional flow, to predict accurately a flow which has significant variations in properties in the lateral direction. It seems likely that if the same calculation method were subsequently used in an attempt to predict a flow which is genuinely two-dimensional, then the results would be more accurate.

Data which depend predominantly upon local measurements, the wall characteristic for example, will not be affected by flow in the lateral direction significantly. However, any derivatives with respect to the ordinate 'x' will be adversely affected because predominant changes are not taking place in that direction, but at some angle to it. In fact the reduction of experimental data, to yield flow angles in the viscous flow, involves the use of the x- derivative of  $\rho e u_e \delta^m$ . Hence it was considered desirable to carry out a brief investigation into the uniformity



of the flow in the windtunnel, particularly near the bottom liner. This investigation involves the measurement of three variables; the stagnation pressure, static pressure and the boundary layer displacement thickness.

To investigate the lateral variation of stagnation pressure in the windtunnel working section, a rake with twelve pitot tubes was used, with an overall width of 190 mm. This was mounted at various longitudinal positions, approximately 35 mm above the bottom perforated liner. The Mach number of the flow approaching the rake was in the region of 0.7. In each measured distribution, the stagnation pressure remained steady within 0.2% across the majority of the working section. Only very near the sidewalls (where the sidewall boundary layer flow was encountered) did the stagnation pressure drop significantly. This level of variation is considered acceptable. An earlier brief investigation of the flow uniformity across the working section on the centre-line (rather than close to the bottom liner) also revealed the stagnation pressure to vary by only 0.2% across the majority of the width. This investigation was carried out approximately half way along the working section at two Mach numbers; 0.63 and 0.72. The variations mentioned in these investigations did not reveal any clear pressure gradients across the working section.

A similar investigation was carried out into the static pressure variations across the working section. A seven tube static rake, 135 mm wide was employed, and mounted 35 mm above the bottom liner, as before. Static pressure distributions were measured at three longitudinal positions covering the majority of the length of the working section and at Mach numbers between 0.65 and 0.9. Across the 135 mm of the working section width examined, the static pressure varied consistently by 0.6% or less (135 mm represents 60% of the 9 inch windtunnel width). This variation was considered acceptable. Also, no clear pressure gradient was observed across the windtunnel. The same rake was used to examine the nature of the flow across the windtunnel centre-line as it entered the working section. Here, at Mach Numbers close to 0.75, the static pressure varied by approximately 2% across the wind-tunnel. The vertical distribution of static pressure at that position

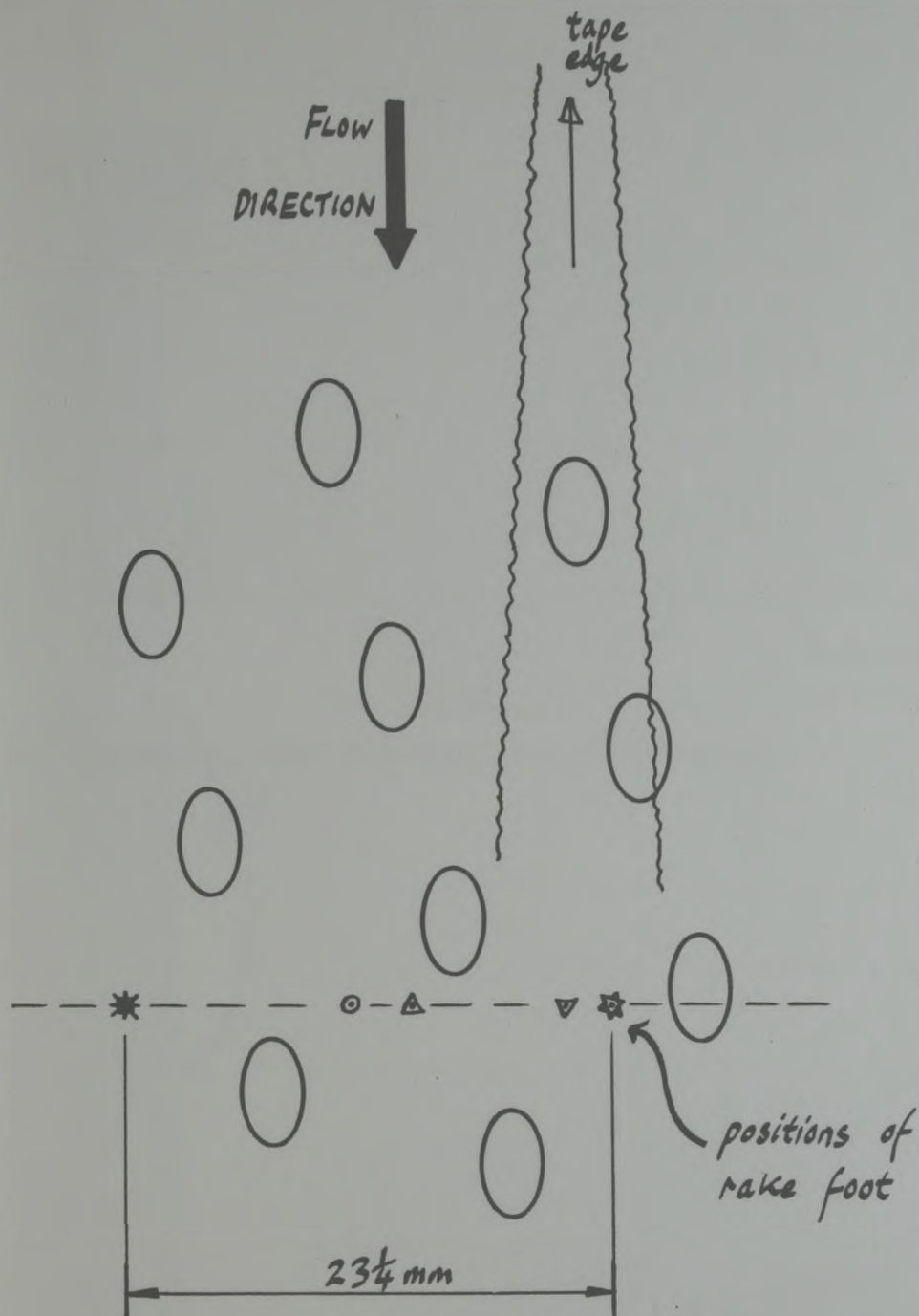


varied by slightly more, namely 3%. The static pressure variations discussed in this section may be due, to some extent, to inaccurate production or positioning of the individual rake tubes.

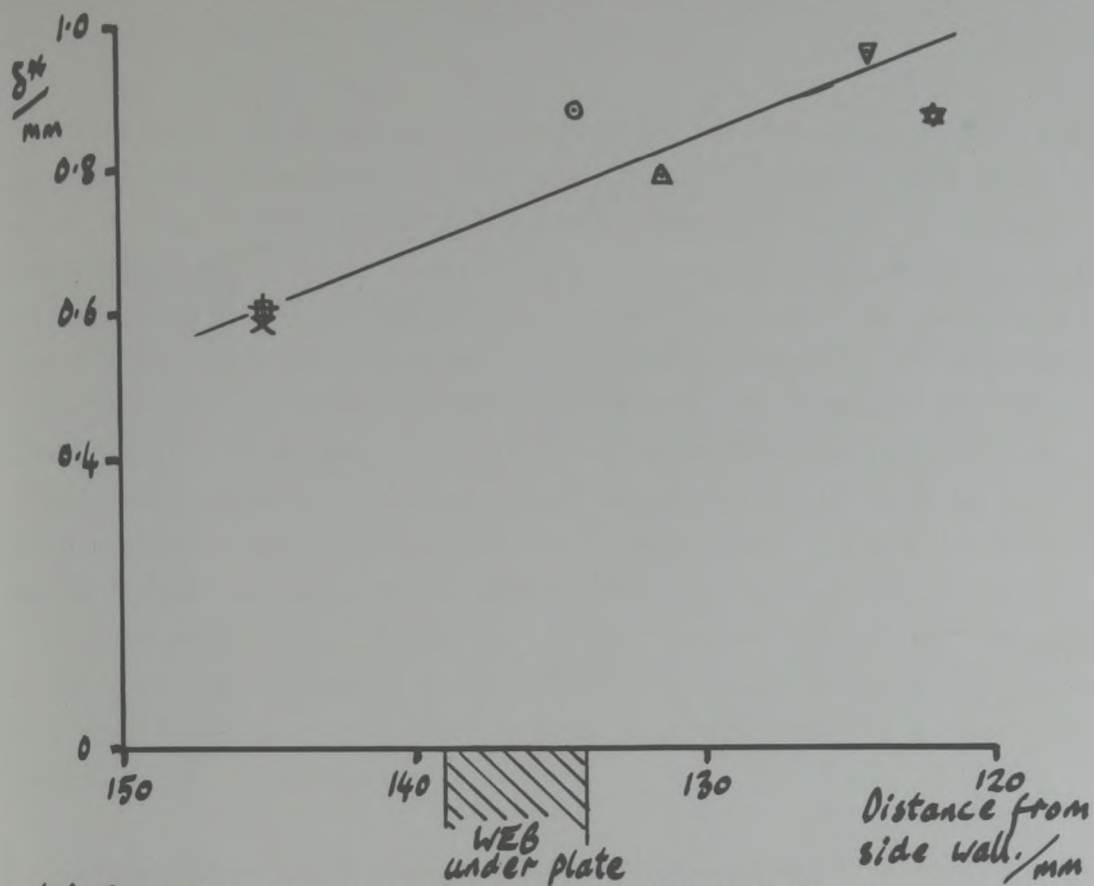
The final investigation to be discussed is that into the variation of the boundary layer displacement thickness,  $\delta^*$ , in the lateral direction. Here, because of the limited freedom in yaw provided by the rake support mechanism, the boundary layer was investigated only across a very limited width of the bottom liner. Experiments were carried out with the rake mounted 50 mm from the upstream end of the perforated section of the working section. The perforations were open and significant outflow was produced through them during the tests. The flow Mach Number approaching the rake was 0.90 for each experiment. Thus, the only significant variable between individual experiments was the lateral position of the rake. The position of the rake foot during the various experiments is shown in Figure (34). A nearby wall pressure tapping was employed to provide local values of static pressure. The values of the boundary layer displacement thickness obtained from these experiments are shown in Figure (35,a). The various symbols shown are used to link Figures (34) and (35). Although Figure (35,a) has a false origin on the vertical ordinate and a strongly magnified vertical scale, it is clear that there is a disturbing lack of uniformity in the value of  $\delta^*$ . The three separate tests denoted by the symbols  $+$ ,  $\times$  and  $\square$  repeat extremely well, thus indicating that the apparent lateral variation in  $\delta^*$  is not merely a result of the unrepeatability of experiments. There may well be a strong influence of local perforations on the values of  $\delta^*$ . For example the experiment denoted  $\blacktriangle$ , which was performed with the rake immediately behind a perforation (with outflow present), has a marked decrease in  $\delta^*$ . The boundary layer profile for this experiment is shown in Figure (35,b). Clearly at the base of the profile, there is a region of high energy flow relative to the other two profiles plotted, which were obtained away from perforations. If there is a genuine influence of local perforations, then it becomes essential, at least to site the rake foot in the same manner relative to local perforations during separate tests. Although individual values of  $\delta^*$  may be in error then, the gradient of  $\delta^*$  in the longitudinal direction would be correct.

FIGURE (34)

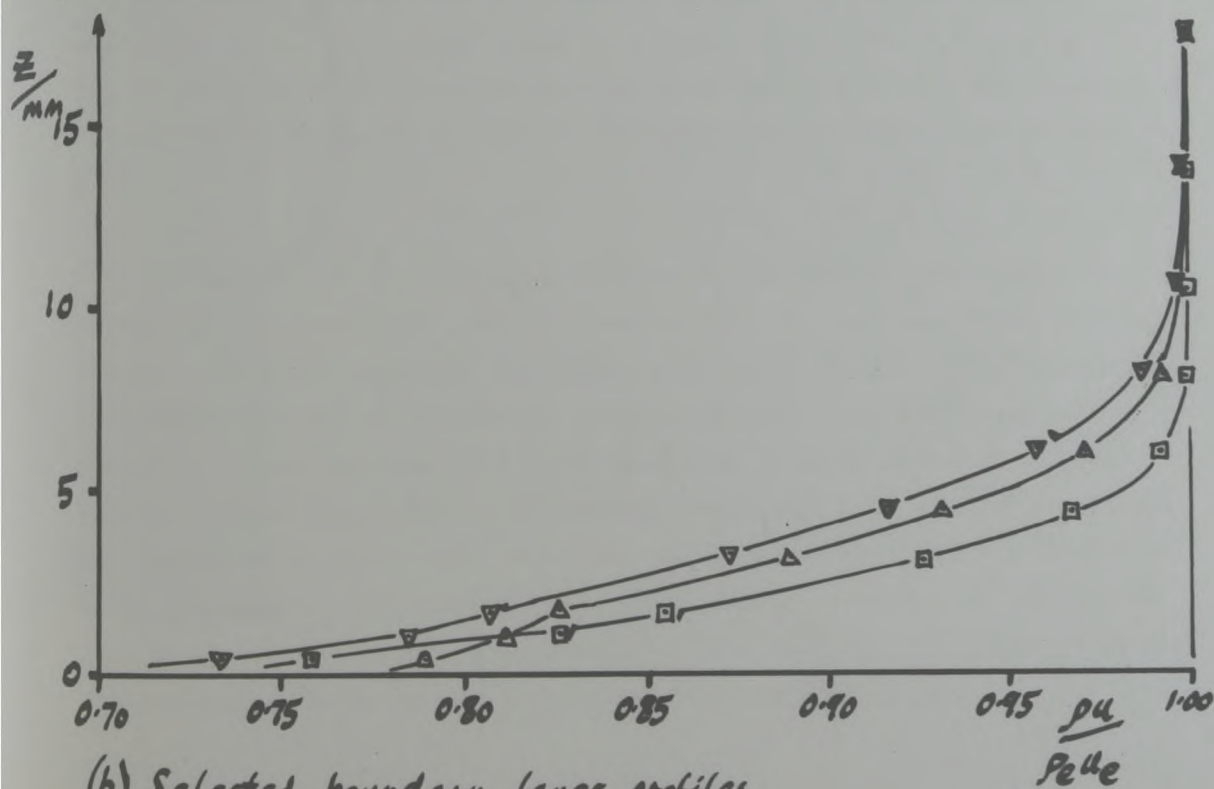




Positions of boundary layer rake foot  
 FIGURE (34) during non-uniformity investigation.



(a) Boundary layer displacement thicknesses



(b) Selected boundary layer profiles.

FIGURE (35) Boundary layer results obtained during non-uniformity investigation.



In Figure (35,a) there is a strip marked as 'web under plate'. This longitudinal web necessarily obscures some perforations. This would cause a longitudinal region where suction through the wall is damped. The values of  $\delta^*$  would then rise over the web, and fall on either side of it. This may be apparent in Figure (35,a) but with the data available, this conclusion could not be made with confidence. Another possible cause of non-uniformity is marked at the top of Figure (34) as 'tape edge'. This comment refers to adhesive tape, used to seal the transition region at the front of the perforated wall, where holes are progressively introduced in a streamwise direction. The band of tape which covers the width of the bottom liner, had a longitudinal gap in it, where static tapings, but no open perforations are sited. One edge of this gap is referred to in the Figure. A region of turbulence may be released from the longitudinal edge of this tape, causing a local increase in  $\delta^*$  downstream of itself.

Although the three possible causes mentioned above may contribute to the non-uniformity observed (particularly the influence of individual perforations), perhaps the most likely cause is a lateral gradient in the value of  $\delta^*$ . The line drawn on Figure (35,a) has an angle of  $1^\circ$ . This figure of  $1^\circ$  is comparable with the gradients of the longitudinal  $\delta^*$  distributions measured during the main experiments described in Section (4.3).

In summary, it is not clear what level of lateral uniformity in variables is necessary, for the results of this research to be entirely valid. The investigations mentioned here gave results which appeared acceptable so far as static and stagnation pressures are concerned. However, there appears to be a significant lateral gradient in the boundary layer displacement thickness. With the data available, it is not possible to decide the exact magnitude or cause of this non-uniformity. Though not conclusive, this brief investigation does reveal the need for a more thorough examination of the size and influence of three-dimensional effects on the proposed calculation methods.

### 4.3 Experiments and Initial Analysis

#### 4.3.1 Experimental Conditions.

The experiments to be described serve the three purposes outlined in Section (4.1). These are, to provide data for the comparisons with the results of the programs PREDICT and PILOT, and to provide sufficient information for the generation of the wall characteristic. The last of these tasks is considered to be the most demanding and so, in defining experimental conditions, chief consideration is given to satisfying that particular objective.

The computer program PILOT was used to indicate typical distributions of the variables  $\theta_w$ ,  $C_p$  and  $\delta^*$  which might exist along a windtunnel wall when an aerofoil is being tested. It was apparent from the distributions that a particular value of  $\delta^*$  may only exist at one position along the liner during a given experiment. If the wall characteristic is to include significant information regarding crossflow at a particular value of  $\delta^*$ , then it would seem necessary that the particular  $\delta^*$  be in evidence in a number of experiments, but with different values of  $C_p$  and  $\theta_w$  associated with it in each case. The most simple method of achieving this, is to use differing suction or blowing rates from experiment to experiment. Thus the chosen value of  $\delta^*$  will be in existence at varying longitudinal positions on the liner and probably with differing associated values of  $C_p$  and  $\theta_w$ .

The transonic windtunnel used has two compressed air driven ejectors. One controls the pressure at the downstream end of the working section. This ejector has the major influence on the flow condition. The second ejector is used to evacuate the plenum chambers and so controls the suction or blowing rate at the perforated walls. The following approach is used to achieve the various flow conditions required. The main ejector is set at a fixed condition throughout the tests. The pressure in the diffuser at the downstream end of the working section is thus also fixed. Eight different settings of the secondary ejector are chosen to give conditions of suction and blowing through the perforated wall. Naturally, with a fixed pressure downstream and varying transpiration rates through



the wall, the upstream mass flow rate and thus static pressure must vary. Indeed, the Mach Number at entry to the working section varies from 0.63 (the case of maximum wall blowing) to 0.80 (the case of maximum suction), while the downstream Mach Number remains approximately 0.76. Under these conditions, no supersonic flow is present along the bottom perforated liner.

Static pressures measured at a tapping 109 mm upstream of the entry to the working section, on one sidewall, are used to determine freestream conditions. Based upon pressures measured there, the wall pressure coefficients ( $C_p$ ) along the bottom perforated liner remain almost exclusively between 0. and -0.2. However, the first 88 mm of the perforated liner is sealed and therefore the true working section commences somewhat downstream, where the contoured top liner has already produced a considerable pressure reduction in the flow. Relative to conditions at entry to the perforated section of windtunnel, the above pressure coefficient range is changed to -0.15 to +0.15. This range more than fulfills the requirements set out in Section (4.2.3).

For each of 5 longitudinal rake positions (ranging over a distance of 170 mm along the bottom liner), the eight flow conditions mentioned were established. Thus forty sets of data were obtained.

#### 4.3.2 Experimental Method.

Having specified the settings for the two windtunnel ejectors, the bulk of the experiments were then carried out. The rake position furthest upstream was still 50 mm downstream from the rear edge of the tape used to seal the graduated perforations at the working section entry. In this way it is hoped that the boundary layer profile, which may undergo rapid changes at the edge of the tape, will have settled before reaching the rake. At each longitudinal position, the foot of the boundary layer rake is arranged to be sited in a similar way relative to the surrounding perforations and particularly, relative to the nearest wall static tapping. It is expected that this approach will remove most of the effects that individual perforations may have on local flow parameters, at least when

those parameters are differentiated with respect to the longitudinal ordinate.

At each position chosen, the foot of the rake is jacked down using the mounting block mechanism, until it is firm on the wall of the windtunnel. The actual position of the foot relative to the local features of the wall is marked in Figure (34) as 'O'. This position is 22.5 mm to the port side of the relevant static tapping (there being no longitudinal displacement relative to the tapping) and 20 mm to port of the windtunnel centre line.

The tubes on the boundary layer rake, despite being quite flimsy, have been found to be disturbed only to a negligible extent during an operation of the windtunnel. As such, it was unnecessary to record the heights of each tube relative to the bottom wall before or after each operation of the windtunnel. However, once the rake device was firmly located in a chosen position, the heights of the following items were recorded using a travelling telescope. First, the tip of yawmeter Number 1 and the tail pin on the elbow of that yawmeter mounting. These two measurements permit the calculation of the incidence of the yawmeter reference line. Second, heights of the wall at the base of the boundary layer rake and the top tube on the rake were measured. All the other boundary layer tube heights are then calculated from these two, using measurements made previous to the experiments.

As close as possible to the time of operating the windtunnel, the atmospheric pressure and the mercury column attached to the pressure transducer are measured. The windtunnel is then started, and when it is likely that the air pressures in the instrumentation reservoirs have settled, the tube clamp is operated to isolate the instrumentation ducts from the working section. The windtunnel is then stopped. The 'Scanivalve' is then used to sample the air in each reservoir, as described in Section (4.2.7). The paper tape out-put, produced by the 'Creed' punch is finally retained for subsequent processing by computer.

During each experiment, the pressure distribution along the complete bottom wall of the working section was measured. However, it was not used



to provide the longitudinal derivatives of interest (such as  $\frac{dp_{\text{static}}}{dx}$ ). This pressure distribution would be different (even for identical ejector settings) for each longitudinal position of the rake. It was considered simpler to use only one local pressure (corrected for the effect of the flow field around the rake) for each longitudinal position of the rake. These were then combined to calculate the derivative mentioned. In the case of measured boundary layer displacement thickness, the above approach was necessary anyway as only the five discrete values of  $\delta^*$  were evaluated for each flow condition. In taking this approach, there is a slight loss of accuracy, as the precise local variation of parameters is not accounted for. However, it is not expected that this error will be very significant.

#### 4.3.3. Initial Analysis of Experimental Data.

This description is carried out in as practical a way as possible. The actual data referred to are shown in Table (5). For each approximate flow condition, data are shown for five longitudinal positions along the bottom liner.

The data are referred to by Column Number.

Initially, all pressure data are converted from transducer voltages to actual pressures using the transducer calibration equation (a typical example being Equation (2) of Appendix (8)). All pressures are then non-dimensionalized with respect to the highest pitot pressure recorded on the boundary layer rake for that particular operation of the windtunnel. Plenum pressures in this form are shown in Column (2). From the freestream reference pressure, measured 110 mm upstream of the start of the bottom liner, the value of the reference Mach Number  $M_\infty$  is calculated using isentropic relationships (Column (3)).

The static pressure measured alongside the rake tip is then corrected to represent the pressures at the foot of the rake and at the yawmeter tips. This is achieved using the simple corrections described in Appendix (7) and Equation (4) of that Appendix, namely



Col:-	1	2	3	4	5	6	7	8	9	10	11	12	13	14	15	16	17	18	19	20	21
Confid- interval symbol	X	$\frac{P_{VL}}{P_0}$	$M_{\infty}$	$\frac{P_S}{P_0}$	$\frac{\delta^*}{r_{min}}$	$\frac{\Delta P}{\rho a_1}$	$\theta/\theta_0$	$\theta/\theta_0$	$M_{\infty}$	$\frac{P_{VL}}{P_0}$	$\frac{P_S}{P_0}$	$\frac{\delta^*}{r_{min}}$	$\theta/\theta_0$	$C_p$	M	$\frac{\Delta P}{\rho a_1}$	$\frac{P_{UE}}{P_{\infty U_0}}$	$\frac{d\delta^*}{dx}$	*	$\tan \theta_e$	$\theta_m$
⊙	137½	0.7635	0.633	0.7525	1.836	0.06796	0.94	1.39		0.7607	0.7497	1.798	1.32	-0.05464	0.655	-0.04886	1.01549	0.00217	0.00121	0.02304	0.02208
	181	0.7601	0.638	0.7456	2.441	0.00470	1.57	1.81		0.7621	0.7452	2.471	1.84	-0.07554	0.662	-0.07341	1.02098	0.02740	0.00381	0.03213	0.00854
	223½	0.7597	0.639	0.7367	3.685	0.11481	2.03	2.50	0.636	0.7635	0.7363	3.839	2.62	-0.11679	0.676	-0.11122	1.03138	0.03848	0.00396	0.04576	0.01126
	266	0.7611	0.638	0.7280	5.364	0.11087	2.60	2.46		0.7635	0.7263	5.490	3.08	-0.16314	0.691	-0.15294	1.04261	0.03886	0.00386	0.05381	0.01881
	309	0.7604	0.637	0.7154	7.009	0.10425	1.76	2.29		0.7615	0.7138	7.154	2.27	-0.22107	0.711	-0.18880	1.05669	0.03886	0.00533	0.03964	0.00611
□	137½	0.7312	0.669	0.7272	1.459	0.04314	0.39	0.60		0.7284	0.7206	1.469	0.52	-0.071473	0.700	-0.03151	1.01935	0.00206	-0.00066	0.00908	0.00636
	181	0.7271	0.676	0.7199	1.774	0.06107	0.80	1.04		0.7295	0.7206	1.845	1.15	-0.07143	0.700	-0.03595	1.01920	0.01466	0.00140	0.02007	0.00681
	223½	0.7282	0.674	0.7139	2.506	0.07972	1.22	1.69	0.673	0.7296	0.7142	2.553	1.61	-0.10206	0.710	-0.06103	1.02560	0.01923	0.00144	0.02811	0.01082
	266	0.7301	0.673	0.705	3.708	0.10480	1.88	2.24		0.7286	0.7113	3.826	2.07	-0.11444	0.715	-0.06797	1.02826	0.02915	0.00183	0.03614	0.00882
	309	0.7271	0.678	0.6980	4.942	0.09201	1.48	2.01		0.7297	0.7008	4.909	2.06	-0.15978	0.731	-0.11019	1.03832	0.03030	0.00338	0.03597	0.00905
△	137½	0.7117	0.692	0.7061	1.395	0.01350	-0.24	0.21		0.7113	0.7047	1.370	0.18	-0.08706	0.725	-0.02544	1.02123	0.00250	-0.00013	0.00314	0.00051
	181	0.7077	0.697	0.7027	1.601	0.04928	0.55	0.79		0.7129	0.7043	1.623	0.77	-0.08871	0.716	-0.03311	1.02152	0.00856	0.00074	0.01344	0.00562
	223½	0.7127	0.692	0.7033	1.944	0.04324	0.42	0.89	0.692	0.7132	0.7002	2.114	1.16	-0.10554	0.732	-0.04948	1.02518	0.01653	0.00138	0.02025	0.00510
	266	0.7176	0.685	0.7032	3.082	0.09182	1.48	1.84		0.7127	0.6990	2.438	1.58	-0.11047	0.734	-0.05197	1.02610	0.02242	0.00083	0.02758	0.00599
	309	0.7165	0.688	0.6965	4.204	0.07944	1.21	1.73		0.7135	0.6892	3.936	1.62	-0.15072	0.749	-0.08977	1.03462	0.02381	0.00046	0.02828	0.00543
∅	137½	0.6861	0.719	0.6825	1.254	0.00217	-0.45	-0.74		0.6845	0.6795	1.271	-0.25	-0.10756	0.764	-0.01801	1.02352	0.00086	-0.00232	-0.00436	-0.00204
	181	0.6814	0.727	0.6707	1.352	0.00913	-0.30	-0.06		0.6868	0.6769	1.376	0.21	-0.11766	0.768	-0.03542	1.02550	0.00444	-0.00032	0.00367	-0.00445
	223½	0.6804	0.730	0.6738	1.560	0.01861	-0.10	0.37	0.721	0.6881	0.6771	1.646	0.55	-0.11688	0.767	-0.03938	1.02531	0.01020	-0.00060	0.00960	-0.00066
	266	0.6850	0.712	0.6886	2.252	0.04927	0.56	0.91		0.6887	0.6772	2.162	0.90	-0.11649	0.767	-0.04118	1.02517	0.01190	0.00086	0.01571	0.00467
	309	0.6872	0.713	0.6803	2.341	0.07446	0.03	0.55		0.6874	0.6711	2.686	0.71	-0.14018	0.777	-0.05749	1.02971	0.01294	-0.00057	0.01234	-0.00117
∅	137½	0.6665	0.740	0.6624	1.242	-0.01308	-0.77	-0.56		0.6628	0.6586	1.212	-0.52	-0.12554	0.796	-0.01438	1.02477	-0.00086	-0.00247	-0.00908	-0.00575
	181	0.6641	0.744	0.6567	1.249	0.00747	-0.34	-0.10		0.6649	0.6548	1.234	-0.18	-0.13910	0.802	-0.03427	1.02721	0.00256	-0.00040	-0.00314	-0.00530
	223½	0.6597	0.752	0.6561	1.448	0.00746	-0.34	0.14	0.744	0.6673	0.6584	1.388	0.14	-0.12618	0.796	-0.03045	1.02494	0.00463	-0.00070	0.00244	-0.00289
	266	0.6745	0.738	0.6673	1.887	0.03101	0.16	0.52		0.6686	0.6596	1.725	0.40	-0.12181	0.794	-0.03088	1.02414	0.00812	0.00086	0.00697	-0.00114
	309	0.6618	0.748	0.6561	1.905	0.00543	-0.61	-0.08		0.6647	0.6608	1.898	-0.08	-0.11734	0.792	-0.01342	1.02338	0.00086	-0.00036	-0.00140	-0.00456
Δ	137½	0.6438	0.763	0.6454	1.127	-0.01987	-0.91	-0.46		0.6454	0.6417	1.162	-0.68	-0.14052	0.822	-0.01219	1.02528	-0.00204	-0.00152	-0.01187	-0.00831
	181	0.6436	0.765	0.6385	1.097	-0.00718	-0.64	-0.40		0.6468	0.6383	1.141	-0.42	-0.15280	0.827	-0.02780	1.02716	0.00200	-0.00016	-0.00733	-0.00949
	223½	0.6533	0.760	0.6483	1.249	0.00333	-0.38	0.09	0.762	0.6501	0.6444	1.219	-0.15	-0.13077	0.818	-0.01884	1.02385	0.00342	-0.00122	-0.00227	-0.00691
	266	0.6520	0.762	0.6447	1.561	0.01290	-0.22	0.13		0.6512	0.6470	1.459	0.03	-0.12138	0.814	-0.01400	1.02237	0.00356	-0.00121	-0.00052	-0.00425
	309	0.6440	0.762	0.6412	1.442	0.03536	-1.25	-0.72		0.6452	0.6579	1.406	-0.66	-0.08200	0.797	-0.04340	1.01571	-0.00505	-0.00492	-0.01152	-0.01139
▽	137½	0.6231	0.787	0.6202	1.070	-0.02921	-1.10	-0.80		0.6336	0.6301	1.120	-0.76	-0.15123	0.840	-0.01125	1.02540	-0.00253	-0.00152	-0.01327	-0.00922
	181	0.6379	0.771	0.6354	1.107	-0.00842	-0.67	-0.43		0.6340	0.6280	1.082	-0.54	-0.15387	0.843	-0.01920	1.02645	0.00081	-0.00119	-0.00943	-0.01143
	223½	0.6386	0.772	0.6378	1.282	0.01596	-0.16	0.32	0.774	0.6381	0.6357	1.108	-0.29	-0.13140	0.851	-0.00780	1.02766	0.00200	-0.00083	-0.00506	-0.00799
	266	0.6380	0.774	0.6398	1.239	0.04949	-0.14	0.14		0.6385	0.6396	1.306	-0.20	-0.11754	0.845	-0.00361	1.02062	0.00316	-0.00291	-0.00349	-0.00956
	309	0.6323	0.771	0.6446	1.174	-0.05227	-1.61	-1.08		0.6311	0.6594	1.139	-1.00	-0.04675	0.794	-0.04777	1.00875	-0.01099	-0.00609	-0.01746	-0.01256
Δ	137½	0.6161	0.789	0.6162	1.040	-0.04445	-1.35	-0.90		0.6168	0.6133	1.041	-0.85	-0.16889	0.866	-0.01088	1.02511	-0.00167	-0.00005	-0.01484	-0.01332
	181	0.6217	0.784	0.6192	1.034	-0.00539	-1.02	-0.78		0.6148	0.6149	0.995	-0.85	-0.16137	0.863	-0.00031	1.02451	-0.00025	-0.00093	-0.01135	-0.01203
	223½	0.6210	0.789	0.6184	1.046	-0.00720	-0.64	-0.17	0.791	0.6200	0.6244	0.938	-0.48	-0.12861	0.868	-0.01398	1.02044	0.00025	-0.00112	-0.00838	-0.00975
	266	0.6067	0.800	0.6250	1.132	-0.01800	-0.87	-0.51		0.6184	0.6312	1.107	-0.50	-0.10517	0.838	-0.04059	1.01723	0.00204	-0.00507	-0.00873	-0.01584
	309	0.6105	0.790	0.6719	0.843	-0.06553	-1.89	-1.37		0.6094	0.6679	0.844	-1.37	-0.02138	0.782	-0.20471	0.99561	-0.01101	-0.00509	-0.02392	-0.01900
Probable error	0.0002	0.0002	0.002	0.0015	0.011	0.0064	0.23	0.23	—	0.0002	0.0015	0.011	0.23	0.00057	0.002	0.00798	0.0013	0.0024	0.00003	0.0027	0.0037

$$* = (1 - \delta^*) \left( \frac{P_{\infty U_0}}{P_0} \right) \left( \frac{P_{UE}}{P_{\infty U_0}} \right)$$

TABLE (5)

Data reduced from  
main experiments.



$$\left(\frac{P_s}{P_o}\right)_{\text{CORR.}} = \left(\frac{P_s}{P_o}\right)_{\text{UNCORR.}} + \Delta C_p \frac{\gamma}{2} \frac{P_\infty}{P_o} M_\infty^2.$$

However, in the present use of this equation, it was considered more accurate to use local values of static pressure and Mach number, rather than freestream values, because the simple corrections assume that the only disturbing influence in the flow, from the freestream, is that of the rake. In the present case of course, the freestream condition may be considerably different from the conditions in the flow just ahead of the rake. Values of the static pressure corrected to the position at the foot of the rake are shown in Column (4).

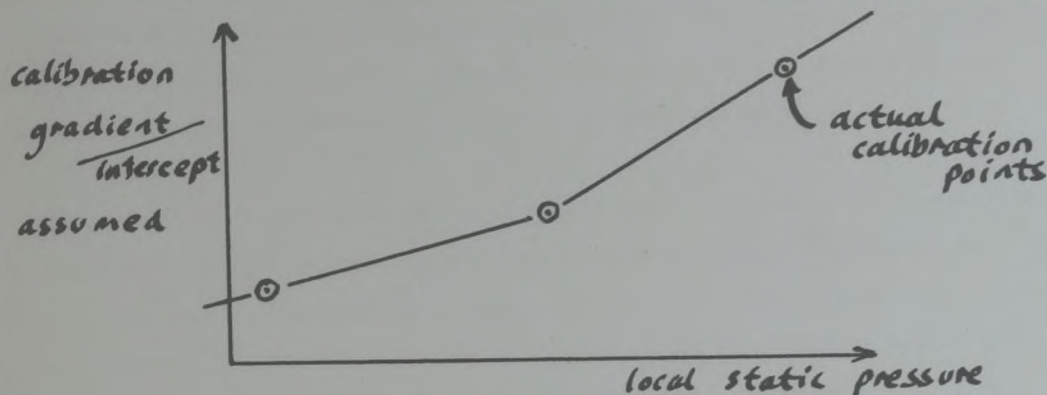
This static pressure, together with the pitot pressures measured on the boundary layer rake, are then used to calculate the characteristics of the boundary layer. This is done using a computer program entitled 'PROF'. This program is described briefly in Appendix (9). The chief parameter of interest is the displacement thickness ( $\delta^*$ ) which is listed in Column (5). The majority of values of  $\delta$  (the boundary layer thickness) are less than 20 mm. Only in one case did the value of  $\delta$  reach 22 mm. Thus yawmeter Number 1, which is approximately 20 mm above the wall never dips more than about 10% into the boundary layer. On the basis of the argument in Appendix (5), it is then permissible to use all flow angles measured with this yawmeter.

The flow angle at the yawmeters, relative to the wall is calculated in the following manner. The non-dimensional difference in pressure measured across the yawmeter head is calculated as

$$\frac{\Delta p}{q} = \left(\frac{P_1}{P_o} - \frac{P_2}{P_o}\right) / \left(\frac{P_s}{P_o}\right)_{\text{CORR.}} \cdot \left(\frac{\gamma}{\gamma-1}\right) \cdot \left(\left(\frac{P_s}{P_o}\right)_{\text{CORR.}}^{\frac{1-\gamma}{\gamma}} - 1\right) \quad (4.6)$$

(Equation (5) of Appendix (7)). Here,  $P_1$  and  $P_2$  are the pressures measured on the lower and upper surfaces of the yawmeter head respectively. These values of  $\frac{\Delta p}{q}$  for yawmeter Number 1 are shown in Column (6). For the reasons described in Section (4.2.6), no data from yawmeter Number 2

are presented or discussed. The yawmeter calibration given in Table (4) is used to obtain values of the flow angle relative to the yawmeter reference line, from the calculated  $\frac{\Delta p}{q}$  data. In Table (4), the gradient (m) and intercept (c) of the calibration are specified for three local static pressures. There appears to be a trend in the calibration with static pressure and some account is taken of this by allowing a linear variation of the gradient and intercept between successive static pressure. This is illustrated below.



The predicted flow angles are shown in Column (7). The heights of the tip of yawmeter Number 1 and the tailpin on the rake, measured in the experiments, are used to calculate the angle of the yawmeter reference line relative to the horizon. Combining these angles (which are usually less than  $0.5^\circ$ ) with those in Column (7) permits the calculation of the angle of the flow at the yawmeter relative to the horizon. Before the flow angle relative to the wall can be evaluated, the angle of the wall relative to the horizon must be known. The height of the wall was measured at a number of positions along its centre-line. These were then used to estimate the angle of the wall at the positions required. Naturally it is intended that the wall be flat and horizontal. Indeed the angle of the wall is small, not much greater than  $0.1^\circ$  at any point. However, the correction is still made. The final flow angle relative to the wall ( $\theta_e$ ) is shown in Column (8).

So far, in this description of the data analysis, no mention has been made of the repeatability of the windtunnel results. This is because it has not been necessary yet to link data from one operation of the wind-tunnel with that from any other operation. The freestream reference Mach

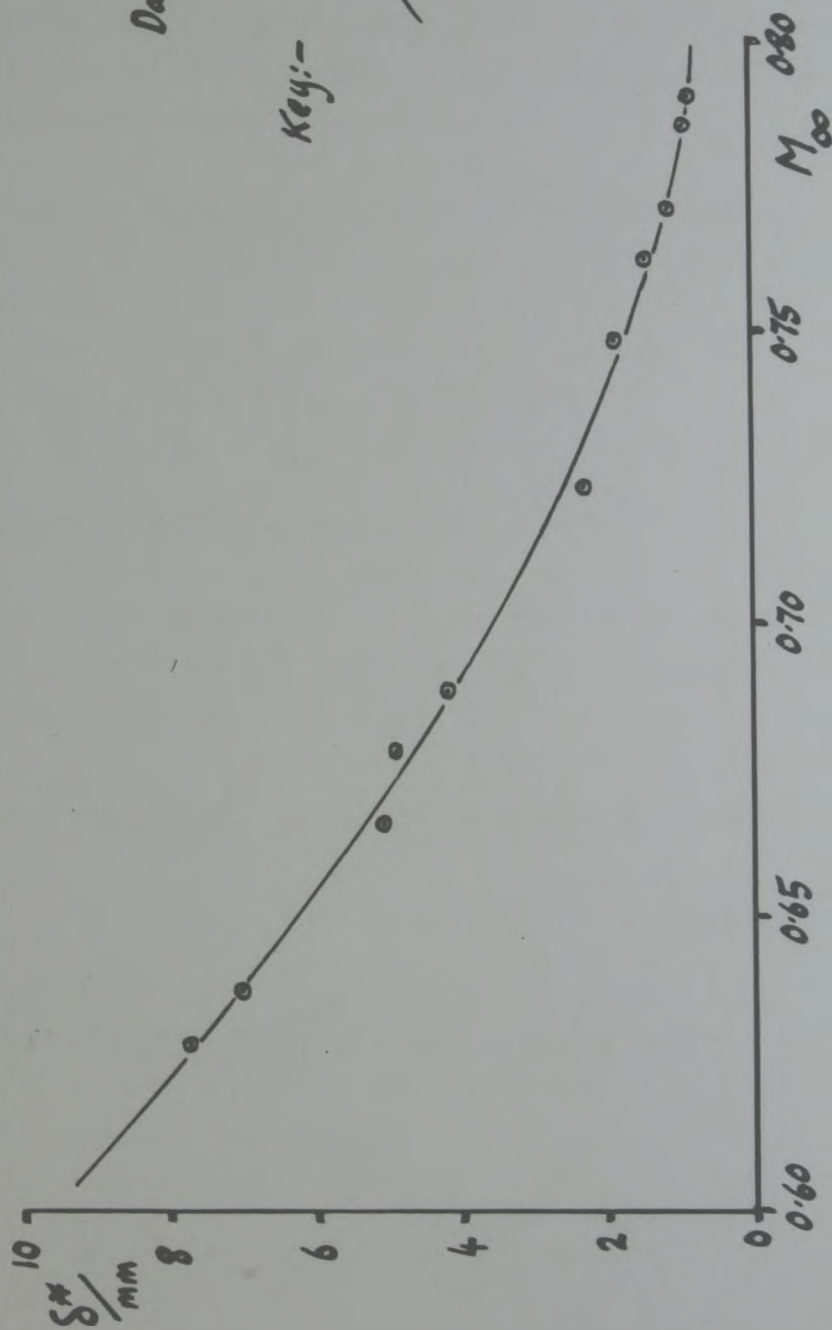


Number ( $M_{\infty}$ ) is chosen as an indicator of repeatability. In Column (3) the values of  $M_{\infty}$  can be seen to vary within each 'configuration' group, though it is intended that this should not be the case. In one case the variation in  $M_{\infty}$  within a group is as much as 0.02. Such a variation would significantly affect measured properties at any given position in the working section, for example  $\delta^*$  could be affected by as much as 20% for positions towards the downstream end. This value is drawn from Figure (36). This Figure shown calculated values of  $\delta^*$ , plotted against respective values of the freestream Mach Number for the rake position 309 mm downstream of the start of the bottom wall. It is not implied here that  $\delta^*$  is directly dependant upon  $M_{\infty}$ , but that for the experiments concerned the two variables are to some extent correlated.

To correct the experimental data to a set of prescribed freestream Mach Numbers, the relationships between the variables  $P_{p1}/P_0$  (Col. 2),  $P_{p2}/P_0$  (Col. 4),  $\delta^*$  (Col. 5) and  $\theta_e$ , (Col. 8) and the freestream Mach Number,  $M_{\infty}$  (Col. 3) are fitted to third or fourth order polynomials, for each longitudinal position of the rake. The decision between a third or fourth order polynomial was made purely on the basis of which gave the closer fit to the data. In Figure (36) the predicted relationship between  $\delta^*$  and  $M_{\infty}$  is shown as a continuous line on the graph. In this case at least, which is typical, one would feel confident about using the fitted curve. It is almost certain that all the relationships fitted are in reality monotonic, and it is hoped that the use of such high order polynomials will serve only to improve the closeness of the data fit, rather than artificially alter the entire character of the relationships.

Before it was possible to use the calculated relationships to predict corrected data, it was necessary to specify a set of freestream conditions. This was done by taking an average freestream Mach Number from each configuration group. This would then minimise the magnitude of the corrections which were effectively applied to each variable. These Mach Numbers (which are shown in Column (9)) were supplied directly to the fitted polynomials to generate values of  $P_{p1}/P_0$ ,  $P_{p2}/P_0$ ,  $\delta^*$  and  $\theta_e$  (Columns 10 - 13 respectively).

To calculate values of the wall pressure coefficient,  $C_p$ , the following



Graph of  $S^*$  with  $M_{\infty}$  for experimental data obtained at  $X=309\text{ mm}$ .

FIGURE(36)



expression is used.

$$C_p = \left( \frac{P_s}{P_0} - \frac{P_{\infty}}{P_0} \right) / \frac{\gamma}{2} \cdot \frac{P_{\infty}}{P_0} \cdot M_{\infty}^2 \quad (4.7)$$

In this equation,  $\frac{P_{\infty}}{P_0}$  is calculated from  $M_{\infty}$  using isentropic relationships. Values for  $\frac{P_s}{P_0}$  and  $M_{\infty}$  are taken from Columns (11) and (9) respectively. The calculated values of  $C_p$  are shown in Column (14). From the data in Column (11), values of the local wall Mach Number,  $M$  (Col. 15) are calculated, again using isentropic relationships.

The local non-dimensional pressure difference across the perforated wall,  $\frac{\Delta p}{q}$ , is calculated from data in Columns (11), (14) and (15) using the expression,

$$\frac{\Delta p}{q} = \left( \frac{P_s}{P_0} - \frac{P_{pl}}{P_0} \right) / \frac{\gamma}{2} \cdot \frac{P_s}{P_0} \cdot M^2 \quad (4.8)$$

This is then displayed in Column (16).

The last major parameter to be calculated is the average crossflow in the viscous flow at the wall position ( $\Theta_w$ ). To calculate this, Equation (3.1) namely

$$(L - \delta^*) \frac{d(\rho_e u_e)}{dx} - \rho_e u_e \cdot \frac{d\delta^*}{dx} + \rho_e v_e - \rho_w v_w = 0$$

is used. By dividing all terms in the equation by  $\rho_e u_e$ , it becomes

$$\frac{(L - \delta^*)}{\rho_e u_e} \cdot \frac{d(\rho_e u_e)}{dx} - \frac{d\delta^*}{dx} + \frac{\rho_e v_e}{\rho_e u_e} - \frac{\rho_w v_w}{\rho_e u_e} = 0.$$

After re-arrangement, this becomes

$$\frac{\rho_w v_w}{\rho_e u_e} = \frac{v_e}{u_e} + \frac{(L - \delta^*)}{\rho_e u_e} \cdot \frac{d(\rho_e u_e)}{dx} - \frac{d\delta^*}{dx}. \quad (4.9)$$

The term on the lefthand side of this equation is equivalent to the required crossflow parameter,  $\Theta_w$ . Also the first term on the righthand

side is related to the previously calculated  $\theta_e$ , in the following way.

$$\frac{V_e}{u_e} = \tan \theta_e \quad (4.10)$$

In order to calculate the terms on the right hand side of Equation (4.9), which contain  $\rho_e u_e$ , use is made of the freestream condition  $\rho_\infty u_\infty$ . Local edge conditions are related to freestream conditions by the non-dimensional parameter;  $\frac{\rho_e u_e}{\rho_\infty u_\infty}$ . Re-writing Equation (4.9) and incorporating Equation (4.10) and the change mentioned,

$$\theta_w = \tan \theta_e + (L - \delta^*) \cdot \left( \frac{\rho_\infty u_\infty}{\rho_e u_e} \right) \cdot \frac{d}{dx} \left( \frac{\rho_e u_e}{\rho_\infty u_\infty} \right) - \frac{d\delta^*}{dx}. \quad (4.11)$$

It now remains to calculate the parameter  $\left( \frac{\rho_e u_e}{\rho_\infty u_\infty} \right)$  in terms of known variables. This is performed in Appendix (10). Using Equation (7) and (8) of that Appendix, it can be written that

$$\left( \frac{\rho_e u_e}{\rho_\infty u_\infty} \right) = \left( \frac{\rho_e}{\rho_\infty} \right)^{\frac{1}{\gamma}} \cdot \left\{ 1 - \tan^2 \theta_e - \left[ \left( \frac{\rho_e}{\rho_\infty} \right)^{\frac{\gamma-1}{\gamma}} - 1 \right] \cdot \frac{2}{(\gamma-1)} \cdot \frac{1}{M_\infty^2} \right\}^{\frac{1}{2}}, \quad (4.12)$$

where

$$\left( \frac{\rho_e}{\rho_\infty} \right) = \left( \gamma \cdot \frac{\gamma}{2} \cdot M_\infty^2 + 1 \right) \quad (4.13)$$

Using the relevant data from the Table, and these two equations, values of  $\left( \frac{\rho_e u_e}{\rho_\infty u_\infty} \right)$  are calculated and displayed in Column (17).

The values of  $L$  (the distance between the wall and the 'edge' line; in our case the tip of the yawmeter) measured during experiment are used directly in Equation (4.11). Unfortunately, for the most upstream position of the rake, the experiments were carried out in three separate groups. As such, three slightly different values of  $L$  apply. In the calculations, an average value of  $L$  is used and the maximum error in  $\theta_w$  caused by this never exceeds  $0.01^\circ$ , which clearly is acceptable.

A graphical approach is used to calculate the two derivatives in Equation (4.11). In Figure (37), the distributions of  $\delta^*$  (Col. 12) in



Graph of boundary layer displacement thickness with longitudinal position - experimental results.

See Table(5) for Key

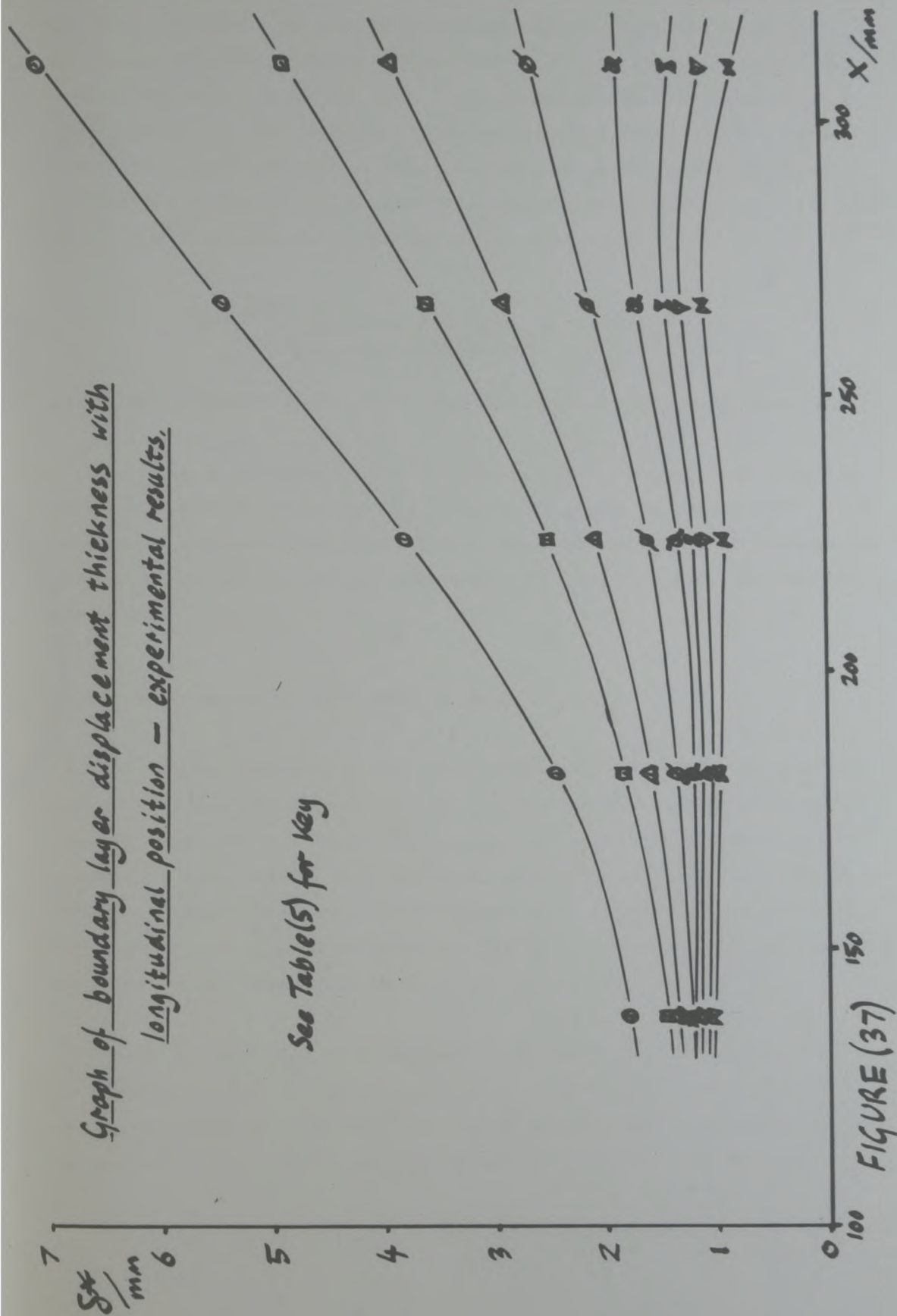


FIGURE (37)

the longitudinal direction for the eight flow configurations are shown. The various symbols used to identify the curves are also shown on Table (5) for reference. At each of the longitudinal positions where data are specified, the gradient of the curves is calculated by hand. The results are shown in Column (18). In a similar manner, the values of  $\frac{\rho_e u_e}{\rho_w u_w}$  (Col. 17) are shown as distributions in x (Col. 1) for the eight conditions, in Figure (38). The gradients of these curves are also calculated. These are then multiplied by the respective values of  $\frac{\rho_w u_w}{\rho_e u_e}$  and  $(L - \delta^*)$  and the final values of the function

$$(L - \delta^*) \cdot \left( \frac{\rho_w u_w}{\rho_e u_e} \right) \cdot \frac{d}{dx} \left( \frac{\rho_e u_e}{\rho_w u_w} \right)$$

are shown in Column (19). In Column (20), values of  $\tan \theta_e$  are shown.

The data in Columns (18), (19) and (20) are then used in Equation (4.11) to provide values of  $\theta_w$ , which are shown in Column (21). This final step concludes the initial data analysis required, to provide information for use in the wall characteristic and the programs PREDICT and PILOT.

#### 4.3.4 Accuracy of Experimental Data.

The errors involved in the main results calculated in the previous sub-section are now estimated. In contrast to the rather crude approach taken in Appendix (8) in predicting the errors in the yawmeter calibration, a somewhat more careful and realistic method is adopted here. It is not however, claimed that the present approach is exhaustive or precise. For example, no account is taken of any errors incorporated in the results, when the major 'freestream Mach Number correction' is made.

It is assumed that in each basic experimental observation, an error is incorporated which would be normally distributed about the true value of the observation. In addition, it is assumed that all errors are uncorrelated. This latter assumption may in certain cases be false.

Using the assumption of a normal distribution of errors, a standard



$\frac{\rho_{e4e}}{\rho_{\infty 4\infty}}$   
 1.07  
 1.06  
 1.05  
 1.04  
 1.03  
 1.02  
 1.01  
 1.00  
 0.99

Graph of  $\frac{\rho_{e4e}}{\rho_{\infty 4\infty}}$  with longitudinal position - experimental results.

See Table(5) for key

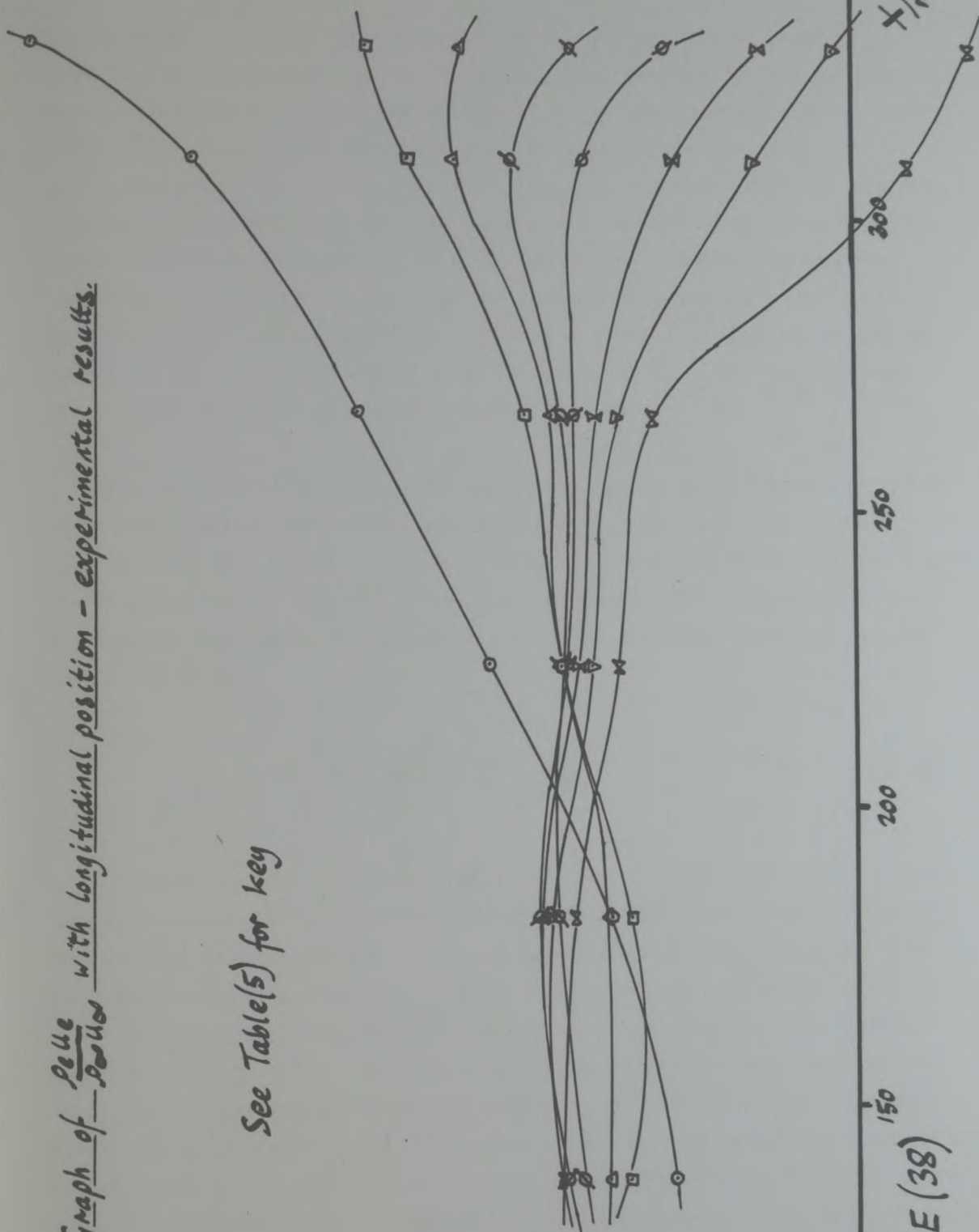


FIGURE (38)

deviation,  $\sigma$ , is used for each observation and calculated result. According to the properties of the normal distribution, it can be stated that a value has a probability of 95% of being within  $1.96\sigma$  of the true figure. In Appendix (8) the approach of worst errors was used. It is now assumed that the 'worst errors' quoted for the basic data in Appendix (8) represent  $1.96\sigma$ , or that the errors are, in fact, 95% certain to be better than those quoted. Hence a set of values for  $\sigma$  are calculated for these basic data. It can also be deduced from the properties of the normal distribution that results have a probability of 50% of being closer to the true values than an error of  $0.677\sigma$ . One may say that the probable error in a result is equal to  $0.677\sigma$ .

From the raw data state, the calculation procedure of Section (4.3.3) is followed and at each stage the standard deviations of the various data are combined in an appropriate manner (Bevington, 1969, Chapter 4.). For example, when a result (x say) is calculated from a function of two independent variables (u and v say), then the standard deviation of the result ( $\sigma_x$ ) is

$$\sigma_x = \left\{ \sigma_u^2 \left( \frac{\partial x}{\partial u} \right)^2 + \sigma_v^2 \left( \frac{\partial x}{\partial v} \right)^2 \right\}^{\frac{1}{2}}. \quad (4.14)$$

In Equation (4.14) it may be that the derivatives shown, will depend upon the values of u and v themselves. In the calculation of standard deviations, typical values of the independent variables are used. The standard deviations of error of most of the raw data are shown in Table (6) with brief explanation where appropriate. Some items need perhaps further clarification. The value of  $\sigma$  quoted for the predicted inviscid flow angle  $\theta_{rym}$  (relative to the yawmeter) of  $0.19^\circ$  is taken from the short discussion at the end of Section (4.2.6). The extra component of error added to the values of  $\sigma$  for the boundary layer displacement thickness and the local static pressure are intended to represent the increased uncertainty caused by the three-dimensional effects described in Section (4.2.8). These effects may not be swept along the perforated wall, parallel to the axis of the working section, but may wander sideways. For example in Figure (35), it is assumed that the change in  $\delta^*$  due to an effective 6.5 mm lateral movement of the rake is incorporated, namely



VARIABLE	ERROR ASSUMED	COMMENTS
DIGITAL VOLTMETER READING (V)	$0.5 \times 10^{-5}$ VOLT 0.5 DIGITS	
TRANSDUCER CALIB- RATION CONSTANTS. A B	0.0238 ( $\sigma$ ) 10 ( $\sigma$ )	TYPICAL VALUES:- A = 31.5 Pa volt <sup>-1</sup> ( $\times 10^{-5}$ ) B = 85300 Pa.
ALL MEASURED HEIGHTS.	0.016 ( $\sigma$ ) mm	
NON-DIMENSIONALIZED STATIC PRESSURE $\frac{P_s}{P_o}$	0.0025 (worst) 0.001 (worst) 0.001 (worst) 0.0015 ( $\sigma$ )	DUE TO PRESSURE DISTRIBUTION CAUSED BY INDIVIDUAL PERFORATIONS. ASSUMED ERROR IN RAKE INTERFERENCE CORRECTION. ERROR DUE TO THREE-DIMENSIONAL EFFECTS. APPROXIMATE TOTAL ERROR.
BOUNDARY LAYER DISPLACEMENT THICK- NESS $\delta^*$	0.12 (worst) mm 0.10 (worst) mm 0.11 ( $\sigma$ ) mm	DUE TO DATA ANALYSIS DUE TO THREE-DIMENSIONAL EFFECTS. APPROXIMATE TOTAL ERROR.
ANGLE CALCULATED DIRECTLY FROM YAWMETER CALIBR- ATION $\theta$	0.19 ( $\sigma$ )°	

$\sigma$  - STANDARD DEVIATION ERROR

TABLE(6) Uncertainties in basic experimental data.

Values of the standard deviation and probable error in results are shown at the base of the data columns in Table (5). Notably, the standard deviation for the calculated flow angle relative to the wall,  $\theta_w$ , is not much greater than the starting value from the calibration of  $0.19^\circ$ , at  $0.23^\circ$ . This is encouraging for future work where the initial value of  $0.19^\circ$  may be reduced significantly.

In calculating the value of  $\sigma$  relevant to the final parameter  $\theta_w$ , considerable effort was involved. The complexity of processing the standard deviations through Equation (4.11) caused this difficulty. For the critical variables, a range of typical values was used to ensure that strange properties of the equation would not cause an otherwise undetected increase in possible error. Not surprisingly, the most significant contributions to the value of  $\sigma$  for  $\theta_w$  of  $0.0054$  (or  $0.31^\circ$ ) come from  $\frac{\sigma_{v_e}}{u_e}$  and from  $\frac{\sigma_{16''}}{2x}$ . Clearly these terms will need to be improved before a significant reduction in  $\sigma_{\theta_w}$  can be achieved. As it is mentioned in Appendix (7), there is obvious room for improvement in the yawmeter calibration. However, it is not so clear how the evaluation of  $\delta^*$  can be carried out with significantly improved accuracy, as errors in this parameter come either from three-dimensional effects or from the result of calculating the boundary layer displacement thickness from erroneous pressure data; data which cannot apparently be easily improved. However as it was pointed out at the beginning of this sub-section, the present analysis of errors may still be too severe and, for example, pressure data used to evaluate  $\delta^*$  may be correlated such as to remove some of the errors assumed.

From Figure (35) it is clear that the rake mounting position was over the edge of a longitudinal web under the perforated wall. This could alter some of the parameters of interest which are derived from experiment (such as  $\theta_w$  and  $\delta^*$ ). However, so far as the overall scheme of this work is concerned, the affected results may be considered merely to represent those from a perforated wall with altered properties; perhaps with an increased resistance to crossflow. If the scheme in general (and the computer program PREDICT in particular) manages to prove successful under such conditions, there is no reason why it should not also prove successful given more favourable conditions.



#### 4.3.5 Discussion of Experimental Results

The results from the main experiments are discussed here from two points of view. Firstly, they are used to explain the overall nature of the flow in the perforated working section with the contoured top wall fitted. Secondly, they are discussed with respect to local variations of parameters and interrelation of parameters. The two discussions generally run concurrently through the text.

During the investigation into the three-dimensional effects in the working section (described in Section 4.2.8), a static rake with very elongated rake tubes was used. This was mounted near the bottom wall but, when in its rearmost position would cause little disturbance along that wall. The longitudinal distribution of pressure measured on the perforated wall is shown in Figure (39). The working section is considered under these conditions to be effectively empty. Prior to the upstream end of the perforated section of wall, a region of acceleration, probably due to the opposite contoured wall exists. The pressure distribution in the perforated section will also be influenced by the contoured wall, but the effects of transpiration prevent a simple explanation of the flow in this region (where it is considered likely that outflow exists). For the flow with a freestream Mach Number of 0.84, a region of supersonic flow exists along the wall. During this experiment, use of a Schlieren system revealed a shock wave in this region which emanated from the contoured wall. It is almost certain that this wall produced a large region of supersonic flow which reached to the bottom wall. In Section (4.2.8), regions of severe conditions at the beginning and end of the perforated wall were discussed. Such regions also appear to be present in the graphs in Figure (39). For the highest speed case, there appears to be a 'convex corner' flow on entry and for the low speed case a 'concave corner' flow on exit. The perforated wall, which normally terminates as a trailing edge in the diffuser was for these tests, effectively solid for the final centimetre or so. It is considered that this condition causes the particular corner flow experienced on exit from the working section.

When the combined boundary layer rake is installed in the windtunnel

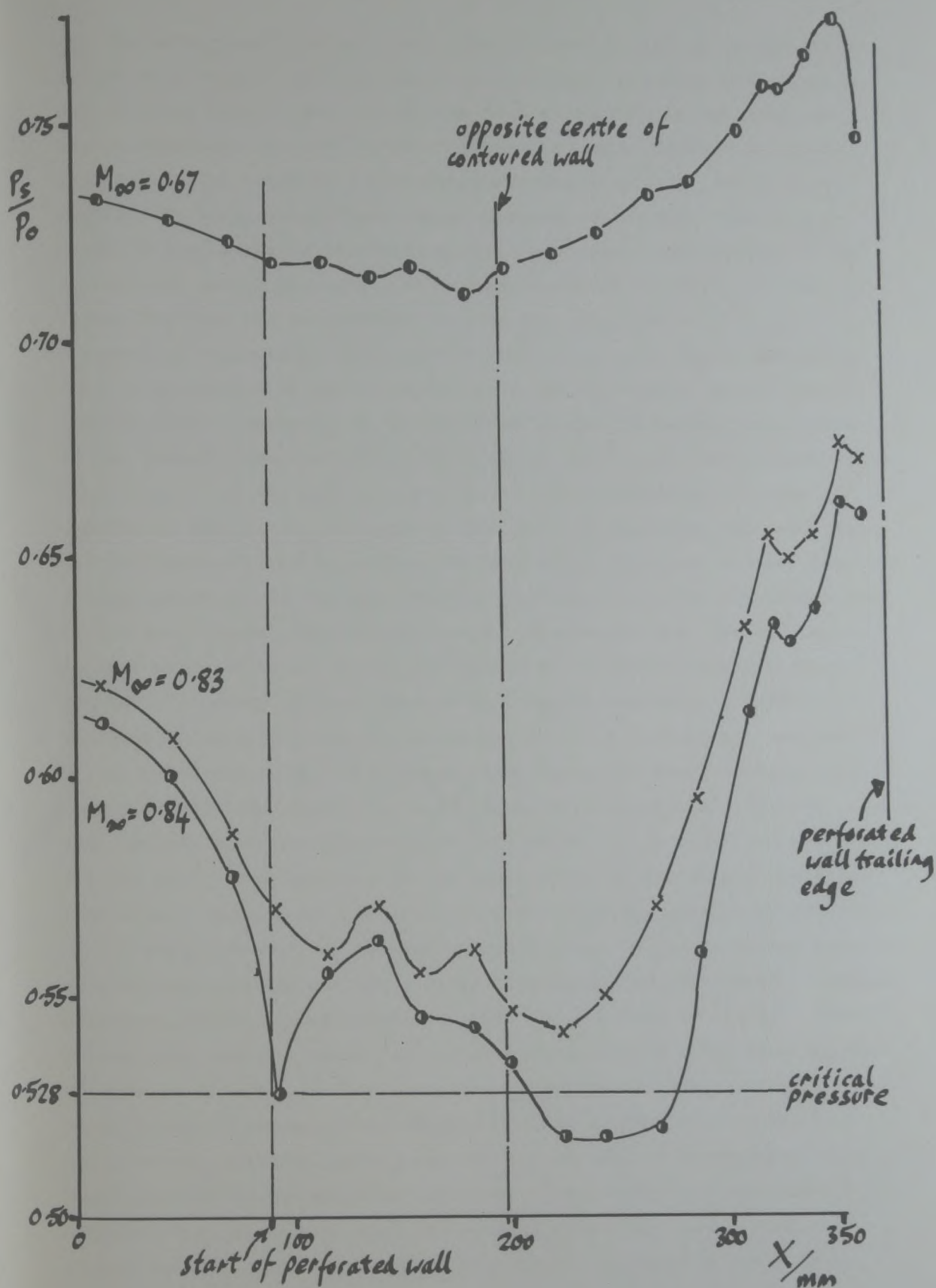
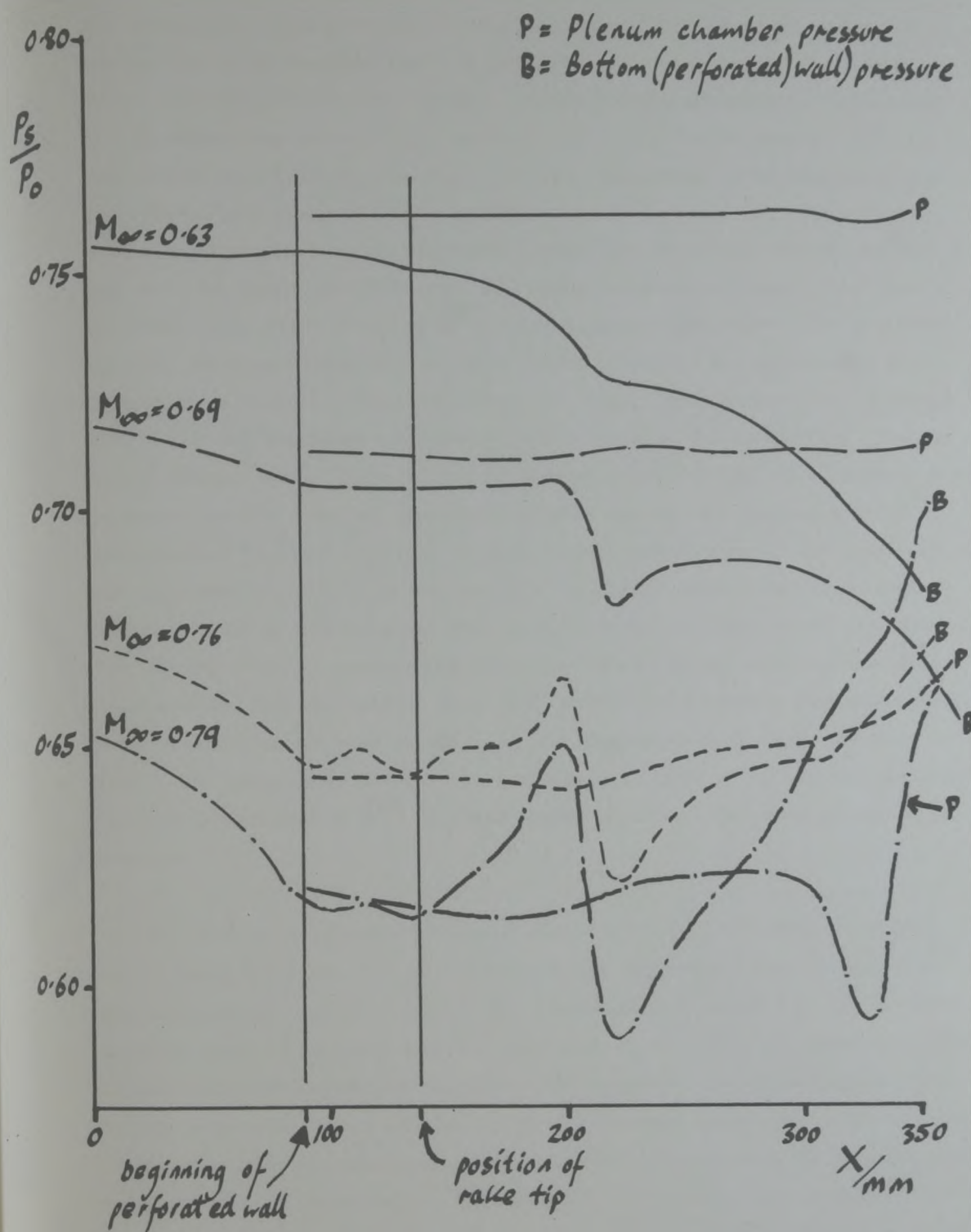


FIGURE (39) Pressure distributions along perforated wall - opposite wall contoured, no rake mounted.



for the main group of experiments, the pressure distribution along the bottom wall changes considerably. Some of these pressure distributions are shown in Figure (40). Here, the rake is mounted in its most upstream position. It may be recalled that, at each longitudinal position, eight flow conditions were generated and measured. The data in Figure (40) indicate the full range of these conditions. The disturbance in the centre of the working section in each distribution is due to the side arm of the rake. This runs laterally out from the main supporting tube and is circular in section. It gives rise to a compression followed by an expansion along the wall. This disturbance (not surprisingly) increases severely as the local Mach Number rises towards unity. However, at the position of the tip of the rake (marked in the Figure), the disturbance in pressure due to the rake is encouragingly small. In the perforated section, the presence of the rake appears to affect the pressures sufficiently to hide the influence due to the contoured wall opposite. The variation of plenum chamber pressure is also shown in the Figure. For the configuration with the lowest free-stream Mach Number, the plenum pressure is greater than the working section pressure by an amount sufficient to initiate blowing through the wall. Clearly, moving downstream, the blowing process reduces the working section pressure and causes air to flow into the windtunnel at an increasing rate. This takes place along the whole working section length despite the shape of the contoured wall which would tend to increase the pressure downstream of its crest (which is at the position,  $x = 197$  mm). The opposite effect takes place in the curves for free-stream Mach numbers of 0.76 and 0.79 where (besides the localized effect of the rake) the working section pressure rises above the plenum pressure, causing accelerating outflow. It is interesting to note that the plenum pressures remain almost constant except for the case of highest free-stream Mach number. There, at the downstream end of the plenum chamber, it appears that the outflow is strong enough to actually affect the local static pressure. This could be due to a rough 'jet' under the wall, turning sharply against the downstream wall of the chamber to pass back upstream to the auxiliary ejector. The strong flow curvature combined with high speed flow there could cause the sudden rise in plenum pressure, if not the fall in pressure immediately prior to it.

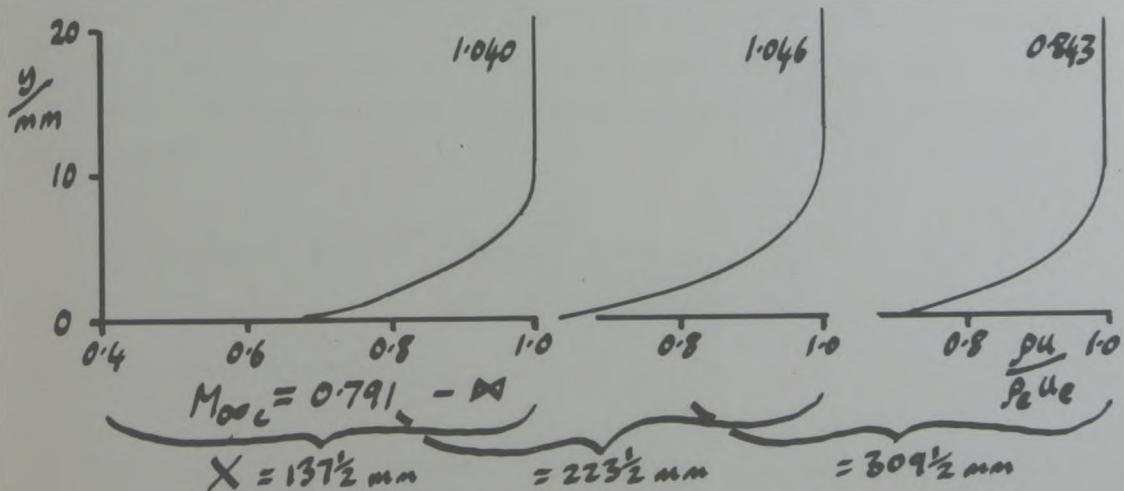
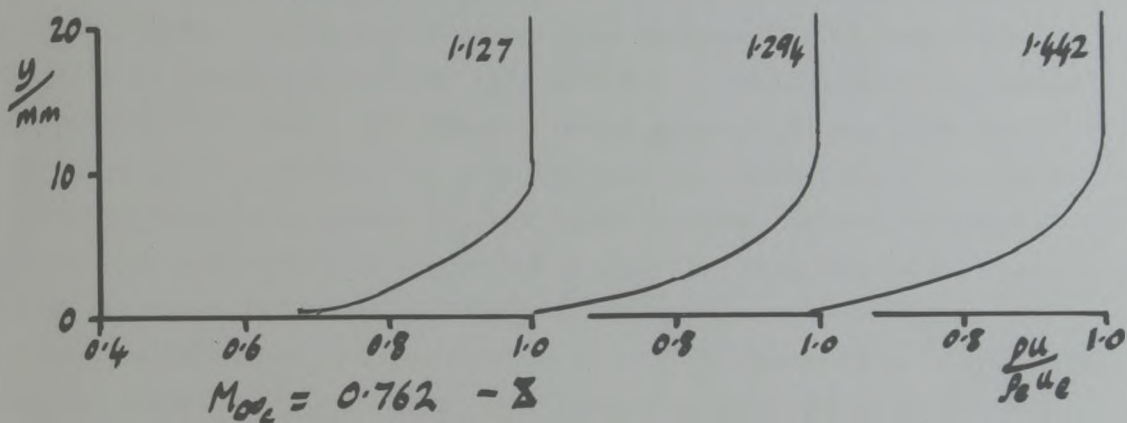
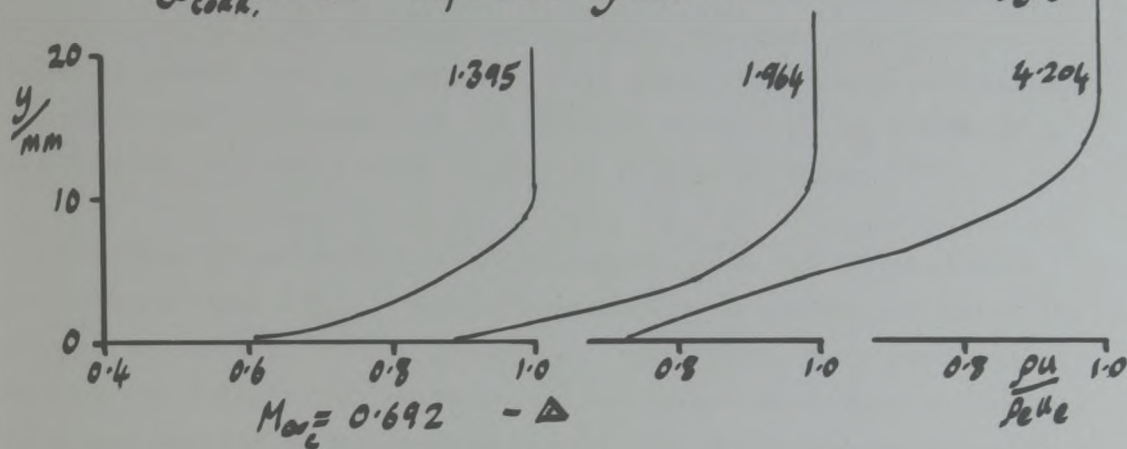
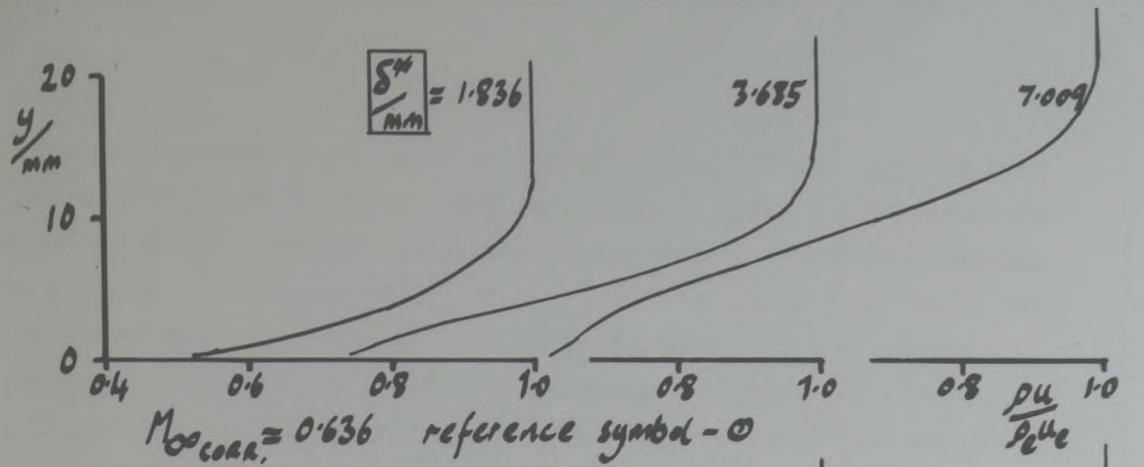


Pressure distributions along perforated wall -  
 FIGURE (40) opposite wall contoured, rake installed.



Attention is now turned to the boundary layer profiles measured during the main experiments. A selection of these is shown in Figure (41). On each of the four graphs, three curves are shown. These are the profiles measured at the upstream ( $x = 137.5$  mm), middle (223.5) and downstream (309.5) positions of the rake (thus, two positions are not shown) for a given flow configuration. The configuration is identified by the freestream Mach Number and reference symbol which may also be found on Table (5) and other relevant Figures. It should be noted that the values of  $\delta^*$  quoted against each curve are relevant to that precise curve and are not, at that stage, corrected for free-stream Mach number. These figures are drawn from Column (5) of Table (5). All the profiles in Figure (41) appear to be sensible. In the first graph, the effects of wall blowing are evident. Low speed air is injected at the base of the profile with consequent increase in  $\delta^*$ . This effect is less apparent in the second graph and in the third it is not apparent at all (it can be seen in Figure (44) that the boundary between blowing and suction does indeed occur between these two graphs). The strong suction associated with the fourth graph does reduce  $\delta^*$  to some extent, but certainly does not remove the boundary layer altogether. This effect can be seen clearly in the corresponding curve in Figure (37). It would seem that it is extremely difficult to rid the perforated wall of a measurable  $\delta^*$ , a point which will be discussed later in this section.

The curves in Figure (37) are remarkably well defined (although it is recalled that, at each longitudinal position, the values of  $\delta^*$  are drawn from a fitted function). Between the beginning of the perforated section of wall and the position of the first measuring station, little wall transpiration can have taken place, in either sense, and so the curves are very close together. Moving downstream, the effects of various blowing and suction rates, cause the curves to diverge from each other. In particular, the growth rate of the displacement thickness in the curve marked with the symbol ' $\emptyset$ ', is of interest. It will be seen in Figure (44) that these data are obtained with little transpiration through the wall. The rate of streamwise growth of  $\delta^*$  in this curve is approximately 0.0052. On a flat, smooth plate (with zero transpiration and no pressure gradient) this rate of growth for a



Boundary layer velocity profiles obtained at various longitudinal positions, with a range of freestream Mach numbers.

FIGURE (41)



turbulent boundary layer would be approximately 0.0017. Clearly the experimental value is three times this figure. Very little variation in pressure was observed during the experiments for the configuration in question (see Figure (43)) and so it is considered very likely that the additional rate of growth may be attributed to the roughness effectively constituted by the perforations. In Appendix (7) the influence of wall roughness on the rate of growth of  $\delta^*$  was mentioned in connection with the yawmeter calibration. The same effect, of increased growth rate, was observed there also. This could well explain the surprising 'reluctance' of the boundary layer to be much reduced by wall suction (an effect which is clearly visible in Figure (37)).

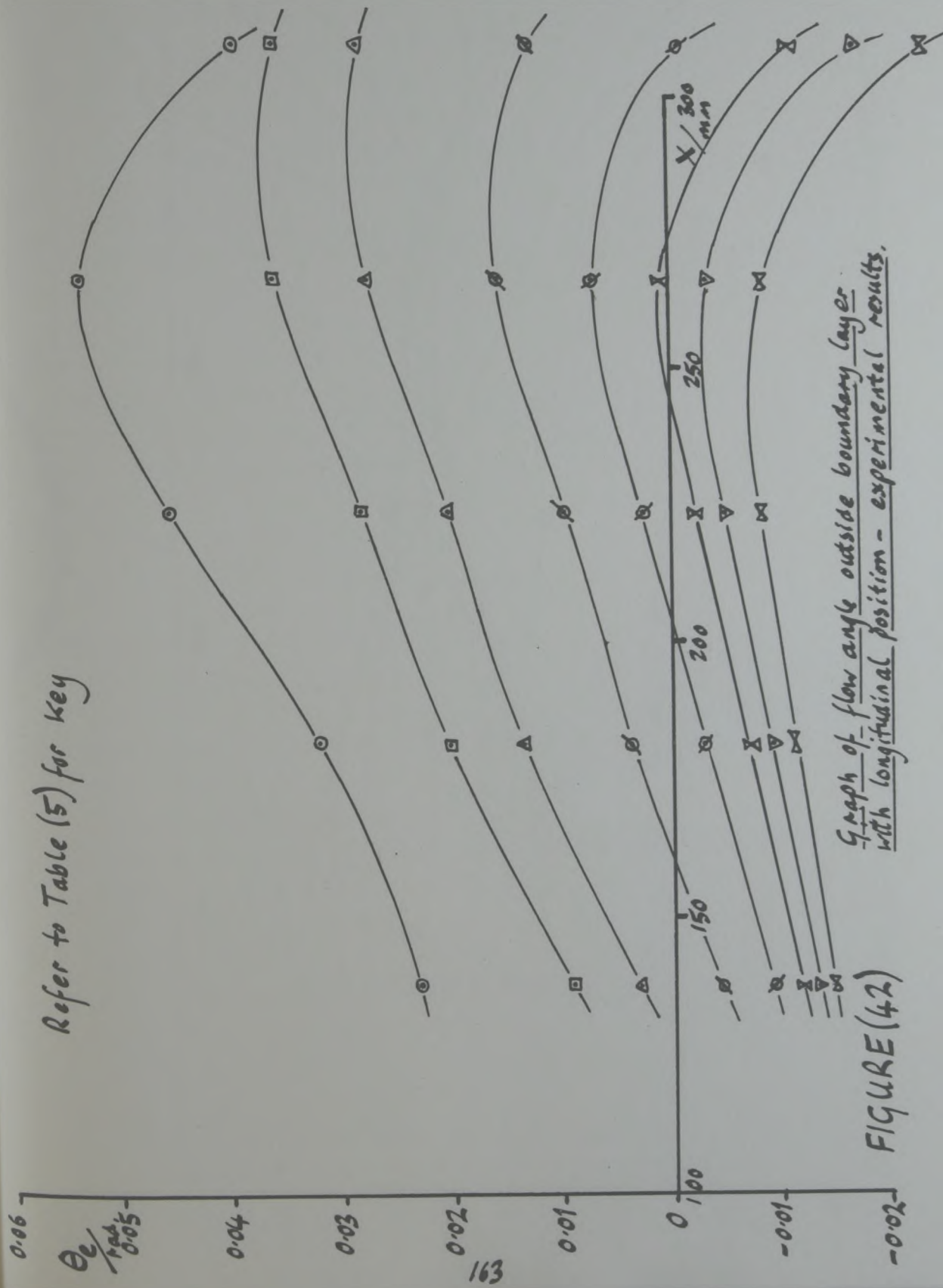
Attention is now turned to the distributions of crossflow outside the boundary layer ( $\theta_e$ ). These are presented in Figure (42), where the vertical ordinate is scaled in radians. Considering the uncertainty of the yawmeter calibration, these curves are surprisingly smooth. Towards the downstream end of the working section some swift changes appear to be taking place. It will be recalled from Section (3.8.2) that severe crossflow is experienced in the last fraction of working section, before the perforations cease. The changes taking place in Figure (42) are attributed to this effect. It is clear that the systematic variation of freestream Mach Number does have the desired effect (in our windtunnel at least) of progressively altering the crossflow near the wall. The general increase in the values of  $\theta_e$  as one moves down the working section can be linked to Figure (37). It will be observed in that diagram, that the value of  $\frac{d\delta^*}{dx}$  for each curve increases continually up to the approximate position;  $x = 270$  mm. Returning to Figure (42), the values of  $\theta_e$  also cease to increase at this longitudinal position. It is considered that the direct interrelation between  $\theta_e$  and  $\frac{d\delta^*}{dx}$  in Equation (4.11), namely

$$\theta_w = \tan \theta_e + (L - \delta^*) \left( \frac{\rho_{\infty} u_{\infty}}{\rho_e u_e} \right) \cdot \frac{d}{dx} \left( \frac{\rho_e u_e}{\rho_{\infty} u_{\infty}} \right) - \frac{d\delta^*}{dx}$$

is responsible for the rising values of  $\theta_e$  in Figure (42).

In Figure (43), the longitudinal distributions of pressure ( $C_p$ ) on

Refer to Table (5) for key



Graph of flow angle outside boundary layer with longitudinal position - experimental results.

FIGURE (42)



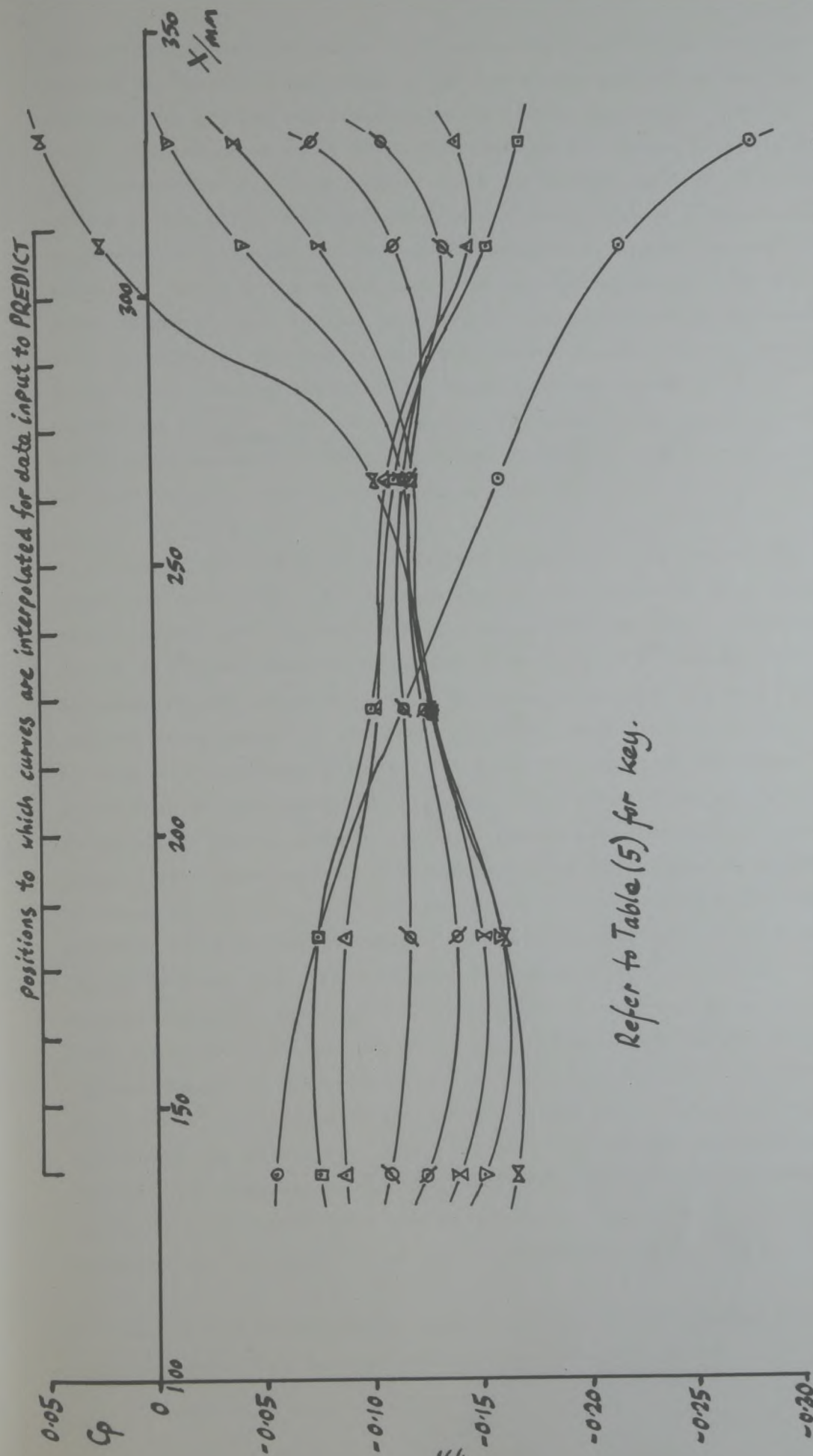


FIGURE (43) Graph of wall pressure coefficient with longitudinal position - experimental results.

the perforated wall are shown. As in the previous Figure, some severe changes in the flow take place at the downstream end of the working section. It is very noticeable that the curves are offset from the origin (in the sense of  $C_p$ ). This effect is due to the location of the 'freestream' pressure tapping which is mounted upstream of the start of the bottom wall. The contoured wall opposite causes a significant depression in pressure before the perforated zone begins. If one considers that all the curves return to zero  $C_p$  upstream of the section which is shown, then for all the curves, some influence of the contoured wall is evident. Fundamentally, this diagram reveals little information which is not already available in Figure (38) (the graph of the variations of  $\frac{p_{e16}}{p_{o16}}$  with  $x$ ). However, it is presented, as it is values of the wall pressure coefficient rather than  $\frac{p_{e16}}{p_{o16}}$  which will be used as input data for the computer program PREDICT.

Finally, the values of the average crossflow at the wall,  $\theta_w$ , are shown in Figure (44). The irregularity of the curves in this Figure are in marked contrast to those in Figures (37) and (42). Although values of  $\theta_w$  are directly calculated from those of  $\delta^*$  and  $\theta_e$  using Equation (4.11), it is considered that the complexity of that equation, and the large number of variables involved, cause the undesirable scatter of data in the present Figure. The scatter of data in the curves is sufficient to prevent clear conclusions being drawn about any longitudinal trends which may be present in  $\theta_w$ . However, in contrast, there appears to be a very clear general progression in crossflow from one configuration or curve to the next. In Section (4.3.4) it was deduced that the probable error in the calculated values of  $\theta_w$  was 0.0037. With this figure in mind, the data in Figure (44) appear more reasonable, and clearer trends in the longitudinal direction could well be evident if this error were reduced. From Section (4.2.6) it may be concluded that an improvement in the accuracy of the yawmeter calibration by approximately  $0.1^\circ$  to a standard deviation of error of  $0.1^\circ$  would be necessary to satisfy the objectives of the research. A similar improvement in accuracy is essential in the values of  $\theta_w$ . The two main methods of achieving this improvement are; improvement of the yawmeter calibration accuracy, and the accuracy of evaluating the derivative  $\frac{d\delta^*}{dx}$ .

Despite the disappointing disorder in the values of  $\theta_w$ , a remarkable comparison may be made with the data of Chan (1980a).



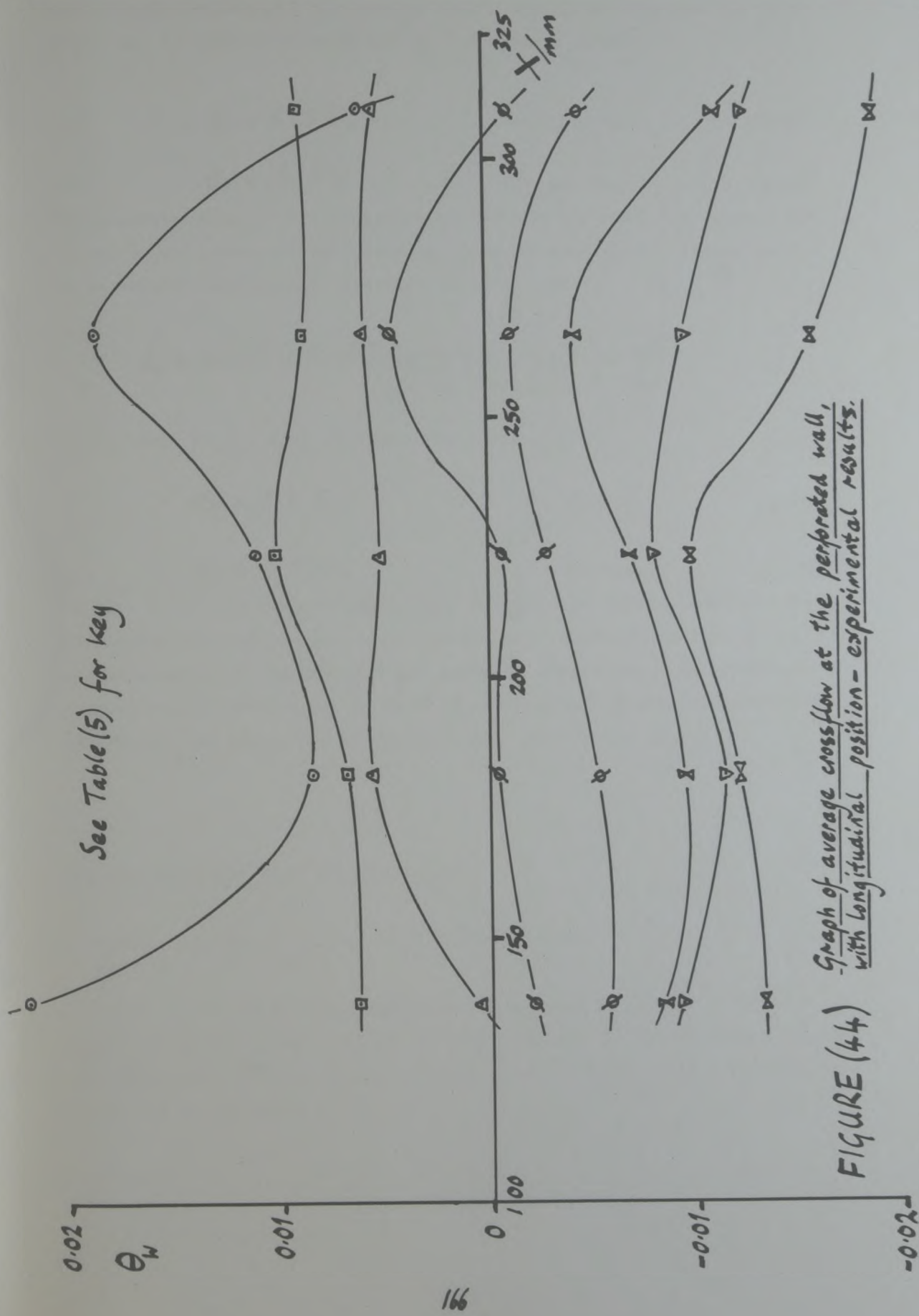


FIGURE (44) Graph of average crossflow at the perforated wall, with longitudinal position - experimental results.

Chan considers the mechanisms of wall blowing and wall suction to be essentially different. He deduces that a strong correlation (in each case) may be made between  $\theta_e$  and  $\theta_w$ . He states that

$$\theta_e = 3.25 \cdot \theta_w \quad \text{for blowing} \quad (4.15)$$

and  $\theta_e = 1 \cdot \theta_w \quad \text{for suction.} \quad (4.16)$

The amplification of the crossflow in the blowing case, is clearly due to the swift growth of the boundary layer in such flows. Again here, it is helpful to consider Equation (4.11), namely

$$\theta_w = \tan \theta_e + (L - \delta^*) \left( \frac{\rho_{\infty} u_{\infty}}{\rho_e u_e} \right) \cdot \frac{d}{dx} \left( \frac{\rho_e u_e}{\rho_{\infty} u_{\infty}} \right) - \frac{d\delta^*}{dx}$$

An analysis of our data in Table (5) reveals that

$$\theta_e = 3.7 \cdot \theta_w \quad \text{for blowing} \quad (4.17)$$

and  $\theta_e = 0.97 \theta_w \quad \text{for suction.} \quad (4.18)$

It must be stated however that these are average figures and that the individual data vary about these values considerably, in fact by an amount similar to the size of the averages themselves. Nevertheless the comparison is encouraging in that it highlights a general observation concerning the mechanism of the flow near perforated liners.

#### 4.4 The Empirical Wall Characteristic

##### 4.4.1 Evaluation of the Wall Characteristic.

Some of the data shown in Table (5) are now processed to provide the required empirical wall characteristic. Values of the variables  $\theta_w$  (Col. 21),  $\Delta p_q$  (16),  $\delta^*$  (12) and M (15) are used. A polynomial function is developed of the form



$$\theta_w = f\left(\frac{\Delta p}{q}, \delta^*, M\right).$$

This function is chosen such that it represents a good fit to the experimental data. It is very likely that there is an interaction between the 'independent' variables chosen above and so a new set of independent variables are developed, by combining the three variables above in various ways. For example, the new variable  $\delta^* M$  may appear in the final characteristic function.

Clearly, the realistic choice of the new set of variables will influence the closeness of the final fit between the function and data. To provide a guideline in the choice of variables, Figures (11.23a) and (11.24) of Goethert(1961) are used. These are reproduced here as Figures (2) and (3) respectively. From Figure (2), where the Mach number is held constant, it would appear that a function of the form

$$\theta_w = (b_0 + b_1 \delta^*) + (b_2 + b_3 \delta^*) \frac{\Delta p}{q} + (b_4 + b_5 \delta^*) \left(\frac{\Delta p}{q}\right)^2 + (b_6 + b_7 \delta^*) \left(\frac{\Delta p}{q}\right)^3$$

describes the curves adequately. Also in Figure (3) the function

$$\theta_w = (c_0 + c_1 M + c_2 M^2) + (c_3 + c_4 M + c_5 M^2) \frac{\Delta p}{q} + c_6 \left(\frac{\Delta p}{q}\right)^2 + c_7 \left(\frac{\Delta p}{q}\right)^3$$

appears to be adequate to describe the curves shown, where  $\delta^*$  is now held constant. Combining the two expressions above, such as to allow variation of  $\delta^*$  and M simultaneously gives the following expression.

$$\begin{aligned} \theta_w = & [d_0 + d_1 M + d_2 \delta^* + d_3 M^2 + d_4 \delta^* M + d_5 \delta^* M^2] \\ & + [d_6 + d_7 M + d_8 \delta^* + d_9 M^2 + d_{10} \delta^* M + d_{11} \delta^* M^2] \frac{\Delta p}{q} \\ & + [d_{12} + d_{13} \delta^*] \left(\frac{\Delta p}{q}\right)^2 + [d_{14} + d_{15} \delta^*] \left(\frac{\Delta p}{q}\right)^3. \end{aligned} \quad (4.20)$$

The expression above contains sixteen variables. From these will be chosen those which are most significant. From an engineering standpoint, it is tempting to try to visualize the physical significance of the variables chosen. However, even though there may be physical significance in the variables, their chief aim is to provide a function which fits closely the experimental data. Thus they have mathematical significance rather than physical significance.

To carry out the curve fitting process, a commercial computer program was used. This program is designed to carry out multiple linear regression with up to ten independent variables. The program employs the method of least squares to optimize the chosen function. It was decided to use the full capability of ten variables, and the ten most significant from the sixteen available were chosen by a process of trial and error.

The final wall characteristic function is;

$$\begin{aligned} \theta_w = & (+3.7856 \times 10^{-1}) + (-8.8046 \times 10^{-1}) M \\ & + (-3.9602 \times 10^{-1}) \delta^* + (+4.9733 \times 10^{-1}) M^2 \\ & + (+1.0349 \times 10^0) \delta^* M + (-6.7327 \times 10^{-1}) \delta^* M^2 \\ & + (-9.3175 \times 10^{-2}) \left(\frac{\Delta p}{q}\right) + (+3.4528 \times 10^{-2}) \left(\frac{\Delta p}{q}\right) \delta^* \\ & + (+4.2904 \times 10^{-1}) \left(\frac{\Delta p}{q}\right)^2 \delta^* + (-9.0049 \times 10^{-1}) \left(\frac{\Delta p}{q}\right)^3 \\ & + (+2.4327 \times 10^0) \left(\frac{\Delta p}{q}\right)^3 \delta^* . \end{aligned} \quad (421)$$

This equation is non-dimensional, the values of  $\delta^*$  in fact representing the term  $\frac{\delta^*}{d}$ , where  $d$  is the perforation diameter or 2.95 mm. To examine the significance of this function it is necessary to define some statistical properties which may be used as indications of closeness of fit and of the significance of the various terms.



First the familiar term  $\chi^2$ . It is defined here as

$$\chi^2 = \sum_1^N (\theta_{w_i} - \theta_w \{ \frac{\Delta p}{q_i}, \delta_i^*, M_i \})^2, \quad (4.22)$$

where N is the total number of observations from experiment (40).

The subscript 'i' indicates an observation and the term in curly brackets is intended to represent values of  $\theta_w$  calculated from the function, Equation (4.21). Thus  $\chi^2$  is a measure of the distribution of the experimental data about the function. In choosing the characteristic function, careful consideration was given to the magnitude of  $\chi^2$ , with the aim of minimizing it. However, this information alone could be somewhat misleading. In some cases, the value of  $\chi^2$  might be very small, only because the experimental data is closely packed. To allow the significance of a particular function to be more clearly understood, another statistical parameter,  $F_R$ , is used. This parameter or property is rather more complex to explain than  $\chi^2$  (see Bevington, 1969, Chapter 10). Suffice it to say that  $F_R$  represents the ratio of the distribution of the experimental data in absolute terms, to the distribution of the experimental data about the chosen function. It is possible to decide whether all the variates in a given function are significant, or whether one or more are not, by examining the size of the property,  $F_R$ . For a function with one variable, where forty observations are used to generate the function,  $F_R$  must be greater than 7. When the number of variables rise to ten, the critical value of  $F_R$  falls to 2.65.

For all the functions examined, the value of  $F_R$  remained above 39 and for the final function chosen it was 41.6, indicating that all variables were significant (at least mathematically). Also for the chosen function, the value of  $\chi^2$  was  $2.3 \times 10^{-4}$ . From the data supplied by the computer program, it was possible to calculate that the standard deviation of the discrepancy between experimental values of  $\theta_w$  and those drawn from the function is 0.0028 radian. It cannot be stated that the function chosen and the ten variables in it are the best possible. However, during the 'trial and error' process involved in choosing the function, it appeared unlikely that any other function would be significantly better than that chosen.

Concerning the accuracy of the characteristic, it must be remembered that the experimental data used to generate it were themselves in error. For example the error in values of  $\theta_w$  was calculated to have a standard deviation of 0.0054 radian. One might consider that the scatter of the experimental data about the chosen function (0.0028 radian) should be added to this. It has been suggested by Baker (1980) that the matrix inversion process which is likely to be used in the fitting program, would cause the errors in the function constants to be of the same order as that in the values of  $\theta_w$  supplied, namely 0.0054. If this were the case, it would be unnecessary to add on the fitting error. In the present work, the former more pessimistic approach is pursued.

#### 4.4.2 Discussion of the Characteristic.

Before discussing the wall characteristic in its functional form, it is helpful to make some observations about the distribution of the experimental data used to determine the function. As  $\theta_w$  is considered to be a function of three basic variables, it is quite difficult to present this information clearly. In Figure (45), an attempt is made. The data (which are drawn from Table (5)) are shown with variables  $\frac{\Delta p}{q}$  and  $\theta_w$  on the vertical and horizontal axis respectively. This choice may appear to contradict the idea of  $\theta_w$  being the dependent variable, but it allows easier comparison with data produced by other workers. The data points are shown in three distinct groups, each group representing a broad range of values of  $\delta^*$ . The respective Mach number of each data point is indicated, to two decimal places by the point itself (e.g. '(82)' represents a Mach number of 0.82).

We can compare Figure (45) with Figure (2). It should be noted that in Figure (2), outflow is considered positive, rather than negative as it is in our analysis. It appears in our data that the influence of displacement thickness is in exact contrast to that in Goethert's data. However, Goethert's data is mainly concentrated in the outflow region (where we have data with only a limited range of  $\delta^*$ ) and ceases to exist at all only 0.005 radian into the blowing region (where we have a considerable range of  $\delta^*$ ). Thus, the effective overlap of the present data with that of Goethert is in fact quite limited, especially when one



(73)  $\delta^* = 0.844$

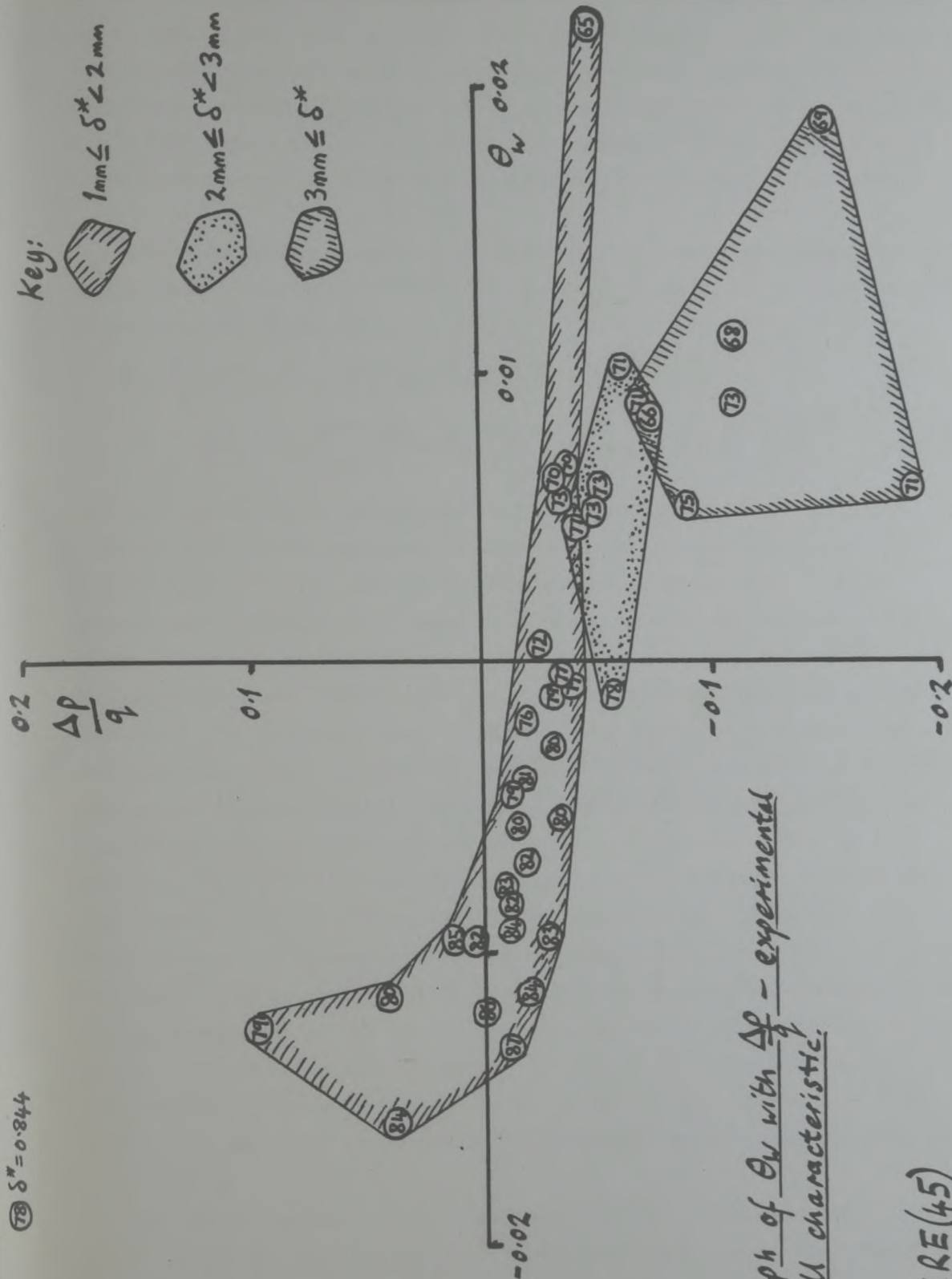


FIGURE (45)

considers that the minimum Mach number in Goethert's data is 0.9, which exceeds all values in our data. It can only be concluded that the data in the two Figures are in the same approximate areas of the graph. Only if one set of data were extended suitably could any statement be made concerning agreement in trends or other more detailed features. It was however calculated in Section (4.3.4) that the likely error in values of  $\theta_w$  was 0.0037 radian and if this error were reduced significantly, a more careful comparison could be made between the two Figures in question.

Attention is now turned to the final set of variables chosen to represent the characteristic function. Re-writing Equation (4.20) with only the chosen ten variables;

$$\theta_w = [d_0 + d_1 M + d_2 \delta^* + d_3 M^2 + d_4 \delta^* M + d_5 \delta^* M^2] \\ + [d_6 + d_8 \delta^*] \left( \frac{\Delta p}{q} \right) + d_{13} \delta^* \left( \frac{\Delta p}{q} \right)^2 + [d_{14} + d_{15} \delta^*] \left( \frac{\Delta p}{q} \right)^3. \quad (4.23)$$

It must be remembered again here that the exact mixture of variables probably has limited physical significance compared to its mathematical significance in being able to predict the experimental data used to generate it. Despite this, some brief observations can be made. First, there is a close link (via isentropic relations) between  $M$  and  $\frac{\Delta p}{q}$ . It was observed (Carr, 1980) that the function contains these two parameters separately, in ascending orders of power, but never with interdependence, as is strongly the case with  $\frac{\Delta p}{q}$  and  $\delta^*$ . This is logical if  $M$  and  $\frac{\Delta p}{q}$  are indeed closely related. Carr also commented that the presence of the term  $M^2$  may indicate some direct influence of compressibility on the results. It could be imagined that a form of the Prandtl-Glauert factor ' $\beta$ ' (where  $\beta^2 = (1 - M^2)$ ) were included somewhere in Equation (4.23). Chan (1980b), in discussing very similar work, suggested that even accounting for  $\delta^*$  alone, could involve Mach number automatically because of the strong dependence of the former upon the latter. In Chan (1980a), he concludes that the normal velocity at the wall is a non-linear function of the pressure difference across the wall and is also dependent on  $\frac{d\delta^*}{dx}$ . This latter variable is one which we deliberately neglected (Section (3.6)).

The wall characteristic is now presented in a graphical form in Figure (46). A few discrete values of  $\delta^*$  and  $M$  have been chosen to illustrate



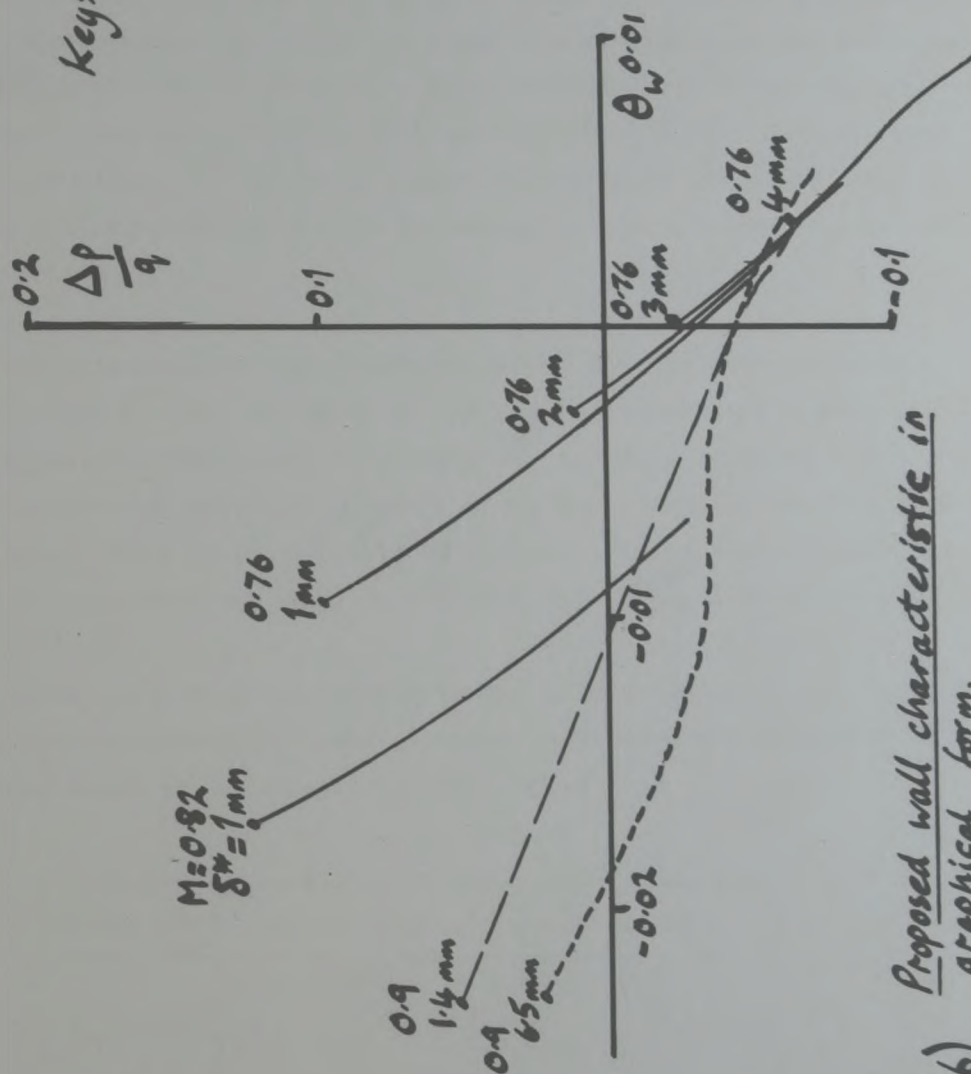


FIGURE (46) Proposed wall characteristic in graphical form.

the function. The individual curves are only drawn in the region where there is supportive experimental data in Figure (45). Also displayed on this graph are some of Goethert's data from Figure (2). In the region of outflow at least, there is considerable discrepancy between the two sets of data. Once again however, the rather different values of  $\delta^*$  and  $M$  between the graphs should be noted. In Figure (3), it will be noted that as  $M$  decreases (at least below 1.2) the curves drop towards the  $\frac{(\rho v)^{1/2}}{(\rho v)_\infty}$  axis. This feature is retained in Figure (46), although it must be admitted the gradient of the curves does not alter with Mach number. It may be that if we were able to use our function to predict data at Mach numbers up to 0.9, that our data in Figure (46) would fall much closer to Goethert's. One point of clear encouragement is the intercept on the  $\Delta p_q$  axis. As in Goethert's data, the majority of curves congregate and cross the axis at approximately  $\Delta p_q = 0.04$ . This feature is almost certainly due to the inclined perforations and highlights the need in a wall boundary condition to account for this offset of the curves from the origin.

Observing the cluster of predicted curves for the  $M = 0.76$  case, it appears that  $\delta^*$  has little effect on the characteristic. Even if this were true for the relation between  $\Delta p_q$  and  $\theta_w$ , it would not necessarily be true when the boundary condition is applied to the flow calculations. This is because the effective inviscid flow at the wall position is dependent not only upon  $\theta_w$  but upon  $\frac{d\delta^*}{dx}$  (see Equation (3.3)).

One final feature of the curves which is important in later calculations is their gradient. For some typical conditions, the gradients of the curves (and those of Goethert) are given below.

data due to:-	Function	Goethert
$\theta_w = -0.01$	$M=0.76 \frac{\partial \Delta p_q}{\partial \theta_w} = -18.2$ $\delta^*=1$	$M=0.9 \frac{\partial \Delta p_q}{\partial \theta_w} = -4.0$ $\delta^*=1.4$
$\theta_w = +0.005$	$M=0.76 \frac{\partial \Delta p_q}{\partial \theta_w} = -10.2$ $\delta^*=3$	$M=0.9 \frac{\partial \Delta p_q}{\partial \theta_w} = -9.5$ $\delta^*=3$



Clearly for suction cases, there is a large difference between the gradients. Some of this discrepancy may be due to the differences in Mach number and  $\delta^*$  between the two sources of data. In contrast for the strongest blowing cases cited by Goethert, where  $\phi_w = 0.005$ , the gradients are very similar. In summary, the functional characteristic shows clear indications of being sensible but is limited (so far as comparing it with other data is concerned) by the restricted spread of data upon which it is founded.

## 5 PREDICTION OF FLOW NEAR THE PERFORATED WALL.

### 5.1 Objectives of the Computer Program 'PREDICT'

In Section (3) of this report, a proposal was made for an improved boundary condition to be applied at the position of the perforated walls in two-dimensional windtunnel flow calculations. This new boundary condition was to be applied in practise using a computing scheme also described in that Section. This scheme required the provision of a boundary layer prediction method (an example of which was described in Section (3.5)) and an experimentally derived wall characteristic. The fulfilment of the latter requirement was described in detail in Section (4).

It would naturally be the long term objective of this research to apply the new boundary condition to a practical inviscid flow calculation method. However, such an application would only be constructive if it had been demonstrated that this boundary condition accurately represented the nature of the flow near the perforated walls. Let us consider that the flow near and through the perforated wall can be termed the 'wallflow'. Then it is required, using the new boundary condition, to predict a set of given experimental wallflows. The computer program used in this prediction is termed simply 'PREDICT'.

PREDICT then, must incorporate the chosen boundary layer prediction method and empirical wall characteristic in the new boundary condition (Equation (3.51), namely,

$$\phi_x \pm \frac{1}{\rho} \phi_z = K, \quad (5.1)$$

where  $P$  and  $K$  are permitted to vary with  $x$ . This new boundary condition must be used in a scheme similar to that described in Section(3), to predict the nature of the flow near the perforated wall, given suitable starting conditions (chosen to be chiefly the pressure coefficients on both sides of the wall).



## 5.2 Details of the Computer Program 'PREDICT'

### 5.2.1 The Overall Scheme.

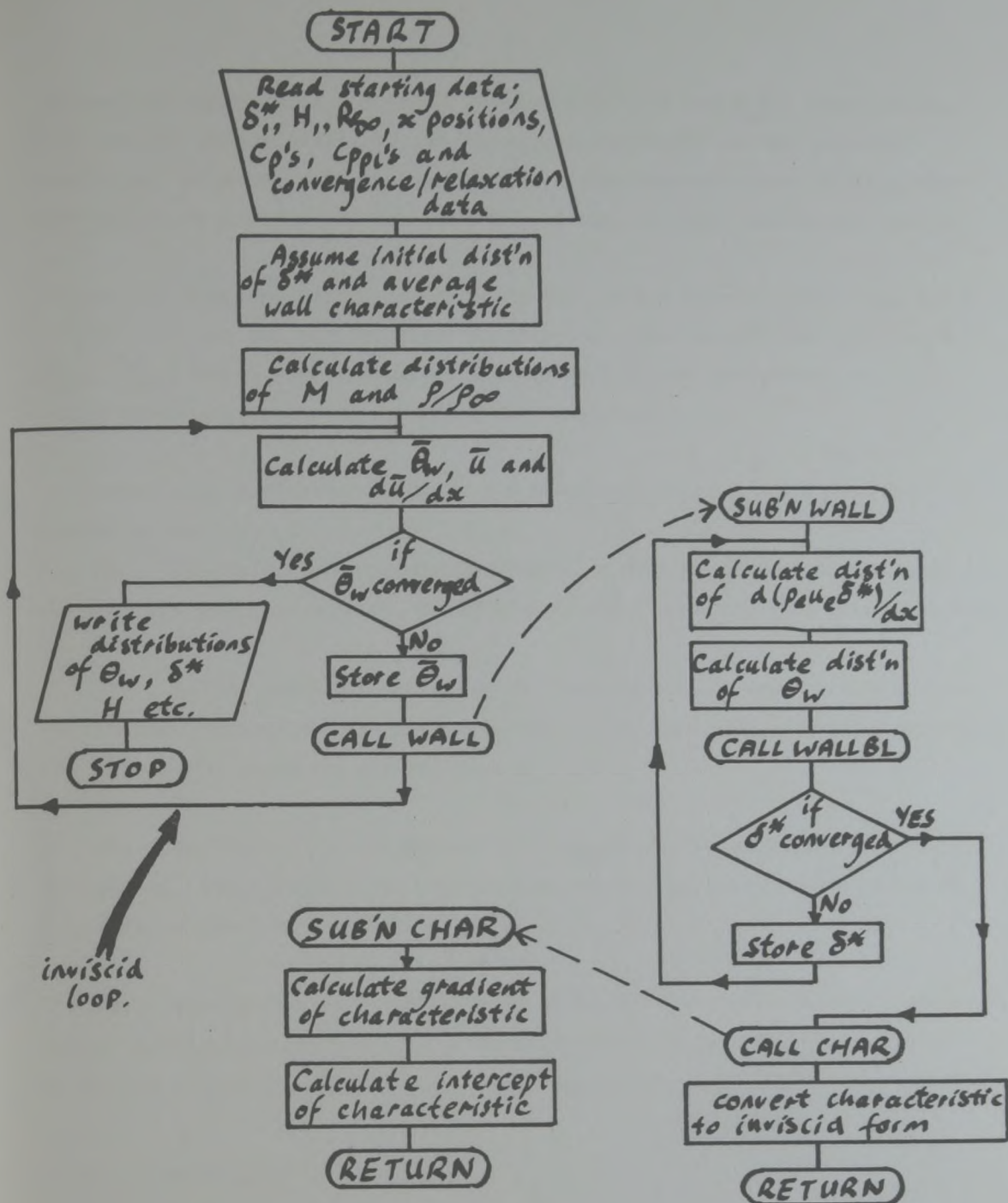
The computing scheme used in the program PREDICT is very similar to that in the program PILOT. Naturally, PILOT, which calculates the complete windtunnel flow, is more comprehensive than PREDICT. Although it is the objective of PREDICT to incorporate the overall scheme of PILOT, it would not strictly be necessary to do this. By suitable interaction merely between the boundary layer analysis and the wall characteristic (with starting data of relevant pressure coefficients) it would be possible to calculate the flow near and through the perforated wall. However, it is intended to test the usefulness of the new boundary condition (Equation (5.1)) in an interactive mode with some inviscid flow calculation. As such, the original scheme is retained here.

A simplified flow diagram of the program PREDICT is shown in Figure (47). It will be helpful to refer also to Figure (11), the PILOT flow diagram. The chief difference between the programs is the replacement of the inviscid flow calculation in PILOT with a simple, equation, namely,

$$C_p = C + D \bar{\theta}_w . \quad (5.2)$$

Here  $\bar{\theta}_w$  is the crossflow parameter in the effective inviscid flow at the wall ( $\bar{v}_w/\bar{u}_w$ ). This equation is in fact another form of the new boundary condition. The constants C and D (which actually may vary with x) are obtained from the 'viscous' side of the calculation procedure. Fixed values of  $C_p$  from experiment are supplied to this equation, resulting in the prediction of a distribution of  $\bar{\theta}_w$ . This distribution is then supplied to the 'viscous' calculation to calculate an improved set of values of C and D. The process described is then repeated. Thus an iteration loop is formed and this is denoted "inviscid loop" on Figure (47). In contrast to PILOT, it was found necessary here to use under-relaxation in this loop.

As the inviscid iteration loop begins with a calculation of the effective inviscid flow at the wall, it is necessary to provide a wall boundary condition prior to entering the loop. The wall characteristic



FIGURE(47) Flow diagram of computer program PREDICT.



is used to supply this. Typical values of  $\delta^*$ ,  $M$  and  $\theta_w$  are used (2 mm, 0.76 and 0. respectively) to calculate the constants in the boundary condition, from the wall characteristic. The boundary condition is then altered to be relevant to the effective inviscid flow before application.

As the pressure distribution along both sides of the perforated wall is specified at the beginning of the program, all parameters (such as  $M$ ,  $p/p_\infty$ ,  $\rho/\rho_\infty$ ) which are related in a fixed way to the pressures are calculated once, prior to entering any iteration.

Additional difference between the programs PREDICT and PILOT are listed below.

(1). All references to an 'aerofoil', opposite wall or windtunnel centre-line are removed, as PREDICT deals only with the flow near one wall.

(2). At the end of calculation, no alteration is made to freestream conditions, because in the present program the inviscid stream is specified (in terms of a pressure distribution).

(3). In PREDICT, no reference is made to any solid regions of wall, because all experimental data were obtained in the perforated region of the working section.

(4). The option in PILOT of specifying either plenum chamber pressure or the nett volumetric flow rate through the wall is deleted, a distribution of plenum pressure always being specified in PREDICT.

#### 5.2.2 Details of the Scheme.

In Figure (47), the major subroutines of the program PREDICT are shown, in addition to the controlling segment. The latter segment was outlined in the previous sub-section. We refer now to the subroutines in order of priority.

Subroutine WALL is called directly from the main segment. It is the task of this subroutine to calculate a distribution of boundary layer displacement thickness ( $\delta^*$ ) which is compatible with the distributions

of effective inviscid crossflow ( $\bar{\theta}_w$ ) and pressure coefficient ( $C_p$ ), supplied by the main segment. This calculation involves an iteration with under-relaxation and is carried out in the same manner as the analogous calculation in PILOT. When this compatible flow has been achieved, the subroutine CHAR is called, to provide a wall boundary condition which is of the form,

$$\frac{\Delta p}{q} = A + B \bar{\theta}_w. \quad (5.3)$$

This boundary condition (which is evaluated at each control point along the wall) represents the viscous crossflow at the wall. It is then converted into the form of Equation (5.2), where only quantities representing the effective inviscid flow are present. Control then returns to the main segment of the programme.

During the course of the iteration in WALL, the subroutine WALLBL is repeatedly called. This subroutine, which is almost identical to subroutine BL in PILOT, is used to calculate the distribution of boundary layer displacement thickness along the perforated wall. WALLBL is slightly more accurate for present purposes than BL in that it takes some account of compressibility. The details of the boundary layer method were described in Section (3.5).

Finally, subroutine CHAR. This embodies the wall characteristic equation (4.21). For each discrete point on the perforated wall, values of  $M$ ,  $\delta^*$  and  $\frac{\Delta p}{q}$  are used to predict a boundary condition which is locally linear. This condition (Equation (5.3)) is then returned to subroutine WALL. It should be noted that the entire calculation procedure in PREDICT is carried out using a discrete set of values (15 in all) of each variable concerned.

Having compared the structure of PREDICT with that of PILOT, attention is turned to the major changes made from the actual equations used in PILOT.

As mentioned earlier in this section, the inviscid flow calculation in PILOT is now replaced by a simple boundary condition equation, namely



$$C_p = C + D \bar{\theta}_w . \quad (5.3a)$$

This is almost identical to the analogous inviscid flow boundary condition in PILOT, namely Equation (3.15) or

$$[u] = [A'] + [B'] \cdot [v]$$

but the perturbations parallel and normal to the freestream direction have been left in a more usable form.

The remaining major differences between the equations used in the programs, are concerned with the introduction of compressibility to the calculation. All simple calculations are carried out using isentropic relations. The first major relation to be mentioned, is that used to relate the viscous and effective inviscid crossflows. This relation is Equation (3.3), namely

$$\delta^* \cdot \frac{d(\rho_e u_e)}{dx} + \rho_e u_e \cdot \frac{d\delta^*}{dx} + \rho_w v_w - \overline{\rho_w v_w} = 0. \quad (5.4)$$

When used in PILOT, all reference to density was removed from this equation. The variation in pressure, and thus also in the term ' $\rho u$ ' across the depth of the boundary layer in the effective inviscid flow is neglected (Cebeci and Smith, 1974, pp 73-75). Thus we can write

$$\rho_e u_e = \overline{\rho_w u_w} . \quad (5.5)$$

Dividing all the terms in Equation (5.4) by this new parameter,  $\overline{\rho_w u_w}$ , we find

$$\frac{\rho_w v_w}{\overline{\rho_w u_w}} = \frac{\overline{v_w}}{\overline{u_w}} - \frac{1}{\overline{\rho_w u_w}} \cdot \frac{d}{dx} (\overline{\rho_w u_w} \delta^*) . \quad (5.6)$$

This equation is then non-dimensionalized with respect to freestream properties,  $\rho_\infty$  and  $u_\infty$ , and for length dimensions, with respect to the wall perforation diameter,  $d$ . The resulting equation, which is expressed

in the same form as Equation (5.6) is then used in PREDICT. In this equation, the value of  $\bar{u}_w$  is obtained using Equation (5) of Appendix (10), namely

$$\left(\frac{u_e}{u_\infty}\right) = \left\{ 1 - \left(\frac{v_e}{u_\infty}\right)^2 - \left[ \left(\frac{p_e}{p_\infty}\right)^{\frac{\gamma-1}{\gamma}} - 1 \right] \cdot \frac{2}{\gamma-1} \cdot \frac{1}{M_\infty^2} \right\}^{\frac{1}{2}},$$

which is exact for isentropic flow. In this equation the subscripts 'e' are replaced by the subscript 'w', and the term  $(p_w/p_\infty)$  is calculated from the wall pressure coefficient. As all terms are calculated as being in the effective inviscid stream, we may write

$$\bar{u}_w = \left\{ 1 - \bar{v}_w^2 - \left[ \left(\frac{p_w}{p_\infty}\right)^{\frac{\gamma-1}{\gamma}} - 1 \right] \cdot \frac{2}{\gamma-1} \cdot \frac{1}{M_\infty^2} \right\}^{\frac{1}{2}}. \quad (5.7)$$

Another notable difference between the equations involved in PILOT and those in PREDICT is concerned with the definition of the plenum chamber pressure coefficient. In PILOT this was defined in a reversed manner;

$$C_{ppl} = \frac{p_\infty - p_{pl}}{\frac{1}{2} \rho u_\infty^2} \quad (\text{Equation (3.19)}).$$

In PREDICT, it is defined more logically as;

$$C_{pp} = \frac{p_{pl} - p_\infty}{\frac{\gamma}{2} M_\infty^2 p_\infty}$$

and to make use directly of the available data in Table (5), as

$$C_{pp} = \frac{\frac{p_{pl}}{p_0} - \frac{p_\infty}{p_0}}{\frac{\gamma}{2} M_\infty^2 \frac{p_\infty}{p_0}}. \quad (5.8)$$

Finally the freestream Reynolds number is calculated using the equation,

$$Re_\infty = \frac{\rho_\infty u_\infty d}{\mu}$$

Here,  $\rho_\infty$  and  $u_\infty$  are calculated from the freestream Mach number and an average value of the freestream stagnation pressures, measured during the tests in question. The value of the stagnation temperature is also



required, to determine  $\rho_\infty$  and  $U_\infty$ . Based on several measurements which showed little variation, this is assumed to be 2°C below the ambient room temperature. In Equation (5.9), 'd' is the perforation diameter, 2.95 mm (0.00295 m) and  $\mu$ , the dynamic viscosity, is assumed to be  $1.796 \times 10^{-5} \text{ kgm}^{-1} \text{ s}^{-1}$ . This value of  $\mu$  was incorrectly calculated on the basis of local stagnation pressure, but it is not considered that the resultant 10% error in  $Re_\infty$  will significantly affect the conclusions from this work.

Before proceeding to describe the operation and results of PREDICT, a comment is made concerning a confusion which may arise as the reader attempts to understand the procedures involved in the program. Whenever reference is made to a boundary condition, Equation (5.3a) for example, the condition involves some pressure coefficient or longitudinal velocity perturbation as the dependent variable. However, the wall characteristic, Equation (4.21) is expressed with  $\theta_w$  as the dependent variable. Until quite close to the end of the period of research in question, both boundary condition and wall characteristic were written consistently with a form of  $C_p$  as the dependent variable. However initial tests using the program PREDICT revealed an interesting phenomenon. At the outset of the calculation, the wall pressure coefficients and Mach numbers are specified, but only the Mach number could be used in the wall characteristic to define the 'local' characteristic, as  $C_p$  was the dependent variable. Hence the calculation was less 'tightly specified' than the input data would warrant, and although a converged solution was obtained in one case, it was not sensible. This solution is shown in Figures (49) and (50) as a dashed curve. When the form of the characteristic was reversed, and  $\theta_w$  was made the dependent variable, all the input data were used (being  $C_p$  and M) to specify 'local' characteristics and converged solutions were clearly more sensible. These curves are also shown in Figures (49) and (50). The latter form of the characteristic has therefore been adopted.

A listing of the computer program PREDICT is presented in Appendix (11).

### 5.3 Results from the Computer Program PREDICT.

The computer program PREDICT has been operated using four sets of

experimental data. These data effectively originate from Table (5), although in most cases, some intermediate manipulation has taken place. Of the eight windtunnel configurations presented in Table (5), the central four were chosen for use. The values of the wall pressure coefficient ( $C_p$ ), which are shown on Figure (43), are interpolated to the values of 'x' indicated on the graph. The plenum chamber pressure coefficients ( $C_{pp}$ ) are calculated from the data in Table (5) using Equation (5.8). These are shown (for the four relevant configurations) in Figure (48). Once again, the data are interpolated to chosen values of 'x', for input to PREDICT.

Besides the freestream Reynolds number, which was mentioned in the previous sub-section, three further starting data are required by PREDICT. First a freestream Mach number which is drawn directly from Column (9) of Table (5) for each configuration. Secondly the upstream boundary layer displacement thickness. For each configuration this is taken as the most upstream value on Table (5). Finally, the value of the boundary layer shape parameter,  $H$ , at the same upstream position for each configuration. This was obtained by interpolating the experimental values of  $H$  measured at the upstream position, to determine the value which would have been obtained if the freestream Mach number were equal to that for the chosen configuration. In fact the maximum variation in  $H$  at the upstream position was quite small,  $H$  being confined between 1.46 and 1.54.

It was mentioned in Section (5.2.1) and (5.2.2), that both the inviscid iteration loop in the main segment of PREDICT and the viscous flow iteration in subroutine WALL required under-relaxation to achieve convergence. The outer, inviscid loop involves relaxation in values of the inviscid flow angle,  $\bar{\theta}_w$ . A relaxation parameter of 0.3 was successfully used here. The iteration was terminated when all values of  $\bar{\theta}_w$  agreed with their values in the previous loop to within  $1.0 \times 10^{-6}$  radian. For the inner, viscous loop involving relaxation in the viscous flow angle,  $\theta_w$ , a relaxation parameter of 0.1 was used successfully (the corresponding value in PILOT was 0.4). This iteration process was terminated when all values of  $\delta^*/d$  were within 0.0003 (0.00089 mm) of their values in the previous iteration.



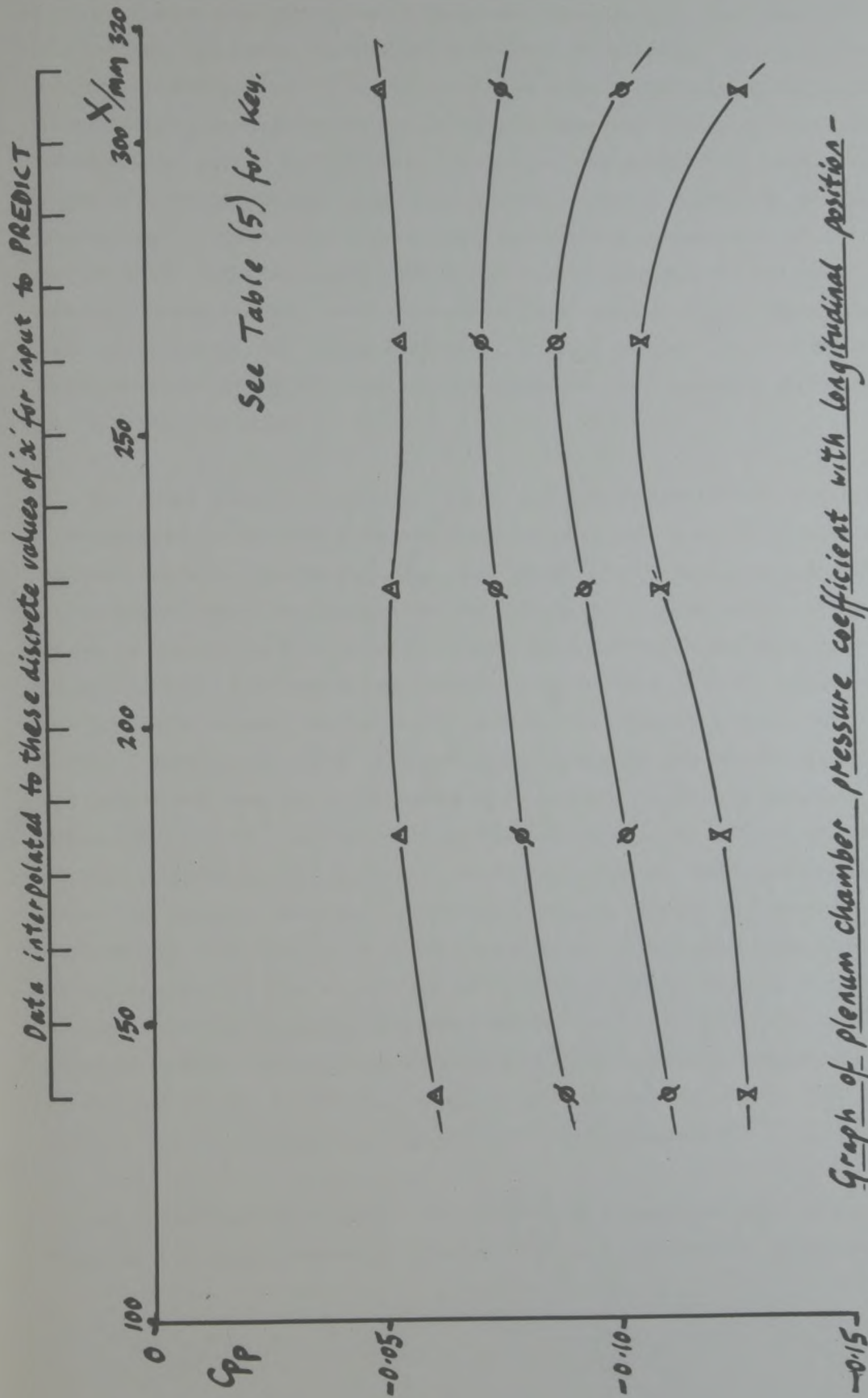


FIGURE (48)

When operating successfully, the program was used to predict the four configuration mentioned, during one calculation. On a Honeywell Level 66/60 computer, this calculation took 84 seconds. It involved a total of 266 inviscid iterations. Thus each iteration (which would be considered as a complete evaluation of the wall boundary condition) takes approximately 0.31 second. This time requirement is likely to be a linear function of the number of discrete control points on the perforated wall. Thus, for a practical calculation method with 80 grid points along the wall, this time becomes 1.65 second. If the wall boundary condition was re-evaluated perhaps twenty times in a complete flow calculation, the total additional computing time required by the wall 'package' would not represent a significant proportion of the overall calculation time.

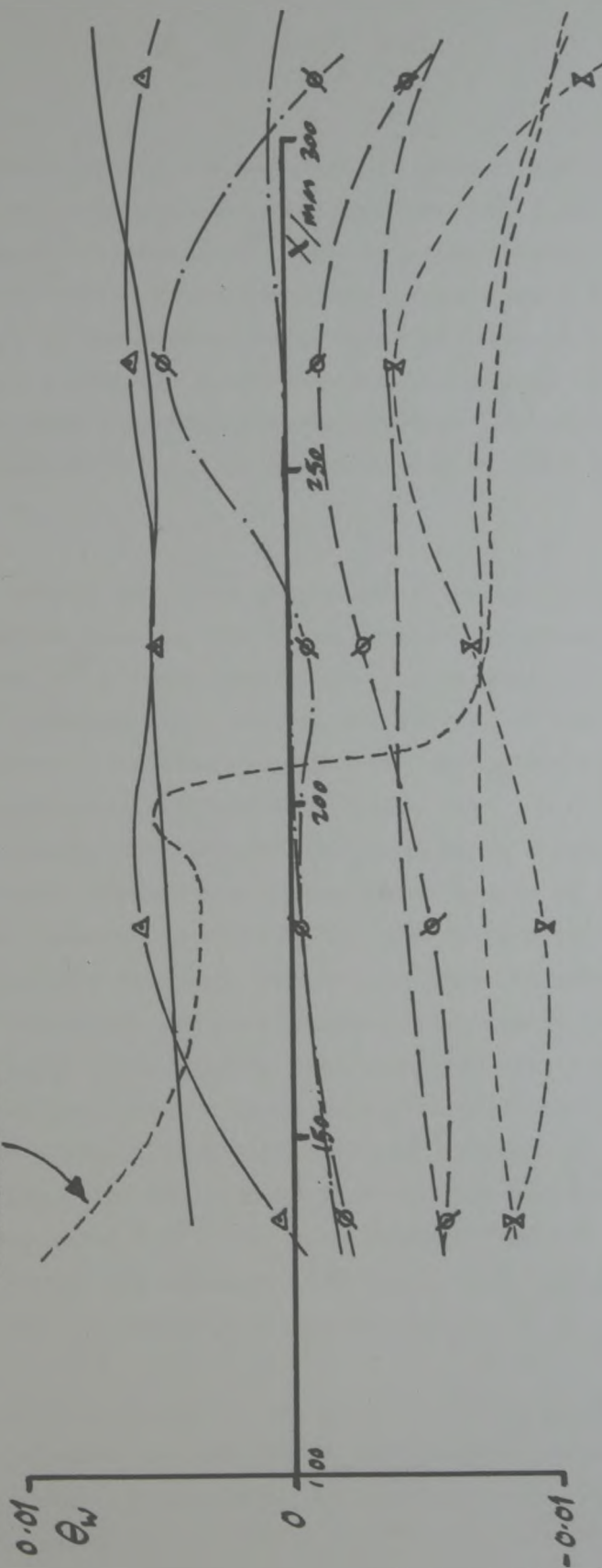
The chief results from the program are now presented and discussed. A comparison is made between experimental and predicted values of the viscous crossflow parameter,  $\theta_w$ , in Figure (49). Those data are shown as variables with the longitudinal ordinate 'x'. Also shown on this graph is the prediction obtained using the wall characteristic expressed in a reversed form, which was discussed in Section (5.2.2). For each configuration shown, the predicted curve only roughly follows the trends of the experimental curve. However, the trend in the overall levels of the crossflow from one configuration to another is well predicted. It seems likely that the predicted curves are unique for each configuration, or that PREDICT is, as required, producing a unique solution for each case. It appears that the theoretical results follow an 'average' path through the experimental data as though they represented a smoothed form of those data. It is considered that this is due to the curve fitting process involved in the development of the wall characteristic function. Although a more critical assessment will be made of the comparison later, in Section (5.4), it can be stated at this stage that Figure (49) represents a distinctly encouraging point in this research.

No comparison is made in this Section with results which would be obtained by using a conventional wall boundary condition, Equation (2.6);



see Table(5) for key.

Results from PREDICT  
for  $\beta$  case with reversed  
characteristic



curve through data points - experiment  
matching curve - theory PREDICT.

FIGURE(49) Results from PREDICT compared with experiment - crossflows at wall.

$$\phi_x \pm \frac{1}{\rho} \phi_z = 0$$

for example. There are two distinct reasons for this. First, the concept of a viscous crossflow parameter,  $\theta_w$ , and a boundary layer displacement thickness,  $\delta^*$ , do not arise in such a boundary condition, and as such, comparisons with present data cannot be made. Secondly, in the present data, there is a significant difference between local and freestream pressures, and as Equation (2.6) is based upon perturbations from freestream conditions, it could not be expected to predict sensibly the flow angles caused by local pressure differences across the wall.

The second and final comparison to be made between predicted and experimental data is that of values of the boundary layer displacement thickness,  $\delta^*$ . This comparison is presented in Figure (50). Again, for one configuration, results are shown from the reversed characteristic calculation. The comparison between prediction and experiment here is rather more disappointing than Figure (49). The calculation procedure appears unable for three of the cases shown to predict trends in the longitudinal direction with any useful degree of accuracy. It is interesting that although in Figure (49), the increments in  $\theta_w$  between successive configurations are quite regular, it does not appear to be the case for  $\delta^*$ . The neutral and suction cases are crammed quite closely together and only the clear blowing case separates itself from this grouping. Thus, so far as the boundary layer calculation is concerned, blowing through the wall has a significant influence on  $\delta^*$  in contrast to the weaker influence of suction. One could state that only extreme suction rates would ever cause the value of  $\delta^*$  to be significantly reduced. In fact, it may be recalled that the boundary layer prediction method incorporated a fixed lower limit on momentum thickness (in fact on  $Re_\theta$ ).

In Section (3.5), it was shown that the boundary layer method was unable to predict the effects of wall roughness caused by relatively large perforations. It is almost certain that this inability is to blame for the consistent underestimation of  $\delta^*$  in Figure (50).



see Table (5) for key

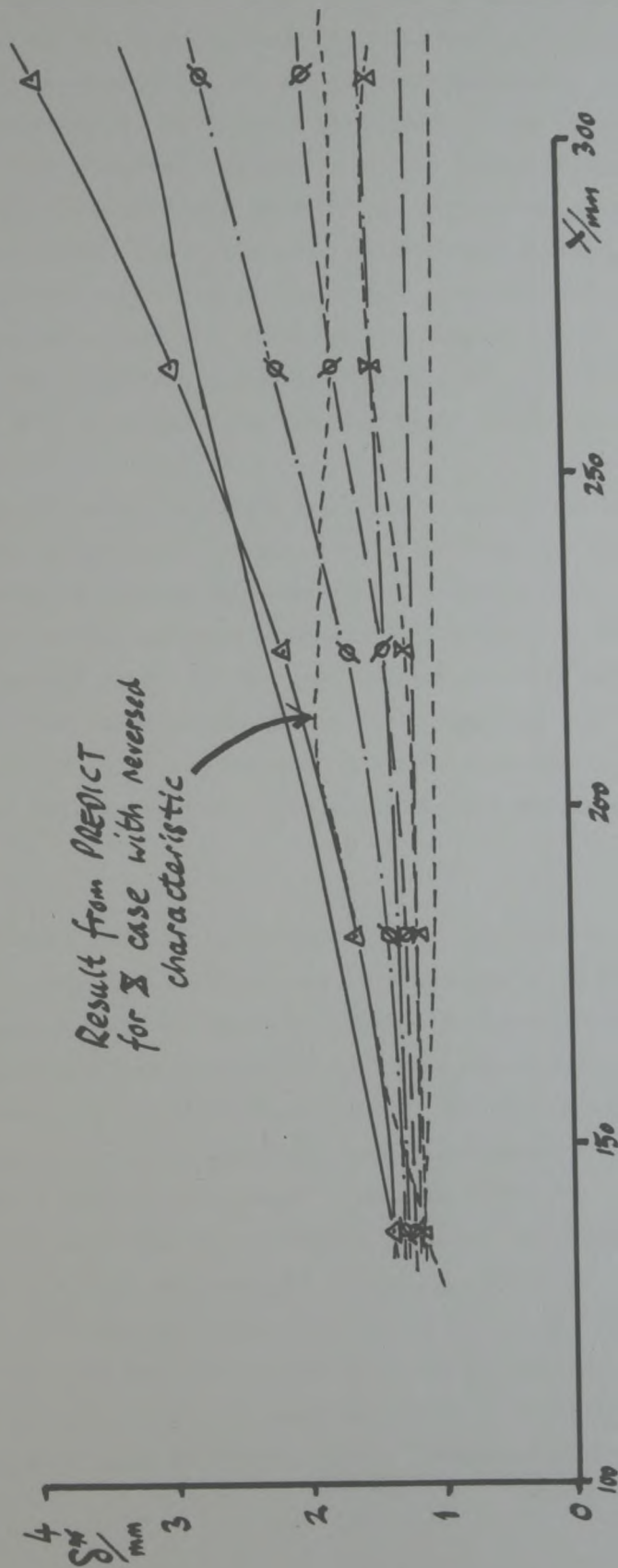


FIGURE (50) Results from PREDICT, compared with experiment - boundary layer displacement thickness.

#### 5.4 Discussion of the Accuracy of PREDICT.

Considerable effort has been invested in understanding not only the accuracy of the results from PREDICT, but the implications of this accuracy on the objectives of the present research. It will be helpful in this discussion to refer to Figure (51). This is not intended to be a computer flow diagram, but merely a very simple diagram indicating the transfer of information within PREDICT. Experimental data is supplied to the calculation, which iterates between the characteristic function and the boundary layer prediction until convergence is achieved. Then the solution is output and compared with the relevant experimental results. As the calculation consist chiefly of the two components mentioned, it will be helpful to discuss these separately.

Firstly the characteristic function. The values of  $\theta_w$  which are output from the program are effectively drawn from the characteristic. They are however, not in agreement with experimental values (see Figure (49)). This is because the characteristic function does not exactly fit the experimental data, and because the values of  $\delta^*$  delivered to the function in the calculation are in error from the experimental values. In Section (4.4.1) it was deduced that the standard deviation of the discrepancy between function and experimental values of  $\theta_w$  is 0.0028 radian.

From Figure (50) it is estimated that the standard deviation ( $\sigma$ ) of the error between theoretical and experimental values of  $\delta^*$  is 0.5 mm. It has been possible to estimate (using the assumption of normally distributed errors) that incorporating these erroneous values of  $\delta^*$  in the function would not significantly affect the values of  $\theta_w$  produced. Thus it is possible to state that the main discrepancy between values of  $\theta_w$  calculated in PREDICT and those from experiment will be the 0.0028 radian standard deviation due to the curve fitting. In Figure (49), the value of  $\sigma$  found for this discrepancy is 0.0019, which is actually less than that which is expected. Both the figure of 0.0019 radian and 0.0028 radian relate the results of PREDICT only to the experimental results. It should be noted that the experimental values of  $\theta_w$  were themselves in error from true data by 0.0054 radian (standard deviation). Thus in



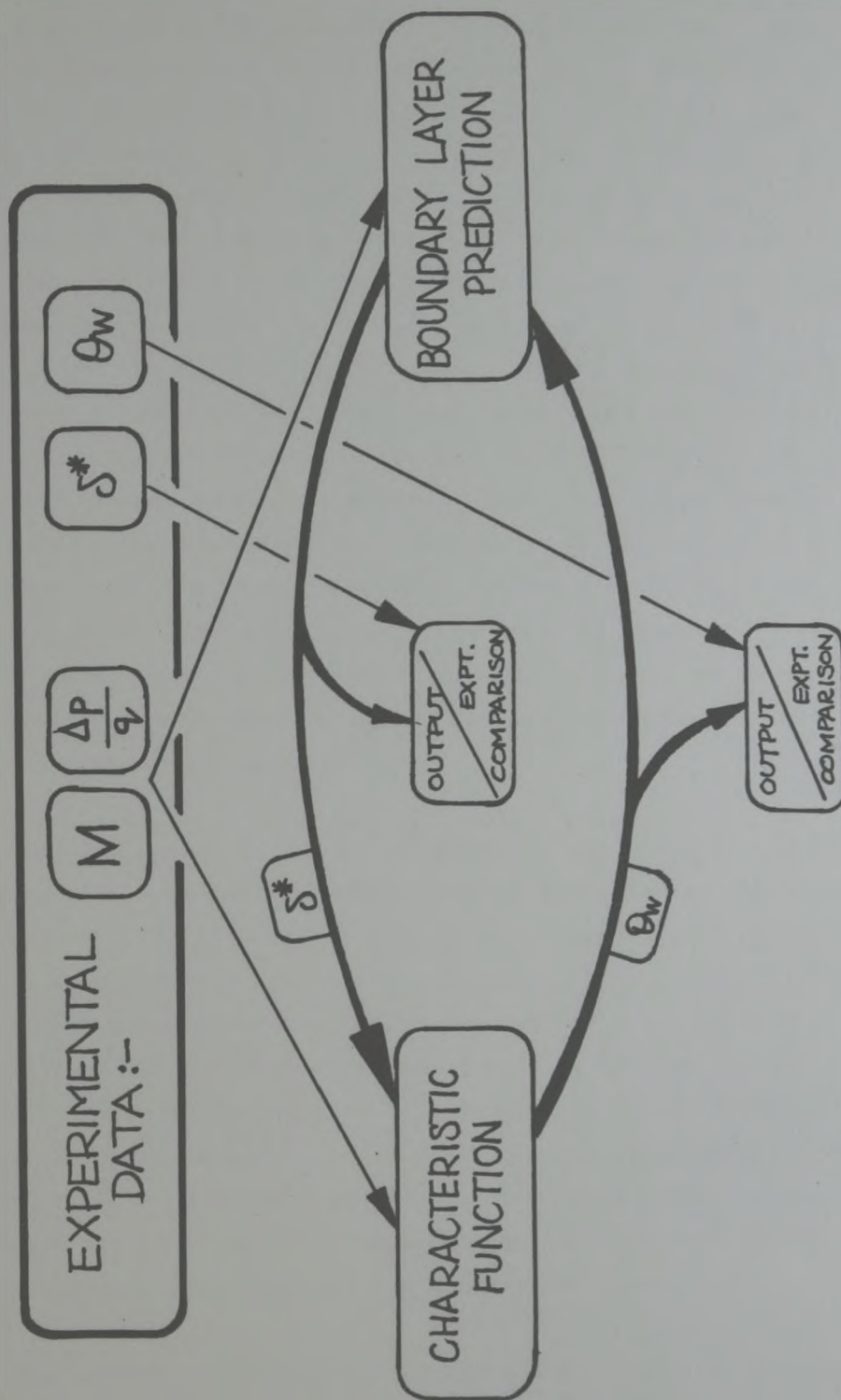


FIGURE (51) Diagram showing transfer of information within program PREDICT.

absolute terms, the results from PREDICT may well be rather less accurate than at first supposed.

We deal now with the boundary layer prediction method. Once again, results from this part of the calculation are in error because the prediction method itself is inaccurate and also because false data (chiefly  $\theta_w$ ) are delivered to it. By altering PREDICT slightly, it was possible to impose correct (experimental) values of  $\theta_w$  on the boundary layer calculation. The resulting values of  $\delta^*$  were however only slightly better than those in Figure (50), the standard deviation of the discrepancy between experiment and theory being then 0.44 mm compared with 0.5 mm previously. To examine the influence of the false values of  $\theta_w$  normally delivered to the boundary layer calculation, the same imposed values of  $\theta_w$  mentioned above were used, but one discrete value was put into error by 0.0022 radian (being the standard deviation of the error in the values produced by the characteristic function in an earlier calculation). Although this step produced a small visible alteration in the predicted results, it did not significantly increase the value of  $\sigma$  of 0.44 mm quoted above, when combined with it. The influence of an inaccurately defined freestream Reynolds number was also investigated, but this also proved to have negligible effect.

The discrepancy in Figure (50) between experimental and theoretical results of 0.5 mm ( $\sigma$ ) is then not fully explained by the investigations carried out. It is possible that some values of  $\theta_w$  are systematically in error, thus having a cumulative influence on the values of  $\delta^*$ . This might then account for the difference between the 0.44 mm  $\sigma$  of the method itself, and the 0.5 mm  $\sigma$  experienced when it is used correctly in PREDICT. Also if one were to consider the accuracy of the boundary layer method in absolute terms, it is clear that in specifying experimental values of  $\theta_w$  as input data for the boundary layer method (which have a standard deviation of error of 0.0054 radian) the results are likely to be in error by more than the 0.5 mm discovered already.

Thus we have been able to account for the level of discrepancy between experiment and prediction for values of  $\theta_w$ . However the full cause of the errors in the predicted values of  $\delta^*$  is not yet clear.



In summary of Section (5) it can be stated that the program PREDICT can be used to calculate uniquely the 'wallflows' required. However, the chief parameter to be calculated, namely  $\theta_w$ , can only be estimated approximately. The probable discrepancy between calculated values and experimental results is 0.0019 radian. The error in the calculated results is likely to be larger however if one considers discrepancies relative to true data. In Section (4.2.6) it was considered that the flow angle at the wall would need to be estimated to within 0.0017 radian ( $0.1^\circ$ ). As the error in our data is probably greater than twice the maximum required, there is clearly a need for improvement. The situation is however, probably not quite as bad as it appears, because the estimate in Section (4.2.6) assumed the flow angle along the entire perforated liner to be in error, while we are considering a more random situation in the present Section. In any case, using the proposed boundary condition based upon experimental data, we are able to predict the flow (and by inference the correct boundary condition) near a perforated wall more accurately than would be possible using the conventional linear boundary condition. The investigation of sources of error in this sub-section reveals that both components of the method, namely the characteristic function and the boundary layer analysis, produce erroneous results which are due to a large extent to inaccuracies in the components themselves. The boundary layer analysis, which was described in Section (3.5) is certainly amenable to improvement. The characteristic function, which was developed in Section (4.4) may be improved to some extent by the alteration of its form. In addition its accuracy could well be improved if the experimental data upon which it is based were made more accurate. Some suggestions regarding this step were made in Section (4.3.4).

## 6 COMPARISON BETWEEN EXPERIMENTAL RESULTS AND THOSE FROM 'PILOT'

In Section (5), it was demonstrated that the proposed interactive boundary condition, namely

$$\phi_x \pm \frac{1}{\rho(x)} \phi_z = k(x) \quad (6.1)$$

is almost certain to simulate the flow near a perforated wall more accurately than the conventional linear boundary condition, namely

$$\phi_x \pm \frac{1}{\rho} \phi_z = 0 \quad (6.2)$$

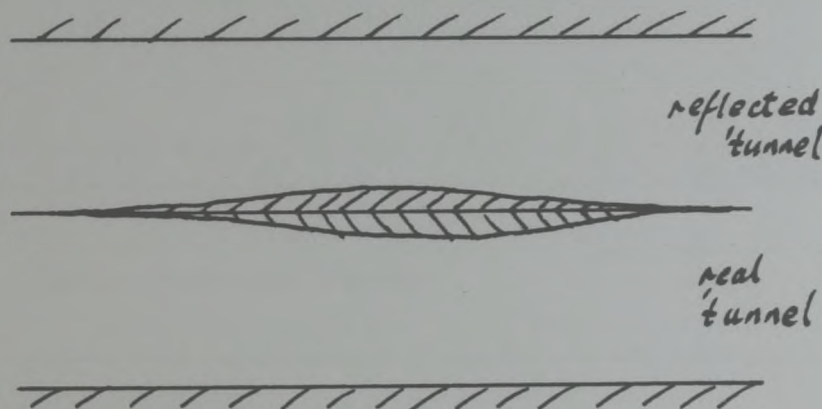
The logical step is now taken, to incorporate the new boundary condition into an inviscid flow calculation, and use the overall method to predict the windtunnel flows which were discussed at length in Section (4). The calculation scheme described in Section (3.4) and entitled 'PILOT' is used in this comparison. The wall characteristic developed in Section (4.4) is used in the program,

An attempt is made to predict the same four windtunnel flows that were investigated using the program PREDICT in Section (5). This work is mentioned in Section (3.7) where it was used to verify the effectiveness of the new boundary condition. In most commercial windtunnels which are used to examine two-dimensional flows, little attention is paid to the nett flow rate of air through the porous walls. Indeed, the majority of these windtunnels incorporate the diffuser suction process and as such, to measure such mass flows in them would be quite difficult. However, to allow the program PILOT to operate, the volumetric rates of air through the wall are specified (as it may be recalled that the option of specifying either plenum pressure or wall flow rate was incorporated into PILOT). These flow rates are determined by graphical integration of the relevant curves in Figure (44), namely the graph of  $\theta_w$  with  $x$ . It should be noted here that the actual viscous flow through the wall is used, rather than any effective inviscid parameter. Once calculated, the mass flow rates are divided by standard sea-level air density to give the volumetric flow rates



which are required by PILOT. Strictly, a lower value of air density should be used, to be consistent with the experimental conditions. This value would be approximately 20% less than the standard figure, but it is not considered that this discrepancy would have a significant influence on the following argument.

To represent the contoured wall used in the experiments, the windtunnel working section is considered to be reflected in that wall, as shown below



Thus the working section height is doubled. The effective cross sectional area of the contoured wall is estimated to be  $0.002 \text{ m}^2$ . This is also doubled and is considered to be the cross sectional area of a circular cylinder mounted at the centre of the wall, or at the centre of the effective working section. Clearly, assuming that a slender shape is concentrated into a circle will cause errors in the solution. However, using equation (3.5), namely

$$\mu = \frac{u_{\infty} A}{\pi},$$

values of the doublet strengths are calculated and used in PILOT. For the various values of  $u_{\infty}$ , they are shown in Table (7). Clearly the contoured wall and its reflection are considered to represent an aerofoil at zero incidence and as such, no vortex is simulated in the wind-tunnel. The walls of the working section are simulated to be very

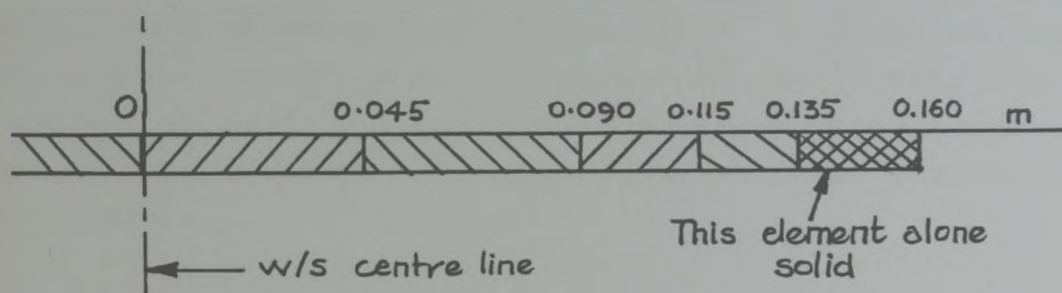
TABLE (7)

Data for operation of PILOT

For all configurations:

Number of source elements: 10 per wall  
 Working section height: 0.4046 m  
 Control Points positioned: 0.0001 x 0.4046 m  
 off wall

Position of ends of elements:



Configuration Symbol from Table 5 Data item	$\Delta$	$\phi$	$\otimes$	$\Sigma$
Doublet Strength $\mu / \text{m}^3 \text{s}^{-1}$	0.2874	0.2984	0.3070	0.3136
$U_{\infty} / \text{ms}^{-1}$ as calculated in Section 5.2.2	225.6	234.2	240.9	246.1
$\delta^*_{\text{INITIAL}}$ taken from upstream position in Col. (12) of Table ( )	1.37 mm	1.27 mm	1.21 mm	1.16 mm
Volumetric flow rate through each wall $/ \text{m}^3 \text{s}^{-1} / \text{unit width}$	-0.208	0.084	0.297	0.594



similar to those in the transonic windtunnel, in terms of the length of the perforated section of liner. All data relevant to the operation of PILOT are shown in Table (7). Unfortunately at the time of operation, the position of the freestream condition was fixed within the program, at twice the windtunnel height upstream of the working section centre-line. This position did not coincide with the freestream reference position in the experiments,

The results from PILOT are now presented and discussed. For the configuration indicated by the symbol  $\phi$  in Table (7), the calculation could not be brought to convergence, despite considerable effort using various levels of under-relaxation in the method. It appears that when the volumetric flow through the walls is near zero, the calculation becomes more unstable. Of the other three configurations (which were brought easily to convergence), only the data for the two extreme cases are presented.

We turn first to the predicted wall pressure coefficients. These are presented in Figure (52) for one wall (both walls being identical as the reflected flow is symmetrical). The experimental data are also shown in the Figure. The longitudinal ordinate is taken relative to the upstream end of the bottom liner used in the experiments, and the data from PILOT are arranged suitably on this ordinate. In the Figure, some data are also shown from an operation of PILOT using a conventional boundary condition of the form of Equation (6.2). To obtain a suitable value of 'P' in that equation, typical values of  $\delta^*$  (1.5 mm) and  $\Delta p/q$  (-0.01) are used in the gradient of the wall characteristic. After converting this gradient to be applicable to inviscid flow, it represents a value of P of 0.116. Observing the predicted and experimental data, it is clear that there is little comparison between them, except that they are of the same order. Mokry et al (1974) in attempting to predict wall pressures in a working section where an aerofoil was present, certainly managed rather better. An example of their work is shown in Figure (29). In Figure (39) the measured wall pressure distribution through our working section is shown. These data were all measured at one operation of the windtunnel. Clearly in the prediction due to PILOT we have the correct shape of curve, revealing the presence

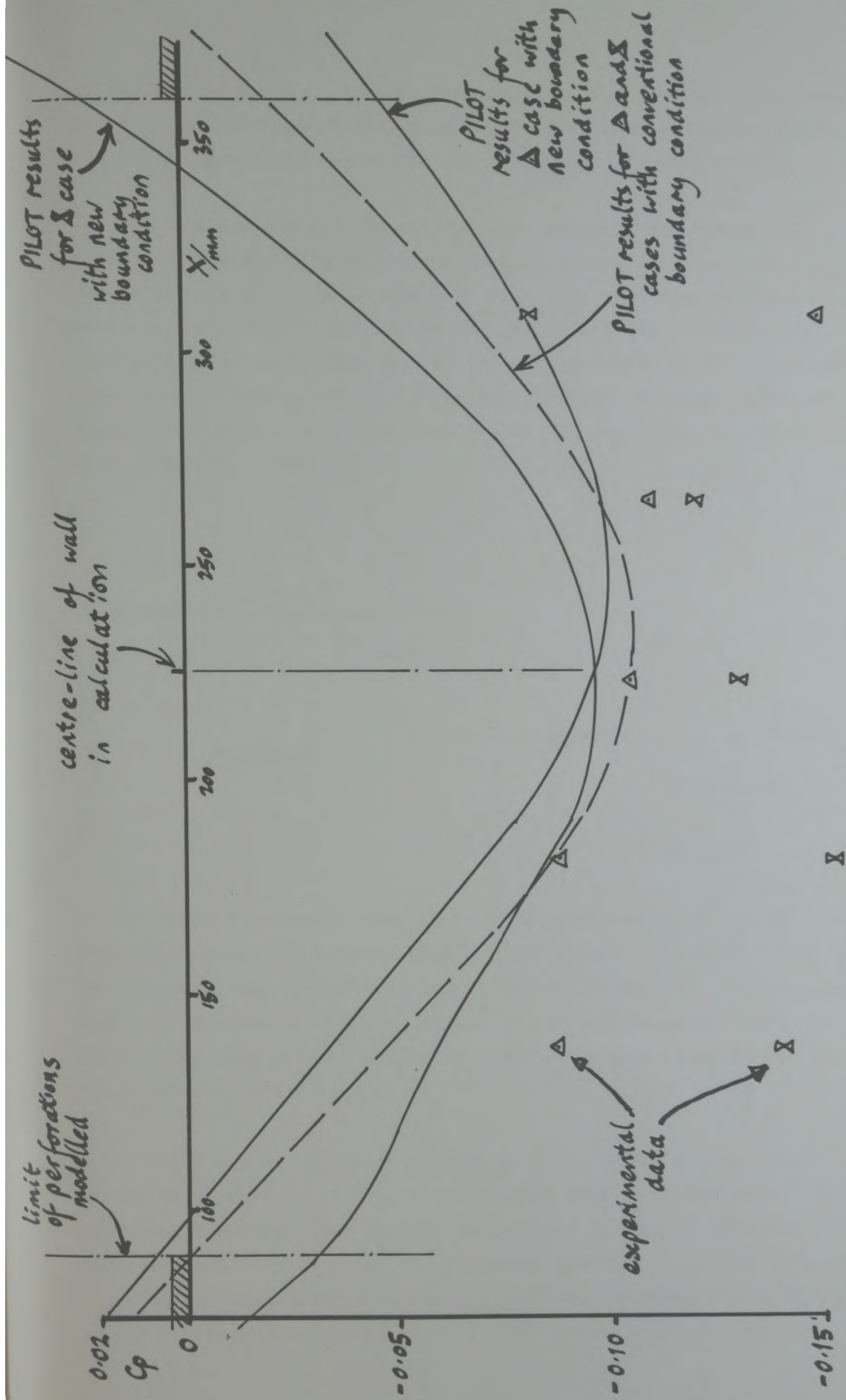
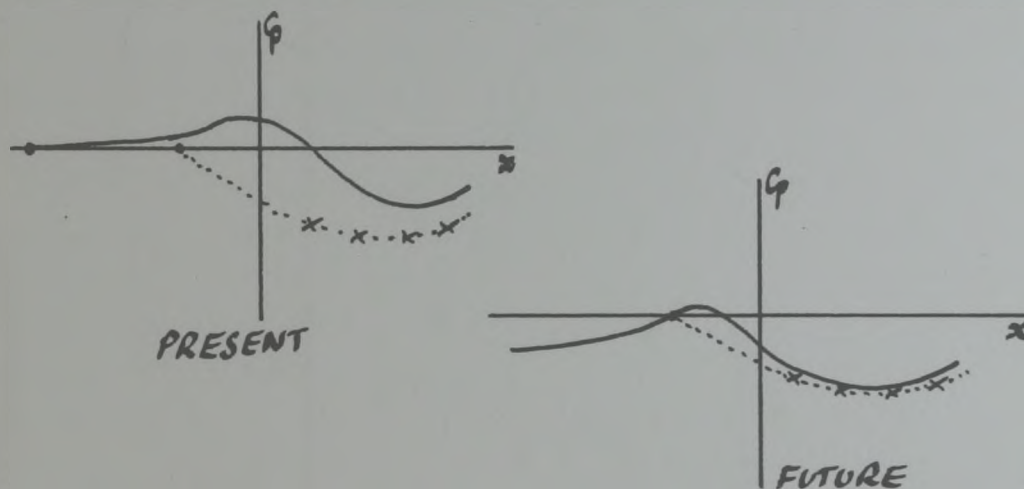


FIGURE (52) Results from PILOT compared with experiment - wall pressures.



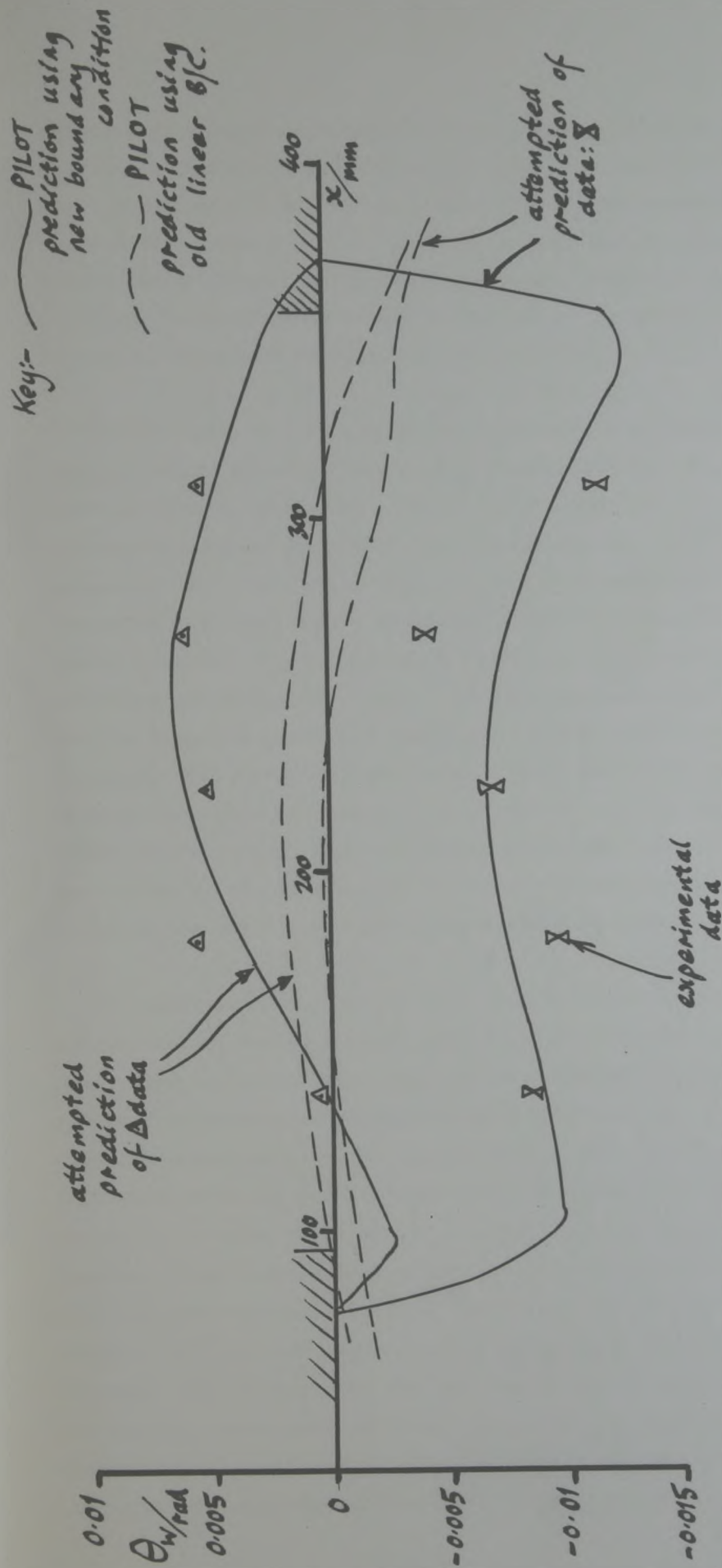
of the contoured wall. However the region of overspeeding experienced at entry to the perforated section in Figure (39) is not modelled by PILOT, nor is the under-speeding at the close of the perforated section.

One probable explanation for the poor prediction concerns the comment made earlier about the position of freeestream reference conditions. For the experimental results, the reference condition was measured at a position -109 mm on the ordinate shown, while for the prediction, it was at -585 mm. If the extrapolation of the  $C_p$  curves were as shown below, then by making the reference position consistent in future calculations, it seems likely that the predicted data would be more accurate.



It appears in Figure (52) that the implementation of the new boundary condition yields little alteration in the overall character of the results. It is interesting to note that both curves for the old boundary condition are concurrent. This is logical since the boundary conditions (including the size of the 'aerofoil') applied to both calculations are fixed and identical.

We turn now to the prediction of the flow angle in the viscous flow at the wall position. These data are presented in Figure (53). It is immediately obvious that the quality of this prediction (for the new boundary condition at least) is in marked contrast with that of  $C_p$  values. It is almost certain that the accuracy of the prediction is a direct result of specifying the volumetric flow rate through the wall.



FIGURE(53) Results from PILOT compared with experiment - wall crossflow angle.



Within a truncated perforated section, the calculation must generate sufficient crossflow to satisfy the nett flow rate of air through the wall specified. Thus, in the absense of strong crossflow surges any where along the wall, it is reasonable that the average crossflow predicted would closely match the experimental values. Although quite a simple 'bonus', there is no reason why it should not be utilized in future calculations to ensure good prediction.

In contrast to the results obtained with the new boundary condition, those obtained with the old linear version are not good. This is considered to be the result of two major deficiencies. First, the boundary condition is unable to take any account of the plenum chamber pressure. As a result of this, it is quite impossible for the nett crossflow required, to be achieved. Secondly, the boundary condition cannot simulate regions of solid wall and thus, continues to predict crossflow all along the liner. It may cause confusion here that there are two separate solutions using the linear boundary condition, whereas in Figure (52) there was one curve. This is because Figure (53) represents the viscous crossflow at the wall, and not the effective inviscid crossflow (for which the two curves would coincide). In conversion from the latter to the former, the different growth rates of the boundary layer in the two flows causes the different viscous crossflows.

It appears in Figure (53) that the discrepancy between the prediction due to the new boundary condition and the experimental data is of the same order as that in the results from PREDICT (where there was a standard deviation of approximately 0.0028 radian). If the present calculation method were to be used to model the flow in a windtunnel where a lifting aerofoil was present, then it would seem reasonable that the crossflow at both walls would be predicted with this accuracy. This accuracy would also appear to be considerably better than that obtained with the conventional boundary condition (for the viscous crossflow at least). If the flow angle at both walls were accurately predicted then it would seem likely that the incidence interference along the windtunnel centre-line would also be predicted well. In this respect, the results appears very encouraging. However, the relationship between the effective inviscid flow and the viscous flow at the wall involves the boundary layer

displacement thickness (see for example Equation (5.4)), so this too must be examined.

The prediction of the displacement thickness due to PILOT is shown in Figure (54). As the viscous crossflow predicted with the new boundary condition is so much better than that due to the old condition, it is not surprising that the values of  $\delta^*$  calculated are also far better. However there remains a considerable discrepancy between predicted and experimental data. Once again this discrepancy is of the same order as that discovered during the discussion of the results from PREDICT (namely 0.44 mm  $\sigma$ ). The significant underestimate in the predicted growth rate of  $\delta^*$  will cause the effective inviscid crossflow modelled to be in error also (for example by  $0.5^\circ$ ) although the viscous crossflow upon which it is based may be far more accurate.

In summary it appears that the computer program PILOT can be used to model complete windtunnel flows and provided that the nett volumetric flow rate of air through the walls is specified accurately, the prediction of the viscous crossflow angle at the walls is quite good. It would seem logical that if the suggestions put forward in Section (5) were implemented, namely improvements in the boundary layer analysis and the wall characteristic, then PILOT would be able to predict even more accurately the values of  $\theta_w$  and also the effective inviscid flow angle,  $\bar{\theta}_w$ . The rather poor prediction of wall pressure coefficients could be improved if the position of definition of the freestream reference condition were altered to be consistent with the experiments modelled. Finally, accounting for compressibility even in a linearized manner would be likely to improve many aspects of the results from the program.



Key:- ——— PILOT results  
using new boundary condition

----- PILOT results  
using old linear boundary  
condition

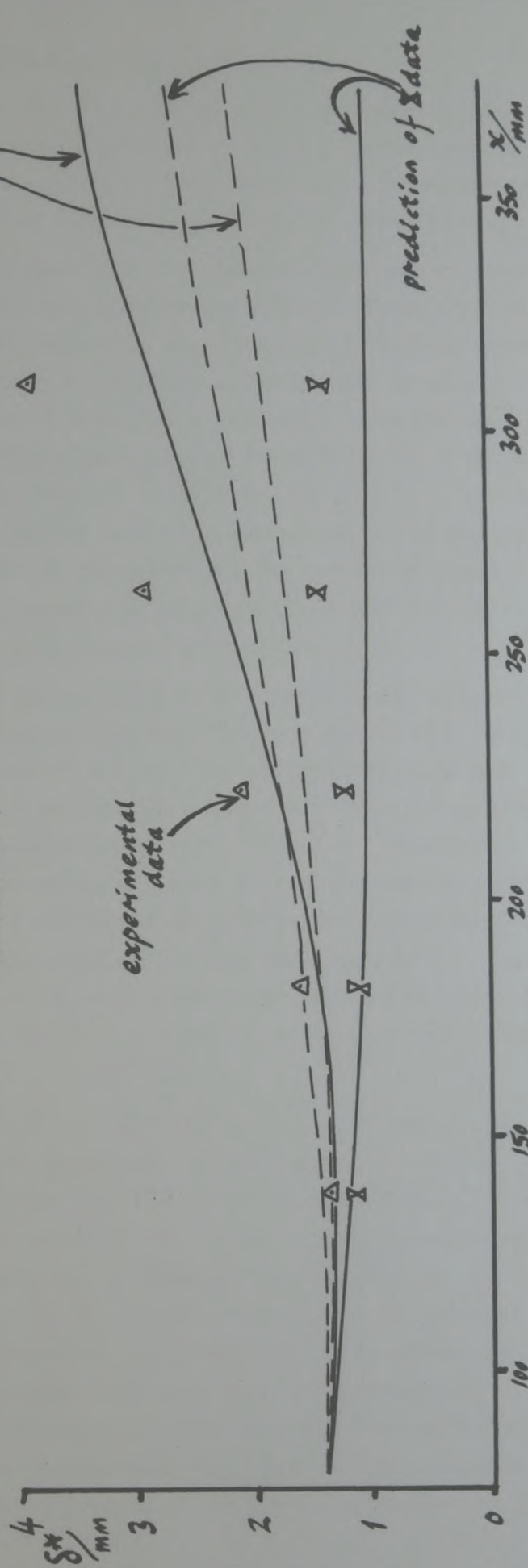


FIGURE (54) Results from PILOT compared with experiment - boundary layer displacement thickness.

## 7 SUMMARY OF CONCLUSIONS, WITH RECOMMENDATIONS

In summarizing the conclusions drawn throughout this report, it is considered more helpful to work in a logical order, rather than to follow the order of report sections. To assist reference, the relevant Section numbers are stated in parentheses.

The scheme proposed and developed in this report could, if successful, be used for a number of tasks. These are (2.2); to assist in the examination of the accuracy of methods used for calculating the flow of air around aerofoils; to predict the size of the influence that the windtunnel walls may have on the flow near the aerofoil; to increase the efficiency of operation of methods such as that of Kemp (1978), by providing values of the crossflow at the wall. Naturally before any of these tasks may be carried out, it is necessary for the proposed scheme to be successfully incorporated into a practical calculation method and it is recommended that this be carried out.

It has been suggested (Mokry et al, 1974 and Chan, 1980a) that the wall characteristic relevant to perforated walls should be evaluated experimentally (2.1). An attempt has been made here to fulfill this objective. The chief difficulty encountered in this work was the measurement of flow angle. The Conrad yawmeters used, were calibrated in a manner which subsequently appeared inadequate. The 0.19 degree standard deviation of error in the calibration did not nearly approach the required 0.1 degree worst error. It is recommended that the calibration be performed again, either with more detailed measurements, or by a more accurate method (4.2.6).

Another uncertainty involved in the experiments, relates to variations in flow parameters in the lateral direction, across the perforated bottom wall of the windtunnel (4.2.8). Particularly, a significant variation in the boundary layer displacement thickness, constituting a gradient of 1 degree, was discovered across the wall. It is not clear what level of non-uniformity may be tolerated for the present scheme to be effective and thus it is recommended that investigations be carried out; first to determine more precisely the nature of the non-uniformities which are present in the windtunnel and second, to examine whether these non-uniformities render the experimental data



inadequate for use in the present scheme.

The most important data derived from the experiments, were those relating to the crossflow at the perforated wall itself. The extensive analysis leading to these data, caused significant errors to be accumulated. The standard deviation of error in the values of the crossflow was calculated to be 0.31degree(4.3.4). This figure must be reduced in future work. There are two major factors which contribute to this error. The first, being the inaccuracy of the yawmeter calibration, was discussed earlier. The second is the error involved in calculating the derivative of the boundary layer displacement thickness with respect to the longitudinal ordinate. It is not clear how this can be reduced, particularly as it is considered to be generated, to no small extent, by the lateral non-uniformities in displacement thickness.

As a result of the experiments carried out, it has been possible to generate an empirical wall characteristic relating the following four parameters; the local crossflow through the perforated wall, Mach number, boundary layer displacement thickness and pressure drop across the wall(4.4). This characteristic takes the form of a polynomial function which is considered to be a good fit to the experimental data. There is evidence to suggest that the chosen function has some physical significance, but because the basic variables are restricted in their range, it has been found difficult to compare the characteristic with that of another worker, Goethert(1961). It has been estimated that the standard deviation of the discrepancy between experimental data and those produced by the characteristic function is 0.16 degree. An interesting phenomenon was discovered when the characteristic function was incorporated into a flow calculation scheme(5.2.2). It was found necessary to arrange the characteristic function in such a way that, at any point in the calculation scheme, as many as possible of the variables in the function may be numerically defined. Failure to achieve this, results in an unrealistic solution to the calculation.

To operate the computing scheme proposed in this work, a boundary layer prediction method has been developed(3.5). For present purposes however, the results from this method are not satisfactory. This is chiefly because the method does not account for wall roughness, which is clearly present for walls with



relatively large perforations. It is recommended that the boundary layer method in question be altered to account for wall roughness, even if in a very simple manner.

The wall characteristic function and the boundary layer method, discussed above, constitute the two 'viscous flow' components of the proposed interactive calculation scheme. The central purpose of this research was to define a boundary condition to interact these components with an inviscid flow calculation scheme. The proposed boundary condition is,

$$\phi_x \pm \frac{1}{\rho(x)} \phi_z = K(x) .$$

where  $\rho$  and  $K$  are calculated from the two 'viscous flow' components, discussed above.

The proposed computing scheme is first used to simulate the flow of air near the perforated wall of the windtunnel(5). The crossflow at the wall is predicted sensibly and uniquely and the values match experimental ones almost certainly more closely than would those generated by the boundary condition,

$$\phi_x \pm \frac{1}{\rho} \phi_z = 0 .$$

The standard deviation of the discrepancy between values of the crossflow drawn from the experiments and those from the prediction is 0.11 degree. This however represents rather more error than that which is required, namely 0.10 degree maximum discrepancy. It is considered that the discrepancy in question may be reduced by altering the form of the wall characteristic function and by improving the accuracy of the experiments upon which the characteristic is based. It is recommended that these improvements be carried out. The prediction of the distribution of boundary layer displacement thickness along the perforated wall is not good and this is considered to be due to the inadequacy in the boundary layer method mentioned earlier. It seems likely that when used in conjunction with a practical flow calculation package, use of the wall boundary condition unit will not significantly increase computing times.



The proposed scheme has been employed to simulate the incompressible flow of air through a perforated working section of finite length where an aerofoil is mounted. The new boundary condition was again used, to link the viscous and inviscid parts of the calculation procedure. The calculation method was successful, producing unique, realistic solutions. It was clear that it would be useful for investigating some aspects of wind-tunnel flows which had previously received little attention(3.8). A comparison with experimental results was made using those from the calculation method with both the conventional boundary condition and the proposed boundary condition employed. The results obtained using the latter condition were in notably better agreement with experiment than those obtained using the former, at least for the values of crossflow at the wall. This is chiefly because the presence of the term  $K(x)$  on the righthand side of the new boundary condition equation permits the plenum chamber pressure(and indirectly the net volumetric flow rate through the wall) to be accounted for. The good comparison with experiment, mentioned above, was obtained by matching the volumetric flow rate of air through the wall in the calculations, with that measured during experiment. The prediction of wall pressure coefficients was not good. This was caused mainly by an inconsistency in the freestream reference position, between the calculation and the experiments. In future calculations, this should be rectified. Also the entire calculation method would be improved by accounting for compressibility, even in a linearized manner. The improvements in the characteristic function and the boundary layer analysis which were recommended earlier, are also likely to yield benefit in the present calculation method.

It has also been demonstrated that the new boundary condition is amenable to use in a typical commercially used flow calculation method, that of Catherall(1975), in Appendix(4).

To summarize, it has been demonstrated that the new inviscid flow boundary condition to be applied at perforated walls, namely

$$\phi_x \pm \frac{1}{\rho(x)} \phi_z = K(x)$$

is a significant improvement over the conventional wall boundary condition, when used in an interactive flow calculation scheme. In this boundary condition,  $P(x)$  and  $K(x)$  are drawn from an empirical wall characteristic and from a calculated distribution of boundary layer displacement thickness on the perforated wall.

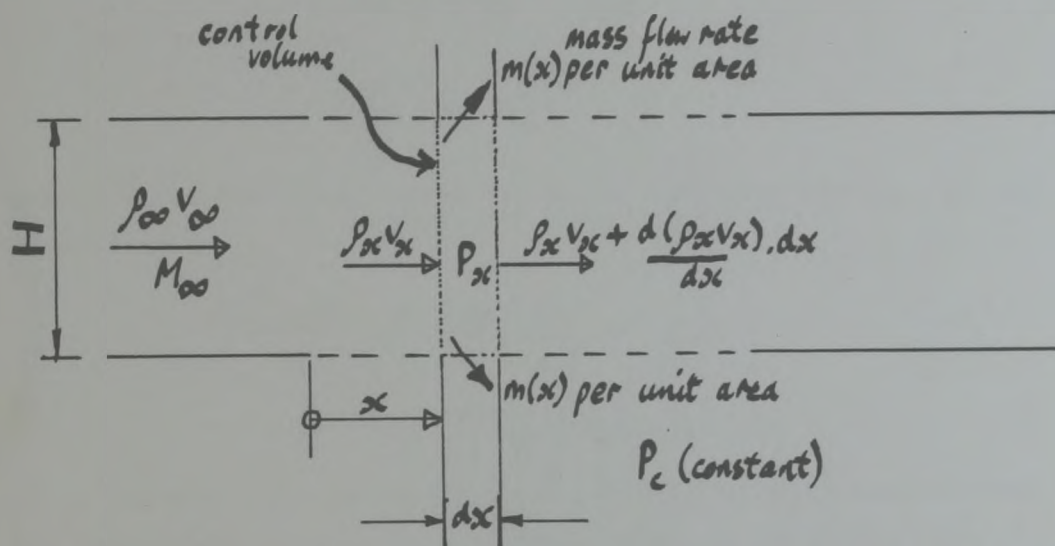


## APPENDIX 1

### Prediction of the pressure distribution in an empty perforated working section.

Goethert(1961, pp287-8) presents an approach for calculating the flow of air through a square working section with four perforated walls. A very similar analysis is used here, except that the working section is not assumed to be square and only two walls are now treated as perforated. The flow through the working section is assumed to be inviscid. In addition, it is assumed to be adiabatic and isentropic. In the following treatment, one-dimensional flow equations are used.

Consider the flow through the working section shown below.



The top and bottom walls are perforated as indicated, while the sidewalls are considered to be wholly solid. The working section has a height 'H' and width 'W'.

Applying the principle of conservation of mass to the control volume indicated, we find that

$$WH \left( \rho_x V_x + \frac{d(\rho_x V_x)}{dx} dx \right) = WH \rho_x V_x - 2W m(x) dx .$$

Thus

$$\frac{d(\rho_x V_x)}{dx} = - \frac{2 m(x)}{H} . \quad (1)$$

Now we may write

$$\frac{d(\rho_x V_x)}{dx} = \rho_x \left( \frac{dV_x}{dx} \right) + V_x \left( \frac{d\rho_x}{dx} \right) . \quad (2)$$

The Euler equation for inviscid, one-dimensional flow may be written

$$V_x \left( \frac{dV_x}{dx} \right) = - \frac{1}{\rho_x} \left( \frac{d\rho_x}{dx} \right) \quad (3)$$

Also in adiabatic flow it may be shown that

$$\left( \frac{d\rho_x}{dx} \right) = \frac{\rho_x}{\gamma P_x} \left( \frac{dP_x}{dx} \right) \quad (4)$$

Combining Equations (1), (2), (3) and (4), we find that

$$\begin{aligned} -2 \frac{m(x)}{H} &= \rho_x \left( \frac{-1}{V_x \rho_x} \left( \frac{d\rho_x}{dx} \right) \right) + V_x \left( \frac{\rho_x}{\gamma P_x} \left( \frac{dP_x}{dx} \right) \right), \\ \text{or} \quad &= \frac{dP_x}{dx} \left( \frac{V_x \rho_x}{\gamma P_x} - \frac{1}{V_x} \right) \quad (5) \end{aligned}$$

Now for a perfect gas

$$\frac{\gamma P_x}{\rho_x} = a_x^2$$

(where ' $a_x$ ' is the local speed of sound) and thus Equation (5) may be written as

$$\begin{aligned} -2 \frac{m(x)}{H} &= \frac{dP_x}{dx} \left( \frac{V_x}{a_x^2} - \frac{1}{V_x} \right) \\ \text{or} \quad &= \frac{dP_x}{dx} \cdot \frac{1}{V_x} (M_x^2 - 1) \quad (6) \end{aligned}$$

If it assumed that the disturbances in the working section from the freestream conditions are small, then we may write that (approximately)

$$-2 \frac{m(x)}{H} = \frac{dP_x}{dx} \cdot \frac{1}{V_x} (M_\infty^2 - 1) \quad (7)$$

At the perforated walls of the working section, Goethert applies a linear relationship between the pressure differences across the walls and the crossflow through them. In the notation of Section (2.1), this relationship would be written

$$\frac{\Delta P}{q_\infty} = K \frac{(\rho v) h}{(\rho v)_\infty}$$

or in present notation

$$\frac{(P_x - P_c)}{\frac{1}{2} \rho_\infty V_\infty^2} = K \frac{m(x)}{\rho_\infty V_\infty} \quad (8)$$



When combined in a suitable manner with Equation(7) we find that

$$-4 \frac{(p_x - p_c)}{KH V_\infty} = \frac{dp_x}{dx} \cdot \frac{1}{V_x} (M_\infty^2 - 1)$$

or that

$$\frac{dp_x}{dx} = \frac{-4 (p_x - p_c)}{KH (M_\infty^2 - 1)} \quad (9)$$

After integration, we find that

$$(p_x - p_c) = C e^{\frac{-4x}{HK (M_\infty^2 - 1)}} \quad (10)$$

Clearly, the pressure difference across the perforated wall is an exponential function of the longitudinal ordinate 'x'. It may be shown that this function has a distance to double amplitude,  $\Delta x$ , where

$$\Delta x = \ln 2 / \frac{-4}{HK (M_\infty^2 - 1)} \quad (11)$$

A distance to double amplitude only exists for values of  $M_\infty$  less than unity. For values of  $M_\infty$  greater than unity, the pressure disturbances in the working section die away in the stream direction and a relevant distance to half amplitude may be defined.

Equation(10), which gives the form of the pressure disturbance along the working section, is considerably simpler than that which Goethert presents. It is however similar in character.

## APPENDIX 2

Development of equations of continuity to be applied at a porous wall.

(A) Assuming viscous flow near wall.

Applying the principle of conservation of mass to the flow through the control volume shown in Figure (6,a) we find that

$$\int_0^L \rho u(z) dz - \int_0^L \left( \rho u(z) + \frac{\partial (\rho u(z))}{\partial x} \cdot \delta x \right) dz + \rho_w v_w \delta x - \rho_e v_e \delta x = 0. \quad (1)$$

Now the boundary layer displacement thickness is defined as

$$\delta^* = \int_0^L \left( 1 - \frac{\rho u(z)}{\rho_e u_e} \right) dz.$$

$$\text{So } \rho_e u_e \delta^* = \int_0^L (\rho_e u_e - \rho u(z)) dz$$

$$\text{or } = \rho_e u_e L - \int_0^L \rho u(z) dz.$$

$$\text{Thus } \int_0^L \rho u(z) dz = \rho_e u_e (L - \delta^*) \quad (2)$$

Similarly;

$$\left( \delta^* + \frac{d\delta^*}{dx} \cdot \delta x \right) = \int_0^L \left( 1 - \frac{\left( \rho u(z) + \frac{\partial (\rho u(z))}{\partial x} \cdot \delta x \right)}{\left( \rho_e u_e + \frac{d(\rho_e u_e)}{dx} \cdot \delta x \right)} \right) dz$$

$$\text{or } \left( \rho_e u_e + \frac{d(\rho_e u_e)}{dx} \cdot \delta x \right) \left( \delta^* + \frac{d\delta^*}{dx} \cdot \delta x \right) = \int_0^L \left( \left( \rho_e u_e + \frac{d(\rho_e u_e)}{dx} \cdot \delta x \right) - \left( \rho u(z) + \frac{\partial (\rho u(z))}{\partial x} \cdot \delta x \right) \right) dz$$

$$\text{or } = L \left( \rho_e u_e + \frac{d(\rho_e u_e)}{dx} \cdot \delta x \right) - \int_0^L \left( \rho u(z) + \frac{\partial (\rho u(z))}{\partial x} \cdot \delta x \right) dz.$$

$$\text{Thus } \int_0^L \left( \rho u(z) + \frac{\partial (\rho u(z))}{\partial x} \cdot \delta x \right) dz = \left( \rho_e u_e + \frac{d(\rho_e u_e)}{dx} \cdot \delta x \right) \left( L - \left( \delta^* + \frac{d\delta^*}{dx} \cdot \delta x \right) \right). \quad (3)$$



Combining equations (1), (2) and (3) we find that;

$$\rho_e u_e (L - \delta^*) - \left( \rho_e u_e + \frac{d(\rho_e u_e)}{dx} \delta x \right) \left( L - \left( \delta^* + \frac{d\delta^*}{dx} \delta x \right) \right) + \rho_w v_w \delta x - \rho_e v_e \delta x = 0.$$

Multiplying out, this equation becomes;

$$\rho_e u_e \frac{d\delta^*}{dx} \delta x - \frac{d(\rho_e u_e)}{dx} \delta x (L - \delta^*) - \frac{d(\rho_e u_e)}{dx} \frac{d\delta^*}{dx} \delta x^2 + \rho_w v_w \delta x - \rho_e v_e \delta x = 0.$$

Neglecting the term containing  $\delta x^2$  we find that;

$$(L - \delta^*) \frac{d(\rho_e u_e)}{dx} - \rho_e u_e \frac{d\delta^*}{dx} + \rho_e v_e - \rho_w v_w = 0. \quad (4)$$

(B) Assuming inviscid flow near wall.

When the principle of conservation of mass is applied to the flow through the control volume shown in Figure (6,b), we find that;

$$L \rho_e u_e - L \left( \rho_e u_e + \frac{d(\rho_e u_e)}{dx} \delta x \right) + \overline{\rho_w v_w} \delta x - \rho_e v_e \delta x = 0, \quad (5)$$

or cancelling, that

$$-L \frac{d(\rho_e u_e)}{dx} + \overline{\rho_w v_w} - \rho_e v_e = 0. \quad (6)$$

Here, it has been assumed that the density and longitudinal component of velocity are constant across the depth of the control volume and are equal to their respective values at the position  $z = L$ . This assumption is approximately correct on the following grounds:-

Cebeci and Smith (1974:73-75) have proved that when the stream curvature is small, the pressure gradient across a turbulent boundary layer with wall transpiration is insignificant when compared with the longitudinal pressure gradients normally experienced.

If we assume that the flow is adiabatic, then the following equation applies;

$$\frac{d\rho_e}{\rho_e} = \frac{1}{\gamma} \frac{dP_e}{P_e} \quad (7)$$

Additionally, as the flow is isentropic, we can show that;

$$\frac{du_e}{u_e} = -\frac{1}{\gamma M_e^2} \cdot \frac{dP_e}{P_e} \quad (8)$$

For small disturbances on the pressure  $P_e$ , using Equation (7) and (8) it can be shown that

$$\frac{\Delta \rho_e u_e}{\rho_e u_e} = \frac{1}{\gamma} \left( 1 + \frac{1}{M_e^2} \right) \left( \frac{\Delta P_e}{P_e} \right) + O\left(\frac{\Delta P_e}{P_e}\right)^2, \quad (9)$$

Except at Mach numbers very close to unity, it is possible to neglect the term in  $(\frac{\Delta P_e}{P_e})^2$  in Equation (9). So;

$$\frac{\Delta \rho_e u_e}{\rho_e u_e} = \frac{1}{\gamma} \left( 1 + \frac{1}{M_e^2} \right) \left( \frac{\Delta P_e}{P_e} \right) \quad (10)$$

It follows that;

$$\frac{\Delta \rho_e u_e}{\Delta x} = \frac{1}{\gamma} \left( 1 + \frac{1}{M_e^2} \right) \left( \frac{\rho_e u_e}{P_e} \cdot \frac{\Delta P_e}{\Delta x} \right)$$

and that;

$$\frac{\Delta \rho_e u_e}{\Delta z} = \frac{1}{\gamma} \left( 1 + \frac{1}{M_e^2} \right) \left( \frac{\rho_e u_e}{P_e} \cdot \frac{\Delta P_e}{\Delta z} \right)$$

But from the work of Cebeci and Smith (1974) mentioned above,  $\frac{\Delta P_e}{\Delta z}$  is at least an order of magnitude less than  $\frac{\Delta P_e}{\Delta x}$ . It follows that  $\frac{\Delta \rho_e u_e}{\Delta z}$  will also be an order of magnitude less than  $\frac{\Delta \rho_e u_e}{\Delta x}$ . Hence in Figure (6,b) it is assumed that the variation in  $\rho_e u_e$  across the depth of the boundary layer is negligible when compared to the longitudinal variations in  $\rho_e u_e$ .



### APPENDIX 3.

#### Practical running of the FORTRAN computer program PILOT

The program, when used on a Honeywell level 66/60 computer occupies approximately 21,000 words of memory. It should be noted that, at present, the maximum number of wall elements permissible is 40. Altering this figure to 80 for example, would move the necessary memory size to approximately 43,000 words.

For a typical windtunnel flow simulation (where an aerofoil is present and 20 wall elements are used) involving compilation and execution for 3 flow configurations, the total computing time is approximately 55 seconds. Of this, 4 seconds is compilation and the three configurations require about 17 seconds each for calculation.

The calculations converge in, between 20 and 30 inviscid iterations each. Each inviscid iteration normally involves about 7 viscous loops.

The structure of the input data for the program is now presented, followed by a program listing and typical input and output data. The listing is marked with the letters used in the flow diagram, Figure (11).

DATA - Denoted by - program variable names

I

NBIG  
H, DH, XUS

POS(1), POS(2), ..., POS(NBIG/4 + 1)

IR

2/7

DOUB, GAM, UFREE, DEL1, NSOLID

ICH, ICON, IBL

if ICH=1	if ICH=2
if ICON=1	if ICON=1
CPW	WF
if ICON=2	if ICON=2
CPB, CPT	WFB, WFT

## EXPLANATION

Number of windtunnel geometries.

(for each geometry considered :-)

Total number of wall elements.

Working section height, Displacement of control points from walls (divided by H), Position of freestream definition (upstream is negative).

Position of ends of wall elements (starting from origin, going downstream only).

Number of flow configurations.

(for each flow configuration)

Doublet strength ( $\mu$ ), Vortex strength ( $\Gamma$ ), Freestream speed ( $U_\infty$ ), Initial (upstream)  $S^*$ , Number of solid elements (at each end of a wall).

Decision constant (1 if plenum pressures to be specified, 2 if wall (low rates),

Decision constant (1 if plena are connected, 2 if separate), Decision constant (1 if boundary layer to be included, 2 if not).

Plenum chamber pressure coefficient (Cp1) Bottom and top plenum pressure coefficients || Nett volumetric flow rate into plena || Nett volumetric flow rate into bottom, and top plena.



**Appendix 3**  
**Listing of the Computer Program**  
**PILOT (p.218-234)**  
**has been removed for copyright reasons**

END

```
1
20 .4046 .0001 -.8092
   0. .045 .09 .115 .135 .160
1   .3136 0. 246.1 .00116 1
   2 2 1
   .594 .594
```

SAMPLE  
INPUT  
DATA.



0.40460 0.00010 0.04500 0.09000 0.11500 0.13500 0.16000  
 WALL FLOW SPECIFIED  
 0.313600 0.246.100000 -0.809200 0.001160 1UNCONNECTED PLENA 0.594 0.594  
 BOUNDARY LAYER VERSION

UPSTREAM DEVIATION FROM UINF 0.09307  
 CPB= -0.11716CPT= -0.11716WMB= 0.59376WMT= 0.59376  
 NO OF INV. LOOPS= 25 AV. NO OF B/L LOOPS= 11  
 POSITION CP VW(INV) DELTA STAR VW(VISC)  
 -0.14750 -0.02115 -0.65351 0.00140 0.00542  
 -0.12500 -0.04251 -3.23902 0.00133 -2.35711  
 -0.10250 -0.05211 -3.26150 0.00122 -2.29680  
 -0.06750 -0.07401 -2.65125 0.00110 -2.02844  
 -0.02250 -0.09777 -1.92947 0.00102 -1.65566  
 0.02250 -0.09603 -1.77321 0.00100 -1.69008  
 0.06750 -0.06328 -2.29546 0.00100 -2.23291  
 0.10250 -0.02515 -2.94489 0.00101 -2.79018  
 0.12500 0.01069 -3.17568 0.00101 -3.24093  
 0.14750 0.03680 0.32082 0.00106 -0.00871  
 -0.14750 -0.02115 0.65352 0.00140 0.00542  
 -0.12500 -0.04251 3.23902 0.00133 -2.35711  
 -0.10250 -0.05211 3.26149 0.00122 -2.29680  
 -0.06750 -0.07401 2.65126 0.00110 -2.02844  
 -0.02250 -0.09777 1.92947 0.00102 -1.65566  
 0.02250 -0.09603 1.77321 0.00100 -1.69008  
 0.06750 -0.06328 2.29546 0.00100 -2.23291  
 0.10250 -0.02515 2.94489 0.00101 -2.79018  
 0.12500 0.01069 3.17568 0.00101 -3.24093  
 0.14750 0.03680 -0.32082 0.00106 -0.00871

OUTPUT FROM  
 PILOT, WHEN  
 RUN ON  
 SAMPLE DATA

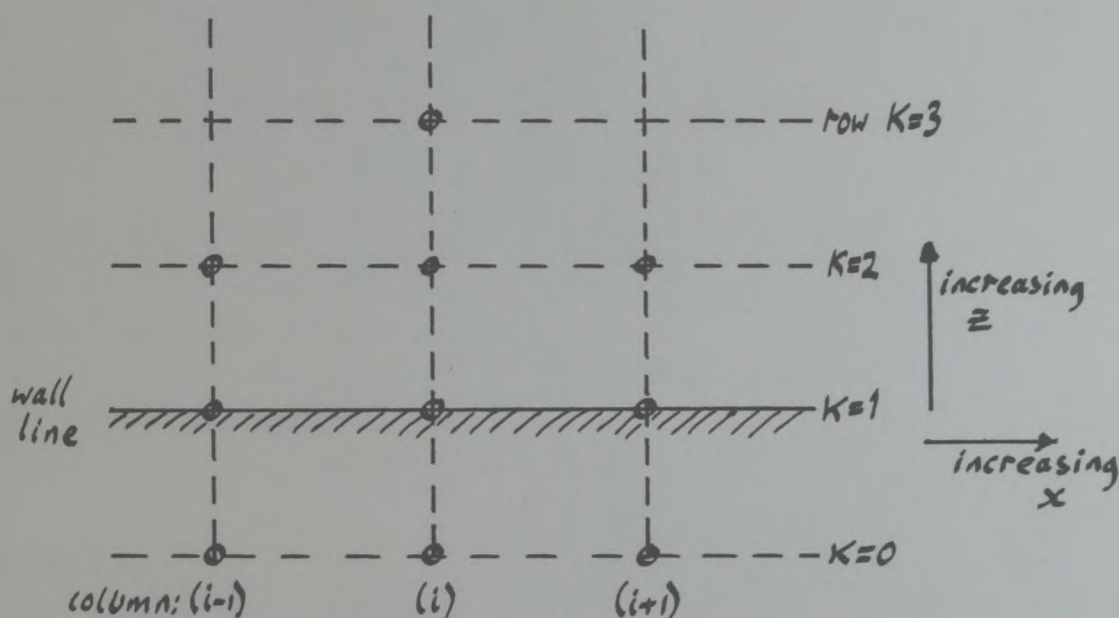
CL CP CL-V  
 -0.01195 -0.00000  
 -0.01244 0.00000  
 -0.01274 0.00000  
 -0.01267 0.00000  
 -0.01124 0.00000  
 -0.00805 0.00000  
 -0.00338 0.00000  
 0.00071 0.00000  
 0.00325 0.00000  
 0.00559 0.00000

}  $\phi$  INTERFERENCE.

#### APPENDIX 4.

Example adaptation of a practical transonic flow calculation to use the proposed wall boundary condition.

In the method of Catherall (1975), the non-linear transonic small perturbation equation is solved using finite difference analogues to the various derivatives. The following detailed explanation is taken from Catherall (1978), where the grid points near the lower wall of a wind-tunnel have the following arrangement.



At each grid point in a given column, an equation is generated, relating the values of  $\phi$  at three points in that column thus;

$$d_K \phi_{i,K-1}^{(n)} + c_K \phi_{i,K}^{(n)} + b_K \phi_{i,K+1}^{(n)} = a_K \quad (1)$$

Here, the superscript 'n' indicates that the values of  $\phi$  are to be generated in the present iteration of the calculation. Clearly, when Equation (1) has been generated for each point in a column (with the exception of  $K=0$  and its equivalent on the top wall), a set of simultaneous equations exist



which could be solved, but for the two extra unknowns,  $\phi_{i,0}^{(n)}$  and its equivalent on the top wall. Considering the bottom wall alone, the solution is achieved in the following way.

Equation (1) written for  $K=1$  is

$$d_1 \phi_{i,0}^{(n)} + c_1 \phi_{i,1}^{(n)} + b_1 \phi_{i,2}^{(n)} = a_1 \quad (2)$$

We use the conventional perforated wall boundary condition in the form

$$E \phi_x - \phi_z = 0 \quad (3)$$

Using finite difference analogues, Equation (3) becomes

$$E_i \left( \frac{\phi_{(i+1),1}^{(n-1)} - \phi_{(i-1),1}^{(n)}}{2 \Delta x} \right) - \left( \frac{\phi_{i,2}^{(n)} - \phi_{i,0}^{(n)}}{2 \Delta z} \right) = 0$$

or in Catherall's notation

$$\phi_{i,0}^{(n)} = \phi_{i,2}^{(n)} - TWL \quad (4)$$

where

$$TWL = \frac{\Delta z}{\Delta x} E_i \left( \phi_{(i+1),1}^{(n-1)} - \phi_{(i-1),1}^{(n)} \right) \quad (5)$$

Note that in Equation (5), the two values of  $\phi$  have either been evaluated in an earlier iteration or already calculated in the present iteration (the solution sweeping through the grid from left to right). Note also that Catherall allows  $E$  to be specific for this value of  $i$  (a provision which he appears not to have used, to date). Combining Equation (2) and (4) we find

$$c_1 \phi_{i,1}^{(n)} + (b_1 + d_1) \phi_{i,2}^{(n)} = (a_1 + TWL d_1) \quad (6)$$

The unknown  $\phi_{i,0}^{(n)}$  has now been eliminated and the solution of the simultaneous equations for the i'th column can now proceed.

Now let us write the improved form of boundary condition as

$$E\phi_x - \phi_z = EK \quad (7)$$

The equation corresponding to Equation (4) is then

$$\phi_{i,0}^{(n)} = \phi_{i,2}^{(n)} - TWL + 2\Delta z EK_i \quad (8)$$

and hence, Equation (6), when adapted becomes

$$c_1 \phi_{i,1}^{(n)} + (b_1 + d_1) \phi_{i,2}^{(n)} = (a_1 + TWL d_1 - 2\Delta z EK_i). \quad (9)$$

Equations (6) and (9) are essentially similar in character, although it is possible that the additional term in Equation (9) will significantly alter the calculated values of  $\phi$ . Note that in this equation, we would make full use of the ability to specify  $E_i$  and  $E K_i$  locally.



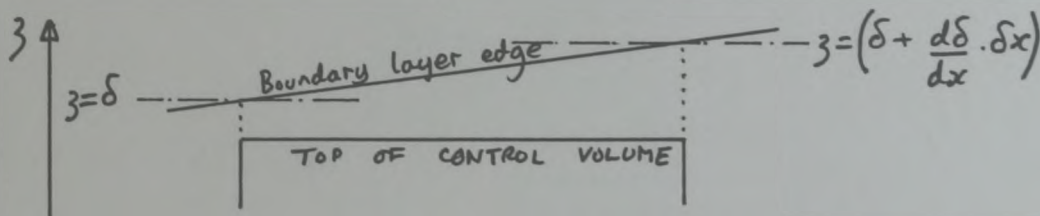
# APPENDIX 5.

Proof that a yawmeter may dip into a boundary layer without this significantly affecting predicted crossflows.

Using the two-dimensional control volume shown in Figure (6,a), and the principle of conservation of mass applied to the flow through it, we find that

$$\int_0^L \rho u(z) dz - \int_0^L \left( \rho u(z) + \frac{d\rho u(z)}{dx} \delta x \right) dz + \rho_w v_w \delta x - \rho_e v_e \delta x = 0. \quad (1)$$

If in Figure (6,a) the edge of the boundary layer were to lie outside the control volume, then we can say that the situation shown below exists.



While continuing to refer to conditions along the top edge of the control volume with a subscript 'e', we now refer to conditions at, or outside the line at which  $z = \delta$  with the subscript ' $\infty$ '.

Now approximately,

$$\delta^* = \int_0^{\delta} \left( 1 - \frac{\rho u(z)}{\rho_{\infty} u_{\infty}} \right) dz. \quad (2)$$

This equation is approximate because strictly, the upper limit on the integral should be outside the boundary layer completely ( $\delta$  being defined as the height at which the longitudinal speed in the boundary layer reaches 99% of its exterior value). Using Equation (2) we can write

$$\rho_{\infty} u_{\infty} \delta^* = \int_0^{\delta} (\rho_{\infty} u_{\infty} - \rho u(z)) dz, \quad (3)$$

or splitting the integral on the right hand side,

$$\rho_{\infty} u_{\infty} \delta^* = \rho_{\infty} u_{\infty} \delta - \int_0^{\delta} \rho u(z) dz \quad (4)$$

Now, integrating from 0 to  $\delta$  in two steps,

$$\rho_{\infty} u_{\infty} (\delta^* - \delta) = - \int_0^L \rho u(z) dz - \int_L^{\delta} \rho u(z) dz \quad (5)$$

or

$$\int_0^L \rho u(z) dz = \rho_{\infty} u_{\infty} (\delta - \delta^*) - \int_L^{\delta} \rho u(z) dz \quad (6)$$

If in Equation (2) we insert values relevant to the downstream end of the control volume, we find

$$\left( \delta^* + \frac{d\delta^*}{dx} \cdot \delta x \right) = \int_0^{\left( \delta + \frac{d\delta}{dx} \cdot \delta x \right)} \left( 1 - \frac{\left( \rho u(z) + \frac{\partial \rho u(z)}{\partial x} \cdot \delta x \right)}{\left( \rho_{\infty} u_{\infty} + \frac{d\rho_{\infty} u_{\infty}}{dx} \cdot \delta x \right)} \right) dz \quad (7)$$

Manipulating this equation in exactly the same manner as Equation (2), we find,

$$\begin{aligned} \int_0^L \left( \rho u(z) + \frac{\partial \rho u(z)}{\partial x} \cdot \delta x \right) dz &= \left( \rho_{\infty} u_{\infty} + \frac{d\rho_{\infty} u_{\infty}}{dx} \cdot \delta x \right) \cdot \left( \left[ \delta - \delta^* \right] + \frac{d[\delta - \delta^*]}{dx} \cdot \delta x \right) \\ &\quad - \int_L^{\left( \delta + \frac{d\delta}{dx} \cdot \delta x \right)} \left( \rho u(z) + \frac{\partial \rho u(z)}{\partial x} \cdot \delta x \right) dz \quad (8) \end{aligned}$$

Combining Equation (1), (6) and (8) and multiplying out, yields

$$\begin{aligned} \rho_w v_w \delta x - \rho_e v_e \delta x - \rho_{\infty} u_{\infty} \delta x \frac{d(\delta - \delta^*)}{dx} - (\delta - \delta^*) \delta x \frac{d\rho_{\infty} u_{\infty}}{dx} - \frac{d(\delta - \delta^*)}{dx} \delta x^2 \frac{d\rho_{\infty} u_{\infty}}{dx} \\ + \int_L^{\delta} \left( \frac{\partial \rho u(z)}{\partial x} \cdot \delta x \right) dz + \int_{\delta}^{\left( \delta + \frac{d\delta}{dx} \cdot \delta x \right)} \rho u(z) dz + \int_{\delta}^{\left( \delta + \frac{d\delta}{dx} \cdot \delta x \right)} \left( \frac{\partial \rho u(z)}{\partial x} \cdot \delta x \right) dz = 0 \quad (9) \end{aligned}$$



The second from last term in Equation (9) is an integral of the upstream distribution of  $\rho u(z)$ , from the height  $\delta$  upwards. For these values of  $z$ , the expression  $\rho u(z)$  must be equal to  $\rho_\infty u_\infty$ , within 1%. The final term in Equation (9) is also an integral from  $\delta$  upwards. Here, it assumed that the error incurred by assuming

$$\frac{\partial \rho u(z)}{\partial x} = \frac{d \rho_\infty u_\infty}{dx}$$

is negligible for  $z \geq \delta$ . With these two alterations, and after some manipulation, Equation (9) becomes

$$\rho_w v_w - \rho_e v_e + \rho_\infty u_\infty \frac{d\delta^*}{dx} - (\delta - \delta^*) \frac{d \rho_\infty u_\infty}{dx} + \frac{d\delta^*}{dx} \delta x \cdot \frac{d \rho_\infty u_\infty}{dx} + \int_L^\delta \frac{\partial \rho u(z)}{\partial x} dz = 0. \quad (10)$$

The second to last term in this equation is an order of magnitude smaller than the other terms. Hence,

$$\rho_w v_w - \rho_e v_e + \rho_\infty u_\infty \frac{d\delta^*}{dx} - (\delta - \delta^*) \frac{d \rho_\infty u_\infty}{dx} + \int_L^\delta \frac{\partial \rho u(z)}{\partial x} dz = 0. \quad (11)$$

We can write

$$\int_L^\delta \frac{\partial \rho u(z)}{\partial x} dz = \int_L^\delta \left( \frac{\partial \rho u(z)}{\partial x} - \frac{d \rho_\infty u_\infty}{dx} \right) dz + \int_L^\delta \frac{d \rho_\infty u_\infty}{dx} dz,$$

or

$$= \int_L^\delta \left( \frac{\partial \rho u(z)}{\partial x} - \frac{d \rho_\infty u_\infty}{dx} \right) dz + (\delta - L) \frac{d \rho_\infty u_\infty}{dx}. \quad (12)$$

Substituting Equation (12) into Equation (11),

$$\rho_w v_w - \rho_e v_e + \rho_\infty u_\infty \frac{d\delta^*}{dx} + \frac{d \rho_\infty u_\infty}{dx} \cdot (-(\delta - \delta^*) + (\delta - L)) + \int_L^\delta \left( \frac{\partial \rho u(z)}{\partial x} - \frac{d \rho_\infty u_\infty}{dx} \right) dz = 0$$

or on re-arranging

$$(L - \delta^*) \frac{d\rho_\infty u_\infty}{dx} - \rho_\infty u_\infty \frac{d\delta^*}{dx} + \rho_e v_e - \rho_w v_w = - \int_L^\delta \left( \frac{\partial \rho u(z)}{\partial x} - \frac{d\rho_\infty u_\infty}{dx} \right) dz. \quad (13)$$

We can compare this with Equation (3.1), namely

$$(L - \delta^*) \frac{d\rho_e u_e}{dx} - \rho_e u_e \frac{d\delta^*}{dx} + \rho_e v_e - \rho_w v_w = 0. \quad (14)$$

In this equation, the terms involving  $\rho_e u_e$  are evaluated using wall static pressures and thus are not affected by the yawmeter lying inside the boundary layer. They will be identical with the terms  $\rho_\infty u_\infty$  in Equation (13). Hence the only error incurred by using Equation (3.1) when the yawmeter dips into the boundary layer is the term

$$\int_L^\delta \left( \frac{\partial \rho u(z)}{\partial x} - \frac{d\rho_\infty u_\infty}{dx} \right) dz.$$

In considering the significance of this term, it is helpful to compare it with the terms in Equation (14) above.

As a specific example, for the simplified case of the turbulent boundary layer with a 'one-seventh' power law profile, that is, one given by

$$\frac{u(z)}{u_e} = \left( \frac{z}{\delta} \right)^{\frac{1}{7}}$$

in a low speed flow without transpiration and with a uniform freestream, the error term relative to the largest term in Equation (14) amounts to 5.7% if the yawmeter dips 30% into the boundary layer. With 20% dip, it is only 2.4% and for 10% dip a mere 0.6%.

For the more general case, where there is a streamwise variation in  $u_e$ , the following argument applies. In the outer part of the boundary layer, the integrand in the error term is likely to be an order of magnitude smaller than the derivative in the first term of Equation (14).



Also the interval on the integral (from  $L$  to  $\delta$ ) will be smaller than the term  $(L - \delta^*)$ . Provided the yawmeter does not dip further than say 30% into the boundary layer, it seems likely that the error term will remain insignificant compared to the first term in Equation (14).

## APPENDIX 6

Proof that the results obtained with the flow angle instruments are not significantly influenced by small angles of yaw.

We define first, the three components of velocity experienced by the yawmeter, in Figure (55). From that Figure, it can be stated that

$$\theta = \tan^{-1} \frac{v}{u} . \quad (1)$$

Also we can define

$$v = q \sin \alpha$$

and

$$u = q \cos \alpha \cos \beta \quad (2)$$

where  $\beta$  is a yaw angle potentially causing errors in the results. Combining Equations (1), (2) and (3) we find

$$\theta = \tan^{-1} \left( \frac{q \sin \alpha}{q \cos \alpha \cos \beta} \right)$$

or

$$= \tan^{-1} \left( \frac{\tan \alpha}{\cos \beta} \right)$$

In the following table, values of  $\theta$  are calculated for various combinations of  $\alpha$  and  $\beta$ .



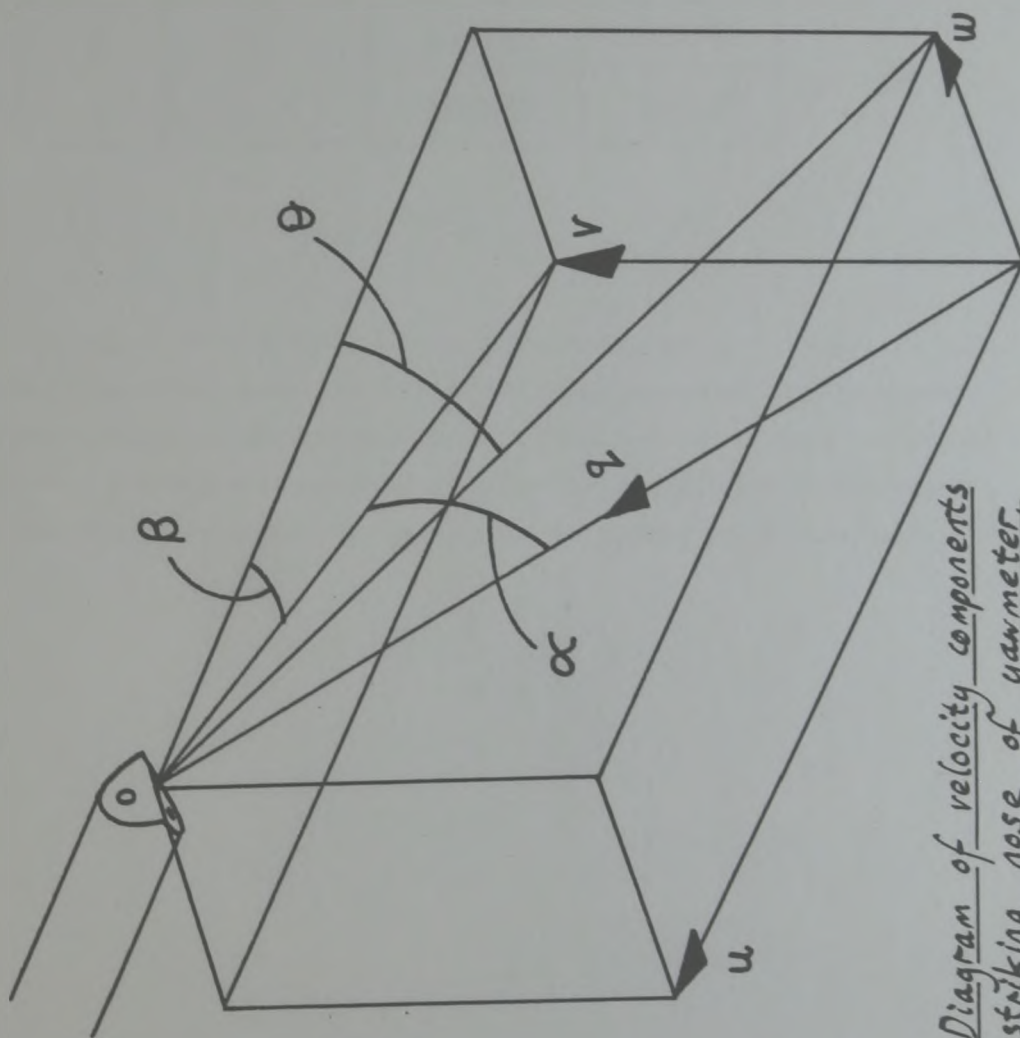


FIGURE (55) Diagram of velocity components  
in flow striking nose of yawmeter.

$\beta/\text{deg}$ \ $\alpha/\text{deg}$	0	2	5
0	0	2	5
2	0	2.0012	5.0030
5	0	2.0076	5.0190
10	0	2.0308	5.0767

Although it is not clear whether the value of  $\alpha$  , or  $\theta$  , or some intermediate value would be effectively registered by the pressure difference recorded at the yawmeter, it can be stated from the above table that the angle registered will not be significantly different from the true flow angle,  $\alpha$  , at least for values of  $\beta$  less than  $5^\circ$ .



## APPENDIX 7.

### Calibration of Yawmeters.

#### Method

Earlier measurements made with the yawmeters indicated that the form of the relation  $\frac{\Delta p}{q} \sim \theta$  for them was a straight line, at least over a limited range of  $\theta$  of about  $\pm 5$  degree ( $\Delta p$  is the difference between the pressures measured on the upper and lower faces of the yawmeter tip). Consequently, the calibration data required (for each yawmeter at any Mach number) were the gradient and the intercept of the straight line, i.e. it was necessary to determine the constants M and C in the equation

$$\frac{\Delta p}{q} = M\theta + C \quad (1)$$

These data were found in two distinct stages. First the gradients were found and then the intercepts.

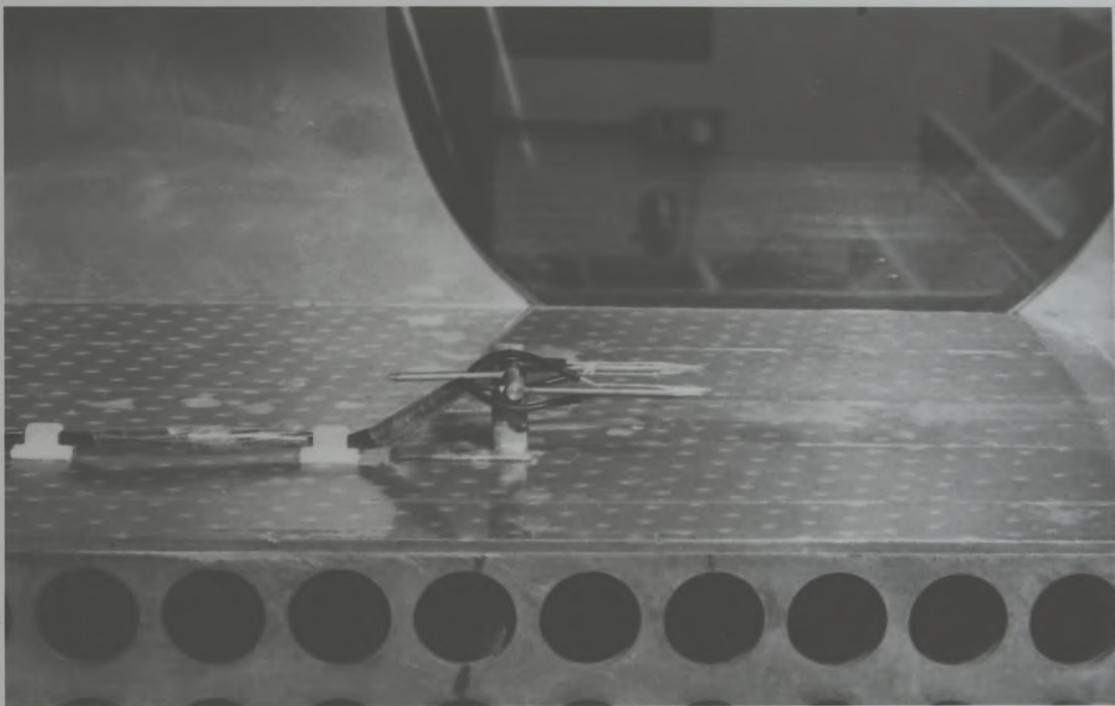
#### Gradient

The yawmeters were mounted together in a small device which fitted into the perforations of the bottom wall of the transonic windtunnel. The other perforations were sealed with plastic tape (see Plate(6)). The device allowed the yawmeters freedom in pitch simultaneously of about ten degree each side of the horizontal (see Figure(56)).

Measurements were made at three Mach numbers between 0.69 and 0.9. At each Mach number,  $\Delta p$  was measured for each yawmeter, at three incidences between  $-5$  and  $+5$  degree, the sense of positive incidence being shown on Figure(56). To avoid errors due to spatial variations in the flow field, the tips of the yawmeters were held in the same position throughout the traverse.

Assuming a negligible pressure gradient in the direction normal to the wall in the turbulent boundary layer, the wall static tapings were used to estimate the static pressures (and hence dynamic pressures) relevant to the yawmeters.

Yawmeter angles were determined from the heights of their tips and the height of the tailspike on the mounting device. These height measurements were made with a vertical travelling telescope. Inadvertent yawing of the mounting device was always kept below  $0.5$  degree (up to  $5$  degrees of yaw are permissible before the effective



PLATE(6) Device for determining the gradient of the  
yawmeter calibration ; mounted in windtunnel.



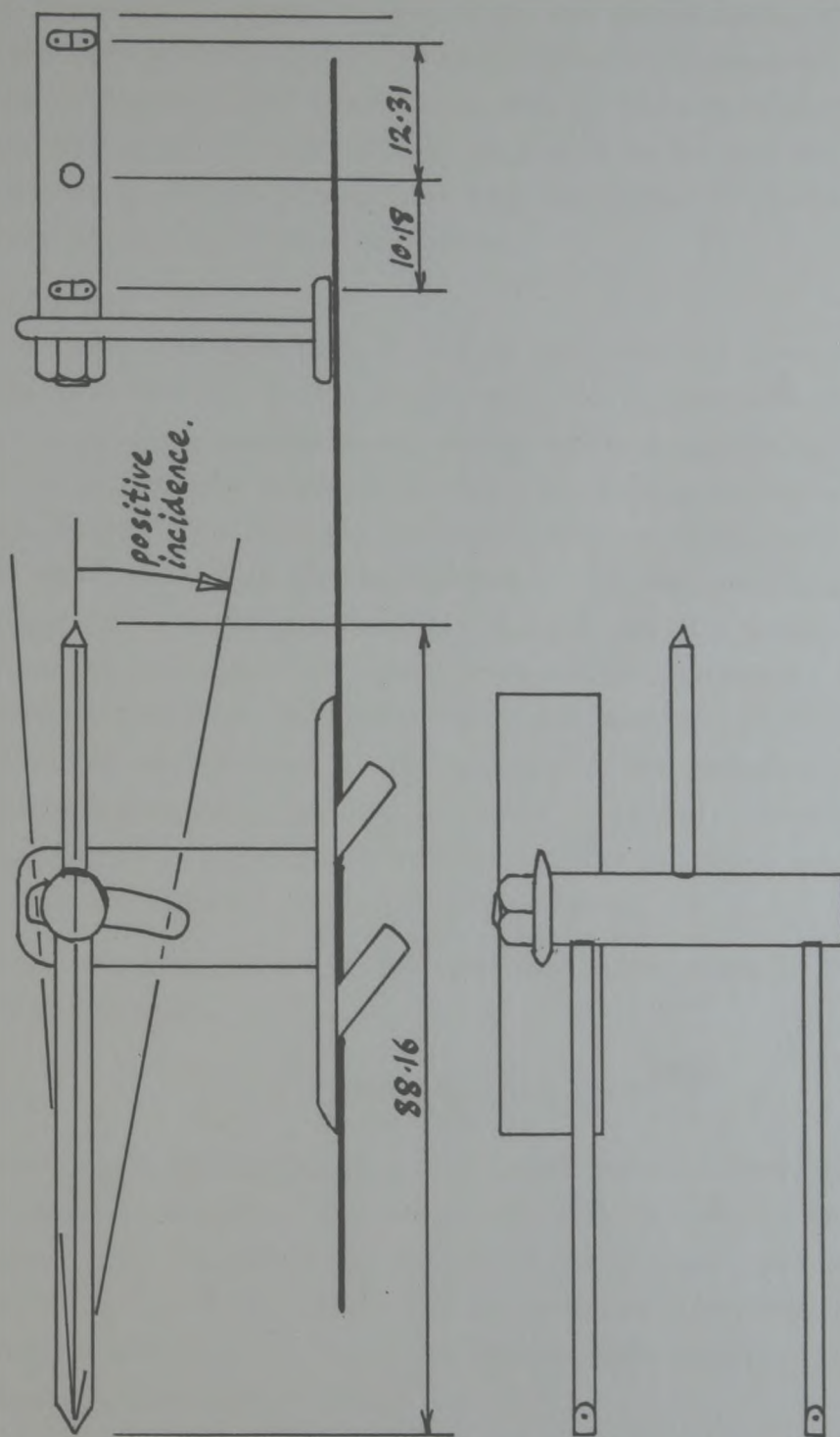


FIGURE (56)

Diagram of Yawmeter Calibration Device

pitch angle of the yawmeters is significantly affected) and rolling below 1.5 degree (again 5 degrees are permissible).

In Figure(56), it can be seen that the tailspike on the mounting device is displaced laterally from both yawmeter tips. Rolling of the mounting device thus caused the height differences between the yawmeter tips and the tailspike to be altered. These alterations in height differences were accounted for before true yawmeter pitch angles were calculated.

### Intercept

The yawmeters were then fitted in the boundary layer rake and the rake mounted in the windtunnel, the bottom wall again being sealed with plastic tape, except for a longitudinal strip about 12 millimetres wide, where the static tappings were situated. In this region, 'Plasticene' was used to block individual perforations.

On the bottom wall of the windtunnel, at the positions 137.5, 223.5 and 309 millimetres from the working section entry, the pressures on the upper and lower faces of the yawmeters, the pressure at the rake stagnation tubes and the wall static pressure distribution were measured. The heights of the yawmeter tips and the tailpin were also measured at these positions. This was done at approximately the same three Mach numbers as those used for the tests to determine the calibration gradients.

Using the mass conservation equation appropriate to flow near a solid wall;

$$\frac{V_e}{u_e} = -\frac{1}{\rho_e u_e} \cdot \frac{d}{dx} (\rho_e u_e (L - \delta^*)) ,$$

the flow angles ( $\theta$ ) relative to the yawmeter tips were calculated from the data recorded. The above equation is adapted from Equation(3.1). Values of  $\Delta p_a$  were also calculated. The respective values of  $\Delta p_a$  and  $\theta$  were then used to determine the intercept of the calibration line at the three Mach numbers chosen. Details of these calculations follow.

### Data Processing.

#### Calibration intercept data

Initially all the pressure data were non-dimensionalized with respect to the effective local freestream pitot pressure( $P_o$ ) which was registered on a rake pitot tube 22 millimetres from the bottom



wall.

A set of simple corrections was then applied to the wall static pressure to account for the pressure field generated by the rake. These corrections were calculated from the pressure disturbances generated at the two yawmeter tips, rake foot and static tapping position by modelling the rake by a set of longitudinal and lateral cylinders in an incompressible potential flow. The corrections are tabulated below. Errors in these calculated corrections will arise from inaccuracies in the modelling and from neglect of compressibility corrections.

POSITION	DISTURBANCE FROM FREESTREAM ( $C_p$ )	CORRECTION FROM WALL STATIC TAPPING ( $\Delta C_p$ )
wall static tapping	0.0097	0.
rake foot	0.0157	0.0060
yawmeter 1 tip	0.0113	0.0016
yawmeter 2 tip	0.0091	-0.0006

Where 
$$C_p = (P_{s_{\text{relevant}}} - P_{\infty}) / \frac{\gamma}{2} P_{\infty} M_{\infty}^2 \quad (2)$$

Thus 
$$\Delta C_p = (P_{s_{\text{corr}}} - P_{s_{\text{uncorr}}}) / \frac{\gamma}{2} P_{\infty} M_{\infty}^2, \quad (3)$$

or, 
$$\frac{P_{s_{\text{corr}}}}{P_0} = \frac{P_{s_{\text{uncorr}}}}{P_0} + \Delta C_p \frac{\gamma}{2} \frac{P_{\infty}}{P_0} M_{\infty}^2. \quad (4)$$

The function  $\Delta p_q$  was then calculated as

$$\frac{\Delta p}{q} = \left( \frac{P_1}{P_0} - \frac{P_2}{P_0} \right) / \left( \frac{\gamma}{\gamma-1} \right) \cdot \left( \frac{P_3}{P_0} \right) \left( \left( \frac{P_3}{P_0} \right)^{\frac{\gamma-1}{\gamma}} - 1 \right) \quad (5)$$

The denominator is a convenient form of 'q', the dynamic pressure local to the yawmeter head calculated from the corrected static pressure mentioned above.

Using the computer program PROF, which is described in Appendix(9), the boundary layer characteristics were computed. All computed boundary layer thicknesses( $\delta$ ) were at least three millimetres less than the height of the lowest yawmeter(Number 1).

From the heights of the tip of yawmeter Number 1 and its tailspike, the angle of the yawmeters relative to the horizon was calculated (this single angle was used for both yawmeters). This angle was then reduced by the value of the local bottom wall angle relative to the horizon to become relative to that wall.

The following list of data was then corrected to a convenient set of three, freestream Mach numbers (0.686, 0.746 and 0.840):

Boundary layer displacement thickness

Static pressure local to the rake foot

Static pressure local to yawmeter Number 1

Static pressure local to yawmeter Number 2

Pressure difference across yawmeter Number 1

Pressure difference across yawmeter Number 2

$\delta^*$   
 $p_s/p_{0r}$   
 $p_s/p_{01}$   
 $p_s/p_{02}$   
 $\Delta p_{q1}$   
 $\Delta p_{q2}$

The mass conservation equation in the form

$$\frac{v_e}{u_e} = -\frac{1}{\rho_e u_e} \cdot \frac{d}{dx} (\rho_e u_e (L - \delta^*))$$

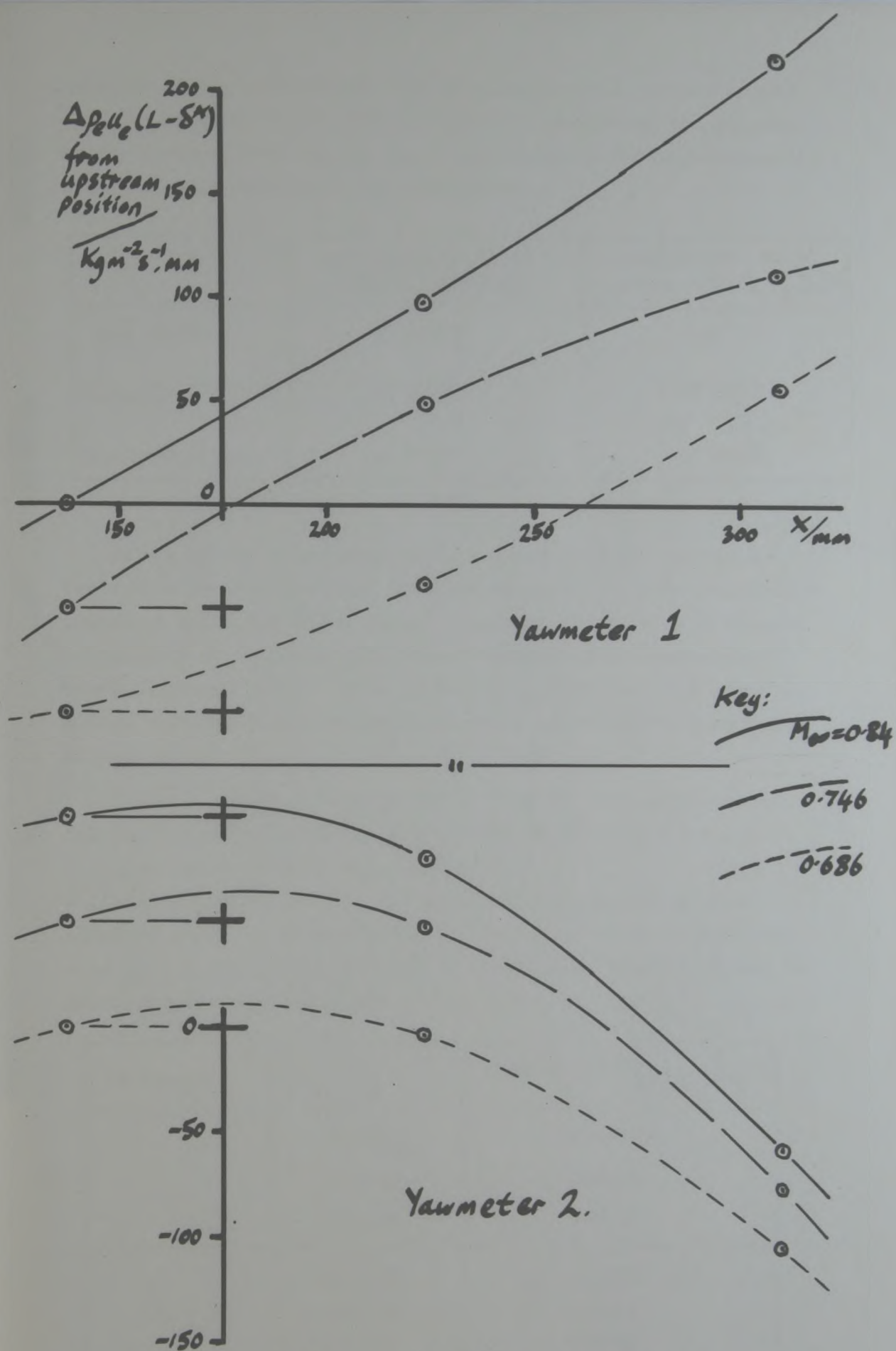
was used to calculate the flow angle at the yawmeter height ( $L$ ) relative to the wall, where  $\rho_e u_e$  was calculated from rake foot static pressures and average values of freestream stagnation pressure and temperature, using isentropic relationships. The derivative with respect to the longitudinal ordinate 'x' on the right-hand side of the above expression was determined as the gradient of the local tangent to the curve of  $\rho_e u_e (L - \delta^*)$  plotted against x (see Figure(57)).

Finally, the angle of the yawmeter relative to the flow was found by adding the local flow angle determined above,  $\frac{v_e}{u_e}$ , to the angle of the yawmeter relative to the wall. Thus a set of points  $(\Delta p_q, \theta)$  were obtained, from which the intercepts of the yawmeter calibration curves were to be calculated. These are presented in Figure(60).

#### Calibration gradient data

In a similar manner to that described above, the pressure data from the calibration gradient device were non-dimensionalized with respect to stagnation pressure in the windtunnel contraction. The wall static pressures were then interpolated in the longitudinal





FIGURE(57) Graph of  $p_{ell_e}(L-\delta^M)$  with longitudinal position  
 -yawmeter calibration tests

ordinate to the yawmeter tip position and using a similar method to that described in the previous section, they were then adjusted to the yawmeter tips in the other two ordinates using incompressible potential flow corrections (listed below).

POSITION	DISTURBANCE FROM FREESTREAM ( $C_p$ )	CORRECTION FROM WALL STATIC ( $\Delta C_p$ )
Wall static	0.0198	0.
Yawmeter 1 tip	0.0181	-0.0017
Yawmeter 2 tip	0.0159	-0.0038

Values of the non-dimensional yawmeter pressure difference, could then be calculated in the same manner as for the calibration intercept data, but these values represent experiments performed unavoidably at slightly different freestream Mach numbers (and hence different local static pressures). They were corrected to a more convenient set of yawmeter static pressures by graphical interpolation.

From the recorded heights of the tips of both yawmeters and the tailpin on the mounting device, the angle of the yawmeters relative to the horizon was calculated. These angles are plotted against the yawmeter pressure differences obtained above, in Figure(58). The method of least squares was then used to fit straight lines to the data in Figure(58) and the gradients of these lines are listed below.

YAWMETER	$P_s/P_0$	Gradient $\partial \Delta P_2 / \partial \theta$ ( $\text{deg}^{-1}$ )
1	0.6054	0.0479
	0.6826	0.0469
	0.7308	0.0438
2	0.6047	0.0458
	0.6820	0.0446
	0.7302	0.0453



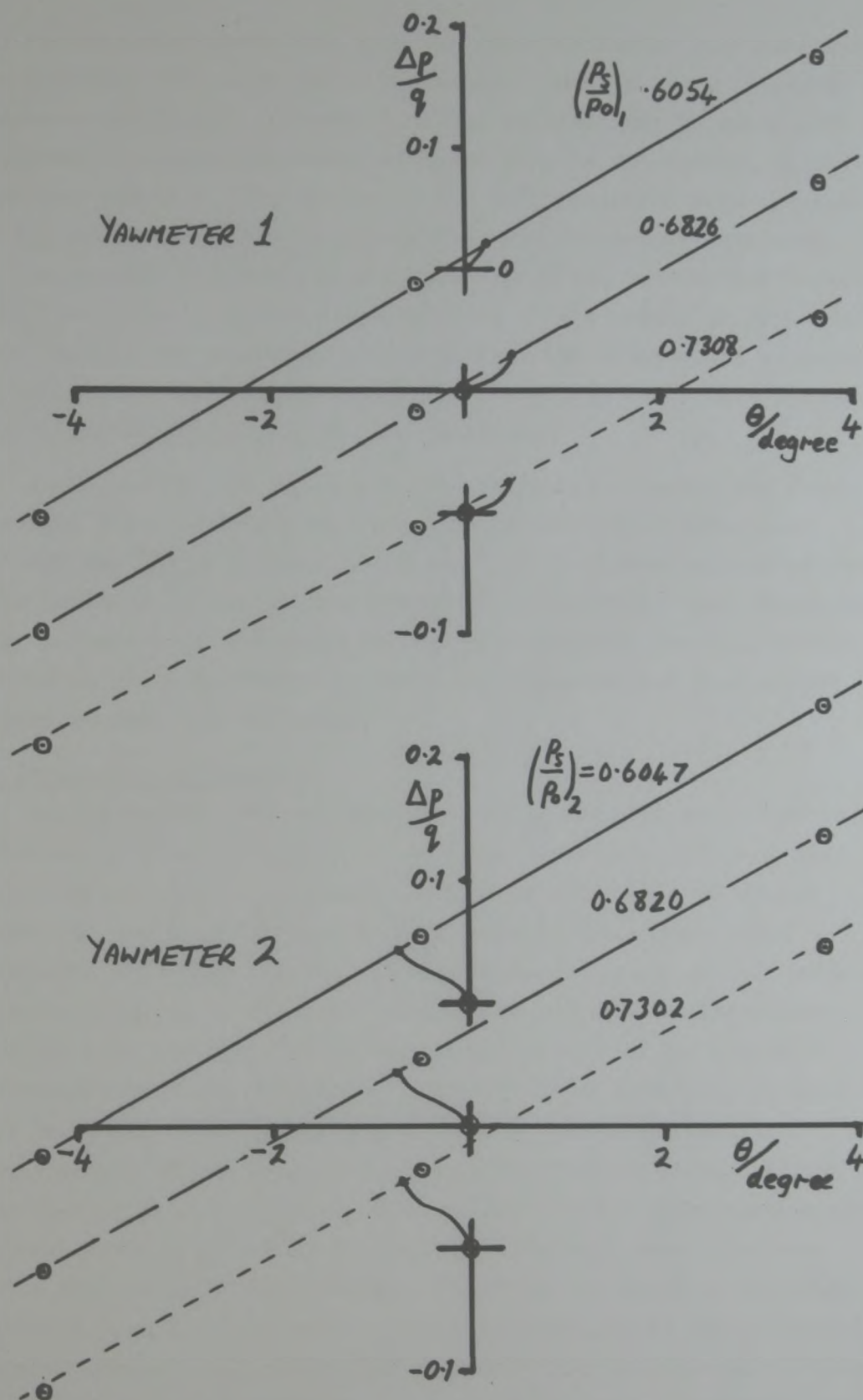


FIGURE (58) Graph of yawmeter pressure difference with yawmeter angle - calibration tests.

In the table above, the data for yawmeter Number 1 is monotonic, the gradient varying by about 10 percent over the range of static pressures tabulated. It seems that the gradient may be genuinely dependant on static pressure, although this is not clearly so for yawmeter Number 2. The gradients for both yawmeters were corrected to the static pressures experienced at the respective yawmeters, in the central longitudinal position during the calibration intercept experiments (The longitudinal derivative of the curves in Figure(57) were used in the preceding calculations. The derivatives calculated at the central longitudinal position are likely to be more accurate than those calculated at the end positions).

In Figure(59) the final yawmeter calibration curves are drawn. Straight lines with the gradients listed above have been drawn through the  $\Delta p_{q, \theta}$  points from Figure(60) that were calculated from data measured at the central longitudinal position. For subsequent use, a summary of the gradients and intercepts of the calibration curves is given in Table(4), where the dependant and independent variables have been reversed.

#### Discussion of results.

In Figure(59), the calibration results are similar to the results produced by other workers (e.g. Ower and Pankhurst, 1969) and the only feature deserving special comment is that the calibration curves do not pass through the origin of co-ordinates. This indicates that when the flow of air approaching one of the yawmeter tips is parallel to the line joining the tip of yawmeter Number 1 and the rake tailpin, the pressures registered on the two faces of the yawmeter are different. This is almost certainly because the faces lie at different angles to the line mentioned, and would happen if the faces are ground at different angles to the centre-line of the yawmeter head, or the yawmeter head centre-line is not parallel to the line mentioned. The non-zero intercept would also occur if there were a significant stagnation pressure gradient normal to the wall in the flow approaching the yawmeter. However during calibration, the yawmeter tips were always outside the wall boundary layer flow, the flow where such stagnation pressure gradients occur.



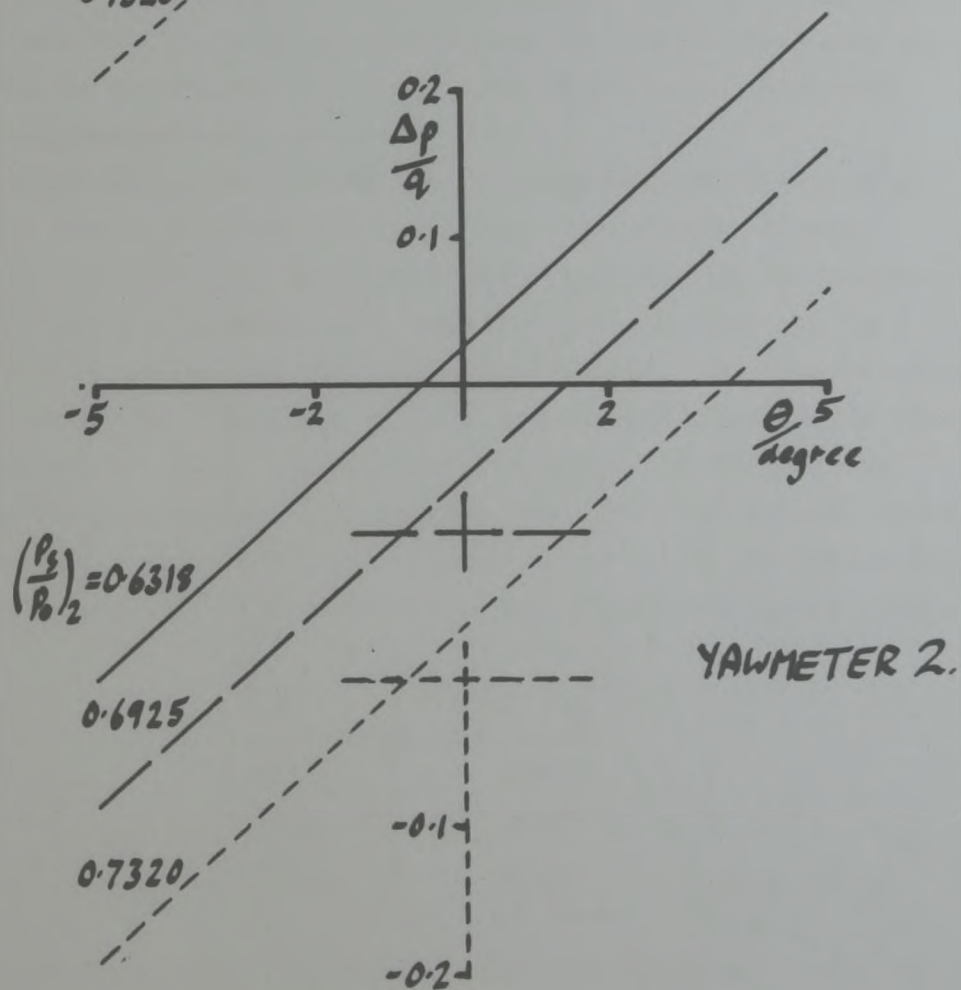
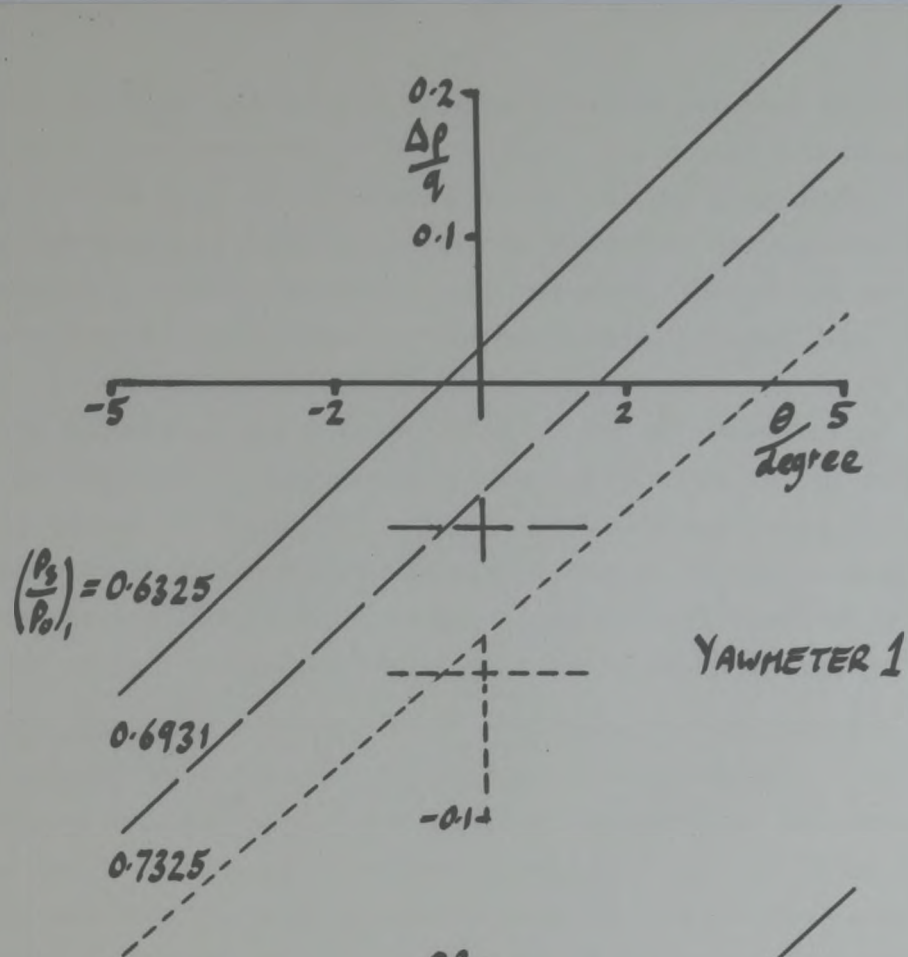


FIGURE (59) Final yawmeter calibration curves.

All the  $\Delta\theta/\theta$  points used to calculate the yawmeter calibration intercepts are presented on Figure(60). The ringed points are those derived from data measured at the central longitudinal position. It is these points which were used to calculate the calibration intercepts. Clearly, at any static pressure, the points may be in considerable disagreement with the relevant ringed one. In terms of the deduced intercept, this disagreement may be as great as 0.75 degrees (or about 0.034 in  $\Delta\theta/\theta$ ). The  $\theta$  component of the data in Figure(60) is affected during calculation by the derivatives of the curves in Figure(57). As these curves are based on data measured at only three longitudinal positions in the windtunnel, the derivatives could be in error. Clearly data measured at a greater number of longitudinal positions would be desirable.

One parameter relevant to the calibration, the boundary layer displacement thickness,  $\delta^*$ , is examined in some detail. The distributions of  $\delta^*$  with x are shown in Figure(61). The steep rises in the values of  $\delta^*$  between x values of 150 and 250mm for the M=0.84 and M=0.746 cases are surprising in view of the facts that the wall is effectively solid and that only gentle favourable pressure gradients are present. Predictions using the boundary layer code developed during this research are also shown on the Figure. The prediction uses pressure distributions measured without the rake in the windtunnel, but ones which are essentially similar to those used for the calculations leading to the calibration curves. Reasonable agreement between the prediction and the experimental results is obtained for the M=0.686 case, but clearly not so for the M=0.84 case. During the experiments, the pressure drop from the working section to the plenum chamber was not maintained at zero, but the actual pressure drops are listed below for the three Mach numbers used.

$M_\infty$	average $\frac{P_s - P_{st}}{P_0}$
0.686	0.05
0.746	0.08
0.840	0.17

The plastic tape used to seal the perforated wall would be noticeably deformed into the perforations by even the smallest of



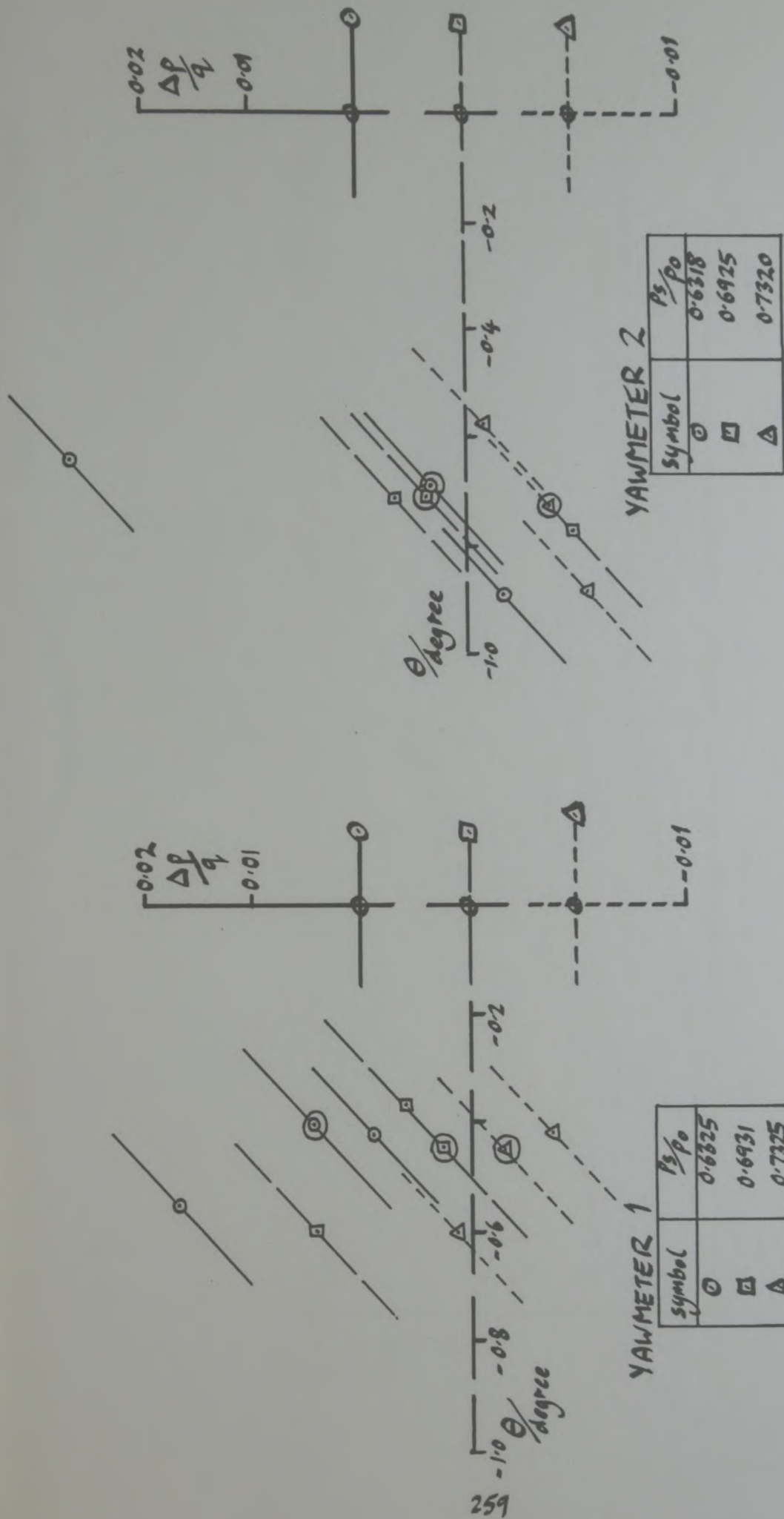


FIGURE (60) Yawmeter calibration curve, intercept data.

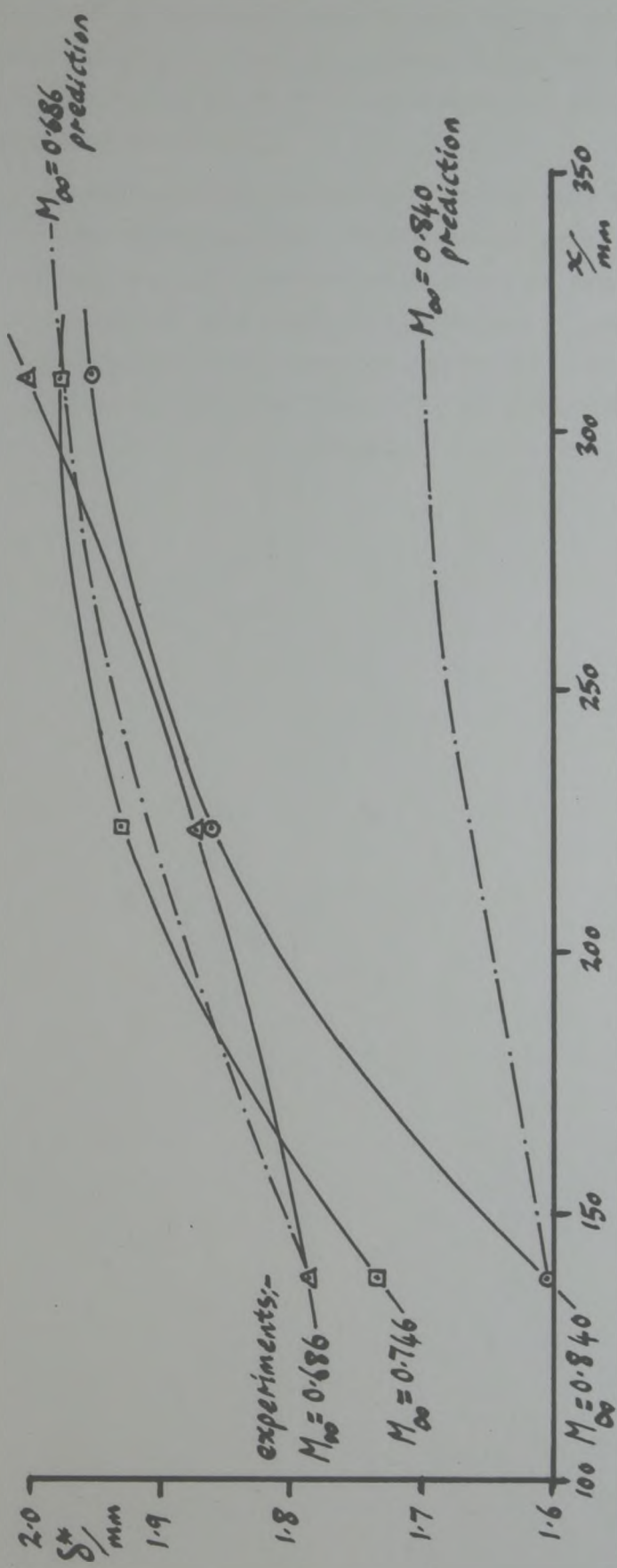


FIGURE (61) Boundary layer displacement thickness distributions - yawmeter calibration tests.



these pressure drops. It would seem reasonable then that the large growth rates of  $\delta^*$  in Figure(61) are caused by the perforations presenting increased roughness with Mach number, which the boundary layer code(which is based on smooth wall measurements) would not be capable of predicting accurately.

The gradients of the yawmeter calibration curves were calculated from the data presented in Figure(58). Measurements were made at only three yawmeter angles. To increase confidence in the gradients calculated, data measured at more angles is required. However, it is encouraging that a separate, more comprehensive, but somewhat less careful calibration of yawmeter Number 1 yielded gradients which differed from the calibration described by less than 4 percent.

## APPENDIX 8

### Estimation of errors in yawmeter calibration.

Here, an estimate is made of the worst error which could be generated during the calculation of any ~~one~~ flow angle which is used for the production of the yawmeter calibration. This work is not entirely rigorous. It should strictly take into account more possible sources of error, but at the same time should not use 'worst' error analysis, but 'likely' errors.

In Appendix(7), the method of evaluating the intercept of the yawmeter calibration is explained. The effective error in these calibration points can be considered to come from three sources. These are (1) The error in calculating the angle of the yawmeter reference line relative to the bottom liner of the windtunnel,

(2) the net error in calculating the value of  $\Delta p/q$  and (3) the error in the calculation of the boundary layer displacement thickness,  $\delta^*$ , which is used to determine the angle of the flow relative to the bottom liner, near the yawmeter.

These contributing errors are considered in order. First, the error in calculating the angle of the yawmeter relative to the bottom wall. This angle is determined by measuring the respective heights of the tip of yawmeter Number 1 and the tail pin, on the combined rake. A travelling telescope is used for this purpose. The worst error possible in measuring the height of a point with the telescope is 0.045mm. Thus the error in calculating the difference in height between two points is twice this figure, namely 0.09mm. The distance between the two points in question is 82.48mm. Thus the error in angle of the reference line is

$$\sin^{-1} (0.09 / 82.48)$$

or 0.06 degree.

Second, the net error in calculating the value of  $\Delta p/q$ . This function is calculated using Equation(5) of Appendix(7), namely

$$\frac{\Delta p}{q} = \left( \frac{p_1 - p_2}{p_0} \right) / \left( \left( \frac{p_s}{p_0} \right) \left( \frac{\gamma}{\gamma - 1} \right) \left( \left( \frac{p_s}{p_0} \right)^{\frac{1-\gamma}{\gamma}} - 1 \right) \right) \quad (1)$$



Here  $p_1$  and  $p_2$  are the pressures at the lower and upper orifice of the yawmeter head respectively, and  $p_s$  is the static pressure in the flow approaching the yawmeter. Each of the pressures in the equation may be in error for various reasons. The transducer used to measure the pressures has a calibration which is evaluated each time the windtunnel is operated. Nevertheless, its calibration equation may be in error. A typical condition for this equation is

$$p = 31.467 V + 85347 \quad , \quad (2)$$

where  $p$  is the relevant pressure in Pascals and ' $V$ ' is the voltage measured across the transducer bridge, in units of  $10^{-5}$  Volt. This unit is chosen, as it represents one digit in the last place on the display of the digital voltmeter used to indicate the transducer output voltage. In the mode of transducer calibration employed, the first constant in Equation (2) may be in error of 0.148% and the second, in error by 0.023%. For one operation of the windtunnel, these errors (at worst) will be applied systematically to the calculation of all pressures measured. As a digital voltmeter is used, there is an additional uncertainty involved in each pressure, of as much as the equivalent of one digit in the last place, namely 30 Pa. The value of  $P_o$ , the stagnation pressure, has been found under extreme conditions to be in error of 0.1% from the true local stagnation pressure. Consider a typical value of the term  $(P_1 - P_2)$  in Equation (1), for example 6661.1 Pa and of  $P_o$ , 100 000 Pa for example. Combining the errors described above in the worst manner in the calculation of the term  $(P_1 - P_2)/P_o$ , we find an error of -1.17% in this expression. The term  $p_s/p_o$  in the denominator of Equation (1) will contain the errors mentioned above, concerning the transducer calibration and the digital voltmeter. In addition, using a wall static tapping mounted between perforations will yield erroneous pressures when there is flow through the local perforations. This problem was discussed in the main text, Section (4.2.6). In that section it was indicated that the maximum error likely to occur as a result of this, is 0.0075 (in pressure coefficient), or 0.0025 in terms of  $p_s/p_o$ . In making a correction to the wall static pressure, to make it represent the pressure at the yawmeter head, certain simplifying assumptions are made concerning the rake geometry. Also compressibility is not accounted for. It is assumed that these



simplifications involve a further error of approximately 0.0003 in terms of  $P_3/P_0$ . Thus the total additional error in the term  $P_3/P_0$  is 0.0028. If all the errors in  $P_3/P_0$  are combined adversely in Equation(1) and the stated error in the numerator of that equation is included, then  $\Delta P_q$  is calculated as 0.2 with a net error of -0.0039. In Table(4), a typical value of  $d\theta/d\Delta P_q$  is 22. Thus the error predicted above of 0.0039 in terms of  $\Delta P_q$  represents  $0.09^\circ$  as an angle.

Thirdly and finally, the error in the calculated yaw angle produced by inaccurate calculation of the boundary layer displacement thickness,  $\delta^*$ , is assessed. The displacement thickness is calculated from the measured values of pressure, using the computer program, PROF. This program is described in Appendix(9). If a set of precise data was input to this program, would the calculated value of  $\delta^*$  represent this data exactly? To answer this question, a boundary layer stagnation pressure profile, typical of those measured during the yawmeter calibration experiments was expressed as a written function. It was then possible to treat this function in two ways. First, to take discrete points from the profile as input data for the program PROF. Second, to process this function directly to yield an exact value of  $\delta^*$ . For the case in question, PROF was found to give a value of  $\delta^*$  0.02mm in excess of the exact figure. In the second investigation mentioned in this Appendix, errors due to the pressure transducer calibration, due to the digital voltameter and due to phenomena in the windtunnel flow are discussed. These same sources of error affect the pressure data used to calculate values of  $\delta^*$ . Supplying erroneous pressure data to the program PROF naturally produces values of  $\delta^*$  which are further in error. In fact, the worst possible combination of errors in the input data for PROF produces an error in the calculated  $\delta^*$  of 0.1mm. One further inaccuracy in  $\delta^*$  which may be caused, is that due to the region of compression just upstream of the boundary layer rake. This region of compression would cause the boundary layer to thicken to some extent, and thus the measured value of  $\delta^*$  would not be that which would exist in the undisturbed flow. However, from the point of view of the yawmeter calibration, the function of interest is  $d\delta^*/dx$ , rather than  $\delta^*$  alone. A brief investigation into the error in this function was carried out using the boundary layer prediction method described in this report (Section(3.5)).



Data relating to the compression ahead of a boundary layer rake of inferior design were supplied as input to the boundary layer calculation. By effectively positioning the rake at different points along the wall, it was possible to examine the influence of the rake's presence on the value of  $\frac{d\delta^*}{dx}$  which would be measured, relative to that in undisturbed flow. This difference in  $\frac{d\delta^*}{dx}$  due to the presence of the rake was  $2.8 \times 10^{-5}$ . Combining the first two causes of error in values of  $\delta^*$  (and thus indirectly in values of  $\frac{d\delta^*}{dx}$ ) with the final direct error in the value of  $\frac{d\delta^*}{dx}$ , the total error becomes 0.0019. When the value of  $\frac{d\delta^*}{dx}$  is used to calculate the angle of the flow relative to the wall for the purposes of yawmeter calibration, the error in the derivative is equivalent to  $0.11^\circ$ .

#### Summary.

The error in the calibration intercept points is considered to consist of three contributions. These contributions have been calculated using a 'worst error' analysis as follows:-

(1) The error involved in the estimation of the angle of the yawmeters relative to the bottom liner, namely  $0.06^\circ$ .

(2) The error due to inaccurate evaluation of the term  $\frac{\Delta p}{q}$ , namely  $0.09^\circ$ .

(3) The error introduced through inaccurate calculation of the boundary layer displacement thickness,  $\delta^*$ , namely  $0.11^\circ$ .

These three errors amount to  $0.26^\circ$  when added directly. This should represent the maximum level of scatter in the yawmeter calibration intercept points in Figure(60).

## APPENDIX 9.

The computer program PROF. for analysing boundary layer profiles.

The experimental data available for calculating the characteristics of the boundary layers measured in the transonic windtunnel are, the local static pressure at the rake position,  $P_s/P_0$ , and the values of the pitot pressure measured on the 14 boundary layer rake tubes,  $P_{0r}/P_0$  (where these pressures are non-dimensionalized with respect to the highest pressure recorded on the rake). From these data, it is required to calculate chiefly the displacement thickness,  $\delta^*$ . It is also helpful to obtain information concerning the boundary layer profile, shape factor and momentum thickness.

### Assumptions.

In carrying out the analysis, it is necessary to make certain assumptions concerning the flow in and near the boundary layer. It is assumed that

- (a) the boundary layer is turbulent (an assumption which is almost certainly justified),
- (b) the perforated wall is adiabatic,
- (c) the static pressure is constant across the depth of the boundary layer (Cebeci and Smith, 1974, pp 73-75). and that
- (d) the recovery of total temperature through the boundary layer is 0.8825 times the recovery if the flow were fully isentropic (Mack, 1954).

### Theory.

Using the above assumptions, it is possible to calculate an important parameter,  $P_{0r}/P_{0e}$ , which is then used to compute values of  $\delta^*$ . In the fourth assumption concerning the temperature recovery, it should be noted that the factor quoted is an average value taken from Mack (1954). If the recovery factor is denoted  $r$ , then using the work of Mack, the total temperature in the boundary layer may be expressed

$$T_0 = T_e + r \left( \frac{u_e^2 - u^2}{2C_p} \right) + \frac{u^2}{2C_p} \quad (1)$$

Here, the isentropic temperature rise has been moderated by the factor,  $r$ , and  $C_p$  is the specific heat of air (at constant pressure)



In the same way, the static temperature in the boundary layer may be expressed

$$T = T_e + f\left(\frac{u_e^2 - u^2}{2C_p}\right), \quad (2)$$

$$\text{or} \quad \frac{T}{T_e} = 1 + f\left(\frac{u_e^2 - u^2}{2C_p T_e}\right). \quad (3)$$

Using the perfect gas law it may be shown that

$$C_p T_e = \frac{a_e^2}{\gamma - 1} \quad (4)$$

and combining this with Equation (3) we find

$$\frac{T}{T_e} = 1 + f\left(\frac{\gamma - 1}{2}\right) M_e^2 \left(1 - \left(\frac{u}{u_e}\right)^2\right). \quad (5)$$

Now

$$\frac{u}{u_e} = \frac{a}{a_e} \cdot \frac{M}{M_e} \quad (6)$$

and

$$\frac{a}{a_e} = \sqrt{\frac{T}{T_e}} \quad (7)$$

Combining Equations (5), (6) and (7),

$$\frac{u}{u_e} = \frac{M}{M_e} \cdot \left\{1 + f\left(\frac{\gamma - 1}{2}\right) M_e^2 \left(1 - \left(\frac{u}{u_e}\right)^2\right)\right\}^{\frac{1}{2}}. \quad (8)$$

After some manipulation, Equation (8) becomes

$$\frac{u}{u_e} = \sqrt{\left(\frac{1}{M_e^2} + f\left(\frac{\gamma - 1}{2}\right)\right) / \left(\frac{1}{M^2} + f\left(\frac{\gamma - 1}{2}\right)\right)}. \quad (9)$$

Again using the perfect gas law,

$$\frac{\rho}{\rho_e} = \frac{p}{p_e} \cdot \frac{T_e}{T},$$

but  $p$  and  $p_e$  are assumed to be the same, so combining this with Equation (5),

$$\frac{\rho}{\rho_e} = 1 / \left\{1 + f\left(\frac{\gamma - 1}{2}\right) M_e^2 \cdot \left(1 - \left(\frac{u}{u_e}\right)^2\right)\right\}. \quad (10)$$

To evaluate  $Me$ , the isentropic expression

$$M_e = \left\{ \left( \left( \frac{P_s}{P_o} \right)^{\frac{1-\gamma}{\gamma}} - 1 \right) \cdot \frac{2}{\gamma-1} \right\}^{\frac{1}{2}} \quad (11)$$

is used. Note that  $P_o$  in Equation (11) has already been chosen to be the highest pitot pressure on the rake, or the freestream stagnation pressure. For the local Mach Number,  $M$ , Equation (11) is also used but  $\frac{P_s}{P_o}$  is replaced by  $\frac{P_s}{P_{or}}$ , where

$$\frac{P_s}{P_{or}} = \left( \frac{P_s}{P_o} \right) \cdot \left( \frac{P_{or}}{P_o} \right)^{-1}.$$

Equations (9), (10) and (11) are then used to calculate values of  $\frac{\rho u}{\rho_o u_e}$ .

In Ower and Pankhurst (1969) it is suggested that a pitot tube mounted in a shear flow, disturbs the flow around it in such a way as to register the stagnation pressure in the flow slightly above its centre-line position. A correction to the actual tube heights is thus required. For the tubes in question (having internal and external diameters of 0.012 and 0.025 inch respectively) they propose a correction of 0.17 diameters. Macmillan (1956) suggests a correction which is smaller by approximately 0.02 diameters. A figure of 0.15 diameters is used and applied to all the heights of the boundary layer pitot tubes.

The boundary layer displacement thickness, momentum thickness and shape factor are calculated using the normal equations;

$$\delta^* = \int_0^{\infty} \left( 1 - \frac{\rho u}{\rho_o u_e} \right) dz, \quad (12)$$

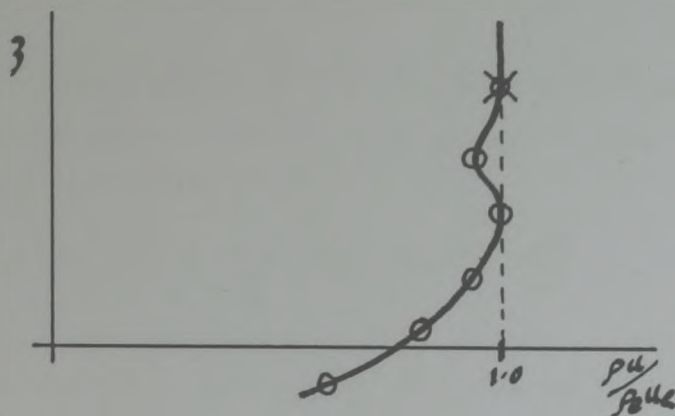
$$\theta = \int_0^{\infty} \frac{\rho u}{\rho_o u_e} \left( 1 - \frac{\rho u}{\rho_o u_e} \right) dz \quad (13)$$

and

$$H = \delta^* / \theta. \quad (14)$$

In our case, the limit of infinity must be adapted. The integrals are performed up to the height of the highest tube where the freestream pitot pressure is recorded. In the illustration below, part of a velocity profile is shown, somewhat magnified.





The discrete points represent the data points from the rake tubes. On some occasions, the experimental profiles do have a minor trough in them after the flow appears to have reached full speed. The integration would be carried up to the data point marked with an X. It is not entirely clear whether the boundary layer ceases at this point or the lower 'full speed' point. In any case the difference in the value of  $\delta^*$  when calculated is of the order of 0.001mm and is considered negligible.

The integrands in Equations (12) and (13) are generated and the integration carried out in the following manner. The profile is first split into groups of three data points. Using the method of Nonweiler (1968), a quadratic function is generated for the curve passing through these points, and the respective contribution to the total integral is calculated. To complete the integral near the wall, one or two points (depending on whether the total number of data points is even or odd) are generated by extrapolating the last calculated quadratic function, and Nonweiler's algorithm is applied once again.

The entire calculation procedure is coded into a FORTRAN program titled PROF. Results from the program are given in Section (4.3.5). In Appendix (8), it was mentioned that for a typical boundary layer profile, the program PROF over-estimated the value of  $\delta^*$  by 0.02mm compared to an exact calculation. To date this is the only examination of the accuracy of PROF which has been carried out.

# APPENDIX (10).

Calculation of the parameter  $\frac{\rho_e}{\rho_\infty} u_\infty$  in terms of known variables.

The exact expression for the local speed of sound (a) in two-dimensional isentropic flow is

$$a^2 = a_\infty^2 + \frac{\gamma-1}{2} (u_\infty^2 - (u^2 + v^2)) \quad (1)$$

where u and v are the local velocity components parallel to and normal to the freestream direction. The flow of interest is that just outside the boundary layer (subscripted 'e'). Dividing Equation (1) by 'a<sub>e</sub>' and using the relevant subscript;

$$\begin{aligned} \left(\frac{a_e}{a_\infty}\right)^2 &= 1 + \frac{(\gamma-1)}{2} \left( M_\infty^2 - \left(\frac{u_e}{a_\infty}\right)^2 - \left(\frac{v_e}{a_\infty}\right)^2 \right) \\ \text{or} \quad &= 1 + \frac{(\gamma-1)}{2} M_\infty^2 \left( 1 - \left(\frac{u_e}{u_\infty}\right)^2 - \left(\frac{v_e}{u_\infty}\right)^2 \right) \end{aligned} \quad (2)$$

Using the perfect gas law and assuming adiabatic, isentropic flow, it can be shown that

$$\left(\frac{a_e}{a_\infty}\right)^2 = \left(\frac{p_e}{p_\infty}\right)^{\frac{\gamma-1}{\gamma}} \quad (3)$$

and

$$\left(\frac{\rho_e}{\rho_\infty}\right) = \left(\frac{p_e}{p_\infty}\right)^{\frac{1}{\gamma}} \quad (4)$$

Re-writing Equation (2) in terms of  $\frac{u_e}{u_\infty}$  and using Equation (3),

$$\left(\frac{u_e}{u_\infty}\right) = \left\{ 1 - \left(\frac{v_e}{u_\infty}\right)^2 - \left[ \left(\frac{p_e}{p_\infty}\right)^{\frac{\gamma-1}{\gamma}} - 1 \right] \cdot \frac{2}{\gamma-1} \cdot \frac{1}{M_\infty^2} \right\}^{\frac{1}{2}} \quad (5)$$

Thus, combining Equations (4) and (5)

$$\left(\frac{\rho_e u_e}{\rho_\infty u_\infty}\right) = \left(\frac{p_e}{p_\infty}\right)^{\frac{1}{\gamma}} \cdot \left\{ 1 - \left(\frac{v_e}{u_\infty}\right)^2 - \left[ \left(\frac{p_e}{p_\infty}\right)^{\frac{\gamma-1}{\gamma}} - 1 \right] \cdot \frac{2}{\gamma-1} \cdot \frac{1}{M_\infty^2} \right\}^{\frac{1}{2}} \quad (6)$$

It would be very simple to calculate the term;  $\frac{p_e}{\rho_\infty}$  thus

$$\frac{p_e}{\rho_\infty} = \frac{p_e}{\rho_o} \cdot \left(\frac{\rho_\infty}{\rho_o}\right)^{-1}$$

(where p<sub>e</sub> could be replaced by p<sub>s</sub>, the wall static pressure, as shown in Section (4.2.6.)). However for later use in the program PREDICT, it is more helpful to express  $\frac{p_e}{\rho_\infty}$  in terms of the wall pressure coefficient. Re-writing Equation (4.7), namely



$$C_p = \left( \frac{P_s}{P_o} - \frac{P_{\infty}}{P_o} \right) / \frac{\gamma}{2} \cdot \frac{P_{\infty}}{P_o} \cdot M_{\infty}^2$$

we find

$$C_p \cdot \frac{\gamma}{2} \cdot M_{\infty}^2 = \left( \frac{P_s}{P_o} - \frac{P_{\infty}}{P_o} \right) / \frac{P_{\infty}}{P_o}$$

or

$$= \frac{P_s - P_{\infty}}{P_{\infty}}.$$

Thus, replacing  $P_s$  by  $P_e$ , we find

$$\frac{P_e}{P_{\infty}} = \left( C_p \cdot \frac{\gamma}{2} \cdot M_{\infty}^2 + 1 \right). \quad (7)$$

The only remaining term in Equation (6) to be considered is  $(v_e/u_{\infty})^2$ . This is replaced by  $(v_e/u_e)^2$ . The error involved in making this step is less than 0.1% in the value of  $\frac{\rho_e u_e}{\rho_{\infty} u_{\infty}}$  in even the most extreme conditions experienced. Thus Equation (6) becomes

$$\left( \frac{\rho_e u_e}{\rho_{\infty} u_{\infty}} \right) = \left( \frac{P_e}{P_{\infty}} \right)^{\frac{1}{\gamma}} \cdot \left\{ 1 - \tan^2 \theta_e - \left[ \left( \frac{P_e}{P_{\infty}} \right)^{\frac{\gamma-1}{\gamma}} - 1 \right] \cdot \frac{2}{\gamma-1} \cdot \frac{1}{M_{\infty}^2} \right\}^{\frac{1}{2}}, \quad (8)$$

when  $v_e/u_e$  has been replaced by  $\tan \theta_e$  as in Equation (4.10).

Equations (7) and (8) may then be used to calculate the required parameter from known variables.

**Appendix 11**  
**Listing of the Computer Program**  
**PREDICT (p.272-278) has been**  
**removed for copyright reasons**



## REFERENCES.

- ALBONE, C.M. (1974) An improved numerical method for solving the transonic small-perturbation equation for the flow past a lifting aerofoil. RAE Technical Report 74056, August 1974.
- BAKER, T.J. (1980) Private communication.
- BERNDT, S.B. (1965) Flow Properties of Slotted Walls for Transonic Test Sections. In: Wind-tunnel Design and Testing. 6-8 October, 1975. Proceedings. AGARD CP174, Paper 17.
- BEVINGTON, P.R. (1969) Data Reduction and Error for the Physical Sciences. (Mc Graw-Hill)
- BRADSHAW, P. (1974). An improved FORTRAN programme for the Bradshaw-Ferris-Atwell method of calculating turbulent shear layers. Imperial College Aero Report 74-02.
- CARR, M. (1980) Private communication.
- CATHERALL, D. (1975) The Computation of transonic flows past aerofoils in solid, porous or slotted wind tunnels. In: Windtunnel Design and Testing Techniques. 6-8 October 1975. Proceedings. AGARD CP 174, Paper 19.
- CATHERALL, D. (1978) Private communication.
- CEBECI, T. (1974). Analysis of Turbulent Boundary Layers. New York; Academic Press.
- SMITH, A.M.O.
- CHAN, Y.Y. (1980). Boundary Layer development on Perforated walls in Transonic Wind Tunnels. Laboratory Technical Report LTR-HA-47 National Aeronautical Establishment National Research Council Canada, Ottawa. 8 February 1980.

- CHAN, Y.Y. (1980) Private communication.
- EBIHARA, M. (1972) A study of Subsonic, Two-Dimensional Wall Interference effects in a perforated Wind Tunnel with Particular Reference to the NAL 2mx2m Transonic Wind Tunnel-- Inapplicability of the Conventional Boundary Condition. Technical Report of the National Aerospace Laboratory TR 252T (Tokyo, Japan) January 1972.
- FREESTONE, M.M. (1979). Private communication.
- FREESTONE, M.M. (1981). Incorporation of Viscous Effects of Perforated Windtunnel Walls in Two-dimensional Flow Calculations. Research Memo. Aero 81/1. City University, London. Department of Aeronautics. January 1981..
- HENINGTON, P.
- GOETHERT, B.H. (1961) Transonic Wind Tunnel Testing. AGARDograph No 49. (Oxford: Pergamon Press )
- GREEN, J.E. (1968) The Prediction of Turbulent Boundary Layer Development in Compressible Flow. Journal of Fluid Mechanics Vol 31 Part 4 pp 753-778.
- HEAD, M.R. (1960). Entrainment in the turbulent boundary layer. Aeronautical Research Council Reports and Memoranda No 3152.
- HEAD, M.R. (1968) Improved Entrainment Method for Calculating Turbulent Boundary Layer Development. Aeronautical Research Council Reports and Memoranda No 3643. March, 1968.
- PATEL, V.C.



- JACOBS, J.L. (1976) An Investigation of the Aerodynamic Characteristics of Ventilated Test Section Walls for Transonic Wind Tunnels. Ph.D. Dissertation, University of Tennessee, December 1976.
- KACPRZYNSKI, J.J. (1976) Transonic flowfield past two-dimensional airfoils between porous Wind-tunnel Walls. AIAA (Journal) Vol 14 April 1976. pp 5335.
- KEMP, W.B. (1976). Toward the correctable-interference transonic wind tunnel. In: 9th. Aerodynamic Testing Conference. Proceedings. pp 32-38.
- KEMP, W.B. (Jr) (1978). Transonic assessment of two dimensional wind tunnel wall interference using measured wall pressures. Advanced Technology Airfoil Research NASA Vol. 1 part 2, p473-486. Star ref. N79-19991.
- KRUSE, H. (1978). Boundary layer calculation of an Effusion cooled turbine blade. AIAA 16th Aerospace Sciences Meeting. (paper 78-90).
- LOCK, R.C. (1975). Research in the U.K. on Finite Difference Methods for Computing steady transonic flows. R.A.E. Technical Memo. Aero 1644. July 1975.
- LOCK, R.C. (1975). Calculation of viscous effects on Aerofoils in Compressible flow. R.A.E. Technical Memo: Aero 1646, September 1975.
- LUDWEIG, H. (1950) Investigations of the wall-shearing stress in Turbulent Boundary Layers. NACA Washington TM 1285.
- TILLMANN, W.

- MACK, L.B. (1954) An Experimental Investigation of the Temperature recovery factor.  
Jet Propulsion Lab., Rep. 20-80.  
California Institute of Technology,  
Pasadena, California.
- MACMILLAN, F.A. (1956) Experiments on Pitot Tubes in shear flow. ARC Reports and Memoranda, 3028.
- MOKRY, M. (1974). Wall interference on two-dimensional Supercritical Airfoils, using wall pressure measurements to determine the porosity factors for tunnel floor and ceiling. NRC/NAE Aero Report LR 575, National Research Council Canada, February, 1974.
- PEAKE, D.J.  
BOWKER, A.J.
- NONWEILER, T.R.F. (1968) The Numerical Evaluation of Curvilinear Integrals and Areas.  
Aeronautical Journal Vol. 72.  
pp887-888, October, 1968.
- OWER, E. (1969) The measurement of Air Flow.  
PANKHURST, R.C. (Pergamon).
- PATEL, V.C. (1965) Contributions to the Study of Turbulent Boundary Layers. Ph.D Thesis.  
Cambridge University, Selwyn College.
- STERLAND, R.W. (1981) An Investigation of the flow through a Perforated Wall in a Low Speed Wind Tunnel. Undergraduate Project Report. The City University, Department of Aeronautics, May 1981.
- VIDAL, R.J. (1975) Experiments with a self correcting Windtunnel. In: Windtunnel Design and Testing Techniques, 6-8 October, 1975. Proceedings. AGARD CP174,  
ERICKSON, J.C. (Jr)  
CATLIN, P.A. Paper 11.